HAL open science

Flow boiling in straight heated tube under normal gravity and microgravity conditions

Marine Narcy

To cite this version:

Marine Narcy. Flow boiling in straight heated tube under normal gravity and microgravity conditions. Fluids mechanics [physics.class-ph]. Institut National Polytechnique de Toulouse - INPT, 2014. English. NNT : 2014INPT0111 . tel-03311950v2

HAL Id: tel-03311950

https://hal.science/tel-03311950v2

Submitted on 26 Oct 2023

HAL is a multi-disciplinary open access archive for the deposit and dissemination of scientific research documents, whether they are published or not. The documents may come from teaching and research institutions in France or abroad, or from public or private research centers.

L'archive ouverte pluridisciplinaire **HAL**, est destinée au dépôt et à la diffusion de documents scientifiques de niveau recherche, publiés ou non, émanant des établissements d'enseignement et de recherche français ou étrangers, des laboratoires publics ou privés.

THÈSE

En vue de l'obtention du

DOCTORAT DE L'UNIVERSITÉ DE TOULOUSE

Délivré par :

Institut National Polytechnique de Toulouse (INP Toulouse)

Discipline ou spécialité :

Energétique et Transferts

Présentée et soutenue par :

Mme MARINE NARCY

le mardi 25 novembre 2014

Titre :

FLOW BOILING IN STRAIGHT HEATED TUBE UNDER NORMAL GRAVITY AND MICROGRAVITY CONDITIONS

Ecole doctorale :

Mécanique, Energétique, Génie civil, Procédés (MEGeP)

Unité de recherche :

Institut de Mécanique des Fluides de Toulouse (I.M.F.T.)

Directeur(s) de Thèse :

Mme CATHERINE COLIN

Rapporteurs :

M. PAOLO DI MARCO, UNIVERSITA DI PISA
M. REMI REVELLIN, INSA LYON

Membre(s) du jury :

M. LOUNES TADRIST, UNIVERSITE AIX-MARSEILLE 1, Président
M. JUNGHO KIM, UNIVERSITE DE MARYLAND, Membre
M. MARC MISCEVIC, UNIVERSITE TOULOUSE 3, Membre
Mme CATHERINE COLIN, INP TOULOUSE, Membre

University of Toulouse

Doctoral Thesis

Flow boiling in straight heated tube under microgravity conditions

Author:
Marine Narcy

Supervisor:
Pr. Catherine Colin

A thesis submitted in fulfilment of the requirements for the degree of Doctor of the University of Toulouse

in the

Interface Group
Institut de Mécanique des Fluides de Toulouse - IMFT

February 2015

Declaration of Authorship

I, Marine Narcy, declare that this thesis titled, 'Flow boiling in straight heated tube under microgravity conditions ' and the work presented in it are my own. I confirm that:

- This work was done wholly or mainly while in candidature for a research degree at this University.
- Where any part of this thesis has previously been submitted for a degree or any other qualification at this University or any other institution, this has been clearly stated.
- Where I have consulted the published work of others, this is always clearly attributed.
- Where I have quoted from the work of others, the source is always given. With the exception of such quotations, this thesis is entirely my own work.
- I have acknowledged all main sources of help.
- Where the thesis is based on work done by myself jointly with others, I have made clear exactly what was done by others and what I have contributed myself.

"When the water starts boiling, it is foolish to turn off the heat."

Nelson Mandela

Also applies to HFE-7000 at IMFT.

UNIVERSITY OF TOULOUSE

Abstract

Institut National Polytechnique de Toulouse - INP Toulouse
Institut de Mécanique des Fluides de Toulouse - IMFT

Doctor of the University of Toulouse

Flow boiling in straight heated tube under microgravity conditions

by Marine Narcy

Forced convective boiling experiments of HFE-7000 in a vertical heated tube were conducted in earth gravity and under microgravity conditions. The experiment mainly consists in the study of a two-phase flow inside a 6mm diameter sapphire tube uniformly heated through an ITO coating. Measurements of pressure drops, void fraction, and liquid and wall temperatures are performed, along with flow visualisations. Data were collected in normal gravity and during four parabolic flight campaigns providing near weightlessness conditions. Flow visualisations, temperature and pressure signals are analysed to obtain flow patterns, void fraction, wall and interfacial shear stresses, and heat transfer coefficient data. These experimental results and comparisons with other available datasets are used to attempt a modelling of flow boiling in microgravity.

Des expériences d'ébullition convective de HFE-7000 dans un tube vertical chauffé ont été menées dans des conditions de gravité terrestre et de microgravité. Ces expériences consistent principalement en l'étude d'écoulements diphasiques dans un tube de saphir de 6 millimètres de diamètre intérieur, uniformément chauffé par effet Joule à travers un dépôt conducteur d'ITO. Des mesures de pertes de pression, de taux de vide, et de températures de paroi ou de liquide sont réalisées simultanément avec des enregistrements vidéo des régimes d'écoulement dans le tube. Les données correspondantes ont été collectées au sol et lors de quatre campagnes de vols paraboliques qui ont fourni des conditions de niveau de gravité proches de l'apesanteur. Les visualisations des films d'écoulement, ainsi que les signaux de température et de pression sont analysés afin d'obtenir des données sur les régimes d'écoulement, le taux de vide, les frottements pariétaux et interfaciaux, et les coefficients d'échange de chaleur. Ces résultats expérimentaux et les comparaisons réalisées avec d'autres jeux de données en microgravité sont utilisés pour proposer une modélisation de l'ébullition convective en microgravité.

Acknowledgements

J'aimerais tout d'abord sincèrement remercier ma directrice de thèse, Catherine Colin. Grâce à elle, j'ai eu la chance de mener pendant ces trois ans et demi un projet de thèse ambitieux et surtout passionnant, riche en expériences (c'est le cas de le dire) et en découvertes. Catherine est une personne que j'apprécie, et que j'admire sur le plan professionnel (non, je n'ai pas touché de pot de vin sous forme de tablette de chocolat pour dire cela), et malgré ses nombreuses responsabilités, elle a toujours su prendre le temps de répondre à mes questions ou de m'épauler. Je garderai un très bon souvenir des campagnes de vols paraboliques avec elle et de notre séjour aux USA.

Sur un plan plus expérimental, la palme d'or du remerciement revient à Greg, sans qui il n'y aurait pas de manip' BRASIL. Merci pour les heures consacrées à ce projet (dont un certain nombre de soirées et de samedis), pour les trajets en camion vers Bordeaux, la bonne humeur et le challenge des deux mètres de pizza. Et pour les mêmes raisons, merci à Erik et Juergen qui ont toujours su conjuguer travail productif et bon moments. Vous m'avez tous les deux manqué quand vous êtes partis après les campagnes de vols.

Et puisqu'on parle de campagnes de vols, j'adresse aussi mes remerciements à toute l'équipe de Novespace, à Bordeaux, avec une dédicace spéciale à Frédéric et Brian qui ont eu la lourde tâche de s'occuper de l'équipe de l'IMFT avec ses pannes accidentelles (si si !) le vendredi soir à 17h. En plus de découvrir de bons restaurants à Bordeaux, j'ai eu l'opportunité de rencontrer beaucoup de personnes différentes lors de ces campagnes (dont certains de mes nouveaux collègues !), ce qui a largement contribué à l'enrichissement de ma culture générale et à l'élargissement de mon réseau professionnel.

Bien sûr, le personnel de l'IMFT a également largement contribué à la construction de l'installation expérimentale et l'organisation des campagnes de mesure. A ce titre, j'aimerais remercier l'équipe de l'Atelier, Sébastien, Hervé et Marie-Hélène.

An interesting part of my PhD work was the collaboration with the University of Maryland about a similar experimental set-up that flew onboard Novespace aircraft. I spent two months in the United States to work with Alex and Jungho Kim, and it was a very good experience, both professionally and personally. I don't think they ever realised how terrified I was when I arrived at College Park (I had never spoken in English before that) but they have been very nice and patient with me. They took me to visit various places and I had a great time with them and the other members of the team (sorry for the few pounds you must have gained in France with the desserts, Alex!).

Mes remerciements vont également aux membres du groupe Interface de l'IMFT qui, si ils n'ont pas contribué directement à mes travaux, ont tout de même participé à cette thèse. Il y a les permanents, ceux qui ont soutenu avant moi, ceux qui soutiendront en

même temps que moi, et ceux qui resteront encore un peu plus longtemps. Merci donc à Véronique, Patricia, Julien, Frédéric, Wladimir, Greg (encore), Elise, Audrey, Nicolas, Michel, Quentin, Benjamin, Lucia, Joël, Marie, Michaël, Jérôme et certainement d'autres. Des mercis tout particuliers à Roberta (j'ai fait bon usage du bureau et du radiateur que tu m'as légués), à Juergen (encore une fois merci car je n'aurais jamais pu monter mes meubles avec mes béquilles sans toi, entre autres choses) et à Auriane (je crois qu'il reste encore des salons de thé que l'on n'a pas essayés à Toulouse, et des films pourris qu'on n'a pas encore regardés !).

Au même titre, j'aimerais remercier ma famille et mes amis, qui ont suivi de plus ou moins près mon avancée dans cette thèse. Merci à Nolwenn, Mylène, Lionel, Cyril et Malik qui m'ont aidée à me changer les idées quand j'en avais besoin. Je vous pardonne d'avoir soupiré aux détails scientifiques ou de m'avoir demandé si c'était pour faire cuire des pâtes pour les astronautes. Et surtout un grand merci à ma famille : à ma petite sœur Fanny (pour les petits plats et les trajets à la Ruche), à mon Papa et ma Maman (le premier s'étant efforcé de lire mon article et la deuxième de retenir le titre de ma thèse, mais tous les deux toujours derrière moi - comment aurais-je fait sans vous ?), et à mes oncle et tante.

Et enfin, un grand merci aux anonymes fournisseurs de bons petits plats, gâteaux et chocolat en tous genres, sans qui je n'aurai pas passé le stade de la rédaction :).

Marine

Ixelles, le 15/10/2014.

Contents

Declaration of Authorship iii

Abstract vii

Acknowledgements ix

Contents xi

List of Figures xv

List of Tables xix

Abbreviations xxi

Symbols xxiii

Introduction 1

1 Description and modelling of flow boiling in pipe 5

1.1 Fundamental description . . . 8
1.1.1 Basic definitions . . . 8
1.1.2 Fundamental equations . . . 9
1.1.3 Dimensionless numbers . . . 11
1.1.4 Simplified balance equations . . . 13
1.2 Models and closure laws . . . 16
1.2.1 Flow patterns and models . . . 16
1.2.2 Wall shear stress modelling . . . 19
1.2.3 Interfacial shear stress modelling . . . 23
1.2.4 Heat transfer coefficients . . . 23
1.3 Two-phase flow in pipe under microgravity conditions . . . 28
1.3.1 Boiling experiments in microgravity . . . 28
1.3.2 Flow patterns . . . 29
1.3.3 Void fraction and film thickness . . . 34
1.3.4 Two-phase pressure drop and shear stresses . . . 35
1.3.5 Heat transfer coefficient . . . 37

2 Experimental set-up and measurement techniques 43
2.1 BRASIL experiment . . . 46
2.1.1 Working fluid . . . 46
2.1.2 Hydraulic loop . . . 46
2.1.3 Test section . . . 49
2.2 Measurement techniques and accuracy . . . 51
2.2.1 Flow parameters . . . 51
2.2.2 Pressure . . . 53
2.2.3 Temperature . . . 53
2.2.4 Void fraction . . . 55
2.2.5 Flow visualisations . . . 63
2.3 Data reduction . . . 64
2.3.1 Vapor quality . . . 64
2.3.2 Wall friction . . . 66
2.3.3 Interfacial shear stress . . . 67
2.3.4 Heat transfer coefficient . . . 69
2.4 Experimental procedures . . . 74
2.4.1 Microgravity conditions . . . 74
2.4.2 Participation in parabolic flight campaigns . . . 76
2.4.3 Test matrix and experimental protocols . . . 78
2.5 Experiment of the University of Maryland (UMD) . . . 80
2.5.1 Experimental set-up . . . 80
2.5.2 Measurement techniques . . . 81
2.5.3 Measurement campaigns . . . 82

3 Experimental results 85
3.1 Flow patterns . . . 88
3.1.1 Visualisation . . . 88
3.1.2 Effects of flow parameters on flow regimes . . . 92
3.1.3 Evolution along the tube . . . 93
3.1.4 Flow pattern maps . . . 94
3.1.5 Comparison with other microgravity datasets . . . 99
3.2 Void fraction and film thickness . . . 102
3.2.1 Void fraction . . . 102
3.2.2 Uncertainty in void fraction . . . 104
3.2.3 Flow pattern transitions . . . 105
3.2.4 Comparison with microgravity datasets . . . 106
3.2.5 Liquid film thickness in annular flow . . . 107
3.3 Pressure drops and shear stresses . . . 110
3.3.1 Total pressure drop . . . 110
3.3.2 Wall shear stress . . . 112
3.3.3 Interfacial shear stress . . . 115
3.4 Heat transfer coefficient . . . 118
3.4.1 Characterisation of heat transfer coefficient measurements . . . 118
3.4.2 Influence of mass flux . . . 120
3.4.3 Influence of wall heat flux . . . 121
3.4.4 Influence of gravity level . . . 124
3.4.5 Comparison with microgravity datasets . . . 127

4 Modelling of flow boiling under microgravity conditions 133
4.1 Flow patterns and transition 136
4.1.1 Transition between bubbly flow and slug flow: 136
4.1.2 Transition between slug flow and annular flow: 137
4.2 Void fraction and film thickness 140
4.2.1 Void fraction 140
4.2.2 Liquid entrainment in annular flow 148
4.2.3 Film thickness in annular flow 149
4.3 Wall and interfacial shear stresses 153
4.3.1 Wall shear stress 153
4.3.2 Interfacial shear stress 165
4.4 Heat transfer coefficient 172
4.4.1 Comparison with correlations 172
4.4.2 Contributions of nucleate and convective boiling 174
4.4.3 Subcooled boiling 176
4.4.4 Saturated boiling 181

Conclusions and Perspectives 193

A Validyne calibration curves 203

B Selected publications 205

Bibliography 235

List of Figures

1.1 Control volume 9
1.2 Flow patterns and models 16
1.3 Lokhart-Martinelli correlation 21
1.4 Ohta's test section 29
1.5 Celata and Zummo test section 29
1.6 Two-phase flow patterns 30
1.7 Slug flow 31
1.8 Microgravity flow pattern map as a function of vapor quality and mass flux 32
1.9 Microgravity flow pattern map as a function of superficial velocities 34
1.10 Friction factor in microgravity bubbly flow 36
1.11 Lui *et al* heat transfer data in microgravity and normal gravity 38
1.12 Ohta and Baba heat transfer data in microgravity and normal gravity . . 39
1.13 Summary of existing microgravity data on heat transfer 39

2.1 BRASIL rack in flight configuration 47
2.2 BRASIL hydraulic loop 48
2.3 BRASIL flow parameters 49
2.4 Test section 50
2.5 Differential thermocouple calibration curve 54
2.6 Parallel-plate capacitor 55
2.7 Typical electrode configuration for the void fraction probes 56
2.8 Void fraction probe 57
2.9 Temperature effect on the void fraction probe 58
2.10 Void fraction probe calibration 59
2.11 Experimental calibration of a void fraction probe 60
2.12 Simplified geometries for void fraction models 60
2.13 Model results for void fraction probe calibration 61
2.14 Geometry in COMSOL simulations 62
2.15 Validation of the pressure drop measurements 68
2.16 Cross-section of the sapphire tube 69
2.17 Validation of the heat transfer coefficient measurements 72
2.18 Validation of heat transfer coefficient measurements 73
2.19 Parabolic flight trajectory 74
2.20 BRASIL team on-board the A300 ZERO-G 75
2.21 Flow parameters profiles during a parabola 77
2.22 UMD experiment 80
2.23 UMD measurement technique with IR camera 81
2.24 UMD heat transfer measurement validation 82

3.1 Bubbly flow visualisations . . . 89
3.2 Slug flow visualisations . . . 89
3.3 Annular flow visualisations . . . 90
3.4 Transition flow visualisations . . . 91
3.5 Flow patterns according to void fraction probes . . . 91
3.6 Influence of the heat flux and vapor quality on flow patterns . . . 93
3.7 Evolution of flow pattern along the tube . . . 95
3.8 Flow pattern maps . . . 96
3.9 Flow pattern map with Reynolds number . . . 98
3.10 Flow pattern map for microgravity datasets . . . 99
3.11 Bubbly flow at very high mass flux . . . 100
3.12 Bubbly flows in different experiments . . . 100
3.13 Annular flows in different experiments . . . 101
3.14 Void fraction according to vapor quality . . . 103
3.15 Experimental uncertainty in the void fraction . . . 104
3.16 Void fraction transitions between flow patterns . . . 105
3.17 UMD and IMFT void fraction data . . . 106
3.18 UMD and IMFT void fraction data (2) . . . 107
3.19 Film thickness according to vapor quality . . . 108
3.20 Experimental uncertainty in the film thickness . . . 109
3.21 Total pressure drop at low mass flux . . . 110
3.22 Total pressure drop at high mass flux . . . 111
3.23 Wall shear stress according to quality . . . 113
3.24 Experimental uncertainty in the wall shear stress . . . 114
3.25 Wall shear stress and flow patterns . . . 115
3.26 Interfacial shear stress according to quality . . . 116
3.27 Experimental uncertainty in the interfacial shear stress . . . 117
3.28 Heat transfer coefficient and flow patterns . . . 118
3.29 Experimental uncertainty in the heat transfer coefficient . . . 119
3.30 Influence of the mass flux on heat transfer coefficient . . . 120
3.31 Influence of the heat flux on heat transfer coefficient . . . 122
3.32 Influence of the heat flux on heat transfer coefficient (2) . . . 123
3.33 Influence of the gravity level on heat transfer coefficient . . . 124
3.34 Influence of the gravity level on heat transfer coefficient (2) . . . 125
3.35 Influence of the gravity level on heat transfer coefficient (3) . . . 126
3.36 ENEA heat transfer coefficient data . . . 128
3.37 Ohta's heat transfer coefficient data . . . 129
3.38 UMD heat transfer coefficient in bubbly flow . . . 130

4.1 Modelling of transitions between flow patterns . . . 138
4.2 Empirical correlations for void fraction . . . 140
4.3 Vapor velocity in subcooled regimes . . . 141
4.4 Drift flux model and void fraction (2) . . . 142
4.5 Steiner correlation and void fraction . . . 143
4.6 Steiner correlation and void fraction (2) . . . 143
4.7 Void fraction in Cioncolini model . . . 144
4.8 Void fraction in Cioncolini model (2) . . . 145
4.9 Liquid entrainment in annular flow . . . 148

4.10 Film thickness in Cioncolini model 150
4.11 Film thickness in Cioncolini model (2) 151
4.12 Film thickness in Cioncolini model (3) 151
4.13 Empirical correlations for pressure drop 153
4.14 Two-phase multiplier and correlations 154
4.15 Two-phase multiplier and correlations (2) 155
4.16 Two-phase multiplier and comparisons 156
4.17 Two-phase multiplier and comparisons (2) 157
4.18 Two-phase multiplier and comparisons (3) 158
4.19 Two-phase multiplier and comparisons (4) 159
4.20 Two-phase multiplier and comparisons (5) 160
4.21 Wall shear stress and Cioncolini's model 161
4.22 Wall shear stress and Cioncolini's model (2) 161
4.23 Interfacial friction and model 166
4.24 Interfacial friction (2) 167
4.25 Influence of gravity level on interfacial friction 168
4.26 Fitting of interfacial friction data 169
4.27 Fitting of interfacial friction data (2) 169
4.28 Fitting of interfacial friction data in microgravity 170
4.29 Shear stresses and gravity 171
4.30 Heat transfer coefficient correlations 172
4.31 Heat transfer coefficient correlations (2) 173
4.32 Heat transfer coefficient and correlations (2) 173
4.33 Heat transfer coefficient and correlations 174
4.34 Contributions of nucleate and convective boiling 175
4.35 Heat transfer coefficient and comparisons in subcooled boiling 177
4.36 Heat transfer coefficient and comparisons in subcooled boiling (2) 178
4.37 Heat transfer coefficient and comparisons in subcooled boiling (3) 179
4.38 Heat transfer coefficient and comparisons 182
4.39 Heat transfer coefficient and comparisons (2) 183
4.40 Heat transfer coefficient and comparisons (3) 184
4.41 Heat transfer coefficient and comparisons (4) 185
4.42 Heat transfer coefficient and comparisons (5) 186
4.43 Heat transfer coefficient and Cioncolini's model 188
4.44 Heat transfer coefficient and Cioncolini's model (2) 189

A.1 Validyne calibration curve 203

List of Tables

1.1 Dimensionless numbers . . . 12
1.2 Order of magnitude of dimensionless numbers . . . 13
1.3 Values of C for the Lockhart-Martinelli correlation . . . 21
1.4 Values of the constants in the Kandlikar correlation . . . 26

2.1 HFE-7000 properties . . . 46
2.2 Uncertainty in the wall heat flux . . . 53
2.3 Electric properties in various materials . . . 56
2.4 Uncertainty in the liquid film thickness . . . 63
2.5 Uncertainty in saturated vapor quality . . . 65
2.6 Uncertainty in subcooled vapor quality . . . 65
2.7 Uncertainty in the wall shear stress . . . 67
2.8 Uncertainty in the interfacial shear stress . . . 68
2.9 Uncertainty in the heat transfer coefficient . . . 71
2.10 Ranges of flow parameters . . . 79

3.1 Influence of the gravity level on the wall shear stress for low mass fluxes . 114
3.2 Heat transfer modes and heat flux . . . 122
3.3 Influence of gravity level on heat transfer coefficients . . . 126
3.4 Influence of gravity level on heat transfer coefficients (2) . . . 127
3.5 Influence of gravity level on heat transfer coefficients (3) . . . 127

4.1 Void fraction and models (2) . . . 147
4.2 Liquid film thickness and model . . . 152
4.3 Liquid film thickness and model . . . 152
4.4 Wall shear stress and models . . . 163
4.5 Wall shear stress and models (2) . . . 164
4.6 Heat transfer coefficient and models . . . 180
4.7 Heat transfer coefficient and models (2) . . . 190

Abbreviations

BRASIL	**B**oiling **R**egimes in **A**nnular and **S**lug flow in **L**ow gravity
CHF	**C**ritical **H**eat **F**lux
CNES	**C**entre **N**ational d'**E**tudes **S**patiales (French Space Agency)
ESA	**E**uropean **S**pace**A**gency
HTC	**H**eat **T**ransfer **C**oefficient
IMFT	**I**nstitut de **M**écanique des **F**luides de **T**oulouse (Institute of Fluid Mechanics of Toulouse)
ISS	**I**nternational **S**pace **S**tation
LHS	**L**eft **H**and **S**ide
MANBO	**M**ultiscale **AN**alysis of **BO**iling
MAE	**M**ean **A**bsolute **E**rror
NASA	**N**ational **A**eronautics and **S**pace **A**dministration
NB	**N**ucleate **B**oiling
NBA	**N**ucleate **B**oiling in **A**nnular flow
PFC	**P**arabolic **F**light **C**ampaign
RHS	**R**ight **H**and **S**ide
TFC	**T**wo-phase **F**orced **C**onvection
UMD	**U**niversity of **M**aryland**D**
VFP	**V**oid **F**raction **P**robe

Symbols

	Roman symbols	
A	cross-section area	m^2
Bo	Boiling number	[-]
C	constant	
Cp	specific heat at constant pressure	$J.K^{-1}.kg^{-1}$
D	diameter	m
e	tube thickness	m
e	rate of entrainment	[-]
Eck	Eckert number	[-]
f	friction factor	[-]
Fr	Froude number	[-]
g	acceleration	$m.s^{-2}$
G	mass flux	$kg.s^{-1}.m^{-2}$
$h_{l,v}$	latent heat of vaporisation	$J.kg^{-1}$
h	heat transfer coefficient	$W.K^{-1}.m^{-2}$
j	superficial velocity	$m.s^{-1}$
Ja	Jakob number	[-]
k	sapphire thermal conductivity	$W.m^{-1}.K^{-1}$
L	test section length	m
$\dot{m}$	mass flow rate	$kg.s^{-1}$
Nu	Nusselt number	[-]
p	pressure	bar
Pch	Phase change number	[-]
Pe	Peclet number	[-]
Pr	Prandtl number	[-]
q	heat flux	$W.m^{-2}$

R	radius	m
r	radial coordinate	m
Re	Reynolds number	[-]
S	perimeter	m
t	time	s
T	temperature	K
u	mean velocity	$m.s^{-1}$
V	volume	m^3
We	Weber number	[-]
x	mass quality	[-]
z	axis coordinate	m

Greek symbols

α	void fraction	[-]
δ	liquid film thickness	m
Δ	difference	
ϵ	permittivity	[-]
Γ	mass transfer	$kg.s^{-1}.m^{-3}$
λ	thermal conductivity	$W.m^{-1}.K^{-1}$
μ	dynamic viscosity	Pa.s
ν	kinematic viscosity	$m^2.s^{-1}$
ρ	density	$kg.m^{-3}$
σ	surface tension	$N.m^{-1}$
σ	dieletric conductivity	$S.m^{-1}$
τ	shear stress	Pa

Subscripts

c	core
$conv$	convective
$crit$	critic
$elec$	electrical
$elec$	electrode
exp	experimental
fr	frictional
g	gas
i	inner
i	interfacial
in	inlet conditions
l	liquid phase
lf	liquid film
liq	liquid phase
m	mixture
$meas$	measured
nb	nucleate boiling
o	outer
out	outlet conditions
sat	saturated conditions
sub	subcooled conditions
t	total
$theo$	theoretical
v	vapor phase
vap	vapor phase
w	wall
∞	to infinity

Dedicated to my family and friends, who supported me troughout these three years even though they don't understand the title of my thesis (no, it's not to cook pasta aboard the ISS!).

Introduction

Two-phase flows (gas-liquid and vapor-liquid flows) are broadly used in various industrial and engineering fields in both normal gravity and reduced gravity environments. Terrestrial applications include transportation, thermal management, process efficiency and safety issues, especially in the petroleum, chemical or nuclear industries. Two-phase flow can also occur in accidental situations. Thus, the understanding of two-phase flow benefits and drawbacks is needed to design the associated systems, particularly under reduced gravity conditions.

Indeed, power, fluid and thermal management systems using two-phase flow are of great interest for space applications. For example, one of the major problems aboard space platforms is currently to remove the heat generated by devices from the inside into space in order to ensure suitable environmental and working conditions. By taking advantage of latent heat transportation, two-phase systems generally enable a good efficiency in heat exchanges. Moreover, with the growing interest for space applications such as communication satellites and the increasing power requirements of on-board devices, the use of two-phase mechanical pumped loop will become ineluctable for thermal and power generation issues with a decrease in size and weight of management systems.

However, up to now, chosen technical solutions often include single-phase mechanical pumped loops because of the lack of reliable predictive models for the sizing of gas-liquid and vapor-liquid flows systems. A better understanding of two-phase flow mechanisms under microgravity conditions is still needed in order to properly design these systems. It is especially necessary to be able to predict corresponding flow patterns, pressure drops, heat transfers and critical heat flux.

But two-phase flow (and especially boiling) is a complex phenomenon which combines heat and mass transfers, hydrodynamics, and interfacial phenomena. Furthermore, gravity affects the fluid dynamics and may lead to unpredictable performances. It is thus necessary to perform experiments directly in (near) weightless environments. Besides the ISS, microgravity conditions can be simulated by means of a drop tower, parabolic flights on board an aircraft or a sounding rocket.

Beyond the design of space systems, reduced gravity two-phase flows can address some fundamental questions which remain unresolved. On earth, the force balance between the two phases is often dominated by gravitational forces. As buoyancy is suppressed, a new balance comes into play between inertia, viscous and capillary forces, leading to a drastic change in the interaction between the two phases.

The present thesis focuses on the vapor-liquid aspect of two-phase flows, with an experimental study of flow boiling. It is mainly supported by the French Space Agency (CNES) and the European Space Agency (ESA) as an IMFT contribution to the MANBO project.

The main objective was to provide experimental results and theoretical analysis on flow boiling in a straight heated tube both under normal gravity and microgravity conditions. To reach this goal, a test facility was designed and built to perform flow boiling experiments on-ground and during parabolic flight campaigns. With this set-up, various measurements such as heat transfer and pressure drop measurements, and flow visualisations can be done at the same time, for a wide range of experimental conditions including different gravity levels.

Special attention was paid to the description of boiling mechanisms that involve a lot of parameters. The definition of these parameters and the fundamental balance equations used in flow boiling are given in Chapter 1, with a dimensionless study and a review including existing database and models that were developed both in normal gravity and microgravity. Chapter 2 describes the experimental test facility, measurement techniques and protocols, as well as the data reduction. The experimental data obtained with this set-up are presented in Chapter 3, with a comparison to the commonly used correlations and flow boiling data that are available for microgravity conditions. Finally, Chapter 4 focuses on the modelling of dynamics and heat transfers in flow boiling under normal gravity and microgravity conditions.

Introduction

Les écoulements diphasiques (écoulements gaz-liquide et liquide-vapeur) sont très largement utilisés dans le domaine de l'industrie ou de l'ingénierie, à la fois en gravité terrestre ou dans des environnements à gravité réduite. Les applications au sol concernent principalement des problèmes de transport, de régulation thermique, d'amélioration des procédés industriels ou de sécurité, en particulier dans le domaine des industries pétrolières, chimiques et nucléaires. Les écoulements diphasiques peuvent également être observés dans des situations off-design correspondant à des défaillances accidentelles. C'est pourquoi il est nécessaire de comprendre quels sont les avantages et les inconvénients liés aux écoulements diphasiques dans la conception de systèmes les intégrant, surtout dans le cas d'applications en gravité réduite.

En effet, les systèmes de régulation (de la chaleur, de la puissance...) qui exploitent les écoulement diphasiques s'avèrent très intéressants pour des applications spatiales. Par exemple, l'un des problèmes majeurs rencontrés à bord des plateformes spatiales est l'évacuation vers l'espace de la chaleur générée par les appareils embarqués, qui est censée assurer de bonnes conditions de fonctionnement et d'environnement. Les systèmes diphasiques permettent généralement d'atteindre un bon rendement dans les échanges de chaleur en tirant avantage de la capacité de transport de la chaleur latente. De plus, avec l'intérêt sans cesse croissant pour les applications spatiales telles que les satellites de télécommunication et l'augmentation de la puissance nécessaire aux appareils embarqués, l'utilisation de boucles diphasiques intégrant des pompes hydrauliques entraînées mécaniquement devient une priorité pour réduire la taille et le poids des systèmes de régulation.

Or, la plupart des solutions techniques actuelles inclut des boucles hydrauliques monophasiques à cause d'un manque de données permettant de prédire de façon fiable les principales grandeurs physiques caractérisant les systèmes à écoulements gaz-liquide ou liquide-vapeur. Une meilleure compréhension des mécanismes d'écoulements diphasiques dans des conditions de microgravité est donc nécessaire afin de dimensionner ces systèmes. En particulier, il est essentiel de savoir prédire les régimes d'écoulement, pertes de pression, échanges de chaleur ou flux critiques correspondants.

Mais les écoulements diphasiques (et l'ébullition convective d'autant plus) représentent un phénomène complexe qui combine transferts de masse et de chaleur, hydrodynamique et phénomènes interfaciaux. De plus, le niveau de gravité joue sur la dynamique du fluide et peut mener à des changements inattendus dans les performance des appareils. Il est donc important de réaliser des expériences directement en l'absence quasi totale de gravité. En dehors de la Station Spatiale Internationale (ISS en anglais), des conditions de microgravité peuvent être simulées dans une tour de chute libre, lors de vols paraboliques à bord d'un avion ou lors de vols de fusée-sonde.

Au-delà des problèmes de dimensionnement de systèmes de régulation, les écoulements diphasiques en gravité réduite peuvent répondre à des questions fondamentales jusqu'ici non résolues. Sur terre, l'équilibre des forces entre les deux phases est souvent dominé par les forces gravitationnelles. Cependant, lorsque la flottabilité est supprimée, un nouvel équilibre s'établit entre les forces d'inerties, de viscosité et les forces capillaires, ce qui peut mener à des changements importants dans les interactions entre phases.

La thèse présentée ici s'intéresse plus particulièrement aux écoulements diphasiques liquide-vapeur, à travers une étude expérimentale de l'ébullition convective. Elle est en grande partie financée par le Centre National d'Études Spatiales (CNES) et l'Agence Spatiale Européenne (ESA en anglais), en tant que contribution de l'IMFT au projet MANBO.

Le principal objectif est de fournir des résultats expérimentaux ainsi qu'une analyse théorique sur l'ébullition convective dans un tube chauffé, dans des conditions de gravité normale (terrestre) et de microgravité. Afin d'atteindre ce but, un banc expérimental a été dimensionné et construit à l'IMFT pour procéder à des expériences en ébullition convective au laboratoire et lors de campagnes de vols paraboliques. Avec cette installation, diverses mesures (telles que des mesures de pertes de pression, de coefficient d'échange ou des visualisations d'écoulement) peuvent être réalisées simultanément pour de larges gammes de conditions expérimentales comprenant différents niveaux de gravité.

Une attention toute particulière a été apportée à la description des mécanismes de l'ébullition, qui implique un grand nombre de paramètres. La définition de ces paramètres et les équations de conservation fondamentales utilisées dans cette analyse sont exposées dans le Chapitre 1, avec une étude adimensionnelle et un compte-rendu des données et modèles disponibles ou développés à la fois en gravité normale et en microgravité. L'installation expérimentale ainsi que les techniques et protocoles de mesure sont détaillés dans le Chapitre 2 qui explicite également le traitement des données. Les résultats expérimentaux obtenus avec ce banc sont présentés dans le Chapitre 3 et comparés aux corrélations de la littérature et aux données disponibles dans des conditions similaires de microgravité. Enfin, le Chapitre 4 traite plus particulièrement de la modélisation de la dynamique et des transferts de chaleur en ébullition convective dans des conditions de gravité normale et de microgravité.

Chapter 1

Description and modelling of flow boiling in pipe

This chapter describes the fundamental parameters and equations used for the description and modelling of flow boiling in a vertical heated tube. A dimensionless analysis is provided in order to highlight the main relevant dimensionless numbers, which will enable a comparison between available datasets both under normal gravity and microgravity conditions and introduce classical correlations and models that are used in the litterature. Simplified equations used in the data reduction and models are presented. For the specific case of microgravity conditions, a state of the art review details existing experiments and the trends they highlight.

Dans ce chapitre sont décrits les principaux paramètres et les équations utilisés pour la description et la modélisation de l'ébullition convective dans un tube vertical chauffé. Une analyse dimensionnelle du problème permet d'énoncer les nombres adimensionnels qui servent à comparer des jeux de données obtenues dans des conditions d'expérimentation différentes, et qui apparaissent dans les modèles et corrélations empiriques usuellement fournis par la littérature. Les équations simplifiées utiles pour le traitement des données sont également détaillées. Enfin, pour le cas de la microgravité, un état de l'art reprenant les principales expériences et résultats expérimentaux est présenté.

Description fondamentale

Afin de correctement décrire les mécanismes de l'ébullition convective en tube, un rappel des principales définitions et notations utilisées est nécessaire, en particulier pour le titre massique en vapeur x, le taux de vide α, les vitesses moyennes des phases liquide et vapeur u_l et u_k, et les vitesses superficielles de ces mêmes phases j_l et j_k.

Ces grandeurs apparaissent dans les six équations bilan qui décrivent le système. Les équations de conservation de la masse, de la quantité de mouvement et de l'enthalpie peuvent en effet être écrites pour la phase liquide et pour la phase vapeur. Les équations de bilan à l'interface sont ajoutées afin de réduire le nombre d'inconnues. Pour résoudre le système, il est cependant nécessaire de fournir des lois de fermeture pour les transferts pariétaux et interfaciaux.

Les corrélations empiriques proposées pour ces lois de fermeture font souvent appel à des nombres adimensionnels également utilisés pour comparer des données acquises dans des conditions quelque peu différentes (avec différents réfrigérants ou gammes de paramètres d'écoulement, par exemple). Ces nombres sont choisis de façon à représenter les paramètres importants de l'écoulement, tout en restant indépendants les uns des autres.

L'ordre de grandeur des nombres adimensionnels permet de supprimer quelques termes des équations de conservation. Des hypothèses supplémentaires telles que des conditions de régime établi permettent d'obtenir des équations simplifiées faisait apparaître les principales grandeurs de l'écoulement en fonction de paramètres facilement mesurables, comme le flux de masse. En particulier, le calcul du titre en vapeur se fait à partir l'équation de conservation de l'enthalpie pour le mélange tandis que celle de quantité de mouvement du mélange permet d'obtenir le frottement pariétal.

Modélisation de l'ébullition

Divers régimes d'écoulement sont rencontrés en ébullition convective en tube pour des flux de chaleur pariétaux inférieurs au flux critique. Les trois principaux régimes correspondent aux écoulement à bulles, aux écoulements à poches-bouchons et churn, et aux écoulements annulaires. Divers modèles leur sont associés puisqu'ils présentent des caractéristiques d'écoulement très différentes.

Les modèles homogènes partent du principe que les phases liquide et vapeur vont à la même vitesse et peuvent être considérées comme une unique phase caractérisée par des propriétés thermodynamiques de mélange. Ils sont surtout valables pour des écoulements à bulles à très hauts débits ou lorsque le rapport des densités liquide sur vapeur est faible. Dans les modèles à phases séparées, chaque phase est caractérisée par ses propres propriétés et vitesses d'écoulement et on résout les équations de conservation de quantité de mouvement pour les deux phases. Pour des écoulements à poches-bouchons, on considère une seule équation de quantité de mouvement pour le mélange, mais des vitesses de phase différentes (modèle à flux de dérive).

A chacun de ces modèles correspondent des corrélations empiriques qui ont été proposées pour la prédiction du frottement pariétal ou des coefficients d'échange de chaleur. Dans le cas des écoulements annulaires, il existe également des corrélations pour déterminer le frottement interfacial.

État de l'art des expériences en microgravité

Très peu de données sont disponibles pour des écoulements bouillants en microgravité, la plupart des résultats expérimentaux en écoulement diphasiques correspondant à des écoulements gaz-liquide adiabatiques. Trois principales expériences ayant fourni des données lors de campagnes de vols paraboliques sont mentionnées ici, l'une ayant fait le sujet d'une collaboration lors de cette thèse. Puisque les installations expérimentales sont conditionnées par les contraintes des vols paraboliques, les fluides de travail et gammes de paramètres d'écoulement sont très proches pour toutes ces expériences.

Comme précisé dans la partie modélisation de ce chapitre, trois principaux régimes d'écoulement ont été identifiés, à la fois au sol et en microgravité : écoulements à bulles, écoulements à poches-bouchons (avec des écoulements de transition difficilement identifiables) et écoulements annulaires. Alors que l'influence du niveau de gravité est clairement visible pour les écoulements à bulles (qui présentent des formes plus sphériques et des tailles plus importantes en microgravité), elle est difficile à distinguer sur les écoulements à poches-bouchons et les écoulements annulaires. Malheureusement, il manque des données pour caractériser expérimentalement les transitions entre les régimes d'écoulements et tracer des cartes de configuration complètes.

Le taux de vide (et l'épaisseur de film liquide dans le cas des écoulements annulaires) a très peu été étudié en microgravité, cette grandeur étant difficilement mesurable : seules des observations qualitatives ont été fournies.

De même, il existe assez peu de résultats expérimentaux sur le frottement pariétal en microgravité. Des mesures ont été réalisées en écoulement gaz-liquide ou en écoulements bouillants dans une section adiabatique. La mesure du frottement interfacial nécessitant la mesure couplée de perte de pression et de taux de vide, il n'existe aucune donnée pour des écoulements bouillants en microgravité. Quelques mesures de frottement interfacial et quelques modélisations existent pour des écoulements eau-air.

La plupart des expériences se sont concentrées sur l'étude des coefficients d'échange de chaleur en microgravité. Des tendances différentes, voire contradictoires, ont été mises en évidence selon les différents auteurs, mais pour des conditions d'opération différentes et parfois mal spécifiées, ce qui rend les comparaisons entre expériences hasardeuses. Quelques auteurs ont tenté de rassembler les différentes données disponibles en distinguant les gammes de paramètres d'écoulement et les zones impactées par un changement du niveau de gravité.

1.1 Fundamental description

Dynamics and heat transfer in flow boiling in pipe can be described at the pipe scale by one-dimensional mass, momentum and energy balance equations for each phase (liquid and vapor), and jump conditions at the interface. These equations involve a large number of parameters that are presented in the following section.

1.1.1 Basic definitions

The subscript k is used to describe the fluid state: $k = l$ for the liquid phase and $k = v$ for the vapor phase.

Geometrical considerations: the present study aims at investigating an upward boiling flow inside a circular vertical tube of constant diameter D. The corresponding total cross-sectional area A is equal to the sum of areas occupied by the liquid (referred to as A_l) and areas occupied by the vapor (referred to as A_v).

$$A = A_l + A_v \tag{1.1}$$

This cross-sectional area is used in the expression of the mass flux G according to the mass flow rate $\dot{m}$:

$$G = \frac{\dot{m}}{A} \tag{1.2}$$

Two-phase parameters: in flow boiling, liquid phase and vapour phase flow together, with a velocity u_k, a pressure p_k and an enthalpy h_k. Two important parameters are necessary to characterise the velocity of each phase: the vapor quality x and the void fraction α. For both parameters, the subscript v is omitted: $x_v = x$, $x_l = 1 - x$, and $\alpha_v = \alpha$, $\alpha_l = 1 - \alpha$.

The vapor quality x is defined as the ratio of the vapor mass flow rate $\dot{m}_v$ over the total mass flow rate $\dot{m}$. If phase change occurs, then the quality also changes along the tube. Further discussion and calculations of x are presented in Chapter 2.

$$x = \frac{\dot{m}_v}{\dot{m}} = \frac{\dot{m}_v}{\dot{m}_l + \dot{m}_v} \tag{1.3}$$

The void fraction α corresponds to the volume occupied by the vapor phase V_v over the total volume V. It can also be expressed in terms of area.

$$\alpha = \frac{V_v}{V} = \frac{V_v}{V_l + V_v} = \frac{A_v}{A_l + A_v} \tag{1.4}$$

Two-phase velocities: two main types of velocity can be expressed for each phase according to the flow parameters.

The mean velocities, denoted u_k, correspond to the actual velocity at which each phase flows in the tube. u_l and u_v are generally different and are determined by the ratio of the phase volumetric flow rate over the cross-sectional area occupied by that phase:

$$u_k = \frac{\dot{m}_k}{\rho_k . A_k} \tag{1.5}$$

According to previous definitions:

$$\begin{aligned} u_l &= \frac{\dot{m}}{\rho_l.A} \cdot \frac{1-x}{1-\alpha} = \frac{G}{\rho_l} \cdot \frac{1-x}{1-\alpha} \\ u_v &= \frac{\dot{m}}{\rho_v.A} \cdot \frac{x}{\alpha} = \frac{G}{\rho_v} \cdot \frac{x}{\alpha} \end{aligned} \tag{1.6}$$

where ρ_l and ρ_v are the densities of liquid and vapor, respectively.

The superficial velocity j_k is the velocity the phase would have if it was flowing alone in the tube ($A_k = A$). According to the definition of u_k:

$$\begin{aligned} j_l &= (1-\alpha).u_l \\ j_v &= \alpha.u_v \end{aligned} \tag{1.7}$$

The sum of the liquid and vapor superficial velocities is the total superficial velocity (or mixture velocity), denoted j:

$$j = j_l + j_v \tag{1.8}$$

1.1.2 Fundamental equations

A system of six equations describes the evolution of a boiling flow in a pipe: the laws of conservation of mass and energy, and the momentum balance equation, applied to each phase k. Jump conditions are added to this system: they are written for mass, energy and momentum at the interface. All these balance equations are integrated on a control volume in the tube, as can be seen in Figure 1.1, z being the direction of preferential flow. Further details are provided in the books of Collier and Thome [1994], Wallis [1969] or Delhaye [2008].

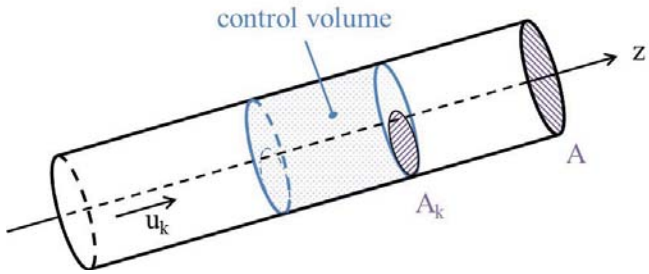

FIGURE 1.1: Control volume for the integration of balance equations

Mass conservation equations: if there is no mass gain or loss through the wall, the temporal variation of mass in the tube is due to phase change (characterised by a mass transfer Γ_k [kg.s^{-1}.m^{-3}]) and to the motion of mass entering or leaving the control volume, which can be expressed by:

$$\frac{\partial(\rho_k.\alpha_k)}{\partial t} + \frac{\partial(\rho_k.\alpha_k.u_k)}{\partial z} = \Gamma_k \tag{1.9}$$

where u_k is the axial component of the mean velocity of phase k.

Momentum balance equations: the momentum variation is determined by the sum of the forces that apply to the control volume such as pressure forces or viscous stresses. $S_{w,k}$ is the wall wet perimeter and $S_{i,k}$ is the interfacial perimeter. The interface travels at the velocity u_i. For turbulent flows, this balance equation is given by:

$$\begin{aligned}\frac{\partial(\rho_k.\alpha_k.u_k)}{\partial t} + \frac{\partial(\rho_k.\alpha_k.u_k^2)}{\partial z} = &- \rho_k.\alpha_k.g - \alpha_k \cdot \frac{\partial p_k}{\partial z} - (p_k - p_i) \cdot \frac{\partial \alpha_k}{\partial z} \\ &- \frac{\tau_{w,k}.S_{w,k}}{A} - \frac{\tau_{i,k}.S_{i,k}}{A} + \Gamma_k.u_i\end{aligned} \tag{1.10}$$

Energy conservation equations: the total enthalpy of phase k, denoted $h_{t,k}$, is determined by the sum of the enthalpy h_k and the kinetic energy $u_k^2/2$. Its temporal variation is due to an enthalpy gain through advection, wall and interfacial heat fluxes, energy associated to mass transfer, to the work of pressure or volumetric forces, and friction at the interface:

$$\begin{aligned}\frac{\partial(\rho_k.\alpha_k.h_{t,k})}{\partial t} + \frac{\partial(\rho_k.\alpha_k.u_k \cdot h_{t,k})}{\partial z} = &\frac{q_{w,k}.S_{w,k}}{A} + \frac{q_{i,k}.S_{i,k}}{A} + \Gamma_k.h_{t,k,sat} \\ &+ \alpha_k \cdot \frac{\partial p_k}{\partial t} + \rho_k.\alpha_k.g.u_k + \xi \cdot \frac{\tau_i.S_i.u_i}{A}\end{aligned} \tag{1.11}$$

The last term of the RHS of Equation (1.11) can be neglected since the heat associated with friction at the interface is very small.

At the interface: these three balance equations can be written at the interface.
Mass conservation: the mass leaving one phase is entering the other one.

$$\Gamma_l + \Gamma_v = 0 \tag{1.12}$$

Momentum balance: the interfacial shear stress from liquid and vapor phases are opposed and equal at the interface, since the surface tension σ is constant along the interface (there is no Marangoni convection):

$$\tau_{i,l} + \tau_{i,v} = 0 \tag{1.13}$$

It is usual to write a two-fluid model assuming that the pressure is constant in the tube section. Then $p_k = p_i$ and the third term of the RHS of Equation (1.10) disappears.

If $p_k \neq p_i$, the normal stress balance reduces to:

$$p_i - p_k = \frac{2\sigma}{R_{i,k}} \tag{1.14}$$

where $R_{i,k}$ is the radius of curvature of the interface.

Energy conservation: the interfacial heat flux from both liquid phase and vapor phase determines the energy variation associated with phase change.

$$(q_{i,l} + q_{i,v}) \cdot \frac{S_i}{A} = \Gamma_l.h_{l,v} \tag{1.15}$$

These 9 balance equations (3 for the liquid, 3 for the vapor and 3 at the interface) include 15 variables: 6 primary variables, α, u_l, u_v, p, h_l, h_v and 9 secondary variables, Γ_l, $S_{w,l}$, S_i, $\tau_{w,l}$, $\tau_{w,v}$, $\tau_{i,l}$, $q_{w,l}$, $q_{w,v}$, $q_{i,l}$.

According to Equation (1.5), velocities can be expressed with the void fraction α and the superficial velocities j_l and j_v (or the vapor quality x and the mass flux G). The primary variables become α, x, G, p, h_l and h_v.

To solve the balance equations, it is then necessary to provide closure laws for the geometrical parameters $S_{w,l}$ and S_i, the wall transfers $\tau_{w,l}$, $\tau_{w,v}$, $q_{w,l}$ and $q_{w,v}$, and the interfacial transfers Γ_l, τ_i and $q_{i,l}$. These closure laws strongly depend on the flow pattern. For the modelling of wall shear stress and heat transfer, global values τ_w and q_w are used for the whole perimeter $\pi.D$. Then, only 6 closure laws are required for Γ_l, S_i, τ_w, τ_i, q_w and $q_{i,l}$.

1.1.3 Dimensionless numbers

A dimensionless description of boiling mechanisms is useful to compare various experiments (different fluides, diameters...). Some dimensionless numbers are highlighted by the non-dimensional form of previously established equations while others are widely used in empirical correlations and models. This section provides details on a dimensionless analysis of boiling in upward flow.

Buckingham Π theorem: the dimensionless numbers that are chosen to describe boiling mechanisms must be based on all involved physical parameters and scales.

There are 18 independent parameters: 4 for the liquid properties (the density ρ_l, the heat capacity Cp_l, the kinematic viscosity ν_l and the thermal conductivity λ_l), 4 for the vapor properties (ρ_v, Cp_v, ν_v and λ_v), 2 for the fluid properties (the latent heat of vaporisation $h_{l,v}$ and the surface tension σ), plus the gravity level g, the tube diameter D, the vapor quality x, the mass flux G, the saturation temperature T_{sat}, the liquid and wall temperatures T_l and T_w, and the wall heat flux q_w.

The pressure p is not listed here: its variations are already accounted for with the thermodynamical properties of the two phases, and p is known if T_{sat} is known. Even though temperatures and fluxes are correlated, both are kept in the list and linked by a Nusselt number. Moreover, the superficial velocities j_l and j_v can be used in place of x and G.

These 18 variables can be expressed by using 4 of the 7 SI base dimensions (mass, time, length and energy). Thus, according to the Π theorem [Buckingham, 1914, Vaschy, 1892], 18 - 4 = 14 independent dimensionless numbers can be built for this problem.

Choice of dimensionless numbers: relevant dimensionless numbers are chosen among the numbers highlighted by dimensionless equations and commonly used models. A summary of these 14 dimensionless numbers is given in Table 1.1.

4 dimensionless numbers denoted Π_i consist in vapor over liquid properties ratios. Most of the other numbers can be written for the liquid phase and the vapor phase. However, the numbers obtained for the two phases are not always independent since one of them can be expressed according to the ratio of fluid properties or other dimensionless numbers. For example:

$$We_l = We_v.\frac{j_l^2}{j_v^2} = We_v.\frac{Re_l^2}{Re_v^2}.\frac{\nu_l^2}{\nu_v^2} \tag{1.16}$$

Dimensionless number	**Formula**	**Signification**
Π_1	$\frac{\rho_v}{\rho_l}$	densities ratio
Π_2	$\frac{Cp_v}{Cp_l}$	specific heat capacities ratio
Π_3	$\frac{\nu_v}{\nu_l}$	kinematic viscosities ratio
Π_4	$\frac{\lambda_v}{\lambda_l}$	thermal conductivities ratio
liquid Reynolds Re_l	$\frac{j_l.D}{\nu_l}$	$\frac{\text{inertia forces}}{\text{viscous forces}}$
vapor Reynolds Re_v	$\frac{j_v.D}{\nu_v}$	$\frac{\text{inertia forces}}{\text{viscous forces}}$
Weber number We_v	$\frac{\rho_v.j_v^2.D}{\sigma}$	$\frac{\text{inertia forces}}{\text{surface tension}}$
Prandtl number Pr_l	$\frac{\mu_l.Cp_l}{\lambda_l}$	$\frac{\text{momentum diffusivity}}{\text{heat diffusivity}}$
Nusselt number Nu	$\frac{q_w}{\lambda_l.(T_w - T_k)}$	$\frac{\text{convection}}{\text{conduction}}$
Jakob number Ja_{sub}	$\frac{Cp_l.(T_{sat} - T_l)}{h_{l,v}}$	$\frac{\text{sensible heat}}{\text{latent heat}}$
Jakob number Ja	$\frac{Cp_l.(T_w - T_{sat})}{h_{l,v}}$	$\frac{\text{sensible heat}}{\text{latent heat}}$
Boiling number Bo	$\frac{q_w}{G.h_{l,v}}$	$\frac{\text{wall heat flux}}{\text{phase change heat flux}}$
Froude number Fr_l	$\frac{j_l^2}{D.g}$	$\frac{\text{inertia forces}}{\text{gravitational forces}}$
Eckert number Eck_l	$\frac{u_l^2}{Cp_l.(T_w - T_l)}$	$\frac{\text{kinetic energy}}{\text{internal energy}}$

Table 1.1: Dimensionless numbers, definition and signification

There are of course other possible choices for the 14 dimensionless numbers, and thus depending on the fluids and the flow patterns of interest, other combinations may be more adapted. For example, in specific cases, some authors use the liquid Ohnesorge number Oh in place of the Weber number We to describe flow patterns transitions.

$$Oh = \frac{\mu_l}{\sqrt{\rho_l.\sigma.D}} \qquad Oh = \frac{\sqrt{We}}{Re} \tag{1.17}$$

Many authors also use an Eötvos number Eo (also called Bond number) to characterise the ratio of gravity forces over surface tension.

$$Eo = \frac{(\rho_l - \rho_v).g.D^2}{\sigma} \tag{1.18}$$

Another relevant dimensionless number can be mentioned: the Martinelli parameter X [Lockhart and Martinelli, 1949]. This number, which expresses the frictional pressure gradient in single-phase liquid flow over the one in single-phase vapor flow, may be written according to the ratios of density and Reynolds number of the two phases. It is not independent of the previously defined numbers, but it is commonly used in various correlations, especially for pressure drops.

$$X = \left[\frac{\left(\frac{dP}{dz}\right)_l}{\left(\frac{dP}{dz}\right)_v} \right]^{1/2} \tag{1.19}$$

Order of magnitude: Table 1.2 gives the order of magnitude of the aforementionned dimensionless numbers for the refrigerant HFE-7000 and ranges of flow parameters corresponding to the experiment described in Chapter 2. The mass flux G ranges from 50 to 400 kg.s^{-1}.m^{-2}, the vapor quality x from 0.01 to 0.8 and the wall heat flux from 0.5 to 4 W.cm^{-2}.

	Normal gravity	**Microgravity**
Re_l	1.5 10^2 - 6.4 10^4	
Re_v	2.6 10^2 - 1.7 10^5	
We_v	1.6 10^{-2} - 6.6 10^3	
Fr	**8.9 10^{-4} - 1.4 10^0**	**8.7 10^{-1} - 1.4 10^4**
Eck	10^{-8} - 10^{-5}	
Bo	9.4 10^{-5} - 6.1 10^{-3}	
Eo	**39**	**0.004 - 0.04**

Table 1.2: Order of magnitude of various dimensionless numbers, for refrigerant flow boiling in millimetric channels

For microgravity conditions where it is considered that the residual gravity level is between $0.001g$ and $0.01g$, the Froude number ranges between 10^{-1} and 10^4, and the Eötvos number between 0.004 and 0.4. The Reynolds number for the liquid and vapor phases cover the ranges of laminar and turbulent flows. The Weber number of the vapor phase may reach important values corresponding to a destabilisation of the interface in annular flow. The Froude number varies over a wide range , and at low mass flux, the effect of buoyancy is expected to be non negligible in parabolic flight conditions.

1.1.4 Simplified balance equations

Writing balance equations applied to the mixture or to a specific phase and using fundamental definitions of velocities allow to express important physical quantities according to flow parameters that can be measured. The simplified equations that are used in the data reduction are presented in this section.

Simplifications: Balance equations can be written according to dimensionless numbers. However, further simplifications can be made by making basic assumptions.

– *pressure model:* a single pressure model is chosen; in a tube section, $p_l = p_v = p_i = p$. This assumption is validated by the value of the Weber number based on the mixture velocity, that is always larger than 1.

– *total enthalpy:* the total enthalpy $h_{t,k}$ splits up into the enthalpy h_k and a kinetic energy term. Since the Eckhert number is very small, the contribution of the kinetic energy can be neglected: $h_{t,k} = h_k$. Moreover, the vapor is generally considered at saturation temperature, which allows to consider $h_v = h_{v,sat}$.

– *steady state:* in steady state, the temporal variations of flow parameters are negligible compared to their spatial variations. Since this study is not interested in transient regime, all time derivatives are simplified.

Enthalpy balance equation for the mixture: in data reduction, the use of a simplified enthalpy balance equation will be required for the calculations of important flow parameters. Since the wall heat flux is small, the vapor is at saturation temperature and it is relevant to write an enthalpy balance equation for the mixture. Writing this equation in steady state allows us to avoid the modelling of interfacial terms.

The enthalpy balance for the mixture, given by Equation (1.21), is obtained by adding together the energy balance equations for each phase (Equation (1.20)).

$$\frac{\partial \rho_k.\alpha_k.u_k.h_k}{\partial z} - \frac{q_{w,k}.S_{w,k}}{A} - \frac{q_{i,k}.S_{i,k}}{A} - \Gamma_k.h_{k,sat} = 0 \tag{1.20}$$

$$\frac{\partial \rho_l.(1-\alpha).u_l.h_l}{\partial z} + \frac{\partial \rho_v.\alpha.u_v \cdot h_v}{\partial z} - \frac{q_w.S_w}{A} = 0 \tag{1.21}$$

The enthalpy h_k can be written according to the temperature of phase k:

$$h_k = Cp_k.(T_{sat} - T_k) + h_{k,sat} \tag{1.22}$$

The vapor can be considered at saturation: $h_v = h_{v,sat}$. With the definitions of Equation (1.5), $S_w = \pi \cdot D$ and $h_{l,v} = h_v - h_l$, Equation (1.21) becomes:

$$G.(h_{l,v} + Cp_l.(T_{sat} - T_l)) \cdot \frac{\partial x}{\partial z} + G.Cp_l.(1-x) \cdot \frac{\partial T_l}{\partial z} - \frac{4.q_w}{D} = 0 \tag{1.23}$$

This equation includes flow parameters that can be easily measured, such as the mass flux G, the heat flux delivered by the wall q_w or the liquid temperature T_l.

Momentum balance equation for the mixture: the same type of analysis applies to the momentum balance (Equation (1.10)) for the mixture: adding the equations for each phase makes the interfacial terms disappear; by using the definitions of the velocities according to x and G (with a mass flux constant along the considered section) and a mixture density ρ_m, this equation in steady state yields, for a vertical upward flow:

$$\frac{dp}{dz} = \frac{-4.\tau_w}{D} - \rho_m.g - G^2 \cdot \frac{d}{dz}\left[\frac{(1-x)^2}{\rho_l.(1-\alpha)} + \frac{x^2}{\rho_v.\alpha}\right] \tag{1.24}$$

$$\rho_m = (1-\alpha).\rho_l + \alpha.\rho_v \tag{1.25}$$

Momentum balance equation in annular flow: when the liquid and vapor velocities are very different, is is more relevant to use 2 momentum balance equations for liquid and vapor. This is the case for annular flows that exhibit a vapor core and a film of liquid flowing at the wall. In this particular case, the momentum balance can be written for each phase separately in order to keep the interfacial shear stress. Following equations are given on an adiabatic section where the acceleration term depending on the profiles of x and α along the tube can be neglected.

Adiabatic annular flow without droplet entrainment: a first approximation consists in considering that all the liquid flows at the wall as a film and that no droplet is entrained in the vapor core. In steady state for an adiabatic flow, with the previous definitions of velocity and $S_i/A = 4\sqrt{\alpha}/D$, the momentum balance equation applied on the vapor core and applied on the liquid film yields, respectively:

$$\begin{aligned} -\alpha \cdot \frac{dP}{dz} - \tau_i \cdot \frac{4\sqrt{\alpha}}{D} - \rho_v.\alpha.g = 0 \\ -(1-\alpha) \cdot \frac{dP}{dz} + \tau_i \cdot \frac{4\sqrt{\alpha}}{D} - \frac{4\tau_w}{D} - \rho_l.(1-\alpha).g = 0 \end{aligned} \tag{1.26}$$

Adiabatic annular flow with droplet entrainment: depending on flow parameters, a liquid fraction α_{le} can be entrained under the form of droplets in the vapor core, while the film at the wall corresponds to a liquid fraction $\alpha_l f$ ($\alpha_l = \alpha_{lf} + \alpha_{le} = 1 - \alpha$). The momentum balance equation in an adiabatic section is then applied on the vapor core + droplets, or on the liquid film:

$$\begin{aligned} -(\alpha + \alpha_{le}) \cdot \frac{dP}{dz} - \tau_i' \cdot \frac{S_i'}{A} - (\rho_v.\alpha + \rho_l.\alpha_{le}).g = 0 \\ -\alpha_{lf} \cdot \frac{dP}{dz} + \tau_i' \cdot \frac{S_i'}{A} - \frac{4\tau_w}{D} - \rho_l.\alpha_{lf}.g = 0 \end{aligned} \tag{1.27}$$

where the interfacial term $\tau_i'.S_i'/A$ accounts for entrainment and deposition of droplets.

The entrained liquid fraction can be calculated by considering that the mean velocity of entrained droplets equals the mean velocity of the vapor phase. Assuming a mass entrainment e, writing $u_v = u_{le}$ yields:

$$\frac{G.x}{\rho_v.\alpha} = \frac{G.(1-x).e}{\rho_l.\alpha_{le}} \qquad \text{with} \qquad e = \frac{\dot{m}_{le}}{\dot{m}_l} \tag{1.28}$$

which gives:

$$\alpha_{le} = \frac{\rho_v}{\rho_l} \cdot \frac{1-x}{x} \cdot e.\alpha \tag{1.29}$$

Equation 1.27 can therefore be expressed according to α_{le}, with $\alpha_{lf} = 1 - \alpha - \alpha_{le}$ and $S_i'/A = 4\sqrt{\alpha + \alpha_{le}}/D$

1.2 Models and closure laws

Dynamical and thermal closure laws are needed for the resolution of the balance equations. Most of the time, these laws are empirical correlations based on experimental datasets, which makes them strongly dependent on the flow patterns or on various flow parameters ranges. The main models and corresponding correlations used in two-phase upward flow in millimetric tubes are presented in this section.

1.2.1 Flow patterns and models

Various flow patterns can be encountered in flow boiling, and a precise description of the distribution of liquid and vapor phases is necessary; indeed, heat transfers and pressure drops are closely correlated to the flow structure.

Flow patterns and models: three main distinct flow patterns are reported for flow boiling at low heat flux, lower than the critical heat flux and in vertical tubes: bubbly flow, slug flow (long bubbles separated by liquid plugs) / churn flow, and annular flow (vapor core with a liquid film at the wall, as mentioned in Section 1.1.4). These regimes are illustrated in Figure 1.2. For further considerations on flow pattern types and transitions, refer to corresponding section on experimental works.

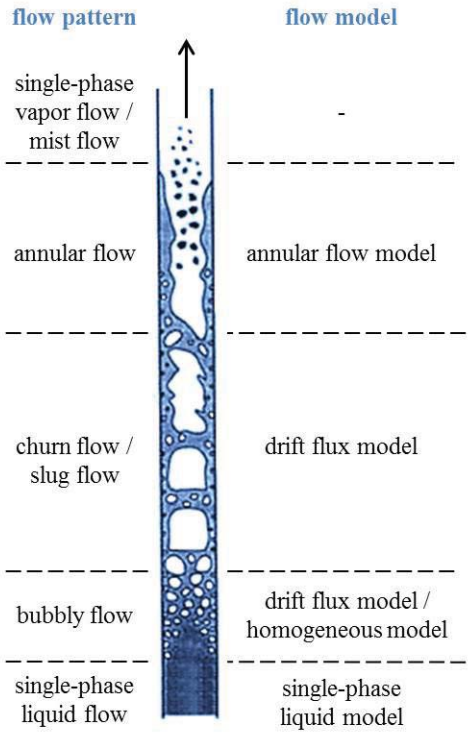

FIGURE 1.2: Flow patterns and models for two-phase flow modelling at low and moderate wall heat flux

Figure 1.2 presents a summary of the one-dimensional two-phase models that can be used depending on the flow pattern, in the specific case of vertical upward flow boiling inside a few millimeters ID tube. Choice and characterisation of the models are discussed in the following sections for the prediction of wall shear stress and heat transfer coefficient.

Two classes of empirical flow models were developed to describe flow mechanisms: homogeneous flow models and separated flow models. More recently, another phenomenological approach took an interest in flow patterns effects and designed models corresponding to specific flow patterns, such as drift flux models or annular flow models.

Homogeneous models: the underlying assumption of homogeneous flow model (or zero-slip model) is that the liquid and vapor phases mix and travel at equal velocities (the relative motion is neglected); thus, it can be considered that there is only one phase. As a result, these models are well-suited for the description of two-phase flows where the differences between the properties of the liquid and vapor are small (near critical point) or where the mean liquid velocity is very high compared to the bubble drift velocity in bubbly flow. Whalley [1987] states that the homogeneous model gives good results for $\rho_l/\rho_v < 10$ or $G > 2000$ kg.s^{-1}.m^{-2}.

The model is described by the typical single-phase equations using the mixture properties ρ_m and μ_m, with the mixture velocity $u_m = j_v + j_l = G/\rho_m$. In particular, the mixture density ρ_m is given by:

$$\rho_m = \left(\frac{1-x}{\rho_l} + \frac{x}{\rho_v}\right)^{-1} \qquad \text{or} \qquad \rho_m = \alpha.\rho_v + (1-\alpha).\rho_l \tag{1.30}$$

Several expressions were proposed for the two-phase viscosity μ_m. Most of these expressions are empirical correlations based on various datasets and written according to the vapor quality x. A list of two-phase viscosity definitions is available in the article of Awad and Muzychka [2008] who proposed effective homogeneous property models.

Drift flux model: in the case of dispersed bubble flow, assuming there is no slip between the phases would lead to think the homogeneous model is well-suited for the calculations. However, for moderate liquid velocities in bubbly or slug flow regimes, a significant drift velocity between gas and liquid phases is observed. It is therefore more relevant to use drift flux models. This class of models was first developed by Zuber and Findlay [1965] and Wallis [1969].

The drift flux model states that the actual vapor velocity u_v in slug flow responds to the axial "centerline" flow velocity in the tube, which is larger than the mixture velocity j. Moreover, due to buoyancy effects, the vapor bubbles experience a drift velocity u_∞. For vertical flow, the actual vapor velocity becomes:

$$u_v = \frac{j_v}{\alpha} = C_0 \cdot j + u_\infty \tag{1.31}$$

where the distribution parameter C_0 depends on the local void fraction and vapor velocity distributions. The expression of the drift velocity u_∞ is adapted to the flow pattern:

$$u_\infty = \begin{cases} 1.53 \cdot \left(g \cdot (\rho_l - \rho_v) \cdot \dfrac{\sigma}{\rho_l^2}\right)^{1/4} & \text{for bubbly flow [Harmathy, 1960]} \\ 0.35 \cdot \sqrt{g \cdot D} & \text{for Taylor bubbles in slug flow [Niklin, 1962]} \end{cases} \tag{1.32}$$

The void fraction needed for the calculations of the gravitational and acceleration terms in the total pressure gradient is calculated from this actual velocity with:

$$\alpha = \frac{j_v}{u_v} \tag{1.33}$$

Two-fluid models: the two-fluid model is the most generic one. It is based on two momentum balance equations (one for each phase) and can be used for all flow patterns. Nevertheless, it is the only relevant model for flows with separated phases like annular flows. In annular flow, the phase distribution is indeed correlated to the balance between gravitational force, wall and interfacial shear stresses.

In annular flow model at high void fraction, the vapor phase occupies the centre of the tube while the liquid phase flows at the wall. Depending on the flow parameters, entrainment of liquid droplets in the vapor core can occur. This type of flow is referred to as dispersed annular flow. Annular flow models often neglect this entrainement since the liquid fraction in the vapor phase remains small in most cases.

Annular flow model without liquid entrainement: in this regime, all the liquid flows at the wall. The liquid film thickness δ is therefore given by:

$$\delta = \frac{D}{2} \cdot \left(1 - \sqrt{\alpha}\right) \tag{1.34}$$

Writing the two momentum balance equations for the liquid film at the wall and for the vapor core, as presented in Equation (1.26), leads to two equations expressed according to the void fraction, and wall and interfacial shear stresses. In order to solve them and to calculate the void fraction (and then the film thickness) and pressure gradient, closure laws are needed for the wall and interfacial shear stresses.

Annular flow model with liquid entrainement: the momentum balance equations for each phase are more complicated in the case where droplet entrainement is considered, as shown in Equation (1.27).

Recently, Cioncolini and Thome [2009] proposed a two-phase pressure drop model for annular flow. The authors then developed this model to take the liquid entrainment into account and to include void fraction, liquid film thickness and heat transfer coefficient predictions [Cioncolini and Thome, 2011, 2012a].

In this model, the rate of entrainment e is given by:

$$e = (1 + 279.6 \cdot We_c^{-0.8395})^{-2.209} \qquad \text{for } 10 < We_c < 10^5 \tag{1.35}$$

where We_c is the Weber number of the vapor core, based on the superficial vapor velocity and on the density ρ_c of the vapor core carrying liquid droplets:

$$We_c = \frac{\rho_c \cdot j_v^2 \cdot D}{\sigma} \qquad \text{with} \qquad \rho_c = \frac{e \cdot (1-x) + x}{\dfrac{e \cdot (1-x)}{\rho_l} + \dfrac{x}{\rho_v}} \tag{1.36}$$

The following expression is used for the calculation of the void fraction α:

$$\alpha = \frac{m \cdot x^n}{1 + (m-1) \cdot x^n} \tag{1.37}$$

where

$$\begin{cases} m = a + (1-a) \cdot \left(\dfrac{\rho_v}{\rho_l}\right)^{a_1} & a = -2.129, a_1 = -0.2186 \\ n = b + (1-b) \cdot \left(\dfrac{\rho_v}{\rho_l}\right)^{b_1} & b = 0.3487, b_1 = 0.515 \end{cases} \tag{1.38}$$

1.2.2 Wall shear stress modelling

This section presents some empirical correlations that are used for the prediction of two-phase frictional pressure drops for the different aforementioned models.

Single-phase flow: for a steady single-phase liquid flow in a tube, the momentum equation provides an expression of the pressure gradient that is the sum of three components: a frictional term, a gravitational term and an acceleration term that is negligible if the density is considered as a constant, as shown in Equation (1.24).

The wall shear stress τ_w is defined as:

$$\tau_w = f \cdot \frac{\rho \cdot u^2}{2} \tag{1.39}$$

where the Fanning friction factor f is empirically determined according to the Reynolds number Re and the relative wall roughness k/D. While the general expression is $f = 16/Re$ in laminar flow, the most commonly used correlation for f in turbulent flow is that of Colebrook and White [1937]:

$$\frac{1}{\sqrt{f}} = -4 \cdot log\left(2 \cdot \frac{k}{D} + \frac{9.35}{Re \cdot \sqrt{f}}\right) \tag{1.40}$$

An older and widely used approximation of this correlation is that of Blasius [1913], in the case of smooth tubes:

$$f = \begin{cases} \dfrac{16}{Re} & \text{in laminar flow, } Re < 3000 \\ 0.079 \cdot Re^{-1/4} & \text{in turbulent flow, } 3000 < Re < 10^5 \end{cases} \tag{1.41}$$

Homogeneous models: for bubbly and slug flows, the flow dynamics can be well reproduced by a momentum balance equation for the mixture (Equation (1.42)) associated with the drift-flux model (Equation (1.31)):

$$\frac{d}{dz}\frac{G^2.(1-x)^2}{\rho_l.(1-\alpha)} + \frac{d}{dz}\frac{G^2.x^2}{\rho_v.\alpha} = -\frac{dp}{dz} - \rho_m.g - \frac{4.\tau_w}{D} \tag{1.42}$$

The frictional pressure gradient is expressed as:

$$\left(\frac{dp}{dz}\right)_{fr} = \frac{4.\tau_w}{D} = \frac{2.f_m.G^2}{\rho_m.D} \tag{1.43}$$

where the friction factor f_m is function of the Reynolds number for the mixture Re_m:

$$Re_m = \frac{G \cdot D}{\mu_m} \tag{1.44}$$

This simple expression only depends on the mixture velocity and properties that are expressed according to the void fraction α:

$$\rho_m = (1-\alpha) \cdot \rho_l + \alpha \cdot \rho_v \qquad \text{and} \qquad Re = \frac{\rho_m \cdot j \cdot D}{\mu_l} \tag{1.45}$$

For homogeneous models, $u_v = u_l$ leads to $\alpha = j_v \ / \ (j_v + j_l)$. For drift-flux models, α is given by Equation (1.31) or other correlations. For example, Steiner [1993] proposed

a modified version of the expression established in the drift flux model of Rouhani and Axelsson [1970]:

$$\alpha = \frac{x}{\rho_v} \cdot \left[(1 + 0.12.(1-x) \cdot \left(\frac{x}{\rho_v} + \frac{1-x}{\rho_l} \right) + \frac{1.18(1-x).[g.\sigma.(\rho_l - \rho_v)]^{0.25}}{G.\rho_l^{0.5}} \right]^{-1} \tag{1.46}$$

Separated flow models: this section presents a few classical empirical correlations that are used to determine τ_w.

Lockhart-Martinelli correlation: the Lockhart-Martinelli correlation [Lockhart and Martinelli, 1949] is one of the very first available correlations for the prediction of two-phase friction. The frictional pressure gradient is calculated by multiplying the frictional gradient obtained in single-phase flow (liquid or vapor, with the superficial velocity of each phase) by a two-phase flow multiplier Φ_l^2 or Φ_v^2:

$$\left(\frac{dp}{dz}\right)_{fric} = \left(\frac{dp}{dz}\right)_l \cdot \Phi_l^2 = \left(\frac{dp}{dz}\right)_v \cdot \Phi_v^2 \tag{1.47}$$

where

$$\begin{aligned} \left(\frac{dp}{dz}\right)_l &= \frac{2 \cdot f_l \cdot G^2 \cdot (1-x)^2}{\rho_l \cdot D} \\ \left(\frac{dp}{dz}\right)_v &= \frac{2 \cdot f_v \cdot G^2 \cdot x^2}{\rho_v \cdot D} \end{aligned} \tag{1.48}$$

The single-phase friction factors f_l and f_v can be calculated with classical expressions of Equation (1.41), with the corresponding liquid or vapor properties.

Equivalent correlations can be determined when considering that each phase flows alone in the tube at the mixture velocity (G) and not at its own superficial velocity ($G.(1-x)/\rho_l$ or $G.x/\rho_v$). In this case, a subscript "o" is added, and the definition of the single-phase frictional gradients and Reynolds number (for the friction factor calculation) change a little.

$$\left(\frac{dp}{dz}\right)_{fric} = \left(\frac{dp}{dz}\right)_{lo} \cdot \Phi_{lo}^2 = \left(\frac{dp}{dz}\right)_{vo} \cdot \Phi_{vo}^2 \tag{1.49}$$

where

$$\begin{aligned} \left(\frac{dp}{dz}\right)_{lo} &= \frac{2 \cdot f_{lo} \cdot G^2}{\rho_l \cdot D} \\ \left(\frac{dp}{dz}\right)_{vo} &= \frac{2 \cdot f_{vo} \cdot G^2}{\rho_v \cdot D} \end{aligned} \tag{1.50}$$

and the calculations of the friction factors are related to:

$$\begin{aligned} Re_l &= \frac{G \cdot (1-x) \cdot D}{\mu_l} & Re_v &= \frac{G \cdot x \cdot D}{\mu_v} \\ Re_{lo} &= \frac{G \cdot D}{\mu_l} & Re_{vo} &= \frac{G \cdot D}{\mu_v} \end{aligned} \tag{1.51}$$

Lockhart and Martinelli [1949] related the two-phase multipliers to the Martinelli parameter X (Equation (1.52)) as shown in Figure 1.3. Since the multipliers depend on whether the single-phase (liquid or vapor) flow is laminar or turbulent, there are four

curves for the correlation.

$$X = \left[\frac{\left(\frac{dP}{dz}\right)_l}{\left(\frac{dP}{dz}\right)_v} \right]^{1/2} \tag{1.52}$$

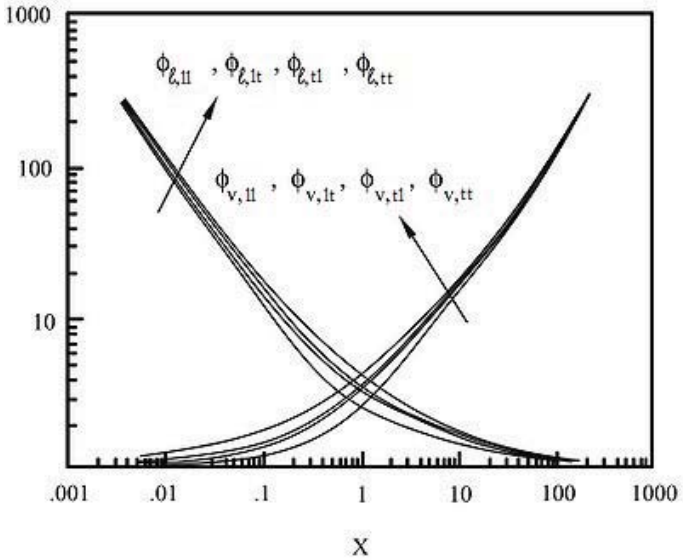

FIGURE 1.3: Lockhart and Martinelli [1949] friction correlation

Chisholm [1967] correlated the curves of Lockhart and Martinelli [1949] with the following relationships, where the constant C depends on the flow structure. Recommended values of C from the same article are given in Table 1.3.

$$\begin{aligned} \Phi_l^2 &= 1 + \frac{C}{X} + \frac{1}{X^2} \\ \Phi_v^2 &= 1 + C \cdot X + X^2 \end{aligned} \tag{1.53}$$

	Liquid	**Vapor**	**C**
(tt)	turbulent	turbulent	20
(lt)	laminar	turbulent	12
(tl)	turbulent	laminar	10
(ll)	laminar	laminar	5

TABLE 1.3: Recommended values of C for Equation (1.53)

Lockhart and Martinelli [1949] also developed a correlation for the void fraction whose expression is needed for the calculation of the total pressure gradient:

$$\alpha = 1 - \left(\frac{1}{\Phi_l^2}\right)^{1/3} \tag{1.54}$$

The Lockhart-Martinelli correlation provides a good prediction for $\mu_l/\mu_v > 1000$ and $G > 100 kg.s^{-1}.m^{-2}$.

Chisholm correlation: for cases where $\mu_l/\mu_v > 1000$ and $G > 100kg.s^{-1}.m^{-2}$, a better-suited correlation was proposed by Chisholm [1973]. This correlation, given by Equation (1.56), is related to the Chisholm parameter Y:

$$Y = \left[\frac{\left(\frac{dp}{dz}\right)_{lo}}{\left(\frac{dp}{dz}\right)_{vo}} \right]^{1/2} \tag{1.55}$$

$$\Phi_{lo}^2 = 1 + (Y^2 - 1) \cdot \left[B \cdot x^{(2-n)/2} \cdot (1-x)^{(2-n)/2} + x^{2-n} \right] \tag{1.56}$$

where n is the exponent of the Reynolds number in the expression of the friction factor (meaning that $n = 1$ for laminar flow and $n = 1/4$ for turbulent flow) and where B is a parameter given by:

$$B = \begin{cases} \frac{55}{\sqrt{G}} & \text{if } 0 < Y < 9.5 \\ \frac{520}{Y \cdot \sqrt{G}} & \text{if } 9.5 < Y < 28 \\ \frac{15000}{Y^2 \cdot \sqrt{G}} & \text{if } Y > 28 \end{cases} \tag{1.57}$$

Friedel correlation: for cases where $\mu_l/\mu_v < 1000$, Friedel [1979] developed another correlation using a database of 25,000 points to provide a better description of two-phase pressure drops.

$$\Phi_{lo}^2 = C_1 + \frac{3.24 \cdot C_2}{Fr^{0.0045} \cdot We^{0.0035}} \tag{1.58}$$

where the Froude and Weber numbers are calculated with the mass flux G and the constants C_1 and C_2 are defined as:

$$\begin{aligned} C_1 &= (1-x)^2 + X^2 \cdot \left(\frac{\rho_l}{\rho_v}\right) \cdot \left(\frac{f_{lo}}{f_{vo}}\right) \\ C_2 &= x^{0.78} \cdot (1-x)^{0.24} \cdot \left(\frac{\rho_l}{\rho_v}\right)^{0.91} \cdot \left(\frac{\mu_v}{\mu_l}\right)^{0.19} \cdot \left(1 - \frac{\mu_v}{\mu_l}\right)^{0.7} \end{aligned} \tag{1.59}$$

with f_{lo} and f_{vo} the single-phase friction factors.

Müller-Steinhagen and Heck correlation: Müller-Steinhagen and Heck [1986] proposed a simple empirical correlation that expressed the total friction pressure gradient as a function of the vapor quality, and of a liquid frictional pressure gradient and vapor frictional pressure gradient (Equation (1.50)), denoted A and B, respectively, and calculated on the total velocity G/ρ_k:

$$\left(\frac{dp}{dz}\right)_{fric} = F.(1-x)^{1/3} + B.x^3 \qquad \text{where} \qquad F = A + 2.(B - A).x \tag{1.60}$$

Annular flow model with liquid entrainement: Cioncolini and Thome [2009] analysed many experimental on annular flows in pipe with droplet entrainment and derived an expression of the wall shear stress:

$$\tau_w = f_{w,l} \cdot \frac{\rho_c \cdot u_c^2}{2} \qquad \text{with} \qquad f_{w,l} = 0.172 \cdot We_c^{-0.372} \qquad \text{for } 100 < We_c \tag{1.61}$$

where the Weber number We_c of the vapor core is this time based on the vapor core density ρ_c, velocity u_c and diameter D_c.

$$\begin{aligned} D_c &= D \cdot \sqrt{\alpha . \frac{x \cdot \rho_l + e \cdot (1-x) \cdot \rho_v}{x \cdot \rho_l}} \\ u_c &= \frac{4}{\pi} \cdot \frac{[e \cdot (1-x) + x] \cdot \dot{m}}{\rho_c \cdot D_c^2} \end{aligned} \tag{1.62}$$

Void fraction determined by Equation (1.37) and wall shear stress are sufficient to calculate the total pressure gradient, according to Cioncolini and Thome [2009].

1.2.3 Interfacial shear stress modelling

In the specific case of annular flow model, an expression of the interfacial shear stress τ_i is needed to calculate the total pressure gradient by using the two-fluid model.

Annular flow model without liquid entrainement: methods for calculating the interfacial velocity u_i and the interfacial friction factor f_i are required to determine the interfacial shear stress τ_i (the interfacial perimeter S_i is calculated with the void fraction and the tube diameter):

$$\tau_i = f_i \cdot \frac{\rho_v . |u_v - u_l| . (u_v - u_l)}{2} \tag{1.63}$$

The liquid interface velocity is selected (in the case of highly turbulent flow): $u_i = u_l$. For the friction factor f_i, empirical models are necessary. The most common one is that of Wallis [1969] developed for pipes of several centimeters ID, assuming that the liquid film is fully turbulent and rough with a roughness equal to the liquid film thickness δ:

$$f_i = 0.005 \cdot \left(1 + 300 \cdot \frac{\delta}{D}\right) = 0.005 \cdot [1 + 150 \cdot (1 - \sqrt{\alpha})] \tag{1.64}$$

The actual liquid and vapor velocities u_l and u_v are calculated with an iterative method using the superficial velocities j_l and j_v (Equation (1.8)). With the wall and interfacial shear stresses, and the void fraction, the system of two-phase equations can be solved.

Annular flow model with liquid entrainement: the calculations of the interfacial shear stress is impacted if the entrainment and deposition of liquid droplets are taken into account. If an entrained liquid fraction α_{le} is considered, the expression of τ_i must be written according to α_{le}, as shown in Equation (1.27) (whereas the calculation of τ_w is the same as for the case without entrainment).

1.2.4 Heat transfer coefficients

For purposes of clarity, the following notations are used: the wall heat flux delivered to the fluid through the wall is denoted q (instead of q_w); it is related to a heat transfer coefficient h that appears in the expression of the corresponding Nusselt number Nu.

Single-phase flow: typically, for forced convection, the Nusselt number is a function of the Reynolds number Re and the Prandtl number Pr. In laminar flow for circular pipes, the local Nusselt number is a constant whose value depends on the surface thermal condition ($Nu = 4.36$ at fixed wall heat flux q or 3.66 at fixed wall temperature T_w). Two main empirical correlations are described here for turbulent flow.

Dittus-Boelter equation: Dittus and Boelter [1930] proposed a simple explicit function for calculating the Nusselt number when forced convection is the only mode of heat transfer. The correlation is applicable in smooth straight circular pipes, for a location far from the pipe entrance ($L/D \gg 10$) and its accuracy is anticipated to be $\pm$ 15 %. When the fluid is heated, the Dittus-Boelter equation defines the Nusselt number as:

$$\begin{gathered} Nu = 0.023 \cdot Re^{4/5} \cdot Pr^{0.4} \\ \text{for } 10^4 < Re \quad \text{and} \quad 0.6 \leqslant Pr \leqslant 160 \end{gathered} \tag{1.65}$$

Gnielinski correlation: the effects of wall roughness and transitional flow conditions may be considered by using the correlation developed by Gnielinski [1976] which is more precise. As the Dittus-Boelter equation, the Gnielinski correlation only applies to fully developed heat transfer conditions.

$$\begin{gathered} Nu = \frac{(f/2) \cdot (Re - 1000) \cdot Pr}{1 + 12.7 \cdot (Pr^{2/3} - 1) \cdot \sqrt{f/2}} \\ \text{for } 3000 < Re < 5 \cdot 10^6 \quad \text{and} \quad 0.5 \leqslant Pr \leqslant 2000 \end{gathered} \tag{1.66}$$

where the Fanning friction factor is best calculated with the Colebrook correlation (Equation (1.40)) or an approximation in the case of smooth tube:

$$f = 4 \cdot (0.790 \cdot \ln Re - 1.64)^{-2} \tag{1.67}$$

Correction for entrance effects: previous correlations only apply for fully thermally developed flows, for locations far from the entrance of the tube (in cases where $L/D \gg 10$). When the flow is not thermally developed, the value of the actual Nusselt number Nu_a is larger than the value of the Nusselt number in the fully thermally developed flow Nu_∞ because of the development of the thermal boundary layer. Al-Arabi [1982] proposed a correlation to correct the entrance effects:

$$\frac{Nu_a}{Nu_\infty} = 1 + \frac{\dfrac{(z/D)^{0.1}}{Pr^{1/6}} \cdot \left(0.68 + \dfrac{3000}{Re^{0.81}}\right)}{z/D} \tag{1.68}$$

where z is distance between the tube entrance and the location corresponding to the actual Nusselt number Nu_a. The fully developed Nusselt number Nu_∞ obtained with the correction can be compared to empirical correlations such as the Gnielinski correlation.

Flow boiling in steady state: two important heat transfer mechanisms are taken into account in steady flow boiling models: nucleate boiling heat transfer (h_{nb}) and convective boiling heat transfer (h_{cb}). The global heat transfer coefficient h is often expressed as a combination of these two heat transfer terms. Some of the correlations that can be applied to refrigerant flow in vertical tubes are discussed here (this list is far from being exhaustive).

Chen correlation: the correlation proposed by Chen [1966] for saturated boiling conditions was extended to include subcooled boiling, which makes it very simple to apply and broadly used. The Chen correlation defined the heat transfer coefficient h as a combination of the nucleate boiling and convective single-phase terms weighted by two dimensionless factors:

$$h = S \cdot h_{nb} + F \cdot h_l \tag{1.69}$$

where S is a supression factor that reduces the contribution of nucleate boiling and F is a two-phase amplification factor that increases the weight of convective boiling due to the presence of vapor, both depending on the Martinelli parameter X.

$$\begin{aligned} F(X) &= \begin{cases} 2.35 \cdot \left(0.213 + \dfrac{1}{X}\right)^{0.736} & \text{if } \dfrac{1}{X} > 0.1 \\ 1 & \text{else} \end{cases} \\ S(X) &= \frac{1}{1 + 2.53 \cdot 10^{-6} . \left(\dfrac{G \cdot D \cdot (1-x) \cdot F(X)^{1.25}}{\mu_l}\right)^{1.17}} \end{aligned} \tag{1.70}$$

The single-phase heat transfer coefficient h_l is calculated with the common turbulent flow correlations (Dittus-Boelter or Gnielinski correlations) whereas the correlation of Forster and Zuber [1955] for nucleate pool boiling can be used to determine h_{nb}:

$$h_{nb} = 0.00122 \cdot \left[\frac{\lambda_l^{0.79} \cdot Cp_l^{0.45} \cdot \rho_l^{0.49}}{\sigma^{0.5} \cdot \mu_l^{0.29} \cdot h_{l,v}^{0.24} \cdot \rho_v^{0.24}}\right] \cdot (T_w - T_{sat})^{0.24} \cdot (p - p_{sat})^{0.75} \tag{1.71}$$

where p is the saturation pressure at the wall temperature T_w.

The Chen correlation is more adapted to water flow. When working at high Prandtl numbers $Pr \gg 1$ (with refrigerants, for example), Chen and Bennett [2004] recommend to multiply the convective multiplier factor F by $Pr^{0.296}$.

Gungor and Winterton correlation: a modified form of the Chen correlation applicable for vertical tubes was proposed by Gungor and Winterton [1986] who worked on refrigerants and water datasets. In this equation, the two-phase convective enhancement factor F is replaced by an other dimensionless factor that depends on the boiling number Bo and the Martinelli parameter X:

$$h_{conv} = h_l \cdot \left[1 + 3000 \cdot Bo^{0.86} + \left(\frac{x}{1-x}\right)^{3/4} \cdot \left(\frac{\rho_l}{\rho_v}\right)^{0.41}\right] \tag{1.72}$$

Kandlikar correlation: Kandlikar [1990] developed a correlation applicable in saturated flow boiling for vertical tubes, in which the heat transfer coefficient is considered to be the larger value between the nucleate boiling term and the convective term. Unlike the Chen correlation, it uses the boiling number Bo to determine the nucleate boiling contribution.

$$h = h_l \cdot [C_1 \cdot C_0^{C_2} + C_3 \cdot Bo^{C_4} \cdot F_K] \tag{1.73}$$

where h_l is calculated with usual turbulent single-phase flow correlations with the velocity j_l. F_K is a constant that can be adapted to suit the working fluid (for refrigerants, $F_K \simeq 1.2$ - 1.4). C_0 is a convection number used to determine the main contribution

term. Constants C_1 to C_4, given in Table 1.4, therefore depend on the value of C_0.

$$C_0 = \left(\frac{1-x}{x}\right)^{0.8} \cdot \sqrt{\frac{\rho_v}{\rho_l}} \tag{1.74}$$

	nucleate boiling region $C_0 > 0.65$	**convective boiling region** $C_0 < 0.65$
C_1	0.6683	1.1360
C_2	-0.2	-0.9
C_3	1058.0	667.2
C_4	0.7	0.7

TABLE 1.4: Values of the constants in the Kandlikar correlation

The Kandlikar correlation can not be applied to subcooled boiling conditions (with low vapor qualities) but it is interesting in saturated boiling since it is based on data with various fluids including refrigerants.

Kim and Mudawar correlation: Kim and Mudawar [2013] recently proposed a new generalised correlation that is constructed by superpositioning the contributions of nucleate boiling and convective boiling:

$$\begin{aligned} h &= \sqrt{h_{nb}^2 + h_{cb}^2} \\ h_{nb} &= h_l.\left[2345.Bo^{0.7}.\frac{p}{p_{crit}}^{0.38}.(1-x)^{-0.51}\right] \\ h_{cb} &= h_l.\left[5.2Bo^{0.08}.We_{lo}^{-0.54} + 3.5 \cdot \left(\frac{1}{X}\right)^{0.94} \cdot \left(\frac{\rho_v}{\rho_l}\right)^{0.25}\right] \end{aligned} \tag{1.75}$$

where h_l is the single-phase heat transfer coefficient calculated with the Dittus-Boelter correlation using superficial velocities, while We_{lo} is calculated with G/ρ_l. This correlation is shown to provide good predictions against several pre-dryout databases.

Sun and Mishima correlation: Sun and Mishima [2009] established a correlation where the heat transfer coefficient is expressed as a function of the liquid Reynolds number Re_{lo} and the boiling number Bo. The equation also takes into account the effect of the liquid Weber number We_{lo}:

$$h = \frac{6 \cdot Re_{lo}^{1.05} \cdot Bo^{0.54}}{We_{lo}^{0.191} \cdot (\rho_l/\rho_v)^{0.142}} \cdot \frac{\lambda_l}{D} \tag{1.76}$$

Unlike most of the other correlations, this prediction method does not depend on the vapor quality. Indeed, the datasets on which it is based mostly correspond to experimental conditions where nucleate boiling is predominant.

Kew and Cornwell correlation: another modified correlation using the liquid only Reynolds number Re_{lo} and the boiling number Bo was proposed by Kew and Cornwell [1997] to fit their database where convective boiling is the dominant heat transfer mechanism. They included a dependency of the heat transfer coefficient on the vapor quality x:

$$h = 30.Re_{lo}^{0.857}.Bo^{0.714} \cdot \left(\frac{1-x}{x}\right)^{0.143} \cdot \frac{\lambda_l}{D} \tag{1.77}$$

Annular flow model: Cioncolini and Thome [2011] proposed a heat transfer model based on the evaporation of the liquid film in annular flow. They use an algebraic eddy viscosity model for describing the velocity profile in the turbulent liquid film in this model.

The liquid film thickness δ is estimated by:

$$\delta = y^*.max\left[\sqrt{\frac{2.\Gamma^*_{lf}}{R^*}}; 0.0066.\frac{\Gamma^*_{lf}}{R^*}\right] \tag{1.78}$$

where y^* is the viscous length scale, R^* is the dimensionless tube radius and Γ^*_{lf} is the dimensionless mass flow rate in the liquid film:

$$\begin{aligned} y^* &= \frac{\nu_l}{u^*} \\ R^* &= \frac{D}{2.y^*} \\ \Gamma^*_{lf} &= \frac{(1-e).(1-x).G.\pi.D^2}{8.\pi.\rho_l.u^*.y^{*2}} \\ \text{and } u^* &= \sqrt{\frac{\tau_w}{\rho_l}} \end{aligned} \tag{1.79}$$

The heat transfer coefficient is given according to the liquid film thickness and wall friction:

$$\begin{gathered} h = \frac{\lambda_l}{\delta}0.0776.(\delta^+)^{0.9}.Pr^{0.52} \qquad \text{with } \delta^+ = \frac{\delta}{y^*} \\ \text{for } 10 < \delta^+ < 800 \quad \text{and} \quad 0.86 < Pr < 6.1 \end{gathered} \tag{1.80}$$

1.3 Two-phase flow in pipe under microgravity conditions

In the past forty years, space applications and new microgravity facilities have simulated the development of gas-liquid and vapor-liquid flows research under microgravity conditions, along with the fact that reduced gravity two-phase flows adress some fundamental issues which remain unsolved. The change in the gravity level induces a drastic change in the force balance between the two phases, in particular with the emergence of the surface tension inertia and viscous forces as driving forces in low gravity conditions.

Because of practical difficulties related to available low gravity environments, data on flow boiling experiments are very limited, and no cohesive dataset has been build. The following section presents a concise overwiew of experimental results concerning flow patterns, void fraction distribution, and pressure drops in adiabatic gas-liquid flow and / or vapor-liquid boiling flow in pipe in microgravity (thereafter also referred to as $\mu - g$) as well as heat transfer coefficients in boiling flows. CHF (Critical Heat Flux) issues are not addressed here. Further details can be found in the state of the art reviews in the papers of Colin et al. [1996], Ohta [2003], Celata and Zummo [2009], DiMarco [2012], Baldassari and Marengo [2013] and Ohta and Baba [2013]. Additional information are presented at the beginning of the section on the experimental apparatus that provided microgravity data.

1.3.1 Boiling experiments in microgravity

This section only deals with two-phase flow boiling experiments in circular tubes under microgravity conditions. Two major datasets are mentioned here, that provided experimental results on flow patterns and heat transfer coefficient as presented thereafter: the experimental set-ups of Ohta [2003], and of Celata and Zummo [2009]. Another experiment, designed and built at the University of Maryland (UMD) by Scammell and Kim is presented in Chapter 2 since it was the subject of a collaboration with IMFT during this PhD work. These experimental apparatus all flew during parabolic flight campaigns.

Experiments of Ohta and coworkers: Ohta [2003] performed upward flow boiling experiments with R113 under microgravity conditions on board the MU-300 japanese aircraft. Authors designed a test section consisting in a 8mm ID Pyrex glass tube, transparent, with a thickness of 1mm and coated on the inner wall with a thin gold film ($\simeq 0.01$ μm thickness). This tube is heated by supplying DC current directly through the coating.

The inner wall temperature, averaged over the heated length, is evaluated by using the gold film as a resistance thermometer. Flow pattern visualisations are simultaneously possible. For the acquisition of the heat transfer data that are discussed in the papers, a tube of 100mm length with a heated length of 68mm is used.

More recently, Ohta and Baba [2013] presented experimental results on heat transfer coefficients under microgravity conditions for boiling flow of FC-72 in 4mm ID tube.

Experiments of Celata and Zummo: Celata and Zummo [2009] built the MICROBO loop for ENEA in order to study upward flow boiling with FC-72 on board the A300 ZERO-G. They also used vertical Pyrex test sections with 6mm or 4mm internal diameter (and thicknesses between 1.5 and 1mm), with a heated length of 165mm. In the Pyrex

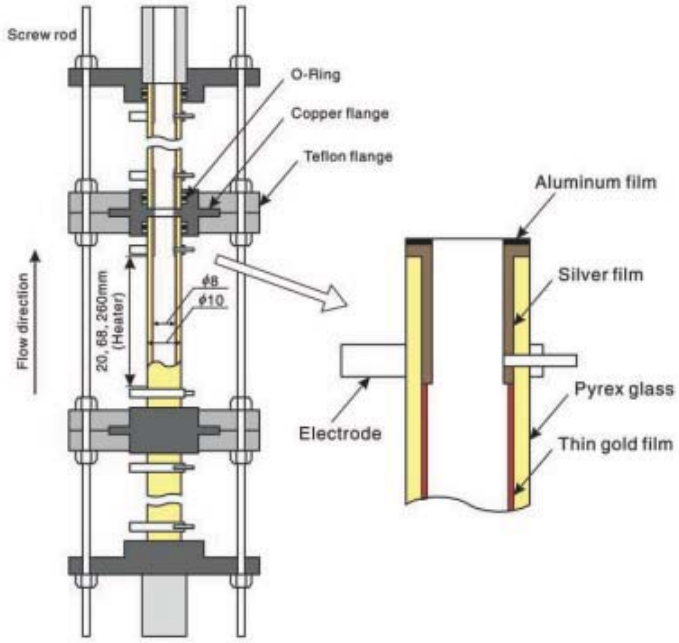

FIGURE 1.4: Experimental test section designed by Ohta [2003]

tubes, the fluid is heated by electrical tape helically twisted on the external surface of the pipe and later by an external ITO semi-transparent resistive layer. One of these test sections is illustrated in Figure 1.5.

FIGURE 1.5: Test section of the experimental MICROBO loop [Celata and Zummo, 2009]

All these experimental set-ups use refrigerants as working fluids. Despite some differences (on the saturation temperature for example), these fluid properties are rather similar, and due to restrictions related to parabolic flight campaigns, the ranges of flow parameters are also very close, which makes possible a careful comparison of experimental data.

1.3.2 Flow patterns

Pressure drops and heat transfer are closely related to the flow structure. For that reason, the variety of flow patterns encountered in two-phase flow is a very important feature, and the prediction of these flow patterns is crucial for describing hydrodynamical and thermal mechanisms.

Flow patterns characterization: Most of the experimental results on flow patterns in microgravity are based on a qualitative approach which uses direct observations from high speed photography or video techniques. The classification is easy to accomplish in this way since it only requires a careful observation, but it is sometimes subjective, especially for the case of transition flows. Additional methods based on quantitative

criteria typical of each flow pattern (on the void fraction or bubble size for example) can hardly be used because of the measurement techniques.

Several studies with and without phase change have been carried out under microgravity conditions in the last decades. Experiments performed by means of a drop tower are not presented here since they only provide a few seconds of low gravity that does not allow a steady state to establish. The working fluids are mostly air and water or boiling refrigerants (R112, R113, R114, FC-72, HFE-7000...).
− in the 90's and early 2000's, adiabatic gas-liquid flows were mainly investigated (Dukler et al. [1988], Colin et al. [1991], Colin et al. [1996], Huckerby and Rezkallah [1992], Zhao and Rezkallah [1993], Bousman et al. [1996], Zhao et al. [2001]...);
− more recently, convective boiling experiments have been performed for heat transfer smaller than the critical heat flux (Ohta [2003], Celata and Zummo [2009], Kim et al. [2012], Ohta and Baba [2013]...).

The same flow patterns are observed in adiabatic gas-liquid flow, condensing flow and convective boiling flow below the CHF, both in normal gravity and microgravity: bubbly, slug / intermittent and annular flows (Figure 1.6). The main difference between adiabatic and boiling flows is the nucleation of bubbles at the wall and the constant evolution of void fraction and vapor quality along the heated tube for boiling flow.

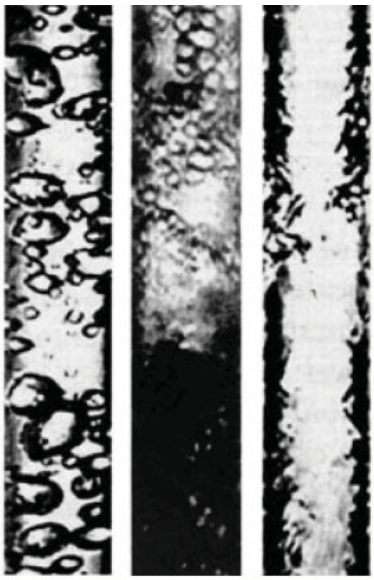

Figure 1.6: Bubbly flow, intermittent flow and annular flow in microgravity - boiling R113 flow in a 8mm ID tube [Ohta, 2003]

A qualitative description of the previously mentioned flow patterns under microgravity conditions is presented here:
· at low void fraction, *bubbly flow* occurs. Small bubbles of a few millimeters appear at high liquid velocity and low vapor velocity; their motion is rectilinear, and the shape tends to be spherical since interfacial forces are predominant on inertial and buoyancy forces. The size of these bubbles is mainly controlled by coalescence, which leads to larger bubbles as the void fraction or vapor quality increases;
· at higher void fractions corresponding to *slug flow*, these bubbles coalesce into cylindrical bubbles with a smooth interface and a spherical shaped nose, known as Taylor bubbles. They are separated by liquid slugs that contain smaller spherical bubbles (as can be seen in Figure 1.7) moving nearly at the same velocity than the cylindrical bubbles.

FIGURE 1.7: Slug flow in microgravity - boiling FC-72 flow in a 4mm ID tube [Celata and Zummo, 2009]

The bubbles in between the liquid slugs are the residues of the initial bubbles that where nucleated at the heated wall, whereas they are more irregular and created by gas entrainment at the rear of the cylindrical bubbles in normal gravity.
· as the gas velocity increases, the liquid slug length decreases until they are short enough to collapse. The resulting flow pattern consisting in the liquid flowing at the wall in the form of a film and gas or vapor flowing in the centre is similar to annular flow. A flow pattern corresponding to a transition between slug flow and annular flow, often called *frothy slug-annular flow* [Zhao and Rezkallah, 1993], can occur at the highest gas superficial velocities: the gas core breaks up and frothy slugs containing many small bubbles appear. In *annular flow*, when the gas velocity is very high, the interface becomes wavy and droplets can be entrained in the gas core.

Transitions: since the modelling of shear stresses and heat transfer depends on the flow pattern, special attention has to be paid to the prediction of the transitions between the flow patterns.

Transition between bubbly flow and slug flow: various models exist for the prediction of the transition from bubbly to slug flow. Some are based on a critical value of the void fraction α [Colin et al., 1991, Dukler et al., 1988] or a critical value of the Weber number [Zhao and Rezkallah, 1993] that can be written according to the void fraction. Since the void fraction is seldom declared in two-phase experiments (due to measurement difficulties and a lack of data), other criteria may be relevant, such as the criteria based on the Suratman number $Su = 1/Oh^2$ (Equation (1.17)) proposed by Jayawardena et al. [1997] or the evolution of the bubble size along the tube [Kamp et al., 2001, Riou et al., 2008, Takamasa et al., 2003]...

The transition from bubbly to slug flow is very progressive with an increase in the bubble size which results from a coalescence mechanism along the tube. For gas-liquid flows [Bousman et al., 1996, Colin et al., 1991] and vapor-liquid flows [Lebaigue et al., 1998, Reinarts, 1993], two regimes of coalescence have been identified, depending on the value of an Ohnesorge number Oh based on the fluid properties and the tube diameter, as expressed in Equation (1.17) [Colin et al., 1996]:
− an inhibiting-coalescence regime with a transition at $\alpha \simeq 0.45$ or $x \simeq 0.54$, for an Ohnesorge number $Oh > 8\ 10^4$;
− a promoting-coalescence regime with a transition at $\alpha \simeq 0.20$ or $x \simeq 0.24$, for an Ohnesorge number $Oh < 8\ 10^4$.

Measurements of bubble size have been performed in order to build a mechanistic model of the bubble coalescence in a turbulent flow; coalescence is indeed responsible for the transition to slug flow, and, according to Kamp et al. [2001], it is promoted by turbulence when the bubble size is smaller than the integral length scale of turbulence (typically $D/4$). When the bubble size is larger than this integral length scale, turbulence is not efficient enough anymore to promote coalescence. In this case, the source of bubble collision and coalescence is the mean shear of the flow [Riou et al., 2008] and the coalescence

rate is much smaller. The ratio of the bubble size to the tube diameter is the relevant parameter to distinguish the two regimes of coalescence. Zhao [2005] also proposed the ratio of the initial bubble diameter to the tube diameter as a criteria for the void fraction at the transition, but the length of the tube must be taken into account in order to correctly predict the evolution of bubble size along the pipe.

Transition between slug flow and annular flow: the transition from slug to annular flow has been investigated by several authors including Dukler et al. [1988], Huckerby and Rezkallah [1992] and Bousman and Dukler [1994]. Based upon experimental results, different approaches have been considered to predict this transition:
– according to Dukler et al. [1988], the void fraction calculated from the slug flow model and the void fraction calculated from the annular flow model must be equal at the transition;
– Zhao and Rezkallah [1993] assume that the transition occurs at a critical value of a Weber number based on the gas properties and superficial velocity;
– Zhao and Hu [2000] propose an other approach similar to that of Reinarts [1993]: they assume that the transition occurs if the impulsive force due to gas inertia is sufficient to overcome the surface tension force which maintains the spherical shape of nozzle of the elongated bubbles. This model should be able to reproduce the transition observed for air-water flow in microgravity, liquid-liquid flows in normal gravity and air-water flow in small tube in normal gravity. However, it includes two constants that have to be adjusted to fit experimental data.

Flow pattern maps: Flow pattern maps are drawn to identify the flow patterns that exist under different operating conditions and to predict the transitions between one type of flow pattern to another type. Properties of the gas / vapor phase and liquid phase have to be incorporated in order to generalize the map and compare maps with different fluids.

Various type of flow pattern maps: flow pattern data are sometimes plotted as a function of exit vapor quality x_{out} and mass flux G, like in Figure 1.8.

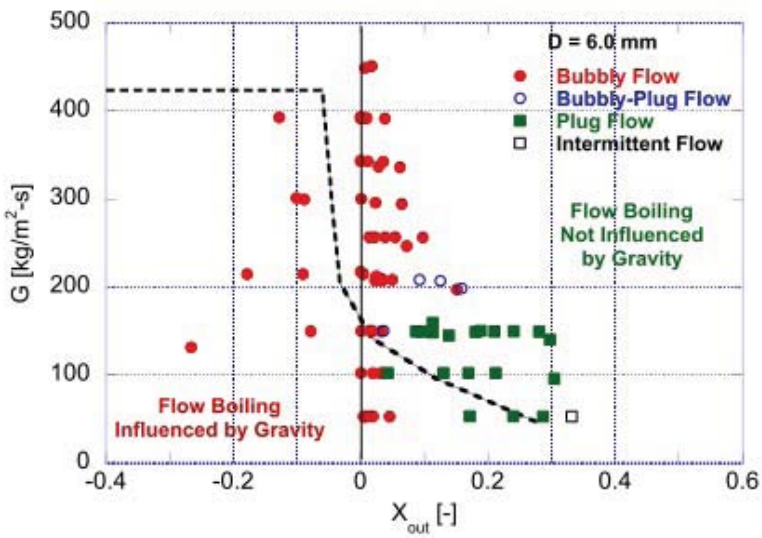

FIGURE 1.8: Microgravity flow pattern data - boiling FC-72 flow in a 6mm ID tube [Celata and Zummo, 2007]

Nevertheless, the thermodynamical vapor quality (which is negative for subcooled regimes) cannot be used to calculate the superficial velocities of liquid and vapor, which explains that some flow pattern maps are plotted versus G and x rather than j_v and j_l

Indeed, the most commonly used flow pattern map is given according to the gas and liquid superficial velocities j_g and j_l. Previously discussed transition criteria can be plotted on this type of map under the form of isocurves for the vapor quality or the void fraction, as can be seen in Figure 1.9 that is derivated from Dukler's microgravity flow pattern map. In the same way, flow pattern maps based on Weber numbers or on the Suratman number can illustrate different transition criteria.

Recent two-phase boiling flow pattern data: since this study focuses on flow boiling experiment, only boiling flow pattern results are presented here (details of corresponding experimental set-ups have been provided at the beginning of the section). Nevertheless, available data are compared to the microgravity gas-liquid flow pattern map and transition criteria established by Dukler *et al* [Colin et al., 1991, Dukler et al., 1988].

Ohta [1997] studied flow boiling of Freon 113 inside 8mm ID tube, and observed bubbly, intermittent and annular flows. For subcooled conditions, an evolution from bubbly flow at the inlet of the tube to frothy-annular flow at the outlet is observed in normal gravity, whereas an important increase in the void fraction promotes the transition to annular flow at lower quality in microgravity. For moderate inlet vapor qualities, annular flow is observed along the entire tube lenght both for $1-g$ and $\mu-g$, but the turbulence in the annular liquid film is reduced in the case of microgravity measurements. At high vapor qualities, the flow pattern is almost independent from the gravity level. More recently, Ohta [2003] performed experiments of flow boiling of R113 in a 8mm ID vertical transparent tube internally coated with a gold film, and observed bubbly, slug and annular flows. In his flow pattern map, the flow pattern is annular for a void fraction $\alpha > 0.8$ which is consistent with Dukler's transition from slug to annular flow in air-water flow.

Celata and Zummo [2007, 2009] carried out experiments with boiling FC-72 in Pyrex tubes of 2, 4 and 6mm internal diameters. They observed bubbly, bubbly-plug, plug and intermittent flows (due to a lack of power, they failed to reach higher vapor qualities and annular flow). Their data were plotted on various flow pattern maps including a map with the transitions established by Dukler *et al.* (Figure 1.9). The authors underline that the influence of the gravity level on flow pattern decreases with an increasing mass flux: at higher mass flux (examples are provided for $G = 355\ kg.s^{-1}.m^{-2}$) no visible difference can be observed.

According to their experimental results, bubbly flow occurs both in the subcooled flow boiling region and in the near zero quality area for saturated flow boiling region. An increase in the vapor quality leads to two types of intermittent flow: slug flow is observed for $G < 230\ kg.s^{-1}.m^{-2}$ while a more disordered flow occurs for $G > 230\ kg.s^{-1}.m^{-2}$. This boundary value of G corresponds to a Reynolds number that is very close to the region of transition from laminar to turbulent flow in single-phase flow. Celata and Zummo [2009] propose a modified criteria for the bubbly-slug flow transition that is not correctly predicted by Dukler's flow pattern map for boiling flow in larger tubes. They postulate that this transition occurs at a maximum value of $\alpha = 0.74$, which is a much higher value than usually observed for air-water flows. This modification, showed in Figure 1.9 with the dashed line, makes the flow pattern proposed by Dukler *et al* a good prediction tool for low gravity data flow pattern for the 6mm tube. No annular data is available to discuss the transition from slug flow to annular flow.

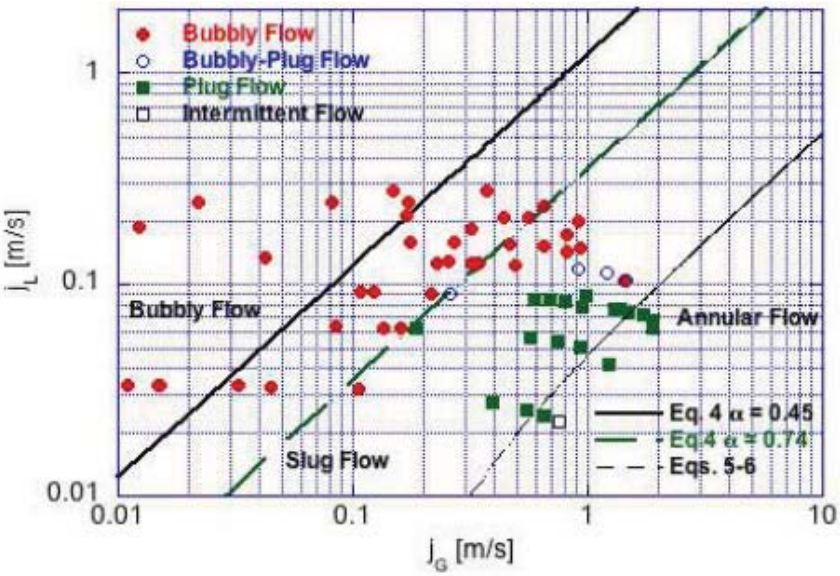

FIGURE 1.9: Microgravity flow pattern data compared with Dukler's predictions - boiling FC-72 flow in a 6mm ID tube [Celata and Zummo, 2007]

1.3.3 Void fraction and film thickness

Along with the vapor quality x, the void fraction α is an important flow parameter to calculate the mean liquid and vapor velocities u_l and u_v. Several authors have published microgravity data concerning either void fraction or averaged gas velocity and film thickness. However, these measurements remain difficult, and a lack of cohesive data can be reported in two-phase flow. Different methods can be used to measure the cross-sectional averaged void fraction: conductance probes [Bousman and Dukler, 1994, Colin et al., 1991], capacitance probes [Elkow and Rezkallah, 1997] or flow visualisations [Lebaigue et al., 1998].

Void fraction in bubbly and slug flows: for subcooled regimes corresponding to bubbly and slug flows, the mean gas velocity u_g in $\mu - g$ is well predicted by a drift flux model (Equation (1.31)) for gas-liquid flows [Colin et al., 1991]: the microgravity coefficient C_0 is approximately equal to 1.2 for a 4cm ID pipe and increases as the pipe diameter increases, which proves that mean drift between gas and liquid phases exists.

For bubbly flow, the concentration of void at the tube axis must be considered to explain the origin of the mean drift. The local bubble drift velocity is close to zero in microgravity (according to Equation (1.32)) [Colin et al., 2012, Kamp et al., 2001]. The main issue in bubbly flow is therefore the prediction of the radial void fraction distribution. An analytical model including the effects of lift force, added mass force and turbulent dispersion was recently developed to predict the void fraction distribution in upward and downward flow, both in $1 - g$ and $\mu - g$. This model clearly points out the role of the interactions between bubbles and the turbulence of the liquid phase under microgravity conditions Colin et al. [2012]. For slug flow, the bubble velocity is approximately equal to the local liquid velocity at the pipe center, which is 1.2 times the mean liquid velocity in a turbulent pipe flow.

Void fraction and film thickness in annular flow: the determination of the liquid film thickness from the void fraction measurements in annular flow is crucial for the characterisation of shear stresses and heat transfers. Film thickness data have mostly been acquired in gas-liquid flows without phase change.

Bousman [1995] measured liquid film thicknesses using conductive probes and cross-correlated signals to obtain velocities. Bousman and Dukler [1994] placed four sets of probe around the tube and determined that the annular liquid film is axisymmetric in microgravity. With a fifth sensor located downstream the other ones, they put in evidence the presence of large disturbances or roll waves, and showed that large liquid velocities increase the averaged film thickness while high gas flow velocities decrease it. These authors also pointed out the effects of liquid viscosity and surface tension on the wave structure and film thickness.

Wang et al. [2004] analysed the structure of the liquid film by using a conductive probe made of two parallel small wires going through the pipe section. Results obtained in vertical upward flow were compared between normal gravity and microgravity. It was found that the wave height and the relative interfacial roughness both decrease with increasing gas Reynolds numbers; in $\mu - g$, they are less than half the corresponding values in $1 - g$.

Ohta [2003] also observed for air-water flows and for boiling R113 flows a decrease in the wave disturbances in microgravity by comparison to normal and hypergravity conditions. At low vapor quality, the frequency of passing disturbances waves increases with gravity. The author developed an analytical model to calculate the velocity and temperature profiles in the liquid film and found that the film thickness is larger in $\mu - g$ than in $1 - g$ or $2 - g$, for qualities $x < 0.8$ and moderate mass fluxes.

Additional experiments are therefore needed to provide accurate measurements of the liquid film thicknes and detailed description of the film structure (interfacial waves, droplet entrainment...).

1.3.4 Two-phase pressure drop and shear stresses

In microgravity flows without phase change (or droplet entrainment in annular flow), the friction at the wall is directly related to the pressure drop (since the gravitational and acceleration terms of the total pressure gradient are negligible). The interfacial shear stress is more difficult to measure since it requires a good accuracy on both the pressure drop and the void fraction measurements.

Most of the studies performed under microgravity conditions concern gas-liquid flows without phase change [Bousman and McQuillen, 1994, Colin et al., 1996, Zhao et al., 2001, Zhao and Rezkallah, 1995]. Few experimental results also exist for vapor-liquid flows [Chen et al., 1991] but in an adiabatic test section downstream the heated section.

For bubbly flow: Colin et al. [1996] presented experimental data for air and water in bubbly and slug flow for tubes of different diameters. In bubbly flow, they pointed out that the friction factor is well predicted by the single phase flow correlation of Blasius (Equation (1.41)) for a liquid Reynolds number $20{,}000 < Re_l < 70{,}000$. Blasius correlation tends to underestimate the friction factor when Re_l is smaller than 20,000, which may be explained by the fact that a decreasing Reynolds number results in an

increase in the thickness of the viscous layer and that the presence of large bubbles affects this layer near the tube wall.

Zhao [2010] proposed an expression of the wall friction factor according to a Reynolds number Re_{tp} based on the mixture velocity and liquid viscosity: $f_{tp} = A \cdot Re_{tp}$ where A is a parameter that depends on the range of Reynolds number and is empirically determined, as shown in Figure 1.10. The agreement with experimental data is better than with the Blasius correlation for Reynolds numbers between 6,000 and 30,000.

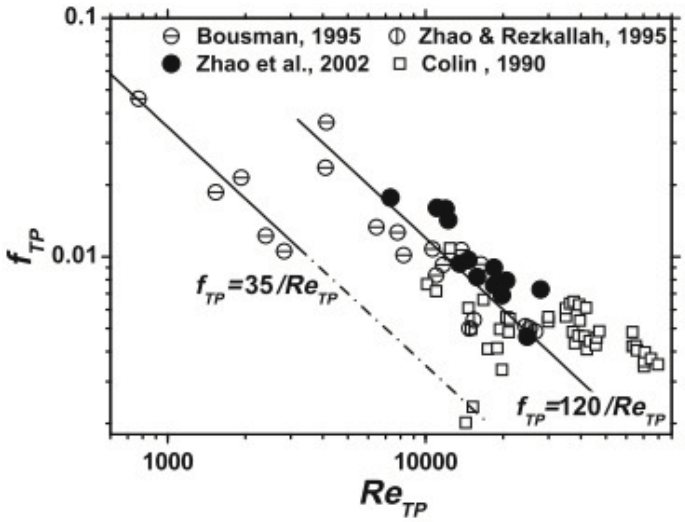

FIGURE 1.10: Pressure drop of two-phase bubbly flow in microgravity [Zhao, 2010]

For slug and annular flows: the frictional pressure drop for slug and annular flows has been compared to various empirical models (such as the Lockhart-Martinelli correlation, the homogeneous model... presented in Section 1.2) [Chen et al., 1991, Zhao and Rezkallah, 1995]. Recently, Awad and Muzychka [2014] and Fang et al. [2012] proposed a modified expression of the two-phase multiplier of the Lockhart-Martinelli correlation which gives a good agreement with experimental data.

$$\Phi_l^2 = \left[1 + \left(\frac{1}{X^2}\right)^n\right]^{1/n} \tag{1.81}$$

with $n = 2/7$ for a robust calculation

Although these correlations provide a reasonable estimation of the pressure drop, a two-fluid model has to be used to correctly reproduce the dynamics of annular flow and predict film thickness and flow velocities. As discussed in the previous section about models and correlations, it is possible to calculate both the wall shear stress and the interfacial shear stress by measuring the pressure drop and void fraction at the same time.

Bousman and Dukler [1993] determined the interfacial shear stress and developed relationships for the interfacial friction factor versus the void fraction in microgravity.

$$\frac{f_i}{f_g} = 211.4 - 245.9\alpha \tag{1.82}$$

More recently, some studies have focused on the analysis of the annular film structure (film thickness, interfacial waves). Wang et al. [2004] related the interfacial friction factor to the roughness of the interface that increase together. Ohta [2003] reported smaller values of the interfacial friction factor in microgravity than in normal gravity for moderate mass fluxes, with his model using a Froude number calculated on the mass flux G:

$$\frac{f_{i,1g}}{f_{i,\mu g}} = 1 + 0.08 \cdot \left(\frac{1-x}{x}\right)^{0.9} \cdot Fr^{-1} \tag{1.83}$$

Very few measurements exist in microgravity because of pratical difficulties related to simultaneous measurements of pressure drop and void fraction, and work has still to be done to confirm the existing results or models.

1.3.5 Heat transfer coefficient

Technical restrictions related to reduced gravity environments (such as low available power or short duration of microgravity conditions during parabolic flights) make the number of existing researches on flow boiling heat transfer rather small. Few data are available and when the heat transfer coefficient measured in $\mu - g$ is compared with the values obtained in $1 - g$, two conflictive trends are highlighted: in some experiments, there is an enhancement of the heat transfer coefficient in microgravity, and in other ones, there is a deterioration of the heat transfer coefficient. Operating conditions are not clearly specified and no cohesive dataset has been highlighted.

Experimental observations: recent experimental results obtained by Japanese, European and American teams in parabolic flights are presented here. Microgravity two-phase flow research for phase change of a single fluid component before 1994 is not treated in this section but further information can be found in the papers of Papell [1962], Feldmanis [1966], Reinarts et al. [1992] and Ohta et al. [1994].

Saito et al. [1994] carried out water flow boiling experiments in a horizontal annulus with a central heater rod during parabolic flights. In normal gravity for low and moderate mass fluxes, stratified flow occurs whereas under microgravity conditions, bubbles hardly detach from the heater rod due to the reduction of buoyancy; they flow along the rod and grow due to heating and / or coalescence, becoming larger and surrounding the heater downstream. Large differences in the flow regimes are observed between $1 - g$ and $\mu - g$ in the case of low inlet fluid velocity, high heat flux and low inlet fluid subcooling. However, the differences in the local heat transfer coefficient remain very small.

Lui et al. [1994] performed heat transfer experiments in subcooled flow boiling with R113 in tubular 12mm ID test section. Subcooled boiling heat transfer is enhanced under microgravity conditions, with heat transfer coefficients 5 to 20 % higher in $\mu - g$ and generally increasing with higher qualities, as can be seen in Figure 1.11. The greater movement of vapor bubbles on the heater surface in 1-g cause more localised turbulences, which is believed to be responsible for the increased heat transfer coefficients.

Ohta [2003] studied flow boiling of R113 in a 8mm ID vertical transparent tube, internally coated with a gold film during parabolic flights, for mass fluxes 150 $kg.s^{-1}.m^{-2} < G < 600$ $kg.s^{-1}.m^{-2}$ and heat fluxes 0.25 $W.cm^{-2} < q < 12$ $W.cm^{-2}$. As previously mentioned, authors examined bubbly, slug and annular flows. No gravity effects were observed at high mass fluxes G or at high vapor quality x. In bubbly and slug flows at low vapor quality, the heat transfer coefficient is rather insensitive to gravity level

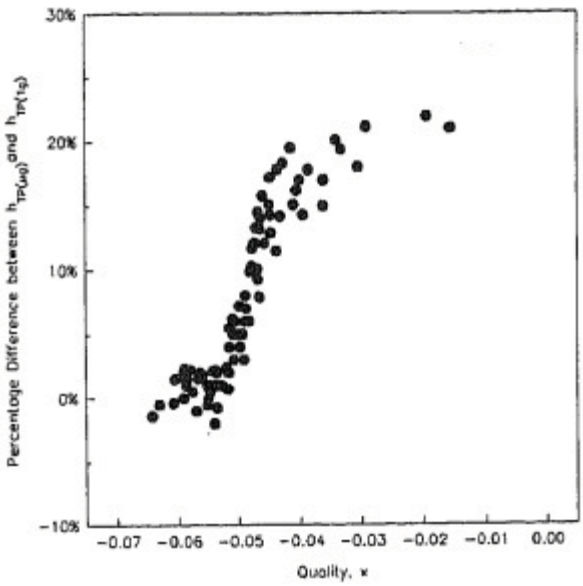

FIGURE 1.11: Percentage difference between normal gravity and microgravity heat transfer coefficients [Lui et al., 1994]

despite the important changes in bubble and slug behaviours, proving that the heat transfer is controlled by nucleate boiling (NB). However, for moderate vapor qualities, a significant deterioration of the heat transfer coefficient is observed in microgravity, in the two-phase forced-convection heat transfer regime (TFC), where the nucleate boiling is completely suppressed.

Celata and Zummo [2009] performed flow boiling experiments in parabolic flights with FC-72 in transparent Pyrex tubes of 2, 4 and 6mm internal diameters. They collected a significant dataset of heat transfer coefficients and flow patterns observations in low and normal gravity. In bubbly and slug flows, microgravity leads to a larger bubble size which is accompanied by a deterioration of the heat transfer coefficient. For moderate vapor qualities, the influence of the gravity level on the heat transfer coefficient tends to decrease as the fluid velocity increases. For high fluid velocities ($u > 25\ cm.s^{-1}$) or high vapor qualities ($x > 0.3$), the influence of the gravity level can be considered as negligible.

Baltis et al. [2012] reported experimental results on heat transfer for subcooled FC-72 flow boiling under various gravity conditions, for 2, 4 and 6mm ID tubes. They showed that the heat transfer coefficient decreases by up to 40 % in $\mu - g$ compared to terrestrial gravity. Experimental data also point out that an increase of the mass flux or of the heat flux leads to a decrease of the influence of gravity level on the heat transfer coefficient: an increase of inertial forces reduces the influence of surface forces acting on bubbles, reducing the effects of gravity. By increasing the heat flux, subcooled boiling flow becomes closer to the saturated regimes, in which the gravity level has a small influence on heat transfer.

Kim et al. [2012] recently developed a new technique for the measurement of heat transfer distributions by using an IR camera to determine the temperature distribution within a multilayer consisting in a silicon substrate coated with a thin insulator. Recent parabolic flight campaigns provided data which point out that the heat transfer coefficient is smaller in microgravity in the case of nucleate boiling regimes at low vapor quality.

Ohta and Baba [2013] reported recent measurements performed with FC-72 in 4mm ID tube for low mass fluxes ($G = 40\ kg.s^{-1}.m^{-2}$ and $G = 60\ kg.s^{-1}.m^{-2}$ and heat flux up to 1.8 $W.cm^{-2}$. On this range of mass fluxes, nucleate boiling always occurs in annular flow (NBA). The heat transfer coefficient is independent of the vapor quality up to the critical heat flux, as can be seen in Figure 1.12, it increases with the wall heat flux and is independent of the gravity level.

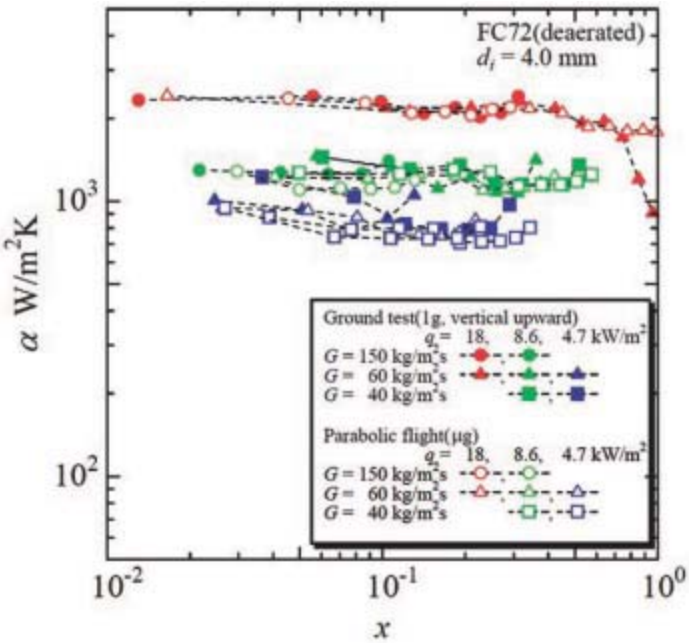

FIGURE 1.12: Experimental heat transfer coefficient in normal gravity and microgravity for very low mass fluxes [Ohta and Baba, 2013]

Summary of existing data on heat transfer: Ohta and Baba [2013] provide a summary table drawn in Figure 1.13 with the observed heat transfer modes according to mass flux, vapor quality and heat flux, with the possible effect of gravity.

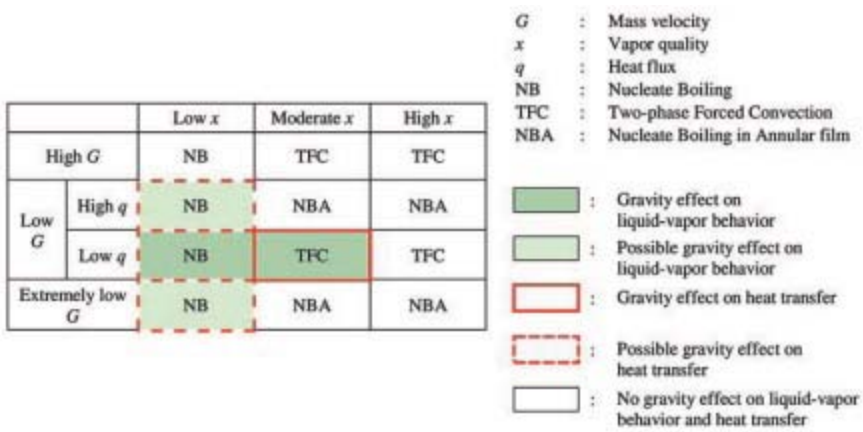

FIGURE 1.13: Summary of the influence of gravity on existing heat transfer data in microgravity [Ohta and Baba, 2013]

Experimental results from aforementioned studies [Baltis et al., 2012, Celata and Zummo, 2009, Ohta, 2003] can be summarized as follow:
− all studies agree on the fact that heat transfer is not affected by the gravity level for high mass fluxes or high vapor qualities;
− at low vapor quality in subcooled boiling regimes, nucleate boiling is observed in bubbly and slug flows. These regimes are sensitive to gravity according to Baltis et al. [2012] but insensitive according to Ohta [2003];
− at moderate quality and low mass flux, Ohta [2003] found that the heat transfer decrases in microgravity compared to normal gravity conditions.

Recent experiments were performed at mass fluxes lower than 100 $kg.s^{-1}.m^{-2}$, and this is also the objective of the future experiment for flow boiling that was designed to fly onboard the International Space Station in the Japanese experiment module "Kibo". Measurements will be performed in 4mm ID copper tube or glass tube with inside gold coating, using FC-72 [Ohta and Baba, 2013].

Regarding measurements in microgravity during parabolic flights, further experiments have to be carried out in order to complete the existing dataset by carrefuly specifying the operating conditions and corresponding regimes.

Conclusion

The main definitions and notations related to the description of flow boiling in tube for wall heat flux lower than CHF have been stated in the beginning of the chapter. Corresponding balance equations have been presented in a general way for each phase and under a simplified form for further use in the data reduction. A dimensionless analysis also allowed to list the most relevant dimensionless numbers that are used in the correlations and experimental comparisons.

Closure laws are indeed necessary for the modelling of boiling mechanisms. Various models are used depending of the flow patterns that can be encountered. A concise description of these models has been provided, and various correlations have been presented for the prediction of wall and interfacial shear stresses, and heat transfer coefficient for each model.

A state of the art review related to microgravity conditions has detailed the few data available in flow boiling along with considerations in gas-liquid flow, on flow patterns, void fraction, pressure drops and heat transfer coefficients, the latter being the most investigated physical quantity in microgravity.

The state of art review highlights a lack of data on some physical quantities under microgravity conditions (such as the void fraction) and a lack of consistency between available experimental datasets. Since the main goal of this thesis is to provide a more complete description of flow boiling in microgravity, a new experimental set-up was designed and built at IMFT to perform simultaneous flow visualisations and measurements of void fraction, pressure drop and heat transfer coefficient during parabolic flight campaigns. Aforementioned dimensionless numbers and simplified balance equations are used in the reduction of data provided by this facility that is presented in the next chapter.

Chapter 2

Experimental set-up and measurement techniques

The state of art review in Chapter 1 highlights a lack of experimental data and cohesive dataset on void fraction, wall and interfacial shear stresses and heat transfer coefficients under microgravity conditions. For that reason, a new experiment named BRASIL was designed and built at IMFT in order to perform void fraction, pressure drop and heat transfer measurements at the same time in microgravity, along with flow visualisations. The experimental set-up, measurement techniques, data reduction and measurement protocols during parabolic flight campaign are presented in this chapter. Additional details are provided with the description of an alternative experimental set-up which was the subject of a collaboration with American researchers during this PhD work.

L'état de l'art présenté dans le Chapitre 1 met en lumière un manque évident de données expérimentales cohérentes pour la caractérisation du taux de vide, des frottements pariétaux et interfaciaux ainsi que des coefficients d'échange de chaleur en ébullition en microgravité. Un nouveau dispositif expérimental, dénommé BRASIL, a donc été dimensionné et construit à l'IMFT afin d'acquérir simultanément des mesures de taux de vide, pertes de pression et températures, couplées à des visualisations de régimes d'écoulement, le tout dans des conditions de microgravité simulées lors de campagnes de vols paraboliques. Ce chapitre traite des principales caractéristiques de l'expérience, des techniques de mesure, et des protocoles d'acquisition et de traitement des données. Un second dispositif expérimental, sujet d'une collaboration entreprise lors de cette thèse avec une équipe de recherche aux États-Unis, fait l'objet d'une discussion dans le dernier paragraphe.

Dispositif expérimental

L'expérience BRASIL (**B**oiling **R**egimes in **A**nnular and **S**lug flow **I**n **L**ow gravity) a été dimensionnée afin d'étudier des écoulements bouillants de réfrigérant dans un tube vertical chauffé, dans des conditions de microgravité. Le HFE-7000 a été choisi comme fluide de travail, principalement à cause de son innocuité et de ses faibles température de saturation (34°C à pression ambiante) et chaleur latente de vaporisation.

Le dispositif est constitué d'une boucle diphasique classique, divisée en deux systèmes : un sous-système d'air permettant de régler la pression grâce à deux soufflets et un circuit hydraulique fermé destiné au réglages des conditions de travail adéquates à l'entrée de la section d'essai. Dans la boucle hydraulique, le fluide est mû par une pompe à engrenages ; le débit correspondant est mesuré par un débitmètre à effet Coriolis avant que le HFE-7000 n'atteigne les préchauffeurs, où il est chauffé jusqu'à la température de sous-refroidissement désirée ou partiellement vaporisé jusqu'à un titre en vapeur donné. Après son passage dans la section d'essai où il est de nouveau vaporisé au contact du tube chauffé, le fluide pénètre dans un condenseur composé de plusieurs plaques froides incluant des modules Peltier, des ailettes et des ventilateurs, afin d'être recondensé et refroidi avant l'entrée de la pompe.

La section d'essai elle-même est montée en trois parties : un premier segment adiabatique permet l'établissement dynamique de l'écoulement ; puis le cœur de l'expérience est constitué d'un tube de saphir de 6 millimètres de diamètre intérieur, 1 millimètre d'épaisseur et 20 centimètres de longueur, translucide et recouvert d'un dépôt d'ITO d'environ 50 nanomètres d'épaisseur : cette couche d'oxyde conductive permet un chauffage uniforme du tube par effet Joule tout en autorisant une visualisation simultanée de l'écoulement à l'intérieur. Enfin, une troisième section droite à la sortie de la partie chauffée est isolée afin de fournir des mesures dans des conditions d'adiabaticité.

Techniques de mesure

La majorité des données est exploitée à partir des mesures réalisées sur la section d'essai, mais l'ensemble de la boucle hydraulique est instrumentée, pour permettre les réglages des conditions d'entrée ou pour des raisons de sécurité.

Les mesures de température se font par l'intermédiaire de thermocouples ou de sondes platine, qui sont plus précises. Tous les capteurs de température sont étalonnés en même temps dans un bain thermostaté à l'aide d'une sonde de référence. Les thermocouples de type K sont utilisés pour mesurer la température du fluide en divers points du circuit. Un thermocouple différentiel de type T sert pour une mesure plus précise de la différence de température entre l'entrée et la sortie de la section chauffée. Une sonde platine en sortie de section d'essai joue le rôle de référence pour les thermocouples dans le liquide tandis que les

autres sondes Pt100 mesurent la température de paroi externe du tube de saphir à plusieurs endroits du tube.

Des capteurs de pression absolue permettent de surveiller la pression de fonctionnement en plusieurs points de la boucle. Des mesures de pression différentielle sont réalisées par l'intermédiaire de trois capteurs Validyne, l'un entre l'entrée et la sortie de la section chauffée, et les deux autres en doublon, sur la partie adiabatique.

La spécificité de BRASIL repose sur des sondes capacitives, dimensionnées et construites à l'IMFT, qui permettent d'obtenir des données de taux de vide. Ce capteur mesure la capacité du milieu compris entre deux électrodes de cuivre excitées à haute fréquence, cette capacité étant directement proportionnelle à la permittivité du milieu et donc à la répartition volumétrique des phases si l'on considère un écoulement diphasique. Des courbes d'étalonnage, obtenues expérimentalement en similant différents régimes d'écoulement ou par simulation numérique, sont ensuite utilisées pour traduire la capacité en taux de vide.

Divers capteurs viennent compléter l'instrumentation de la boucle, tels qu'un accéléromètre, un débitmètre et la caméra rapide qui permet d'obtenir des films d'écoulement.

Campagnes de mesure
Les campagnes de mesure dans des conditions de microgravité sont réalisées lors de vols paraboliques à bord de l'A300 ZERO-G géré par la compagnie Novespace. Un vol parabolique se compose de 31 paraboles pendant lesquelles alternent des phases d'hypergravité et de microgravité, cette dernière correspondant à 20 - 22 secondes de "presque" apesanteur à $\pm$ 0,05g. Des données en gravité normale sont également acquises lors des phases de vols stationnaires, avant d'être complétées par des essais paramétriques au sol, en laboratoire. Avec trois vols complets, cela fournit donc 93 points par campagne. Ces courts intervalles, les brusques changements de niveau de gravité et le nombre limité de points, additionnés aux contraintes de sécurité, représentent des restrictions importantes pour les expérimentateurs.

Au total, l'expérience BRASIL a participé à quatre campagnes de vols paraboliques avec Novespace et les agences spatiales française et européenne, en Mai 2011, Avril 2012, Octobre 2013 et Avril 2014. Les résultats quantitatifs présentés dans la suite de cette thèse proviennent des trois dernières campagnes.

Expérience de l'UMD
Une bourse pour la mobilité internationale a permis de développer une collaboration avec l'équipe du Pr. Jungho Kim et son doctorant Alex Scammell qui travaille à l'Université du Maryland sur un dispositif expérimental similaire à BRASIL afin d'étudier les transferts de chaleur en ébullition, dans des conditions de microgravité. Cette collaboration s'est articulée autour de la conception par l'IMFT de sondes de taux de vide adaptée au banc de l'UMD, et à l'organisation d'une campagne de vols paraboliques en France au mois de Mars 2013.

L'expérience américaine se sert d'une caméra infrarouge pour effectuer des mesures locales de température à la paroi interne d'un tube de silicium chauffé par effet Joule, ce qui permet d'obtenir une distribution du coefficient de transfert de chaleur le long de la section d'essai. Elle utilise du HFE-7100 à plus haute température de saturation, mais le travail effectué en commun a néanmoins permis de confronter des séries de données acquises dans des conditions similaires ; ces comparaisons sont présentés dans le chapitre suivant.

2.1 BRASIL experiment

The **BRASIL** experiment (**B**oiling **R**egimes in **A**nnular and **S**lug flow **I**n **L**ow gravity) was designed and built in order to investigate flow boiling mechanisms in microgravity, on the model of flow evaporator in space platforms. This study includes simultaneous measurements of temperature, pressure and void fraction under microgravity conditions provided by parabolic flights.

2.1.1 Working fluid

The working fluid is the Novec HFE-7000 engineered by 3M^{TM}, whose chemical formula is $C_3F_7OCH_3$ and that is thereafter referred to as HFE-7000. This fluid belongs to a new refrigerant class from the hydrofluoroethers family chosen to replace older refrigerants like R113 or R123, mainly because of their non-toxicity.

Two main reasons motivate the choice of HFE-7000 as working fluid in the experiment: its low saturation temperature (34°C at atmospheric pressure) and low latent heat of vaporization (132 kJ.kg^{-1} against 2270 kJ.kg^{-1} for water) make this refrigerant very convenient to use in flow boiling experiments. Moreover, severe restrictions and safety issues related to $\mu - g$ environment limit the use of some fluids. As a non-toxic and dieletric fluid that does not require a lot of power to reach saturation, the HFE-7000 is well-suited for parabolic flights.

HFE-7000 properties at saturation temperature are presented in Table 2.1 with water and classical refrigerant FC-72 properties for comparison.

		HFE-7000	**Water**	**FC-72**
T_{sat}	°C	34	99.98	51
M	g.mol^{-1}	200	18	288
ρ_l	kg.m^{-3}	1374.7	958.4	1602.2
ρ_v	kg.m^{-3}	7.98	0.59	13.21
ν_l	m^2.s^{-1}	$2.71{\cdot}10^{-7}$	$2.95{\cdot}10^{-7}$	$2.70{\cdot}10^{-7}$
Cp_l	J.kg^{-1}.K^{-1}	1328	4216	1101
$h_{l,v}$	kJ.kg^{-1}	132.2	2270	88.0
λ_l	W.m^{-1}.K^{-1}	0.075	0.679	0.054
σ	N.m^{-1}	$1.240{\cdot}10^{-2}$	$5.891{\cdot}10^{-2}$	$0.793{\cdot}10^{-2}$

Table 2.1: HFE-7000 properties at saturation temperature and atmospheric pressure compared to water and FC-72 properties

2.1.2 Hydraulic loop

BRASIL has been designed in order to investigate upward flow boiling of HFE-7000 in millimetric tubes. But a lot of structural or electrical choices are imposed by restrictions and safety issues related to the microgravity measurement environment.

General structure: the BRASIL experiment is a classical two-phase flow loop that is divided into two sub-systems:

– the hydraulic system, a closed loop that maintains specific pressure, temperature and mass flux in order to obtain the desired conditions at the inlet of the test section;
– the air system, which sets the pressure in the hydraulic system through two bellows that are in contact with the air on one side and with the liquid on the other one. These bellows also allow to compensate the volume variations that occur in the flow loop due to the heating of the liquid or to the production of vapor.

The experiment is installed in a single rack consisting in two frameworks fixed by a common large aluminum base plate, as can be seen in Figure 2.1.

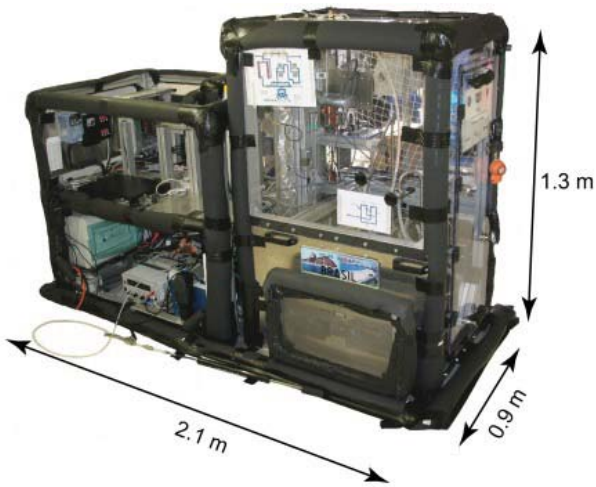

FIGURE 2.1: BRASIL rack in flight configuration - Avril 2012

This design was chosen accordingly to the requirements of parabolic flight campaign during which the measurements under microgravity conditions are performed. The higher framework contains the hydraulic loop and the air system; it is fully sealed by a containment made up of transparent Lexan pannels and aluminium base walls to prevent any leakage. All electrical, setting and acquisition devices that are liquid free are fixed in the second framework that remains open for the experimenters to access them.

Hydraulic system: the hydraulic loop is schematically illustrated in Figure 2.2.

As mentioned, the system is pressurised with the use of two separated bellows. Moreover, the pressure can be manually increased with a bike pump or decreased using an air purge with a manual valve.

In this pressurised loop, a volumetric gear pump (L21755 Micropump, with the DC-305A motor) is used to circulate the working fluid in liquid phase. The mass flow rate can be adjusted by the variation of the rate of gear rotation and a PID is added to maintain the setpoint value since it can change with the pressure drop variations in the hydraulic loop. A Coriolis flowmeter measures the mass flow rate at the outlet of the pump.

The liquid HFE-7000 is first circulated through two handmade serially connected preheaters. There, it can be preheated to a given liquid temperature or partially vaporized at a desired vapor quality. The preheaters are covered with thermal insulation foam to minimize thermal losses, and are electrically powered using a variable phase angle power regulator. The power is manually set by the experimenter.

Then, the fluid enters the test section, which is described in the following section. There, further fluid heating and / or vaporisation can be performed.

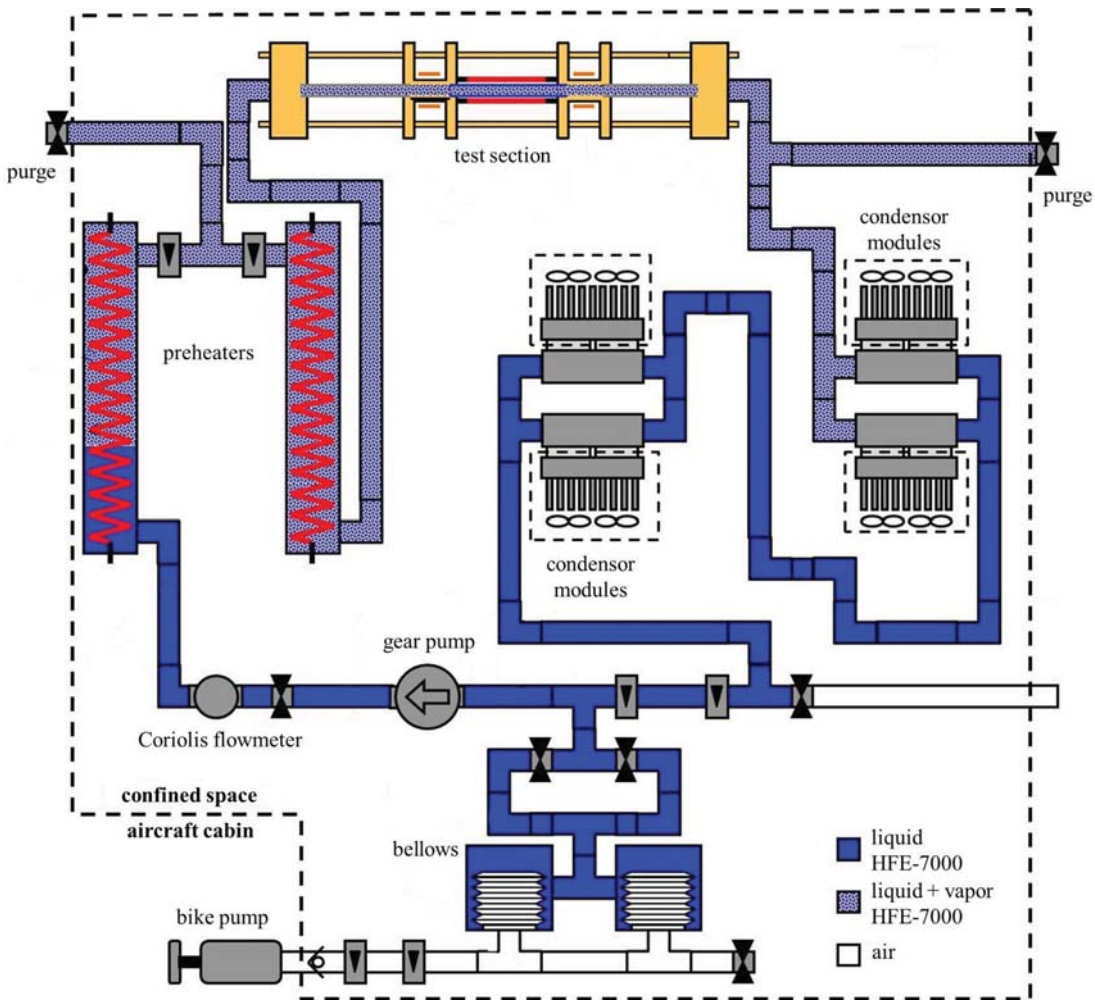

FIGURE 2.2: Schematic representation of BRASIL hydraulic loop

Finally, two serial condensers with two modules each are used to cool the fluid. Each module consists in a cold plate, nine Peltiers modules and a heat sink with fans to remove the heat from the Peltier modules. The regulation of the power input of the Peltier modules is automatic and driven by a PID that maintain the desired temperature at the inlet of the pump. A cooling of 10°C below the saturation temperature is set by the experimenter to ensure that no vapor will enter the pump, which would instantly result in a pump malfunction.

Flow parameters: the HFE-7000 may be in a liquid state or liquid-vapor state depending on the portion of the circuit, but it is never in a pure vapor state. The experimenter has to pay special attention with the flow parameters settings to limit the vapor mass fraction; indeed, at very high vapor qualities, there is a degradation of heat transfers which could result in a consequent increase of the temperature of the heaters. Ranges of the flow parameters that are set by the experimenter are presented in Figure 2.3.

The loop pressure can be set from 1 to 2 bar (the corresponding saturation temperatures for the HFE-7000 are respectively 34°C and 56°C for these pressures); atmospheric pressure is favored but the pressure variations due to heating and phase change are not negligible. On this range of pressure, the pump can be set to make the liquid circulate at mass fluxes between 40 $kg.s^{-1}.m^{-2}$ and 1000 $kg.s^{-1}.m^{-2}$. A heat power ranging from 0 to 900 W is injected to the fluid in the preheaters. There, the fluid reaches

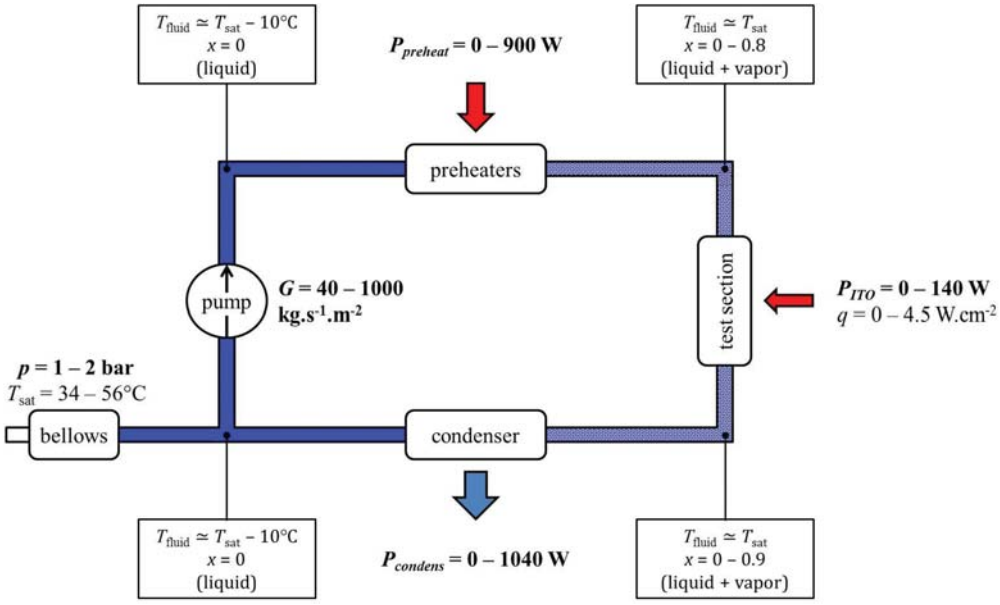

FIGURE 2.3: Settings made by the experimenter and corresponding flow parameters

its saturation temperature and is then partially vaporized until it reaches the desired vapor fraction. The maximal attainable value of x depends on the mass flow rate in the loop (at the minimum mass flux of $G = 40$ kg.s^{-1}.m^{-2}, a value of 0.9 can be reached with a power input slightly lower than 900W). Then, the two-phase flow enters the test section where it is further vaporized. The corresponding power input is however smaller than the power input at the preheaters, meaning that the vapor quality at the outlet of the test section is just slightly higher than at the inlet. Finally, the fluid needs to be condensed and cooled; the condenser has to evacuate the whole heat which is injected at the preheaters and the test section, i.e. a maximal heat of 1100 W. The experimenter set the wanted temperature at the inlet of the pump which is regulated by the Peltier modules in the condenser.

2.1.3 Test section

BRASIL test section is illustrated in Figure 2.4(a). It is composed of two adiabatic sections made of isolated stainless steel tubes located at both ends of a the heated sapphire tube that is the core of the experiment. Thermoplastic elements made of polyether ether ketone (PEEK) serve as interconnections for these three pieces and give space for the elements of the measuring system.

The two adiabatic parts are made of 6mm ID stainless steel tubes whose lenghts are around 22cm and 15cm, respectively. The tubes are covered with thermal insulation foam in order to minimize thermal losses and approach adiabatic conditions. The first tube, the longest one, is used for dynamical flow establishment before the inlet of the sapphire tube. The second one, at the outlet of the sapphire tube, is long enough to enable the measurement of pressure drops along it.

The central part of the test section is a 20cm long sapphire tube with an inner diamater of 6mm and a thickness of 1mm, that can withstand pressures up to 100 bar. The outer surface is coated on a length of 16.4cm with ITO, an electrical conductive coating (with an about 50 nm thickness) that enables a uniform heating of the outer surface by Joule

effect. The coating affects just negligibly the transparency of the tube; thus, a visual display of the flow is possible with the use of a high-speed video camera, which enables flow pattern identification.

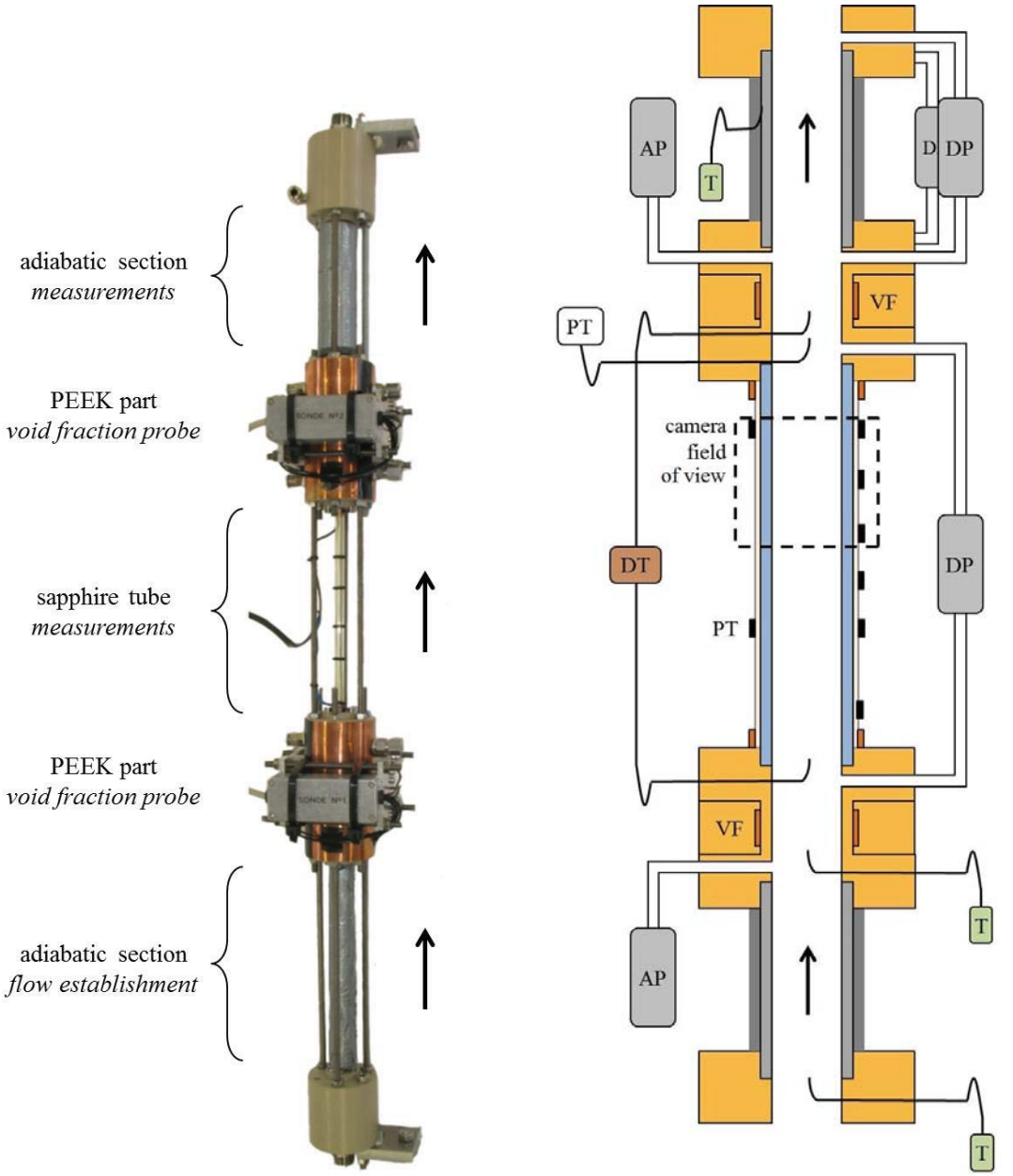

(a) Configuration without sensors

(b) Schematic of the measuring system on the test section - April 2014

FIGURE 2.4: BRASIL test section - AP: absolute pressure, DP: differential pressure, T: temperature, DT: difference of temperature, VF: void fraction, PT: PT100 probe

The measuring system on the test section has been modified several times to improve the measurements. Figure 2.4(b) presents the final version of the test section with its sensors (April 2014). In order to determine closure laws, measurements of liquid and wall temperatures, pressure drop and void fraction are needed, along with flow visualisations. The measurement techniques and their accuracy are discussed in the following section.

2.2 Measurement techniques and accuracy

This section presents the metrology that is used to acquire data with the BRASIL experiment. Various measurement techniques and their accuracy are described, with a more detailed part devoted to void fraction measurements.

Except for the void fraction measurements which are performed with a specific electronics and its own program, the data acquisition system consists in a NI DAQ (National Instrument data acquisition system), two laptops and a PC central unit for the acquisition of images from the high-speed camera. The NI DAQ is equipped with two cards that enable a simultaneous acquisition of 72 measurement signals (depending on the campaign, between 30 and 50 sensors are connected to the acquisition system) with a frequency set at 100 Hz for the experiment. It is well suitable for the temperature measurements since it provides an internal cold junction compensation for the thermocouples. The interface of the NI DAQ is a LabVIEW program designed to display all the important values live and to save the data using a text-based file format for further processing in Matlab or Excel.

BRASIL measuring system includes a lot of sensors and devices that are used for safety controls required to carry out experiments during parabolic flights, such as thermocouples that monitor the surface temperature of the heaters or overpressure valves to avoid large pressure increases. Only the measurements related to the data that are relevant for the investigation of flow boiling under microgravity conditions are presented in the following paragraphes.

Thereafter, the term δX refers to the uncertainty in the variable X in a general and non-specific way, allowing to write:

$$X = X_{mean} \pm \delta X \tag{2.1}$$

This error is somewhat equivalent to the standard deviation σ and can be calculated with the principle of propagation of uncertainty using partial derivatives to propagate error.

2.2.1 Flow parameters

The primary measurements for the determination of closure laws are temperature, pressure drop and void fraction measurements. However, other flow parameters or measured values can induce errors in the calculations. Characterising the accuracy on the mass flux, gravity level or tube thickness, for example, is also important.

Tube dimensions: the tube specifications (both for stainless steel tubes and sapphire tubes) are provided by the manufacturers and verified at the delivery. The uncertainties in the sapphire tube dimensions are the following:
$D_i = 6 \pm 0.05$ mm
$D_o = 8 \pm 0.05$ mm
$L = 200 \pm 0.1$ mm.

Fluid properties: thermodynamical HFE-7000 properties are given by experimental curves depending on the temperature or pressure, that are provided by manufacturers or laboratories. Linear regressions or regressions of 2nd / 3rd order are used to calculate

the fluid properties. For example, with 20°C $< T <$ 60°C:

$$\begin{aligned} \rho_v &= 3.904861 - 0.029404 \cdot T + 0.004386 \cdot T^2 \\ \delta\rho_v &= [-0.029404 + 0.004386 \cdot T] \cdot \delta T \end{aligned} \tag{2.2}$$

For a given saturation temperature of 34°C, $\rho_v = 7.98$ kg.m^{-3} $\pm$ 0.03%. Temperature and pressure measurements are accurate enough to consider that the uncertainties in all the fluid properties are negligible (less than 1%).

Mass flux: a mass flowmeter operating on the "Coriolis principle" contains a vibrating "U" tube in which a fluid flow causes changes in frequency, that depends on the mass flow rate inside the "U" tube. This technolgy is fast and accurate, and above all, the measurement is independent of the fluid properties; a Coriolis flow meter can be used with a dieletric fluid and the output signal is not influenced by the gravity level.

The nominal uncertainty of the Micromotion R025S mass flowmeter that was chosen for the experiment is $\pm$ 0.5% of the measured value. According to Equation (1.2), the mass flux G and the corresponding uncertainty δG can be written as:

$$G = \frac{4 \cdot \dot{m}}{\pi \cdot D_i^2} \qquad \text{and} \qquad \delta G = \sqrt{\left(\frac{4}{\pi \cdot D_i^2} \cdot \delta\dot{m}\right)^2 + \left(\frac{-8 \cdot \dot{m}}{\pi \cdot D_i^3} \cdot \delta D_i\right)^2} \tag{2.3}$$

The mass flux ranges from 40 kg.s^{-1}.m^{-2} to 1000 kg.s^{-1}.m^{-2}. For these boundary values, the uncertainty is:
$G = 40 \pm 0.7$ kg.s^{-1}.m^{-2}
$G = 1000 \pm 17.4$ kg.s^{-1}.m^{-2}.

Gravity level: the gravity level is acquired by a 3 axis SUMMIT 34201A accelerometer that can measure a relative acceleration of $\pm 2g$ with a precision of 0.3% of the full scale. This sensor is fixed on the framework about 15cm away from the sapphire tube.

Heat fluxes: heat powers $P_{preheat}$ and P_{ITO} are delivered to the fluid from the preheaters and from the ITO coating, respectively. The heat losses to the surroundings are assumed to be negligible (this assumption is verified in the heat transfer section). The accuracy on the output voltage U and intensity I delivered by the two power supplies corresponds to uncertainties $\delta P_{preheat}$ and δP_{ITO}:

$$\delta P_n = \sqrt{(U_n \cdot \delta I_n)^2 + (\delta U_n \cdot I_n)^2} \tag{2.4}$$

The accuracy given by the manufacturers are $\pm$ 45 mV and $\pm$ 30 mA for the preheaters power supply (QVR-320 variable regulator with 220V input) and $\pm$ 30 mV and $\pm$ 10 mA for the ITO power supply (EA-PS 3150-04 B). To discuss the accuracy of measurements, only the value of $\delta P_{preheat}$ is needed for the preheaters (for the calculation of the uncertainty in the inlet vapor quality). However, in the test section, the heat flux imposed through the ITO coating is given by:

$$q_{ITO} = \frac{P_{ITO}}{\pi \cdot D_i \cdot L_{heated}} \tag{2.5}$$

with the corresponding uncertainty δq_{ITO} that is calculated in Table 2.2:

$$\delta q_{ITO} = \sqrt{\left(\frac{\delta P_{ITO}}{\pi \cdot D_i \cdot L_{heated}}\right)^2 + \left(\frac{-P_{ITO} \cdot \delta D_i}{\pi \cdot D_i^2 \cdot L_{heated}}\right)^2 + \left(\frac{-P_{ITO} \cdot \delta L_{heated}}{\pi \cdot D_i \cdot L_{heated}^2}\right)^2} \tag{2.6}$$

	U [V]	I [A]	P_{ITO} [W]	q_{ITO} [W/m^2]
Low heat flux	49.5	0.304	15.05 ± 0.50	4867.8 ± 165.2 (± 3.4 %)
High heat flux	140.6	0.859	120.78 ± 1.41	39069.1 ± 559.9 (± 1.5 %)

TABLE 2.2: Uncertainty in the wall heat flux delivered through the ITO coating

2.2.2 Pressure

Absolute pressure measurements and differential pressure measurements are performed, mainly in the test section (as illustrated in Figure 2.4(b) but also for safety issues.

Absolute pressure: the absolute pressure is measured at the inlet and outlet of the sapphire tube, and at the outlet of the pump, preheaters and condenser, by Keller PAA21 absolute sensors (AP in Figure 2.4(b)) with a full scale of 0 - 5 bar and an accuracy of ± 0.25 mbar. These sensors are mostly used to monitor the pressure in the sapphire tube and calculate the corresponding saturation temperature.

Differential pressure: differential pressure measurements are performed with four Validyne pressure transducers (model P305D furnished with various membranes). The deformation of a membrane under a pressure difference is measured by a strain gauge and the output signal is a voltage that linearly depends on that pressure difference. The accuracy given by the manufacturer is ± 0.5% of the full scale.

Three differential pressure sensors (DP) are used in the test section: the first one (membrane n°28, 56 cmH_2O full scale, accuracy of 2.8 mmH_2O $\simeq$ 0.27 mbar) measures the pressure drop along the sapphire tube; two redundant transducers (membrane n°28, 56 cmH_2O full scale, accuracy of 2.8 mmH_2O $\simeq$ 0.27 mbar and membrane n°30, 86 cmH_2O full scale, accuracy of 4.3 mmH_2O $\simeq$ 0.42 mbar) are located on the second adiabatic section, at the outlet of the sapphire tube. This measurement is convenient for the calculation of the wall friction since the acceleration term in the total pressure gradient is null on this adiabatic length. Precise calibrations of these sensors are performed using a water column. The latest version of the calibration curves is provided for two of these Validyne transducers in Appendix A.

2.2.3 Temperature

Like pressure measurements, temperature measurements can be divided into two categories: absolute and differential pressure measurements. Only the temperature measurements in the test section are discussed.

Absolute temperature: temperature measurements in the fluid and at the sapphire wall are needed to characterise heat transfer coefficients.
− sheathed type K thermocouples of 0.5mm diameter (referred to as T in Figure 2.4(b)) are used to measure the temperature of the fluid at the inlet of the test section (before the adiabatic part and before the sapphire tube). Another thermocouple measures the outer surface temperature of the stainless steel tube used for the second adiabatic section, under the insulation layer. All the thermocouples use the internal cold junction compensation of the NI DAQ. The accuracy on the temperature measurement with the thermocouples is ± 0.25°C (experimentally, the maximal error on this type of measurement is ± 1°C);

– resistive Pt100 probes (PT) are used to measure the temperature of the external surface of the sapphire tube at different locations. The accuracy of these sensors is better than the one of the thermocouples (± 0.10°C) but ensuring a good thermal contact between the probe and the wall is an important issue that influences the measurement. Depending on the measurement campaign, following configurations have been tested:
· four equally distant Pt100 probes are pressed against the tube using O-rings, one Pt100 is used to measure the ambient temperature in the containment near the sapphire tube;
· eight Pt100 probes are installed in the configuration reported in Figure 2.4(b): more locations are investigated and two probes are used to double measurements. These probes are pressed against the wall using nylon screws perpendicular to the tube.
During the last campaigns, a 0.5mm Pt100 probe is also used to measure the fluid temperature at the outlet of the sapphire tube, and is considered as the liquid reference to set the offset of the thermocouples.

Differential temperature: the data reduction shows the importance of the measurement accuracy on the temperature difference between the inlet and the outlet of the sapphire tube (especially for the calculation of the vapor quality in subcooled boiling). Therefore, a differential thermocouple is installed to precisely measure this temperature difference. This thermocouple uses a connection between the cold and hot junctions of two different type T thermocouples to measure a difference of temperature with a precision better than ± 0.1°C.

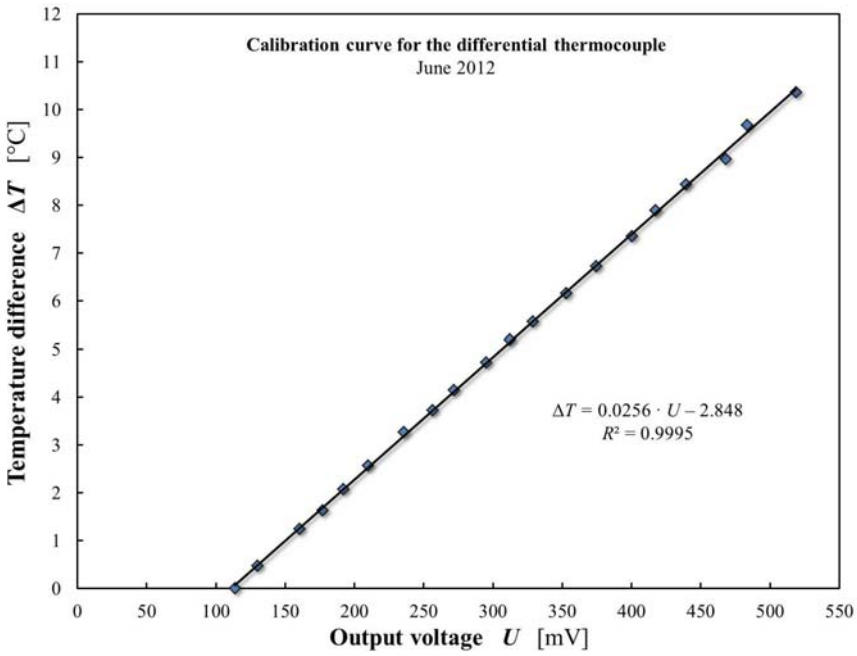

FIGURE 2.5: Calibration curve for the type-T differential thermocouple

Due to changes in the experiment configuration or deterioration, temperature sensors are often added or removed, which requires multiple precise calibrations to ensure relevant measurements. For this purpose, the type K thermocouples and the Pt100 probes are placed into a thermal bath of water or silicon oil whose temperature is varied from 15°C to 50°C. The exact temperature of the bath is obtained from a standard high-precision resistance device which was calibrated in a professional laboratory (precision of ± 0.05°C). The differential thermocouple is calibrated in a similar way using two different calibration baths: the cold junction is dipped into the water at a constant

ambient temperature and the hot junction into a heated bath. Figure 2.5 presents the calibration curve for one of the differential thermocouples that were used.

2.2.4 Void fraction

In BRASIL, two capacitance probes are used to measure the void fraction at the inlet and outlet of the test section. Since void fraction data are crucial to investigate flow boiling mechanisms and difficult to acquire, a detailed description of the measuring principle, sensor design and calibration protocol is presented here.

Measuring principle: capacitance as well as conductivity void fraction sensors are based on the measurement of the electrical impedance Z that is defined as:

$$\frac{1}{Z} = \frac{1}{R} + 2 \cdot \pi \cdot j \cdot f \cdot C \tag{2.7}$$

The impedance Z consists in a resistive term R and a capacitive term $1/2\pi \cdot j \cdot f \cdot C$ in parallel. Let us consider a parallel-plate capacitor, where A is the surface of the plates, d the distance between the plates and f the frequency used to excite the plates, as shown in Figure 2.6.

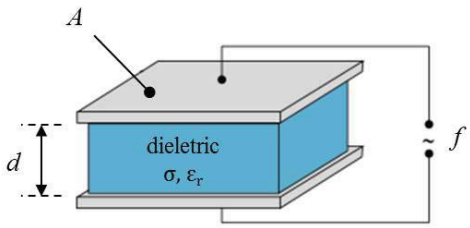

FIGURE 2.6: Parallel-plate capacitor

The effective capacitance C and the electrical resistance R are defined as:

$$C = \frac{\epsilon_0 \cdot \epsilon_r \cdot A}{d} \qquad \text{and} \qquad R = \frac{d}{A \cdot \sigma_{elec}} \tag{2.8}$$

where ϵ_r is the relative permittivity of the medium and σ_{elec} its electrical conductivity.

Applying a high frequency f and using a dielectric (with a low conductivity σ_{elec}) make the resistive term of Equation (2.7) negligible compared to the capacitive term. According to the definition of Equation (2.8), the impedance Z is thus only dominated by permittivity effects. In the case of a two-phase vapor-liquid flow circulating between the parallel plates of the capacitor, the measured capacitance will therefore depends on the volumetric composition of the fluid since the dielectric constants (and especially the permittivity) are different for each phase, as can be seen in Table 2.3. Thus, the void fraction can be deduced from the capacitance measurement using a calibration curve.

In the specific case of BRASIL experiments, an excitation frequency of 31.6 kHz has been chosen. According to Equation (2.8), this value corresponds to a ratio of the capacitive term over the resistive term of about 1300, which allows to conclude that permittivity effects are dominant in this region.

	Relative permittivity ϵ_r [-]	**Conductivity** σ_{elec} [S.m^{-1}]
HFE-7000 liquid	7.4	10^{-8}
HFE-7000 vapor	1.4	
FC-72 liquid	1.75	10^{-15}
FC-72 vapor	1.0	
Teflon	2.1	10^{-25} - 10^{-23}
Air	1	
PEEK	3.2	10^{-16}

TABLE 2.3: Permittivity and dielectric conductivity for HFE-7000, FC-72 and PEEK

Sensor design: Figure 2.7 presents typical non-intrusive electrodes configurations for capacitance void fraction sensors [Caniere, 2009]. In the litterature, the ring type sensor and the configuration with two-half-cylindrical electrodes are the two most favoured geometries because they promote the sensor sensitivity. An attempt to design a ring type sensor at IMFT resulted in a non-linear response and practical difficulties for the fabrication. For that reason, parallel plates type probes were developed: this non-intrusive geometry is the closest one to the two-half-cylindrical electrodes configuration that gives precise measurements, and its construction is very simple.

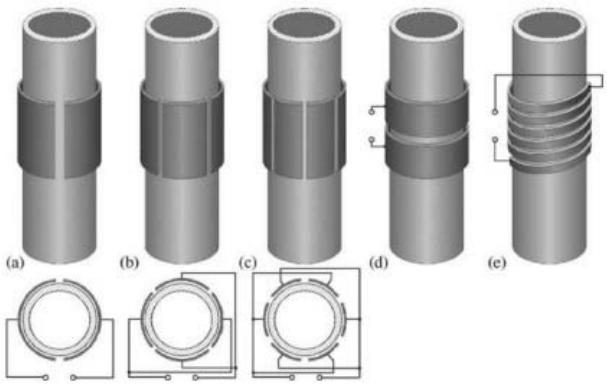

FIGURE 2.7: Typical electrodes configurations for capacitive void fraction measurements in circular geometries [Caniere, 2009]

The general design of the void fraction probe (VFP) used in BRASIL is schematically illustrated in Figure 2.8 and can be seen in Figure 2.4(a). A void fraction probe is principally composed of two measurement electrodes and four guard electrodes which are placed in a face-to-face configuration using plain PEEK-made mountings (in Figure 2.8(a), the electrodes compartments are filled with PEEK pieces that maintain the electrodes pressed against the wall near the tube). In the first design of this probe, the geometrical shape of the measurement electrodes are charaterised by an axial length of 14mm and a width of 14mm. The dimensions of the guard electrodes are 10mm x 14mm, and the separation between the parallel electrodes amounts to 16mm. All the electrodes are made of a thin copper sheet that is very conductive. A copper shield also covers the outer surface of the PEEK mounting to prevent noises. The electronics circuit is embedded into a metallic case and fixed as close as possible to the measuring electrodes to avoid stray capacitance due to important wire lengths.

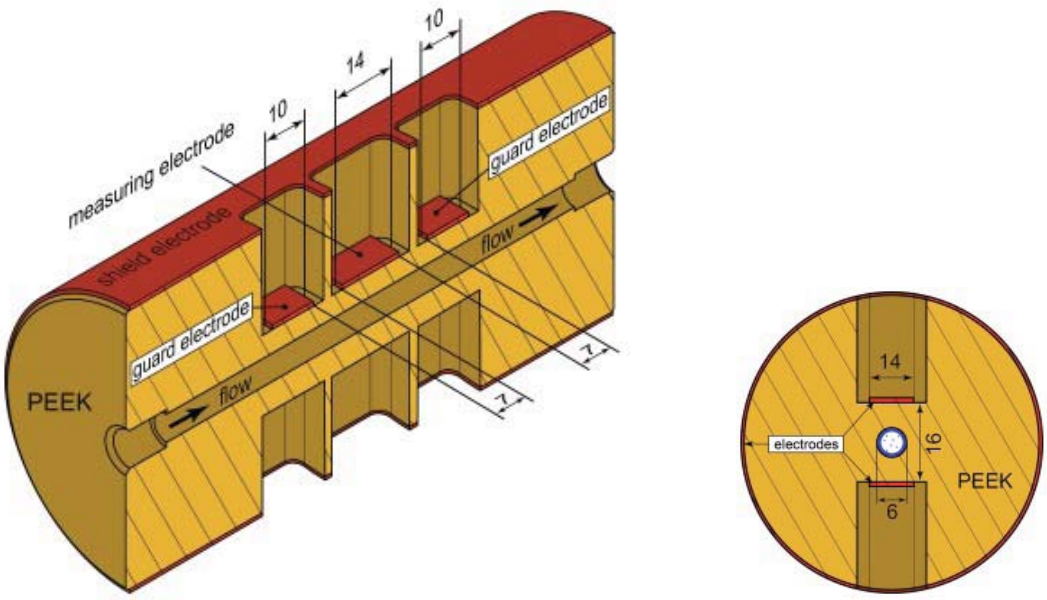

(a) 3D breakout (b) Cross-sectional schematic

FIGURE 2.8: General schematic of a void fraction probe (dimensions in mm)

Sensors features and improvements: an extensive study of the void fractions probes during devoted campaigns and measurement campaigns highlighted some features of the capacitance signals and allowed some improvements. The main conclusions and results of this study are presented here. An extended review of the specifications of the void fraction probes can be found in the report of Eisenbraun [2012].

Sensitivity: the sensitivity of the void fraction probe is described by the total capacitance difference ΔC between the all-liquid and all-vapor states of the fluid inbetween the measuring electrodes:

$$\Delta C = C_{liq} - C_{vap} \tag{2.9}$$

For the first generation of probes, the sensitivity amounts to 0.084 pF and 0.082 pF, respectively (the all-vapor state is briefly reached during the purge of the experiment). It depends on the tube diameter D, the axial electrode length L_{elec}, the electrode width W_{elec}, the parallel electrode separation d and the relative permittivity of the fluid phase $\epsilon_{r,k}$, plus the permittivity $\epsilon_{r,PEEK}$ and the thickness of the PEEK material between same side electrodes.

Maximizing the sensitivity is crucial to ensure accurate measurements. Since the conductivities of the working fluid and of the PEEK are negligible, the influence of the above mentioned parameters that can be studied using a geometrical simplification of the sensor and an equivalent capacitance circuit. A simple model of plate capacitor as described in Figure 2.6 yields $\Delta C = 0.091$ pF and can therefore be considered as relevant to study the influence of the design parameters on the sensitivity.

The model shows that the main feature affecting the sensitivity is the distance between parallel electrodes (which includes the tube diameter and PEEK lengths): ΔC increases non-linearly with the decreasing electrode separation. Another non-negligible parameter is the axial electrode length L_{elec}: the spatial resolution is worsening with long electrodes but the fringe capacitance increases with too important decreases of L. The choice of the working fluids matters too: according to the properties presented in Table 2.3, FC-72 is

not well-suited for capacitance measurements because of its low dielectric constant. As for the electrode width W_{elec}, its influence on the sensitivity is negligible as long as the electrodes are wider than the tube.

Minimizing the distance between the electrodes and the tube and choosing an electrode length $L_{elec} = D$ would result in an improvement of the probe with a higher sensitivity.

Frince capacitance: The edge effects, also known as fringing effects, cause an additional capacitance to be measured outside the electrodes, due to the bending form of the electric field. Thus, guard electrodes are necessary to minimize the influence of fringing field lines on the measurement of the void fraction.

To assess the influence of edge effects on the measured capacitance, measurements of capacitance as a function of liquid level are realised. For void fraction probes without guard electrodes, data show that around 10% of the capacitance measurement corresponds to a volume outside the measuring electrodes and that the lines of the fringe field bend to a distance which is around the half of the electrode length as can be seen from plotting the capacitance according to the height of liquid in the probe. In the first experiments, an increase in the separation distance between same-side electrodes does not allow to conclude on the efficiency of driven guard electrodes. However, recent measurements with smaller separations allow to conclude on the interest of guard electrodes to prevent fringing effects. The influence of the width of the guard electrodes was not studied due to height limitations and practical difficulties.

Stray capacitance: in the case of capacitive sensors, stray capacitances are essentially unwanted capacitances due to wires and capacitive bodies in the proximity of the void fraction probe. Because of the small order of magnitude of the sensitivity, stray capacitances must be minimzed. Adding a copper shield and shortening the wires connecting the electrodes and the electronics have proven efficient, by significantly reducing the signal noise.

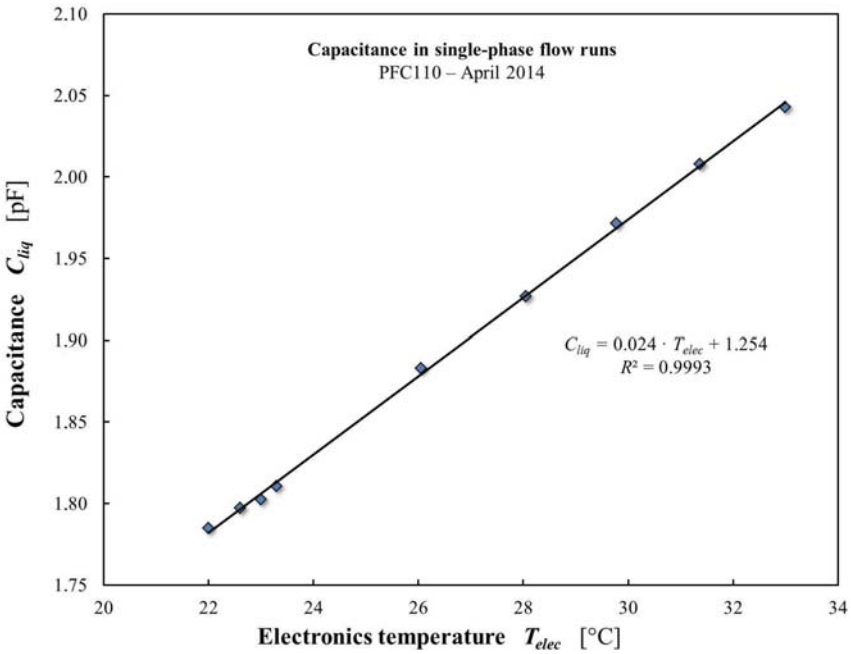

FIGURE 2.9: Effect of the electronics temperature on the capacitance measurements in liquid single-phase flow

Temperature effects: The influence of the temperature on the measurements is a key issue to process void fraction data. Two temperature effects can be taken into account:
– the first temperature effect concerns the fluid temperature, since the permittivity of the fluid depends on the temperature. However, experiments have shown that this temperature effect can be neglected on BRASIL fluid temperature range;
– in contrast, the temperature of the probe electronics strongly affects the measured capacitance. A linear curve describes the relation between this two parameters, as shown in Figure 2.9 from parabolic flight campaign data, and single-phase flow experiments are necessary to correct the effect of the electronics temperature. Indeed, this temperature, that is measured by a thermistor inside the electronics casing, can increase a lot during a series of experiments.

Calibration: for a vapor-liquid flow, the simplest and most reliable method is a statical calibration which simulates each phase by a material of similar permittivity (see Table 2.3). For the case of annular flow, a Teflon rod is dipped into the void fraction probe that is filled with liquid HFE-7000. A bubbly flow is simulated by polystyrene foam (Styrofoam) spheres whose diameter is known and that are placed into liquid HFE-7000. The schematics of these methods are shown in Figure 2.10(a) and 2.10(b), respectively.

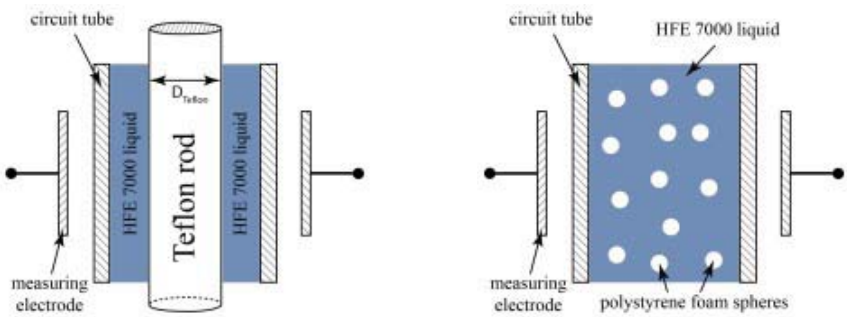

(a) Annular flow calibration (b) Bubbly flow calibration

FIGURE 2.10: Methods used to calibrate the void fraction probes by simulating annular and bubbly flows

To take into account the difference on permittivity between the materials (Teflon or Styrofoam) and the actual fluid properties, a normalized capacitance C^* is used:

$$C^* = \frac{C_\alpha - C_{vap}}{C_{liq} - C_{vap}} = \frac{C_\alpha - C_{vap}}{\Delta C} \tag{2.10}$$

Figure 2.11 presents the results of calibration measurements for one void fraction probe (June 2012). Experimental points for annular flow simulation correspond to various diameters of Teflon rods. Slug flow is treated with the annular calibration curve because the void fraction is dominated by the cylindrical vapor slugs. Previous calibration measurements performed for a ring type sensor are also plotted [Brauckhoff, 2010]; in this configuration, the relation between C^* and α was found to be linear for bubbly flows.

Calibration experiments have to be performed with the utmost care: a small error on the diameter of the Teflon rod or a signal with too many noises can result in an important shift on the calibration curve and therefore an important error on the void fraction. Moreover, practical difficulties related to available Teflon rod diameters are an issue to precisely determine the shape of the curve in the limit $C^* = 0$, i.e. $\alpha = 1$ which is in an area of interest for annular flow experiments. For that reason, theoretical models and COMSOL simulations were set-up to complete experimental calibrations.

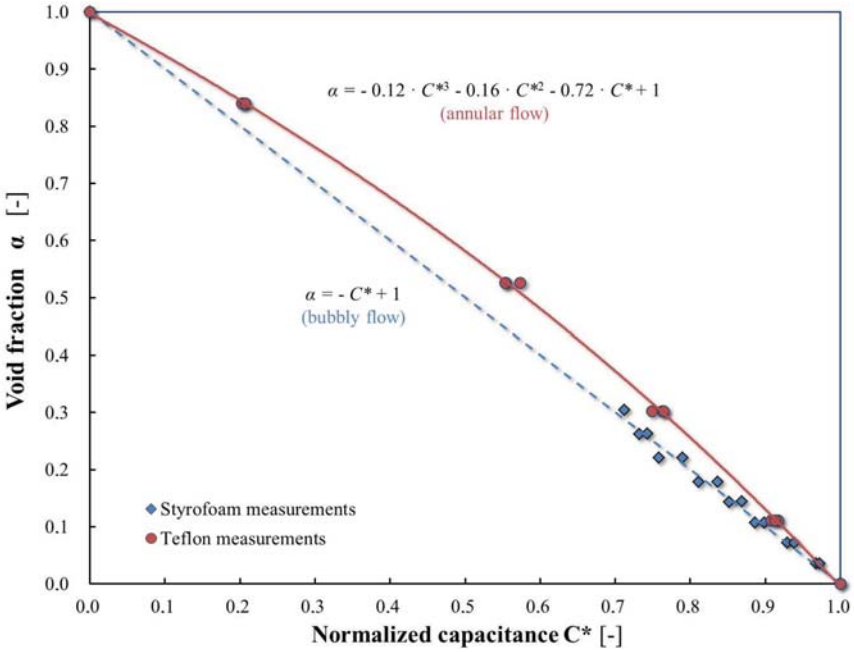

FIGURE 2.11: Experimental data for the calibration of a void fraction probe in the case of annular and bubbly flows

Models and simulations: in order to test the portability of the linear calibration for bubbly flow obtained from a ring type sensor and to improve the accuracy of the calibration curve for high void fractions in annular flow, theoretical models and COMSOL simulations were developed.

Theoretical models: theoretical models using geometrical simplifications and equivalent capacitance circuits have been developped for both bubbly and annular flow cases. The applied geometries are presented in Figure 2.12. The results are illustrated in Figure

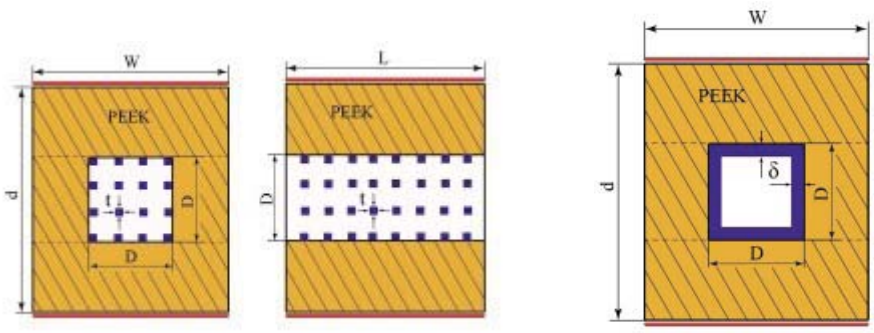

(a) Front and side views - bubbly flow (b) Front view - annular flow

FIGURE 2.12: Simplified geometries of bubbly and annular flows used in theoretical capacitance models

2.13 where the all-liquid and all-vapor capacitances are calculated with the plate capacitor model previously used to determine the sensitivity ΔC. Curves obtained with theoretical models are compared with corresponding experimental data. It can be seen that the theoretical calibration curve for bubbly flow is not linear as expected from the measurements in a ring type sensor. In contrast, the results for the annular flow confirm that Teflon rod calibration is relevant.

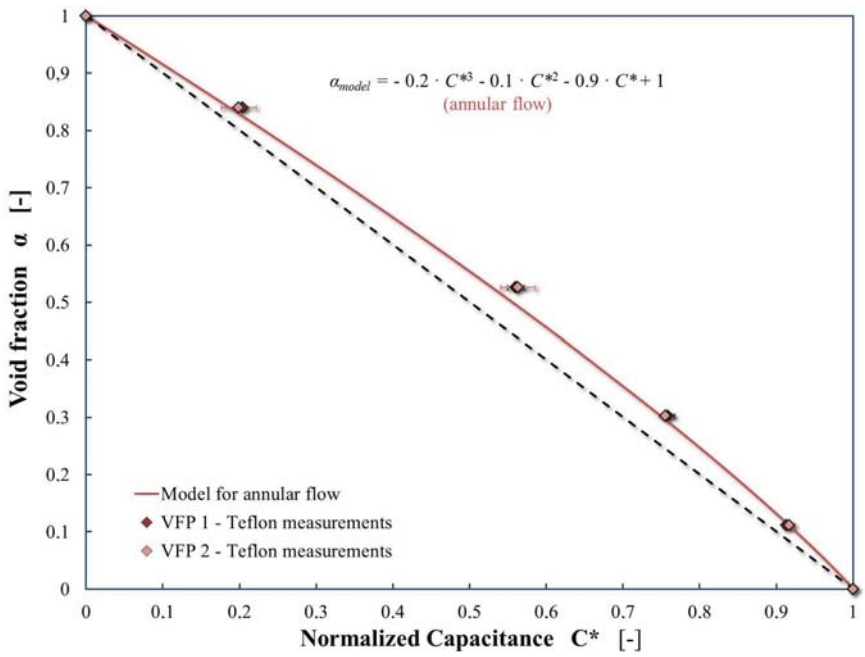

(a) Annular flow

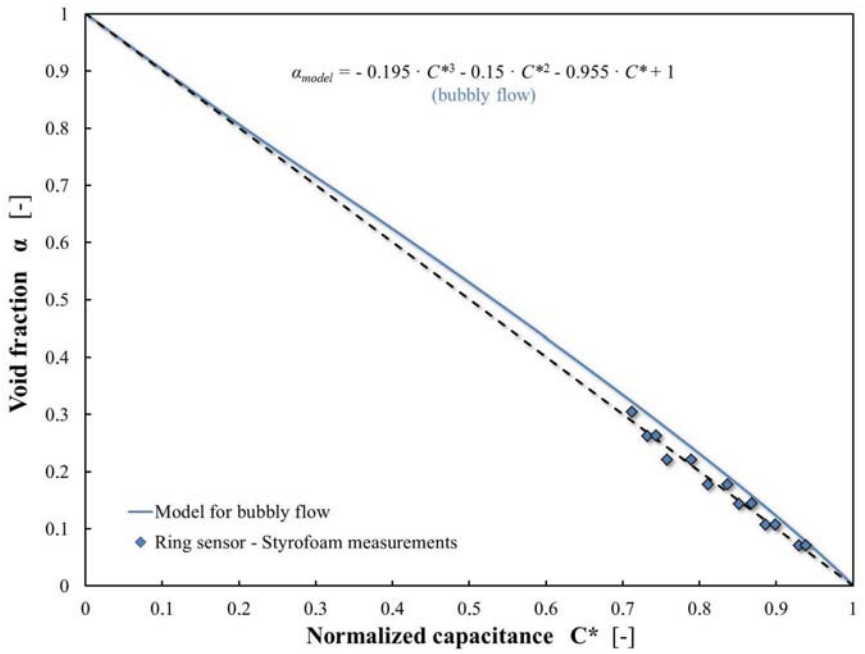

(b) Bubbly flow

FIGURE 2.13: Theoretical model results for calibrations in bubbly and annular flows

The problem with two different non-linear calibration curves concerns the annular flow with droplet entrainment (that is not accounted for in this model) and transition flows where it is difficult to distinguish between slugs and big bubbles. Since no linear calibration curve for all flow patterns has been achieved with the successive designs of the void fraction probes, simulations have been developed with the COMSOL software.

COMSOL simulations: 3D simulations have been performed for calibrations in bubbly and annular flows by using the actual geometry of the probe, including guard electrodes, as illustrated in Figure 2.14.

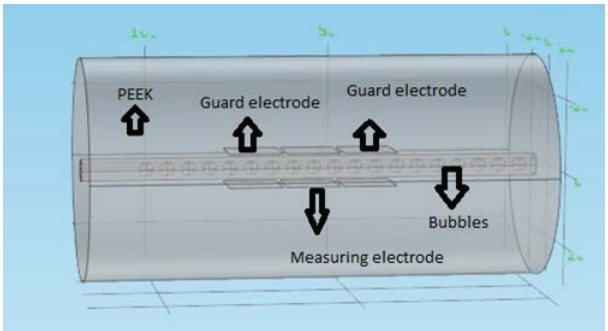

FIGURE 2.14: Void fraction probe 3D geometry in COMSOL simulations

The sensitivities ΔC provided by the COMSOL simulations are consistent with the experimental results for all the void fraction probe designs that have been tested during this thesis. The experimental calibration curves can be completed by adding more points in the area of interest (especially for high void fractions, $\alpha > 0.8$ corresponding to annular flow). For the annular flow case, the theoretical model and COMSOL simulations are in good agreement: the maximal deviation of the two curves is about 5%; for the higher values of α, it is less than 1%. However, the difference is more important between the model and the simulation curves in the case of bubbly flows, except for very low values of void fraction. The accuracy for this configuration is partially due to the number of bubbles used in the simulation / model. Plus, a direct calibration performed by measuring the bubble velocities from image processing for bubbly flows may not be relevant due to the lack of precision on the calculation of the vapor quality. Thus, it was decided to keep the curve provided by COMSOL simulations that was in rather good agreement with experimental calibration points. Moreover, Comsol simulations confirm that the vapor distribution has no influence on the signal, which is confirmed by experiments (by shifting, for example).

Acquisition: capacitance and electronics temperature are acquired by a direct connection of the electronic circuit to a laptop via USB. A stand-alone interface written with Delphi is used to display and save measured data in .txt files. The acquisition frequency, that was limited to 8.05 Hz for the first designs, was improved up to 45 Hz on the final version of the void fraction probes. An attempt on implementing the VFP measurement into the National Instrument DAQ has proven disappointing due to a lot of noise on the signal, which has worsened the precision on the void fraction.

Total accuracy: the total uncertainty in the void fraction value depends on the error on the capacitance measurement and on the precision of the calibration curve.

Precision on the capacitance measurement: the electronic circuit that is used to acquire capacitance data has a theoretical measurement precision of 2 fF (0.002 pF). Nevertheless, it is necessary to quantify the precision of the entire measurement chain. To

achieve this, a raw signal in all-liquid configuration is observed: for a single-phase flow, a constant value is obtained. However, once the temperature effects have been corrected, oscillations are still observed, with a maximal amplitude of about 0.005 pF. The general void fraction probe design that was used to get capacitance measurements corresponds to a sensitivity $\Delta C \simeq 0.080$ pF. The error on the measurement chain is then of $\simeq 6\%$ of the full scale.

Error due to the calibration curve: experimental calibration curves have to very carefully plotted; indeed, a small error on an experimental value can result in a large error on the void fraction. For that reason, calibration curves have been drawned from theoretical models and simulations for two flow patterns. In the end, the two curves can be united in one final calibration curve. Since the maximal deviation between the values obtained from theoretical models, COMSOL simulations and experiments (when available) is about 5%, the maximal error on the void fraction due to the calibration curve is assumed to be $\simeq 5\%$.

Film thickness: assuming there is no droplet entrainment in the vapor core for annular flow, the liquid film thickness δ can be written according to the void fraction and the tube diameter, with a corresponding uncertainty $\delta(\delta)$:

$$\delta = \frac{D}{2} \cdot (1 - \sqrt{\alpha}) \qquad \text{and} \qquad \delta(\delta) = \sqrt{\left(\frac{\delta D}{2} \cdot (1 - \sqrt{\alpha})\right)^2 + \left(\frac{D}{2} \cdot \left(\frac{-\delta\alpha}{2 \cdot \sqrt{\alpha}}\right)\right)^2} \tag{2.11}$$

α [-]	$\delta\alpha$ [-]	δ [mm]	$\delta(\delta)$ [mm]
0.95	0.048	0.076	0.073
0.80	0.040	0.317	0.067

Table 2.4: Uncertainty in the liquid film thickness in annular flow

At moderate void fraction in annular flow, the liquid film thickness is large enough so that the lack of precision on the void fraction does not induce an uncertainty in δ higher than 20%. However, as the vapor quality and α increase, the film at the wall gets thinner and the uncertainty in δ becomes of the same order of magnitude than δ itself. It is therefore necessary to plot this uncertainty along with experimental results on film thickness to be able to make relevant observations.

2.2.5 Flow visualisations

The high-speed video camera that is used to obtain flow visualisations in $\mu - g$ covers a 10mm x 65mm region at the outlet of the sapphire tube (only 10mm x 30mm during the two first campaigns, as illustrated in Figure 2.4(b). It captures around 5 seconds of the flow with a frequency of 1000 to 1500 Hz depending on the test, and is synchronized with the NI DAQ and the other measurements.

During on-ground measurement campaign, an APX high speed camera allowed to film the entire tube to observe the flow pattern evolution for high vapor quality evolution along the heated section.

Since the camera has mostly been used for flow pattern identification, uncertainty in the vapor velocity obtained from flow movies is not discussed here.

2.3 Data reduction

The following section presents the calculations made to determine the vapor quality, the wall and interfacial shear stresses and the heat transfer coefficient. Corresponding accuracies are given according to the uncertainties in the flow parameters as previously reported.

2.3.1 Vapor quality

For clarity purposes, the following notations are used for the calculation of the vapor quality x: q is the inner wall heat flux delivered to the fluid ($q = q_{w,i}$), D is the inner diameter ($D = D_i$) and Cp is the specific heat capacity of the liquid phase. z is the distance from the inlet of the heated test section, x is the vapor quality at z and x_{in} is the quality at $z = 0$.

According to Equation (1.23) demonstrated in Chapter 1, the enthalpy balance equation for the mixture can be written as:

$$\frac{4 \cdot q}{D} = G \cdot (h_{l,v} + Cp \cdot (T_{sat} - T_l)) \cdot \frac{dx}{dz} + G \cdot Cp \cdot (1 - x) \cdot \frac{dT_l}{dz} \tag{2.12}$$

The wall heat flux leads to an increase of the total enthalpy of the mixture both by phase change (first term of the RHS of Equation (2.12)) and by increasing the liquid temperature (second term). The quality x can be calculated with this equation if the heat flux, the liquid temperature and the temperature gradient along the heated test section are known. In our case, the heat flux is imposed through the power supply and the liquid temperatures are measured at the inlet and outlet of the sapphire tube with thermocouples or Pt100 probes.

The pressure drop along the heated length L_{heat} of the sapphire tube is low enough to consider that the induced variations of latent heat of vaporization and fluid properties are negligible; the HFE-7000 thermodynamical properties are therefore considered as constants between the inlet and outlet of the heated test section. The vapor quality at the outlet of the sapphire tube $x(L_{heated})$ is denoted x_{out}.

Two different configurations can occur at the inlet of the heated test section: the fluid enters the sapphire tube in subcooled conditions (characterised by a subcooling $\Delta T_{sub} = T_{sat} - T_{in}$) or the fluid enters the sapphire tube in saturated conditions.

Saturated regimes: in saturated regimes, the liquid temperature reaches the saturation temperature and boiling starts in the preheaters. The quality x_{in} at the inlet of the sapphire tube is considered to be equal to the quality at the outlet of the preheaters. This quality is obtained with an energy balance on the preheaters:

$$x_{in} = \frac{4 \cdot P_{preheat} - G \cdot \pi \cdot D^2 \cdot Cp \cdot (T_{sat} - T_{in,preheat})}{G \cdot \pi \cdot D^2 \cdot h_{l,v}} \tag{2.13}$$

Since the liquid is at saturation in the sapphire tube ($T_l = T_{sat}$), the enthalpy balance Equation (2.12) can be simplified by eliminating the two terms due to liquid heating:

$$\frac{4 \cdot q}{D} = G \cdot h_{l,v} \cdot \frac{dx}{dz} \tag{2.14}$$

The integration yields the expression of x that corresponds to the thermodynamical vapor quality:

$$x(z) = x_{in} + \frac{4 \cdot q}{G \cdot D \cdot h_{l,v}} \cdot z \tag{2.15}$$

Corresponding uncertainties δx_{in} and δx_{out} are presented in Table 2.5 for low and high ranges of vapor quality in saturated boiling regimes. The calculations are made by assuming that the uncertainties in thermodynamical properties are negligible to simplify very small terms, and with $\delta T_l = 0.25°\text{C}$ (the temperatures at the inlet of the preheaters and sapphire tube are measured by thermocouples).

		Low quality	High quality
G	[kg.s^{-1}.m^{-2}]	200 ± 3.5	100 ± 1.8
$P_{preheat}$	[W]	219 ± 2.96	164 ± 2.21
q	[W.m^{-2}]	9969 ± 169.5	30936 ± 433.1
x_{in}	[-]	0.089 ± 0.009 (± 9.7%)	0.277 ± 0.013 (± 4.5%)
x_{out}	[-]	0.131 ± 0.009 (± 6.6%)	0.537 ± 0.014 (± 2.6%)

TABLE 2.5: Examples of uncertainty in the vapor quality for saturated boiling regimes

Subcooled regimes: in subcooled boiling regimes, the fluid enters the sapphire tube in an all-liquid state and the boiling starts in the heated test section. Thus, the vapor quality at the inlet of the sapphire tube x_{in} is equal to zero and $T_l < T_{sat}$. The vapor temperature is assumed to be equal to the saturation temperature. The integration of Equation (2.12) yields the expression of x:

$$\begin{aligned} x &= \frac{4 \cdot q \cdot z - G \cdot D \cdot Cp \cdot (T(z) - T_{in})}{G \cdot D \cdot (h'_{l,v} - Cp \cdot (T(z) - T_{in})} \\ \text{with} \quad & h'_{l,v} = h_{l,v} + Cp \cdot (T_{sat} - T(z)) \end{aligned} \tag{2.16}$$

Note that x is not the thermodynamic vapor quality (which is negative) in this case: it represents the fraction of vapor at the distance z, and the superficial vapor velocity can be expressed according to x. The liquid temperature T(z) is necessary for the calculation; since the liquid temperature is measured between the inlet and outlet of the sapphire tube, a temperature profile can be assumed between these locations. Choosing a linear profile is a relevant option since the difference of temperature $T_{out} - T_{in}$ is rather small, but it is also possible to use a parabolic evolution of the temperature, which is well-suited for the description of boiling temperature profile. The difference in quality values obtained by choosing either linear or quadratic temperature profile is negligible.

Table 2.6 provides examples of uncertainty in vapor quality at the outlet of the sapphire tube ($z = L_{heated}$) for subcooled boiling regimes. The uncertainties in thermodynamical properties are neglected and the uncertainty in the temperature difference $T_{out} - T_{in}$ is considered to be $\delta T = 0.1°\text{C}$ since it is measured by the precise type T differential thermocouple, whereas it is $\delta T = 0.25°\text{C}$ for $T_{sat} - T_{in}$.

		Low quality	High quality
G	[kg.s^{-1}.m^{-2}]	101.3 ± 1.77	47.5 ± 0.83
q	[W.m^{-2}]	9939 ± 167.0	28937 ± 491.9
x_{out}	[-]	0.0627 ± 0.0021 (± 3.34%)	0.4437 ± 0.0116 (± 2.61%)

TABLE 2.6: Examples of uncertainty in the vapor quality for subcooled boiling regimes

As for saturated cases, the uncertainty in x is not very important for subcooled boiling regimes with moderate and high vapor qualities. However, for very low vapor quality ($x < 0.01$ corresponding to very sparse bubbly flows, for example), the error on the vapor quality is of the same order of magnitude than x itself. This error is confirmed by an analysis of flow videos that compares the mean bubble velocity measured from image processing and those calculated using the void fraction and quality values. Subcooled data with very low vapor quality must therefore be carefully processed.

2.3.2 Wall friction

As previously demonstrated, the momentum balance equation for the vapor-liquid mixture in steady state enables to write the wall friction τ_w (with $\tau_w > 0$) along a heated test section according to the pressure drop Δp, the void fraction α, the mass flux G and the vapor quality x:

$$\frac{dp}{dz} = \frac{-4}{D} \cdot \tau_w - \frac{d}{dz}\left[\frac{G^2 \cdot x^2}{\rho_v \cdot \alpha} + \frac{G^2 \cdot (1-x)^2}{\rho_l \cdot (1-\alpha)}\right] - (\rho_v \cdot \alpha + \rho_l \cdot (1-\alpha)) \cdot g \tag{2.17}$$

Expression of the wall shear stress: the total pressure gradient is the sum of three contributions. The second term of the RHS of Equation (2.17) is an acceleration term that has to be taken into account when quality and void fraction evolve along the test section. Since the pressure drops measurements are processed for an adiabatic section in our experiment, this term can be neglected. In this same way, the last term of the RHS is the hydrostatic pressure gradient that is negligible under microgravity conditions. However, on ground and for upward flow, this last term is dominant, thus the accuracy on the wall shear stress measurement is directly related to the accuracy on the void fraction itself.

An averaged value of the wall shear stress is yielded by the integration of Equation (2.17) on an adiabatic section of length L_{adiab}:

$$\tau_w = \begin{cases} \dfrac{-D}{4 \cdot L_{adiab}} \cdot \Delta p & \text{in microgravity} \\ \dfrac{-D}{4} \cdot \left(\dfrac{\Delta p}{L_{adiab}} + (\rho_v \cdot \alpha + \rho_l \cdot (1-\alpha)) \cdot g\right) & \text{in normal gravity} \end{cases} \tag{2.18}$$

with $\Delta p < 0$.

Uncertainty in the wall shear stress: the expression of τ_w under microgravity conditions allows to write the corresponding uncertainty $\delta\tau_w$ according to uncertainties in geometrical parameters δD and δL_{adiab}, and in pressure drop measurements $\delta\Delta p$ (0.27 mbar or 0.42 mbar depending on the sensor).

$$\delta\tau_w = \sqrt{\left(\frac{D}{4 \cdot L_{adiab}} \cdot \delta\Delta p\right)^2 + \left(\frac{\Delta p}{4 \cdot L_{adiab}} \cdot \delta D\right)^2 + \left(\frac{-D \cdot \Delta p}{4 \cdot L_{adiab}^2} \cdot \delta L_{adiab}\right)^2} \tag{2.19}$$

In normal gravity, the uncertainty in the wall shear stress is more important due to the hydrostatic pressure drop and terms depending on the uncertainties in g and α are added to the calculations of $\delta\tau_w$. This is illustrated in Table 2.7. The calculation is made by assuming the most important error on the pressure drop measurements and an uncertainty in L_{adiab} of 1mm (due to measurement tools).

		Low void fraction (bubbly flow)	High void fraction (annular flow)
Δp	[Pa]	77.2 ± 42	720.0 ± 42
α	[-]	0.2490 ± 0.0194	0.9231 ± 0.0721
τ_w in μ-g	[Pa]	0.6293 ± 0.1876 (± 29.8%)	5.867 ± 0.196 (± 3.3%)
τ_w in 1-g	[Pa]	16.051 ± 0.7827 (± 4.8%)	7.5348 ± 1.7452 (± 23.2%)

Table 2.7: Examples of uncertainty in the wall shear stress

For low void fractions ($\alpha < 0.3$ corresponding to sparse bubbly flows with very small pressure drop along the section), the uncertainty in τ_w in μ-g is about 20% - 30% because the measurement range of differential pressure transducers is adapted to two-phase flow with much larger pressure drops. On the contrary, 1-g measurements have a good accuracy since $\delta\alpha$ is rather small for low void fraction. Nevertheless, it must be noted that the use of a second transducer with a lower measurement range provides measurements with better precision than the one presented in Table 2.7. The opposite trend is observed for measurements with high void fraction ($\alpha > 0.8$ corresponding to annular flows): with higher pressure drop along the section, the error on τ_w is small in μ-g whereas $\delta\tau_w$ worsens with $\delta\alpha$ in 1-g even though the contribution of the gravitational term (that remains significant) decreases compared to the frictional term.

Validation in single-phase flow: experiments in single-phase liquid flows have enabled to validate the measurement technique by comparing the data to the Blasius correlation presented in Chapter 1 in Equation (1.41) using liquid Reynolds number Re.

The experimental friction factor f is calculated as follow:

$$f = \frac{\Delta P \cdot D \cdot \rho_l}{2 \cdot L_{adiab} \cdot G^2} \tag{2.20}$$

Figure 2.15 shows the measurements obtained with the three differential pressure transducers that are used in the experiment, for single-phase liquid flows at various mass fluxes and the Blasius correlation for turbulent flows: $f = 0.079 \cdot Re^{-1/4}$ for $Re > 3000$. Experimental points in laminar or transition area are indicated with open symbols. Dashed lines correspond to Blasius correlation at ± 10%. Simplified datasets from only two different campaigns are presented here for a better readability.

The agreement between experimental points and theoretical values is good considering that the measurement range of the pressure sensors is not adapted to single-phase flow with very small pressure drop (for that reason, the uncertainty bars in the friction factor have not been plotted): the mean absolute error (MAE) is around 6% for the values corresponding to turbulent flow.

2.3.3 Interfacial shear stress

In the specific case of annular flow, it is necessary to obtain data on the interfacial shear stress τ_i that controlles the behaviour of the wall liquid film to fully investigate boiling mechanisms in saturated regimes.

Expression of the interfacial shear stress: in saturated boiling, the wall shear stress and void fraction can be used to calculate τ_i by using the momentum balance equation

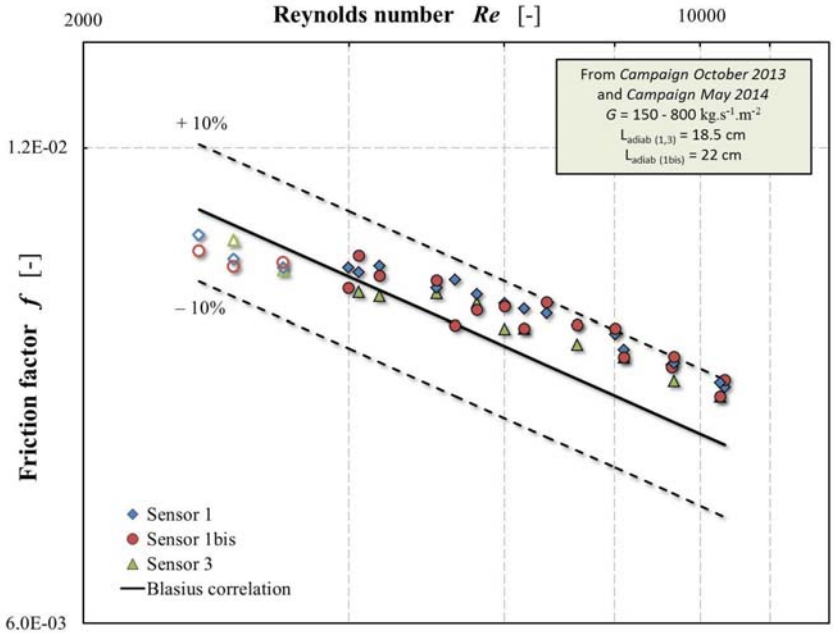

FIGURE 2.15: Validation of the measurement technique of pressure drop in single-phase liquid flows, comparison with the Blasius correlation

applied to the vapor phase. The integration of this equation with frictional data on an adiabatic length yields a two-term expression with a gravitational contribution that can be neglected under microgravity conditions.

Uncertainty in the interfacial shear stress: according to Equation (1.26), the uncertainty in τ_i mostly depends on the measurement accuracy of the pressure drop and void fraction. Under microgravity conditions:

$$\delta(\tau_i) = \sqrt{\left(\delta\tau_w \cdot \sqrt{\alpha}\right)^2 + \left(\tau_w \cdot \left(\frac{-\delta\alpha}{2 \cdot \sqrt{\alpha}}\right)\right)^2} \tag{2.21}$$

In normal gravity, another uncertainty is added for the gravitational term; this additional error is mostly due to the lack of precision on the void fraction. Table 2.8 presents typical uncertainties in the interfacial shear stress near the transition from slug flow with moderate vapor quality and void fraction, and at very high α.

		Moderate void fraction	High void fraction
α	[-]	0.810 ± 0.041	0.953 ± 0.067
τ_i in μ-g	[Pa]	5.22 ± 0.22 (± 4.2%)	5.66 ± 0.28 (± 4.9%)
τ_i in 1-g	[Pa]	12.27 ± 0.53 (± 4.4%)	7.66 ± 0.75 (± 9.8%)

TABLE 2.8: Examples of uncertainty in the interfacial shear stress

In annular flow, the uncertainty in τ_w is always small under microgravity conditions and since the void fraction is square rooted, the error on the interfacial shear stress never exceeds 5% in μ-g. On the contrary, the gravitational term that appears in normal gravity adds an uncertainty in τ_i that increases with the void fraction. Moreover, at very high α, the precision on the wall shear stress is not that good, which leads to an accuracy of ± 10% on the calculation of τ_i at high void fraction in 1-g.

2.3.4 Heat transfer coefficient

The heat transfer coefficient h that is presented in the experimental results is measured at the inner wall of the sapphire tube. A cross-section of the heated tube is represented in Figure 2.16.

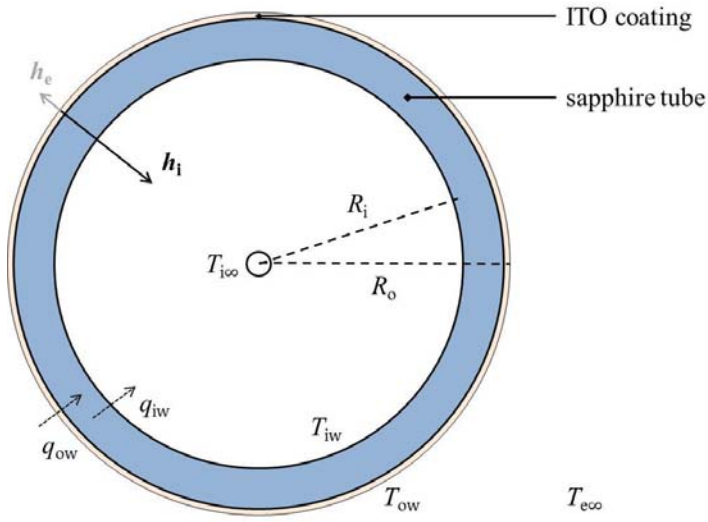

FIGURE 2.16: Cross-section of the sapphire tube - notations used for the calculation of the heat transfer coefficient

T_{iw} and T_{ow} are the inner and outer temperatures of the sapphire tube wall, respectively. $T_{e\infty}$ is the external temperature of the ambient air far from the tube (measured by a Pt100 probe in the first campaigns) and $T_{i\infty}$ is the bulk temperature in the tube. T_{in} and T_{out} are the bulk temperature at the inlet and outlet of the sapphire tube. The inner and outer radii of the tube are denoted R_i and R_o, respectively. The thermal conductivity of the sapphire tube is denoted k and is equal to 22 W.m^{-1}.K^{-1}. The ITO coating on the external surface of the heated test section provides a heat flux q_{ow}. The heat flux q_i delivered to the fluid, also simply denoted q, is considered to be equal to q_{ow} corrected by the radii ratio R_o/R_i. The heat transfer between the environment and the external wall of the sapphire tube (equivalent of thermal losses) is characterised by the heat transfer coefficient h_e. The heat transfer coefficient between the wall and the internal wall of the sapphire tube is denoted h_i.

Expression of the heat transfer coefficient: in order to estimate the heat transfer coefficient at the inner wall h_i, the following hypotheses are made:
– temperature profiles are axisymmetric;
– the axial conduction in the fluid and in the wall is neglected;
– heat transfers by radiation are neglected.

By using a conduction equation, the temperature at the inner wall T_{iw} can be deduced from the temperature at the outer wall T_{ow} (measured by Pt100 probes previsouly described) and the heat flux q_{ow} applied by Joule effect through the ITO coating:

$$T_{ow} - T_{iw} = [q_{ow} - h_e \cdot (T_{ow} - T_{e\infty})] \cdot \ln\left(\frac{R_o}{R_i}\right) \cdot \frac{R_o}{k} \tag{2.22}$$

The heat transfer coefficient at the inner wall h_i can then be deduced from an energy balance between the fluid and the inner wall:

$$h_i \cdot (T_{iw} - T_{i\infty}) = \frac{R_o}{R_i} \cdot [q_{ow} - h_e \cdot (T_{ow} - T_{e\infty})] \tag{2.23}$$

As previously mentioned, the temperature evolution between T_{in} and T_{out} can be considered as linear or parabolic, which enables to calculate the bulk temperature $T_{i\infty}$ at any location along the sapphire tube.

A series of experiments has been conducted in order to evaluate the thermal losses characterised by the heat transfer coefficient h_e. In particular, it can be locally estimated in normal gravity with the measurements of T_{ow} and $q_{e\infty}$ for single-phase or two-phase flow without wall heating by using a known correlation to estimate h_i. In this configuration, thermal losses have been estimated for single and two-phase flows with different correlations for various flow parameter ranges. The maximal heat transfer coefficient h_e that was obtained in normal gravity represents 7% of the heat transfer coefficient h_i. Experiments with single-phase flows at very low mass fluxes and high temperatures have allowed to conclude through a global energy balance about the nature of thermal losses that are therefore neglected.

By combining Equations (2.22) and (2.23) and assuming that h_e is negligible, the expression of the heat transfer coefficient $h = h_i$ can be written according to the measured outer wall temperature, bulk temperature and heat flux q:

$$h_i = \frac{q}{T_{ow} - T_{i\infty} - \frac{R_i}{k} \cdot \ln\left(\frac{R_o}{R_i}\right) \cdot q} \tag{2.24}$$

Accuracy on the heat transfer coefficient: according to Equation (2.24), the uncertainty in the heat transfer coefficient δh depends on geometrical uncertainties and uncertainties on the wall heat flux and measurements of the external wall and bulk temperatures.

The wall temperature T_{ow} is measured by Pt100 probes with a precision of $\pm$ 0.1°C which does not take into account an accuracy loss due to the mechanical contact between the probe and the wall. Two different systems of fixation have been tested during the measurement campaigns, and both require special care in the installation of the probes and testing in order to provide accurate heat transfer data. Thus, the uncertainty calculations are made with a maximal effective uncertainty $\delta T_{ow} = 0.5$°C. The uncertainty in the sapphire thermal conductivity is considered to be $\delta k = 9\%$ as the manufacturer only provided a rough value. The maximal error made on the bulk temperature by assuming a linear profile between both ends of the tube is considered to be $\pm$ 0.2°C. Table 2.9 provides examples of calculations of uncertainty in the heat transfer coefficient.

Validation in single-phase flow: experiments in single-phase liquid flows have enabled to validate the measurement technique by comparing the data to the Dittus-Boelter and Gnielinski correlations presented in Chapter 1 in Equations (1.65) and (1.66) using liquid Reynolds number and liquid fluid properties.

The experimental Nusselt number Nu_{meas} is calculated as follow:

$$Nu_{meas} = \frac{h \cdot D_i}{\lambda_l} \tag{2.25}$$

		Low wall heat flux (in bubbly flow)	High wall heat flux (in annular flow)
q	[W.m^{-2}]	9762.9 ± 165.9	35382.4 ± 601.5
T_{ow}	[°C]	44.09 ± 0.5	45.02 ± 0.5
$T_{i\infty}$	[°C]	33.93 ± 0.2	32.81 ± 0.2
h	[W.m^{-2}.K^{-1}]	912.4 ± 48.6 (± 5.3%)	2514.6 ± 109.6 (± 4.4%)

Table 2.9: Examples of uncertainty in the heat transfer coefficient

Figure 2.17(a) shows the raw measurements obtained with four Pt100 probes that are located at z = 4, 7, 10 and 13 cm from the inlet of the tube, respectively, for single-phase liquid flows at various mass fluxes. Comparisons are made with the Gnielinski correlation for turbulent flows $Re > 2100$. Dashed lines correspond to correlations at ± 12%. Simplified datasets from only two different campaigns are presented here for a better readability.

As can be seen from the graphic, the measured Nusselt number is larger than the values expected from the Gnielinski correlation, and the deviation is in inverse proportion to the distance between the temperature sensor and the inlet of the heated section. Indeed, it is important to note that the heated length is short and the heat transfer regime is not fully established. In order to compare the measurements with the previously mentioned correlations, the entrance effects have been corrected using Al-Arabi's correlation (Equation (1.68)) according to the sensor position. The corrected Nusselt numbers are presented in Figure 2.17(b).

Experimental data meet the correlations with a maximal error of 12%. This is illustrated in Figure 2.18 that presents the measured Nusselt numbers according to the theoretical values calculated with the Gnielinski correlation in fully developed turbulent flow. Uncertainty bars are plotted for the experimental data.

The Gnielinski correlation tends to underestimate the experimental data, but the precision between measurements and correlations is satisfying for the whole set of experiments in single-phase flow, with a mean absolute error of about 6%, which approximately corresponds to the uncertainty range. That also confirms the weak impact of external heat losses on the measurements.

Since only four or six different locations are reported along the heated test section, it is hardly possible to plot an evolution of the heat transfer coefficient or Nusselt number in single-phase flow according to the distance z from the inlet of the sapphire tube. But given the respective measurements of each probe, this experimental evolution seems to be consistent with the expected gradient.

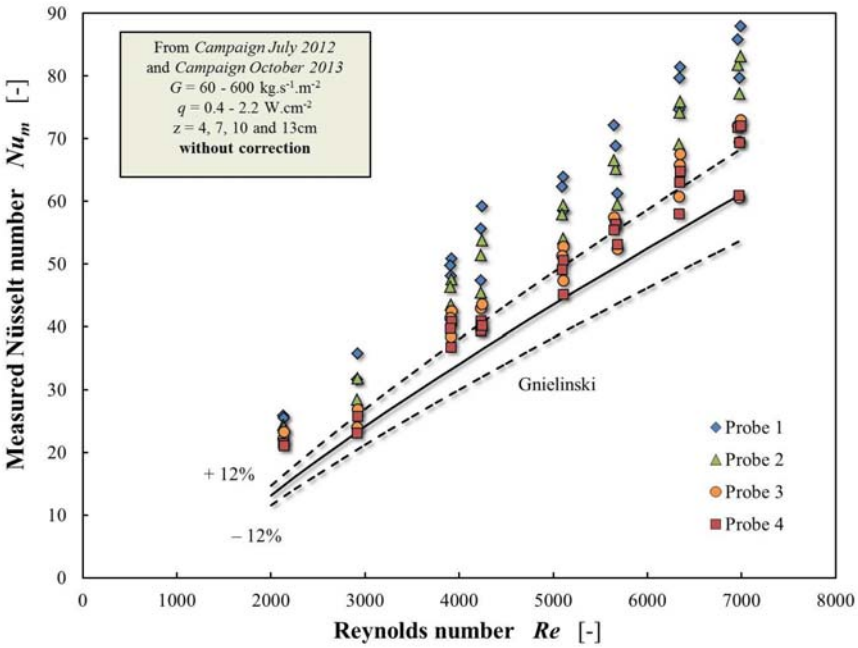

(a) Without entrance effect correction

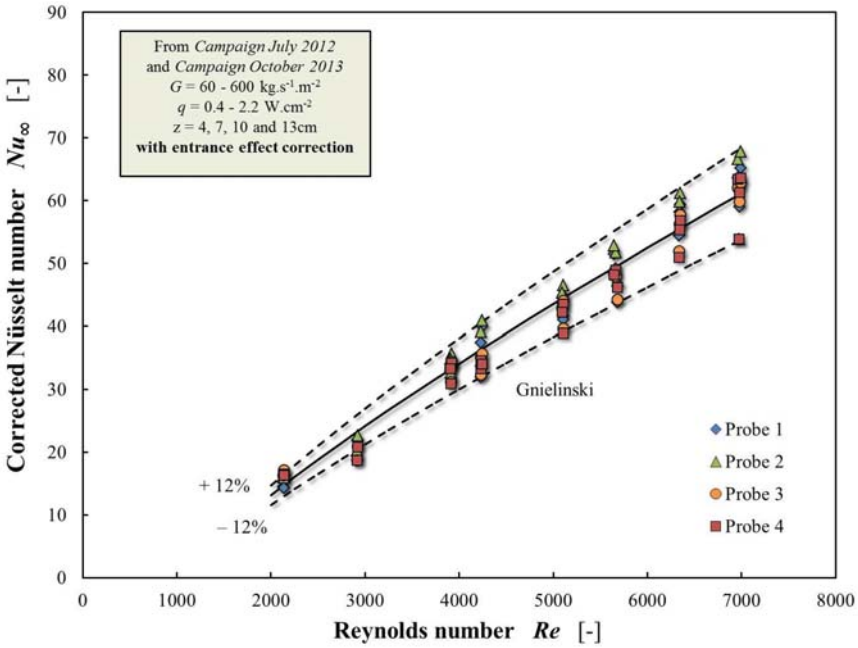

(b) With entrance effect correction

FIGURE 2.17: Validation of the measurement technique of heat transfer coefficient in single-phase liquid flows, comparisons with the Gnielinski correlation

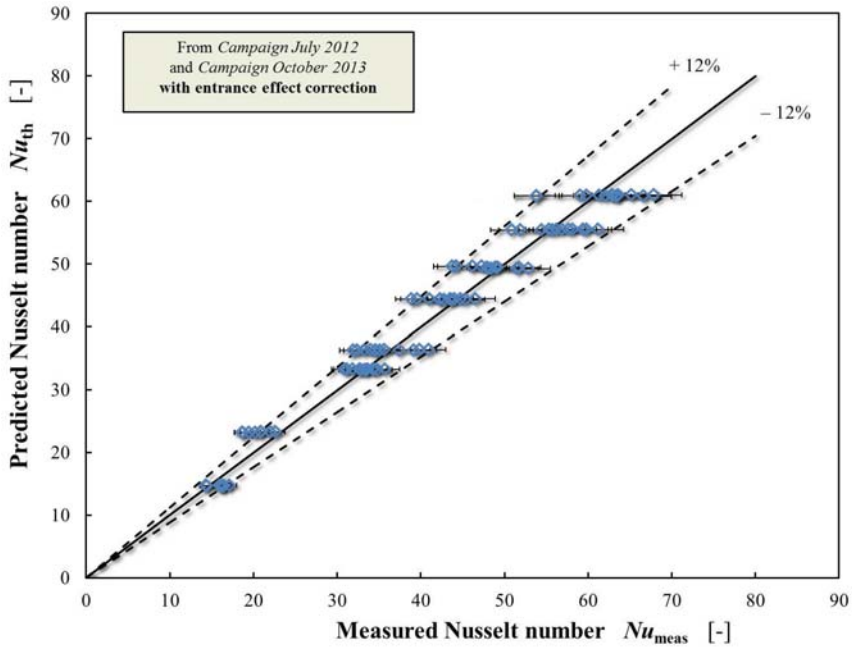

FIGURE 2.18: Validation of the measurement technique of heat transfer coefficient in fully developed single-phase liquid flows, comparison with the Gnielinski correlation; uncertainty bars are plotted

2.4 Experimental procedures

A whole measurement campaign proceeds in three steps: first, some measurements are performed under normal gravity conditions just before the parabolic flights to verify the integrity of the experimental set-up and the conformity of the results with empirical correlations, as presented in the previous section. Then, during parabolic flight campaign (PFC), experiments are conducted under microgravity conditions and finally, relevant parabolas are reproduced with a series of parametric tests in the laboratory in order to compare 1-g and μ-g data.

2.4.1 Microgravity conditions

For this study, experiments were conducted under microgravity conditions, in a near-weightless situation simulated during parabolic flight campaigns. Parabolic flight campaigns are the only sub-orbital opportunity for experimenters to work directly on their experimental apparatus under microgravity conditions without too severe restrictions on the size of their set-up and the available power.

Parabolic flight technique: parabolic flights are flights on-board a modified and specially configured Airbus A300 B2 built in 1973, known as the A300 ZERO-G. This aircraft is based at the Bordeaux-Mérignac airport (France) and owned by the private company Novespace that manages and organises six campaigns per year for the French, German and European Space Agencies (CNES, DLR and ESA, respectively). The A300 ZERO-G realises manoeuvres, called parabolas due to their trajectory form, to simulate microgravity, Lunar gravity or Martian gravity.

The A300 ZERO-G has to be piloted in a way it is subject to gravitational forces only in order to create a wheightless environment for the experimenters and the experiments. This is possible if the aircraft is following a trajectory which takes the form of a parabolic arc (actually a short elliptic arc that can be assimilated to a parabola). During the manoeuvres, the pilots have to both minimize the lift force and balance the drag with the engine thrust.

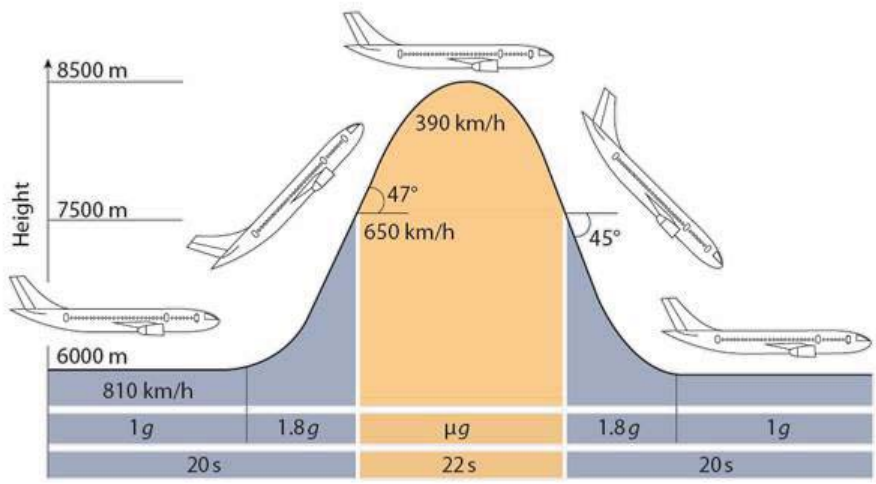

FIGURE 2.19: Typical manoeuvre profile to simulate microgravity conditions

Figure 2.19 presents the typical manoeuvre profile which follows five steps:
− every parabola begins with the aircraft flying at a steady horizontal altitude. This steady flight lasts about 2 minutes and allows experiments or settings in normal gravity;
− the pilot then starts to pull up the nose of the aircraft that climbs for 20 seconds, with an acceleration of 1.5 - 1.8g (this is known as hypergravity phase);
− as soon as an angle of 47° is reached, the engine thrust is reduced to the minimum required to compensate the drag and the free fall trajectory, i.e. the μ-g phase, starts;
− during approximately 20 seconds, only gravitational forces exerce on the A300 ZERO-G that experiences a nearly weightlessness (0g with a residual acceleration of $\pm$ 0.05g);
− at an incidence of -45°, the pilot pulls out of the parabolic arc to return to the initial steady flight situation; this corresponds to a second hypergravity phase.

It means a parabola itself lasts about 1 minute (with two 20s long hypergravity phases, also called 1.8-g phases, and a 20 to 22s long μ-g phase), followed by 2 minutes of steady flight in 1-g. A entire campaign includes three flights, and during one flight, the A300 ZERO-G accomplishes a series of 31 parabolas organised in sets of 5 or 6, with 4 or 8 minutes breaks that are used to carry out time-consuming adjustements and 1-g tests.

Figure 2.20: BRASIL team on-board the A300 ZERO-G, April 2012 - from left to right: Grégory Ehses, Catherine Colin, Marine Narcy, Juergen Eisenbraun

Constraints related to parabolic flights: heavy constraints related to parabolic flight influence the design of the set-up and impose a very specific experimental protocol.

First, for pratical reasons, the experiment must be very compact and easily movable, which limits the size of the test section or establishment length, for example. Then, very severe restrictions are imposed in order to assure the protection of the experimenters: the materials and products used in every experimental set-up are strictly controled, a 9-g mechanical resistance must be reached, the leak-tightness and cleanliness are carefully verified, etc... These restrictions also include staff, instrumentation and power limitations for each experiment.

Since the experiment undergoes 1.8-g phases in addition of the normal gravity and microgravity phases, it must be able to continuously function without being strongly affected by sudden transition between two different phases. The drastic changes in the gravity level can be problematic because they lead to pressure variations in the test section. Without any PID regulation of the rotating speed of the pump, a variation of the mass flux is then observed during the parabola. The profile of the main flow

parameters over a parabola is illustrated in Figure 2.21. The evolution of the gravity level, working pressure and mass flux are presented over a whole parabola including two phases of hypergravity and the microgravity period. Without PID regulation of the pump, significant changes in the mass flux are observed depending on the phase: the flow rate decreases in hypergravity compared to steady flight, and increases during the microgravity phase, which induces changes in the conditions at the inlet of the test section. Moreover, that causes establishment times to be more important and low mass fluxes could not be achieved. The use of a PID allowed to obtain a constant flow rate over the whole parabola, making the comparison of 1-g and μ-g data possible and low mass fluxes reachable.

The last constraint concerns the duration of the experiment and available number of points: a parabola only provides up to 22 seconds of microgravity, which is very short for thermal establishment and measurements (not to mention that experimenters are floating). In addition, the number of parabolas is limited to 93 per campaign; it is therefore very complicated to build exhaustive datasets or to ascertain the repeatability of the measurements.

2.4.2 Participation in parabolic flight campaigns

The BRASIL experiment has participated in four parabolic flight campaigns between 2011 and 2014. Each campaign was an opportunity to acquire microgravity data and to improve the measurement techniques and protocols. Important changes and observations made during these four campaigns are summarized below.

PFC 88 - May 2011: the experiment participated in its first measurement campaign a few days after it was built, during the CNES PFC 88. Under the supervision of post-doctoral researcher Erik de Malmazet, measurements were realised under microgravity conditions with three experimenters per fly, for mass fluxes G between 200 kg.s^{-1}.m^{-2} and 800 kg.s^{-1}.m^{-2}, with a void fraction probe at the outlet of the heated test section.

This measurement campaign mostly highlighted the fact that the influence of the gravity level is negligible at high mass fluxes $G > 400$ kg.s^{-1}.m^{-2}. It allowed to observe some trends in the heat transfer coefficient between 1-g and μ-g, provided results on flow patterns, but data about void fraction and pressure drops were hardly usable. The campaigns in microgravity and on-ground were useful to narrow test conditions for future experiments, in particular with a reduced mass flux range, and to design a lot of modifications in the set-up, including new void fraction probes and improvements in the cooling system where malfunctionings occured. The experimental results presented in the next chapter do not include measurements from this campaign.

PFC 95 - Avril 2012: multiple tests and modifications enabled another team to fly one year later on a CNES campaign, with a fully functioning experiment with two efficient void fractions at 8Hz on a stand alone interface, and a differential thermocouple on the heated test section. Only two differential pressure transducers were used on the adiabatic section at the outlet of the sapphire tube.

For this campaign, moderate mass fluxes were investigated and the range was narrowed to 100 - 400 kg.s^{-1}.m^{-2}. Inlet conditions corresponded to subcoolings up to 15° or vapor qualities up to 30%. Heat flux q ranged between 1 W.cm^{-2} and 3.5 W.cm^{-2}. Interesting data were collected for flow pattern, pressure drops, void fraction and heat

transfer coefficient calculations. Experimental results were published in IJMF [Narcy et al., 2014] and it was decided to investigate lower mass fluxes to complete the dataset.

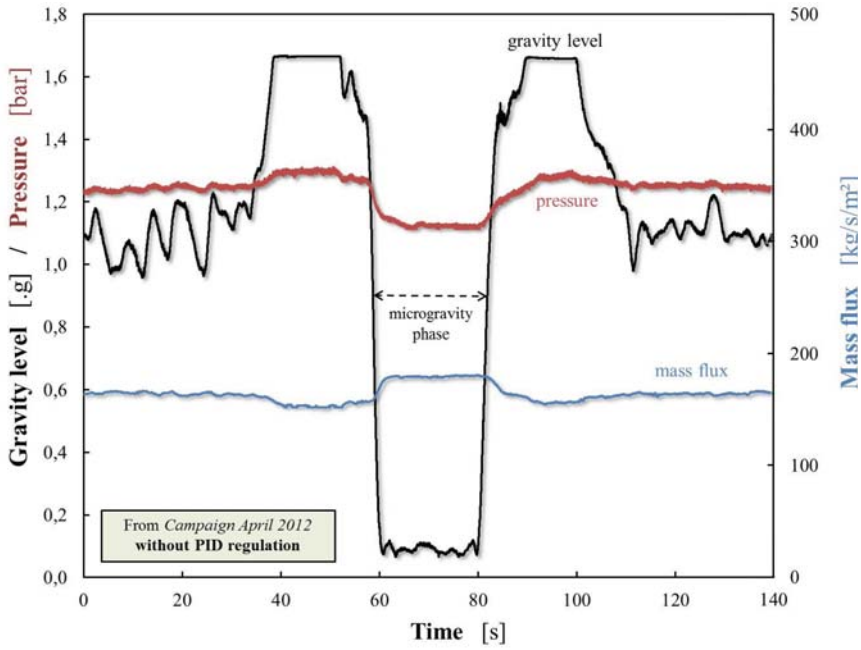

(a) Without PID regulation

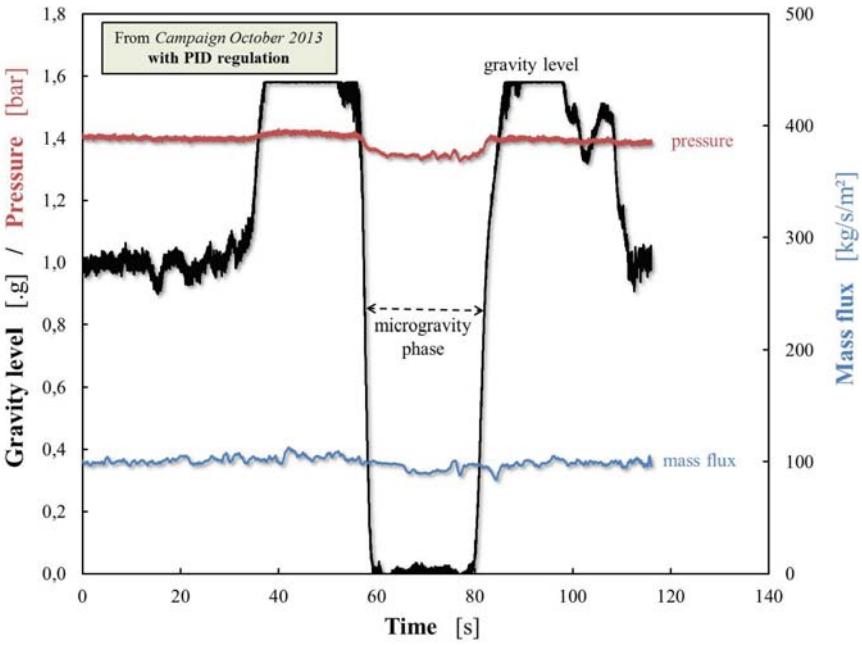

(b) With PID regulation

FIGURE 2.21: Gravity level, pressure and mass flux profiles during a parabola, with and without PID regulation on the pump

PFC 106 - October 2013: some modifications were made for the CNES PFC 106. The pump was replaced by a micropump allowing to reach very low mass fluxes and a PID regulation was added to compensate for the pressure variations due to sudden changes in the gravity level, which enabled to compare data acquired during the steady flight in 1-g and microgravity data. Mass flux profiles without and with the PID regulation are shown in Figure 2.21. The field of view of the high-speed camera was enlarged (a length

of 7cm was imaged near the outlet of the test section). The void fraction probes were slightly modified: the internal design changed a little, the acquisition frequency was increased to 40 Hz and the capacitance signal was acquired on the National Instrument DAQ with the other measurements. A third differential pressure transducer was added on the heat sapphire tube. A new system with Nylon screws was built to press the Pt100 probes on the external surface of the sapphire tube and four probes were added to measure the wall temperature at different locations, including repeatability points.

For this campaign, mass fluxes G between 100 kg.s^{-1}.m^{-2} and 200 kg.s^{-1}.m^{-2} were investigated with a few series at 50 kg.s^{-1}.m^{-2}. For these very low mass fluxes, measurements are hardly usable because of dry-outs that occur when the inlet conditions correspond to very small subcoolings or saturated regimes with $x_{in} > 0$. Moreover, a problem with the cold junction compensation of the NI DAQ made the temperature measurements difficult to process. The acquisition of the capacitance signal on the NI DAQ was very convenient during the parabolic flights but more important noises were observed, which greatly decreases the precision on the void fraction data. Nevertheless, experimental results are presented with the corresponding uncertainties.

PFC 110 - April 2014: the IMFT team with four members flew during the last parabolic flight campaign of BRASIL with ESA. Only the void fraction at the oulet of the sapphire tube worked, and its signal was aquired on a stand alone interface to limit measurement noises. The issue about the cold junction problem was solved. A malfunctioning occured during the campaign in one of the two differential pressure transducers on the adiabatic section, and an overpressure valve failure prevented the acquisition of the very last five parabolas of the campaign.

Same inlet condition were set and special attention was paid to the runs at very low mass fluxes (series at 50 kg.s^{-1}.m^{-2} and additional points at 75 kg.s^{-1}.m^{-2}). For these two mass flow rates, only subcooled regimes were studied, with limited wall heat fluxes between 0.4 W.cm^{-2} and 2 W.cm^{-2}. The use of a different high-speed camera during the laboratory campaign that follows parabolic flights enabled to image the whole tube during parametric runs. Corresponding experimental results are also presented in the next Chapter.

2.4.3 Test matrix and experimental protocols

Test matrix for parabolic flight campaign and on-ground laboratory campaigns are different, mostly due to the limitations in the available number of parabolas and in the duration of microgravity conditions.

During parabolic flight campaign: due to the above-mentioned constraints of parabolic flights and to the campaigns infrequency, test conditions and sequences have to be carefully elaborated and well planed. Therefore, a complete test matrix is developed to structure all the experiments that need to be carried out just before the first flight. Test matrix for the second and third flight are written after a preliminary reduction of the data from the first flight, in order to complete the dataset and adapt or redo failed runs.

The working pressure is maintained between 1 and 1.5 bar but remains hardly adjustable. Not to waste parabolas, relevant combinaisons of mass flux G, inlet conditions ΔT_{sub} or x_{in} (through the setting of the preheaters) and wall heat fluxes q have to be made. However, the choice of flow parameter ranges also depends on the manoeuvre sequence that limits the duration of each phase.

The acquisition of measurement signals from the NI DAQ and the void fraction program starts 10 to 30 seconds before the first hypergravity phase; experimental data therefore cover 1-g, 1.8-g and μ-g phases. However, the time required to save the images from flow visualisations with the high-speed camera between two consecutive parabolas only allows to acquire data corresponding to the microgravity phase. The measurements performed on the adiabatic section are carried out at the same time as the measurements on the heated test section.

Laboratory campaigns: one or two on-ground measurement campaigns follow each parabolic flight campaign to make a comparison between 1-g and μ-g data or to improve the experiment. These campaigns consist in the conduction of 130 to 250 vapor-liquid parametric runs complemented by single-phase tests. Additional experiments can be carried out to replicate the exact test conditions of various runs in microgravity.

No time constraint applies during measurement campaigns in the laboratory. Thus, flow parameters are carefully set and the working pressure is controled. A lot of points are acquired to cover large ranges of boiling flow patterns and regimes. Like for microgravity measurements, experiment at low vapor qualities are conducted first. The measurement procedure of the parametric runs is the following:
– after setting the pressure to slightly more than 1bar, G is adjusted (only one time for a whole series, since the PID regulation efficiently maintains a steady mass flux);
– for a given mass flux, the preheater power input is then changed to reach a specific subcooling or the desired vapor quality at the inlet of the sapphire tube. Due to the important thermal inertia in the preheaters, the power has to be increased very gradually to prevent bubble accumulation inside the heaters. Slight induced pressure variations can help to achieve fine-tuning of these inlet conditions;
– since p increases with the temperature, pressure adjustments are performed to maintain its value around 1.2 bar, by decreasing the power on the preheaters if necessary;
– finally, when the desired mass flux and inlet conditions are reached, the power input of the ITO coating on the sapphire tube, i.e. the wall heat flux, is changed;
– after a few seconds devoted to thermal establishment, the simultaneous acquisition of measurement signals from the NI DAQ, the void fraction probes and the high-speed camera (that all are synchronised) is started. 20 to 30s are aquired before the wall heat flux is changed again.

A whole series consists in 4 to 6 steps of wall heat flux for one given mass flux and one subcooling / inlet vapor quality. Between series with different mass fluxes or inlet conditions, single-phase flow measurements are performed to correct the effects of the electronics temperature drift on the void fraction data or to verify the correct operation of pressure transducers. Table 2.10 presents the different ranges of flow parameters that correspond to the experimental results presented in Chapter 3.

<table>
<tr><th>$p \simeq 1.2$ bar</th><th>$\Delta T_{sub} = 15$, 10 or 5°C</th><th>$x_{in} = 0$, 0.05 or 0.1</th><th>$x_{in} = 0.2$ or 0.3</th></tr>
<tr><td>$G = 400$</td><td colspan="3">$q = 1$, 2, 3.3 or 4</td></tr>
<tr><td>$G = 200$</td><td colspan="3"></td></tr>
<tr><td>$G = 100$</td><td></td><td>$q = 0.4$, 1, 2, 3.3 or 4</td><td></td></tr>
<tr><td>$G = 75$</td><td>$q = 0.4$, 1, 2 or 3.3</td><td colspan="2">-</td></tr>
<tr><td>$G = 50$</td><td colspan="3"></td></tr>
</table>

TABLE 2.10: Ranges of flow parameters set during experiments under microgravity and normal gravity conditions (G is in kg.s^{-1}.m^{-2} and q in W.cm^{-2})

2.5 Experiment of the University of Maryland (UMD)

The UMD experiment (under the supervision of Jungho Kim and Alex Scammell) is described in this section with more details than the other experimental set-ups, because a fellowship granted by the University of Toulouse allowed a 3 months long collaboration between IMFT and the University of Maryland, including work on the American test rig, measurements during a parabolic flight campaign, reduction of microgravity data and a common publication that can be found in Appendix B.

2.5.1 Experimental set-up

The UMD experimental apparatus consists of a hydraulic loop, transducers and supporting electrical equipment required for the rig's functionality both in the lab and aboard parabolic flights, everything being very similar to the BRASIL circuit. The working fluid used during testing is 3M Novec HFE-7100, whose properties are generally very close to the ones of HFE-7000, with a boiling temperature of 61°C at atmospheric pressure.

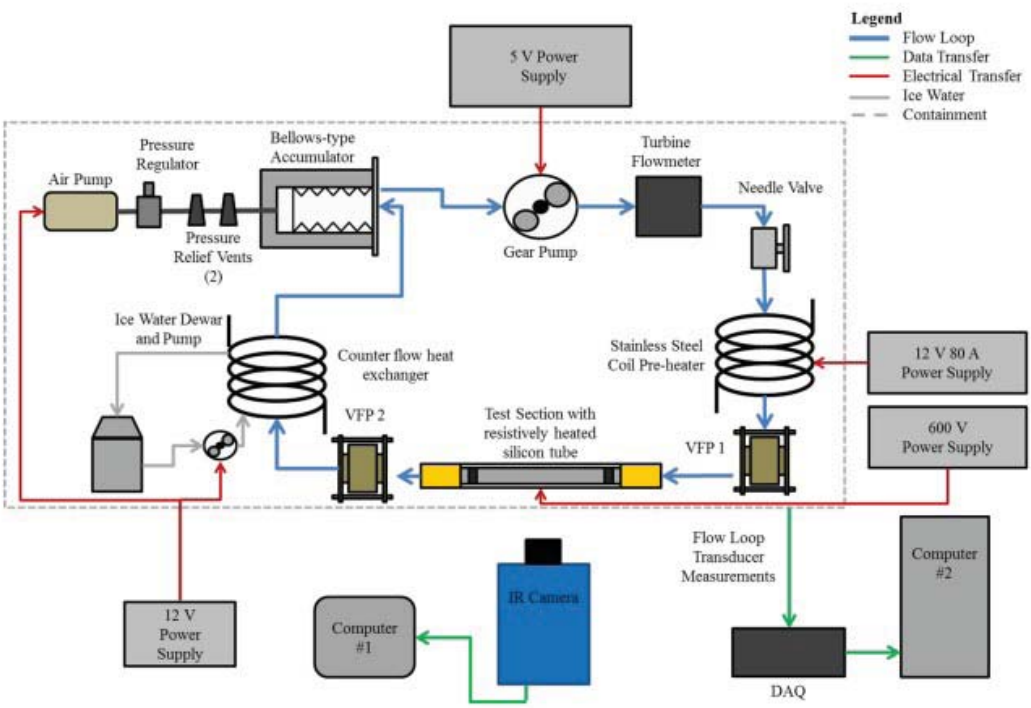

FIGURE 2.22: Functional diagram for UMD test rig

A schematic of the loop is shown in Figure 2.22. Liquid-HFE-7100 is pumped using a micro gear pump and the flow rate is measured using an Omega turbine flowmeter. The liquid is then heated to a specific inlet subcooling temperature or quality using a stainless steel preheater before entering the test section in a vertical upward flow configuration. Preheater input power is supplied by a modified Silverstone computer power unit and controlled using pulse width modulation via a LabVIEW interface.

The test section consists of a heated 6mm ID silicon tube, where the heat transfer measurements and flow visualization are performed, and two void fraction sensors upstream and downstream of the silicon tube. The silicon is resistively heated using a high voltage power supply to either induce or continue boiling within the flow.

Vapor exiting the test section is condensed and subcooled in a counterflow heat exchanger where the secondary fluid is ice water. A bellows-type accumulator is included after the condenser, so that the system pressure can be maintained at nominally 1bar using an air pump regulated by an adjustable pressure relief valve. After leaving the accumulator, the fluid is recirculated through the pump and cycles through the flow loop again.

Data are collected using an Omega 24-channel data acquisition system and recorded at a rate of 100 Hz using a LabVIEW interface. IR video for heat transfer measurements is captured using an Electrophysics Silver 660M camera at a rate of 250 Hz.

2.5.2 Measurement techniques

The UMD experiment is instrumented to study heat transfer coefficient, void fraction and pressure drop, but special attention is paid to the measurements with the IR camera to characterise local heat transfer coefficients under microgravity conditions.

Liquid temperature data are acquired for safety purposes or for the calculations of vapor quality and fluid properties. The UMD experiment uses type T thermocouples, with an accuracy of $\pm$ 0.12°C. Pressure taps are located at the inlet and outlet of the heat transfer measurement section for both differential and absolute pressure measurements. These data are difficult to process since the measurements are performed on a heated section where the acceleration term has to be calculated. Void fraction data are also acquired with capacitance probes designed and built at the IMFT for the rig on the model of the probes from BRASIL (with a better sensitivity and precision, and the same calibration protocols).

Heat transfer measurements and flow visualisations are captured using an IR thermometry technique that utilised the transparency of silicon in the mid-IR optical range [Kim et al., 2012]. HFE-7100 passes through the 6mm ID / 8mm OD single crystal silicon tube whose inner wall is coated with a thin thermally insulating layer of polyimide tape as can be seen in Figure 2.23. One half of the inner circumference is covered with an IR opaque paint containing carbon black, which allows an effective inner wall temperature to be measured through the silicon and polyimide layer. The same procedure is conducted for two strips aligned axially on the outer wall of the tube so that the effective outer wall temperature can be measured.

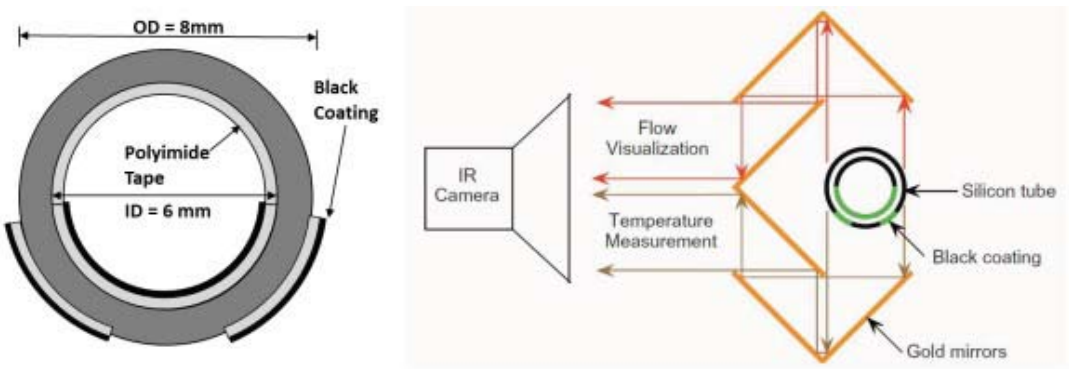

FIGURE 2.23: UMD measurement technique with IR camera

To determine the actual inner and outer wall temperatures, the optical properties of the various layers must be included. A coupled conduction and radiation problem is solved which accounts for absorption, emission, and reflection of thermal energy from the layers

and the surroundings to determine the temperature profiles within the multilayer. The heat flux and heat transfer coefficient can then be calculated for every camera pixel along the axial length of the tube at much higher spatial resolution than traditional methods. To complement these measurements, the flow is also visualised using a set of six gold-plated mirrors (right image of Figure 2.23). In this way, flow visualisation and heat transfer measurements can be captured simultaneously using a single camera. However, the quality of flow video does not allow to precisely observe all flow features.

The infrared thermography is validated through single-phase and two-phase vertical upward flow testing. In the first case, comparison is made between the experimental heat transfer coefficient measured along the silicon length and the Dittus-Boelter correlation (Equation (1.65)) with a correction factor for entrance effects proposed by Al-Arabi (Equation (1.68)), as seen in Figure 2.24. Good agreement between the two is observed.

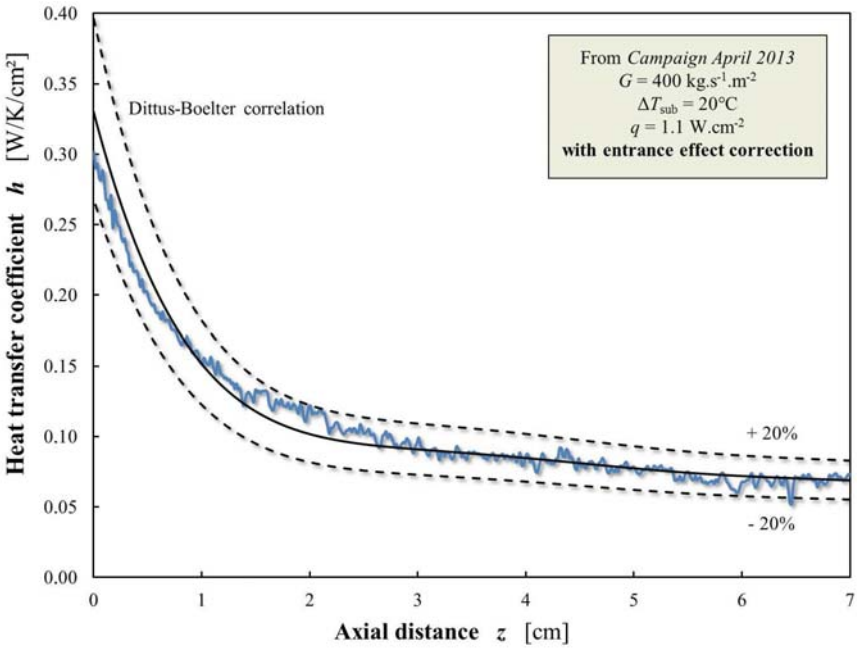

FIGURE 2.24: UMD heat transfer measurement validation in single-phase flow

2.5.3 Measurement campaigns

During the collaboration between IMFT and UMD, the UMD experiment had the opportunity to participate in a parabolic flight campaign with the CNES and Novespace (PFC 102, April 2013). During this campaign, only one void fraction probe at the outlet of the test section was working. An issue in the cooling system caused the experimental points from the first day to be lost, but usable data were acquired on the two last days with subcooled inlet conditions for mass fluxes $G = 50$, 100 and 200 kg.s^{-1}.m^{-2}, and wall heat fluxes $q = 0.3$, 0.6 and 1.2 W.cm^{-2}.

UMD experimentators performed numerous runs in normal gravity after the parabolic flights, during an extensive laboratory measurement campaign, which allows them to widen mass fluxes and heat fluxes ranges and to obtain better flow videos by filming an adiabatic glass section at the outlet of the heated test section. Data obtained during this lab campaign are not reported here and will be presented in Scammell's thesis.

Conclusion

BRASIL experiment has been designed and built at IMFT in order to compensate for a lack of consistent data on flow boiling under microgravity conditions. This hydraulic loop, that circulates HFE-7000, enables the experimenter to study void fraction, interfacial and wall shear stresses, and heat transfer coefficient as well as to obtain flow visualisations during during lab or parabolic flight campaigns. A vertical heated test section consisting in a 6mm ID sapphire tube coated with ITO which allows a uniform heating by Joule effect was used during the measurement campaigns.

The experimental set-up is instrumented to acquire various data and for safety reasons too. Instrumentation includes thermocouples for liquid temperature measurements, Pt100 probes for outer sapphire wall temperature measurements, absolute pressure sensors and differential pressure transducers located on the heated section and on an adiabatic length at the outlet of the sapphire tube. Specific capacitance probes have been carefully designed, built and calibrated at IMFT to acquire void fraction data. Flow regimes are visualised with a high-speed camera.

The corresponding measurement protocols are tested under normal gravity conditions in single-phase flow, by confronting heat transfer coefficients and pressure drops to empirical correlations. Special attention is paid to the estimation of uncertainty to properly characterise every parameter, especially for the calculation of the vapor quality that is used to describe the evolution of other data.

Microgravity conditions are achieved during parabolic flight campaigns operated onboard the aircraft A300 ZERO-G of Novespace (France). Each campaign provides 93 phases of microgravity lasting 22 seconds. BRASIL experiment participated in 4 parabolic flight campaign since April 2011. Parametric lab tests are performed to complete the datasets with runs under normal gravity conditions.

A fifth campaign allowed to fly the experiment from the University of Maryland, as a part of the collaboration between IMFT and UMD. This experimental apparatus, similar to BRASIL, uses an IR camera to obtain local measurements of the heat transfer coefficient. This project provided comparison material to confront datasets under microgravity conditions.

Experimental results provided by the aforementioned experimental apparatus during lab and parabolic flight campaigns as well as the comparisons with other microgravity datasets are presented in the next chapter.

Chapter 3

Experimental results

Experimental results from three parabolic flight campaigns and various on-ground measurements campaigns are presented and discussed in this chapter. Raw data along with calculated values are provided to characterise flow patterns, void fraction, wall and interfacial shear stresses, and heat transfers coefficient. Differences between normal gravity and microgravity conditions are analysed to highlight the influence of gravity level. Comparisons are also drawn with experimental points from the microgravity datasets that have been presented in Chapters 1 and 2.

Les résultats expérimentaux obtenus avec le banc d'essai BRASIL lors de trois campagnes de vols paraboliques et de multiples campagnes de mesure en laboratoire sont présentés et discutés dans ce chapitre. Ils sont fournis sous forme de données brutes et de paramètres calculés afin de caractériser dans un premier temps les régimes d'écoulement, puis le taux de vide et les épaisseurs de film correspondantes en écoulement annulaire, les frottements pariétaux et interfaciaux, et enfin les coefficients d'échange de chaleur. Les différences de comportement induites par les changements de gravité sont analysées afin de déterminer l'influence de la gravité sur les mécanismes de l'ébullition convective. Des comparaisons sont également faites avec les données expérimentales actuellement disponibles en microgravité et qui ont été introduites dans les chapitres 1 et 2.

Régimes d'écoulement

Les régimes d'écoulement sont visualisés par l'intermédiaire d'une caméra rapide qui permet de filmer une portion du tube. Les sondes de taux de vide peuvent également fournir des informations sur le régime suivant la forme du signal délivré. Trois principaux régimes d'écoulement ont été identifiés sur la plage de paramètres étudiés par BRASIL. Les problèmes de flux critique ne sont pas traités dans cette thèse.

Les écoulements à bulles sont observés pour des écoulements en ébullition sous-refroidie, correspondant à de faibles titres en vapeur. Les bulles nucléent sur la paroi chauffée, glissent le long de cette paroi et se détachent. L'influence de la gravité sur ces régimes est clairement visible pour des flux de masse inférieurs à 400 kg.s^{-1}.m^{-2} : en microgravité, les bulles sont plus larges et moins déformées (forme sphérique) qu'en gravité normale. Le phénomène de coalescence est en effet encouragé par la faible différence de vitesse entre les bulles et une augmentation du diamètre de bulles au détachement.

Une augmentation du titre en vapeur proche de la saturation mène à des écoulements de bulles denses incluant des bulles de Taylor, que la coalescence transforme en écoulement poche-bouchon, la taille des bouchons diminuant avec x. Les bouchons de liquide qui alternent avec les poches transportent des nuages de petites bulles. La classification des écoulements de transition et des écoulements à poches-bouchons est très subjective ; ces derniers ont donc été rassemblés dans une même catégorie. Comme ces régimes sont difficiles à décrire et très sensibles aux variations de pression ou de titre, il est également difficile de déterminer l'influence de la gravité sur la structure de l'écoulement.

Les écoulements annulaires sont observés en ébullition saturée : lorsque le titre est important, la vapeur occupe le centre du tube tandis que le liquide s'écoule à la paroi sous forme de film. Selon les conditions d'expérimentation, une fraction liquide peut être arrachée au film et entraînée dans le cœur de vapeur. Dans ce type d'écoulement, la gravité joue surtout sur l'épaisseur du film à la paroi, ce qui n'est pas observable à l'œil nu.

Ces trois catégories de régime d'écoulement peuvent être reportées sur des cartes de configuration présentant l'ensemble des points expérimentaux en fonction des vitesses superficielles de vapeur et de liquide. Ces cartes, tracées en gravité normale et réduite, mettent en évidence des transitions de régime à titre constant, qui se produisent à peu près au même moment, quelque soit le niveau de gravité : les écoulements de transition et poche-bouchon apparaissent à $x \simeq 0.05$ tandis que les écoulements annulaires sont observés pour $x > 0.13$.

Taux de vide et épaisseur de film

Comme pour les régimes d'écoulement, l'évolution du taux de vide est décrite en fonction du titre. Le tracé des données fournies par les sondes capacitives mettent en évidence une influence du flux de masse et du niveau de gravité sur cette grandeur. En ébullition

sous-refroidie, pour les écoulements à bulles (observés pour $\alpha < 0.7$) et écoulements poche-bouchon ($0.7 < \alpha < 0.8$), il est difficile de distinguer des tendances. Cependant, en ébullition saturée, le taux de vide à titre constant augmente avec une diminution du débit, et augmente également avec une diminution du niveau de gravité.

Cette observation se répercute directement sur l'évolution de l'épaisseur de film liquide, calculée en écoulement annulaire : δ diminue lorsque le débit augmente, et est plus importante en gravité normale qu'en microgravité.

Frottements pariétaux et interfaciaux
Le frottement pariétal dépend aussi fortement du titre en vapeur, les deux grandeurs évoluant dans le même sens. Une augmentation du débit à titre donné entraîne une augmentation conséquente de τ_w. Le niveau de gravité joue également un rôle important dans l'évolution du frottement, puisqu'il n'y a pas besoin de soustraire le terme gravitationnel faisant intervenir le taux de vide du gradient total de pression en microgravité. Pour des débits importants, la différence entre gravité normale et gravité réduite est négligeable, sur toute la plage de titre. Au contraire, à faible débit, le frottement pariétal est largement supérieur en gravité normale, quelque soit le titre.

Les mêmes constatations peuvent être faites sur le frottement interfacial calculé en écoulement annulaire. Le coefficient de frottement augmente avec le débit, et est plus important en gravité normale qu'en microgravité, même à flux de masse important. Une différence de comportement est tout de même notable à très faible débit, sur l'évolution du frottement en fonction du titre, avec une décroissance du coefficient de frottement en ébullition sous-refroidie.

Coefficient d'échange de chaleur
Le coefficient d'échange est mesuré localement à plusieurs endroits du tube de saphir. Comme pour les grandeurs précédentes, son évolution est tracée en fonction du titre en vapeur, mais elle est également influencée par le débit et le flux de chaleur imposé à la paroi. D'une manière générale, une augmentation du flux de masse ou du flux de chaleur à titre fixé correspond à une augmentation du coefficient d'échange de chaleur. L'influence du débit sur h est cependant plus conséquente en ébullition saturée, alors que le flux de chaleur pariétal conditionne fortement les échanges thermiques en ébullition sous-refroidie, ou en régime saturé à bas débit, mettant en évidence la contribution importante du terme de nucléation dans ces conditions.

La description de l'influence du niveau de gravité sur h dépend donc fortement des conditions de titre, de débit et de flux de chaleur pariétal. En ébullition sous-refroidie, h est systématiquement inférieur en microgravité, de 10 à 30% par rapport à la gravité normale. En ébullition saturée, aux débits importants pour lesquels les transferts de chaleur sont dominés par l'ébullition convective, la gravité joue peu sur h, quelque soit q. Par contre, à débits faibles et modérés, lorsque le terme d'ébullition nucléée devient prépondérant, le coefficient d'échange de chaleur diminue avec le passage en microgravité.

Afin de mieux appréhender l'influence de la gravité sur les grandeurs étudiées précédemment, les données expérimentales sont confrontées dans le chapitre suivant à des corrélations empiriques et des modèles permettant de les relier entre elles.

3.1 Flow patterns

A description of two-phase flow patterns is given in this section for boiling HFE-7000 flow under normal gravity and microgravity conditions. The observation of flow patterns is mostly based on the processing of images provided by the high-speed camera and only lab data are available for 1-g conditions (the flow data corresponding to steady flight at 1-g during parabolic flight are not acquired). The flow patterns that are encountered in both situations are characterised through camera images. The influence of flow parameters on these flow patterns is presented in flow pattern maps that allow to discuss experimental transition criteria.

3.1.1 Visualisation

The high speed camera allows to visualise flow patterns for various mass fluxes G, inlet conditions (corresponding to a subcooling ΔT_{sub} or an inlet vapor quality x_{in}) and heat fluxes q through the ITO coating. Three main flow patterns, easily identifiable, have been observed under both normal gravity and microgravity conditions: bubbly flow, annular flow and a transitional flow pattern between bubbly and annular flows corresponding to slug and churn flows. This last flow regime is characterised by its intermittency on the void fraction α.

The relevant parameter used to study the evolution of two-phase flow patterns is the vapor quality x.

Bubbly flow: at low vapor qualities corresponding to subcooled regimes ($T_l < T_{sat}$), bubbly flows occur. Bubbles are nucleated on the heated inner surface of the sapphire tube, they slide along the wall and detach. Bubbles grow due to phase change and also to coalescence phenomenon. Bubbles whose length is smaller than the inner diameter of the tube D are categorised as "small bubbles" whereas bubbles that are larger in length than D are known as "elongated bubbles". Bubbly flows as classified in this study mostly corresponds to small bubbles distributions, with dispersed bubbly flows at low vapor quality and dense bubbly flow near the transition to slug flow.

Figure 3.1 shows a comparison between bubbly flows in 1-g and μ-g for the same flow parameters (G, x and q). Two different mass fluxes are illustrated here: a "high" mass flux $G = 540$ kg.s^{-1}.m^{-2} and a "moderate" mass flux $G = 220$ kg.s^{-1}.m^{-2}, both at $\Delta T_{sub} = 12$°C and $q = 2$ W.cm^{-2}. The impact of gravity level on the bubble size and shape is not significant in the videos for high mass fluxes, such as in Figure 3.1(a) but it can be clearly seen for moderate and low mass fluxes, such as in Figure 3.1(b).

For mass fluxes $G < 250$ kg.s^{-1}.m^{-2}, under microgravity conditions, bubbles are larger than in 1-g and are not deformed because they have a very small relative velocity compared to the liquid velocity. The larger bubble size in microgravity can be explained by both the higher rate of coalescence due to the small relative motion of the bubbles and the larger diameter at detachment, since only the liquid drag is responsible for the detachment in μ-g.

Slug flow: from bubbly flow, as quality increases, dense bubbles distributions including a few Taylor bubbles (bullet shaped bubbles with a smooth interface) can be observed. Coalescence phenomenon then leads to slug flow with Taylor bubbles, whose length increases with vapor quality. The liquid plugs in between the elongated bubbles carry

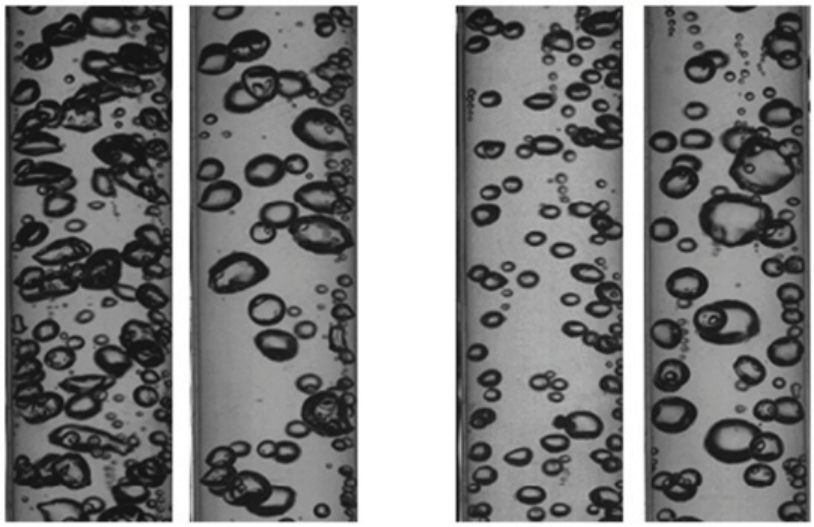

(a) $G = 540$ kg.s^{-1}.m^{-2} in 1-g (left) and in μ-g (right)

(b) $G = 220$ kg.s^{-1}.m^{-2} in 1-g (left) and in μ-g (right)

FIGURE 3.1: Flow visualisations for bubbly flows, $\Delta T_{sub} = 12°$C, $q = 2$ W.cm^{-2}

small bubbles distribution whose density mostly depends on the conditions at the inlet of the sapphire tube; these bubbles move nearly at the same velocity than the cylindrical Taylor bubbles.

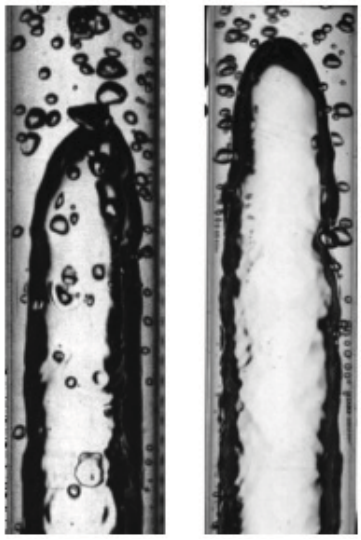

FIGURE 3.2: Flow visualisations for slug flows in 1-g (left) and in μ-g (right), $G = 220$ kg.s^{-1}.m^{-2}, $x_{in} = 0.05$, $q = 2$ W.cm^{-2}

Figure 3.2 shows pictures from slug flows with very close flow parameters values, in 1-g and μ-g, at $G = 220$ kg.s^{-1}.m^{-2} with a low inlet vapor quality $x_{in} = 0.05$ and a moderate wall heat flux $q = 2$ W.cm^{-2}. The difference between the two gravity levels is hardly visible on the flow videos, even at moderate and low mass fluxes. The nose of the Taylor bubbles is almost perfectly spherical in μ-g while it can be destabilised in 1-g, depending on the flow rate and wall heat flux. The small bubbles in between the liquid plugs are more spherical in μ-g since they are the residues of the bubbles coming from the preheaters, that are not deformed; in 1-g, these small bubbles are more irregular and

created by entrainement at the rear of Taylor bubbles. In the liquid film around Taylor bubbles, nucleation of small bubbles is visible both in normal gravity and microgravity.

Annular flow: once the gas core from elongated bubbles in slug flow is no longer interrupted by liquid plugs, annular flow is observed. These regimes correspond to saturated flow boiling for vapor quality above 10%. The liquid is flowing at the wall around a vapor core. The liquid film can become very thin and wavy because of the strong interfacial shear stress induced by the vapor core flow. Roll waves at the vapor-liquid interface are visible on the videos depending on the flow parameters. At the highest qualities and mass fluxes, some liquid droplets are also detached from the film surface and entrained into the vapor core. The settings of the high-speed camera and the investigated flow parameter ranges have not allowed to clearly see nucleation in the liquid film at the wall. The classification "annular flow" groups together wavy-annular flow and smooth annular flow, with or without liquid entrainment in the core.

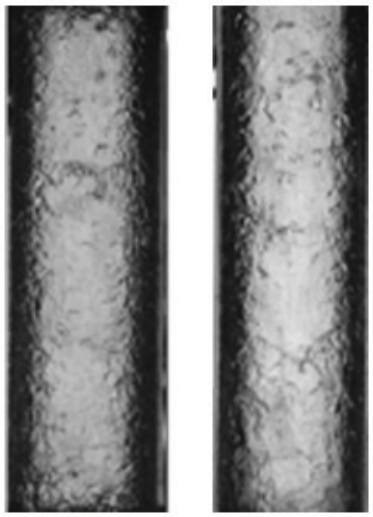

FIGURE 3.3: Flow visualisations for annular flows in 1-g (left) and in μ-g (right), $G = 200$ kg.s^{-1}.m^{-2}, $x_{in} = 0.20$, $q = 2$ W.cm^{-2}

Figure 3.3 shows annular flow visualisations at the same flow parameters values, in 1-g and μ-g, at $G = 200$ kg.s^{-1}.m^{-2} with a high inlet vapor quality $x_{in} = 0.20$ and a moderate wall heat flux $q = 2$ W.cm^{-2}. The difference between the two gravity levels is not visible to the naked eye on the flow videos since the spatial resolution and the optical distortion do not allow to appreciate the variations in the liquid film thickness, even with thicker films at moderate vapor qualities.

Transition flow: several intermediate regimes are observed between bubbly, slug and annular flow regimes which are themselves clearly described. These regimes are classified as transition flow since their description is very subjective. They occur for low liquid subcooling or for saturated boiling at low inlet qualities. Transition flows include bubbly-slug flows (alternation of bubbles and small slugs between bubbly flow and slug flow, as can be seen in Figure 3.4(a)), and frothy slug-annular flows (between slug flow and annular flow, where frothy slugs containing very small bubbles appear when the gas core breaks up, as illustrated in Figure 3.4(b)). This category also contains churn flow characterised by the presence of a very thick and unstable liquid film, but that specific regime has rarely been observed in 1-g experiments and is hardly distinguishable.

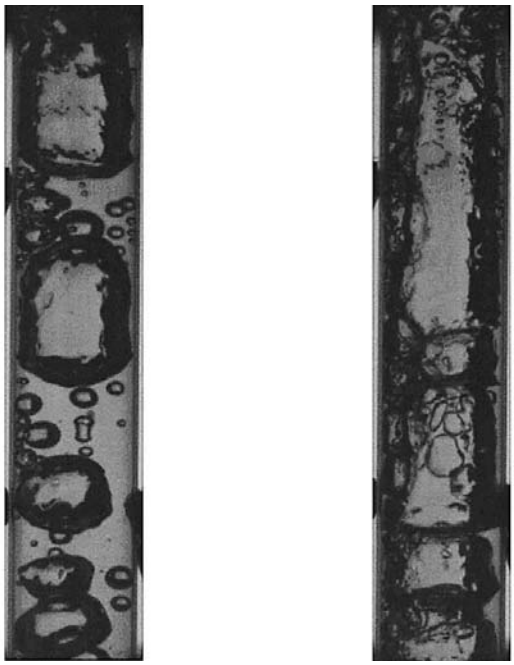

(a) Bubbly-slug flow, $\Delta T_{sub} = 9°C$

(b) Frothy slug-annular flow, $\Delta T_{sub} = 5°C$

FIGURE 3.4: Flow visualisations for transition flows, $G = 50$ kg.s^{-1}.m^{-2}, $q = 2$ W.cm^{-2}, in μ-g

No comparison has been drawn between normal gravity and microgravity conditions for transition flow visualisations because a small variation in the flow parameters (including working pressure) leads to a change in the flow structure that can hardly be objectively described.

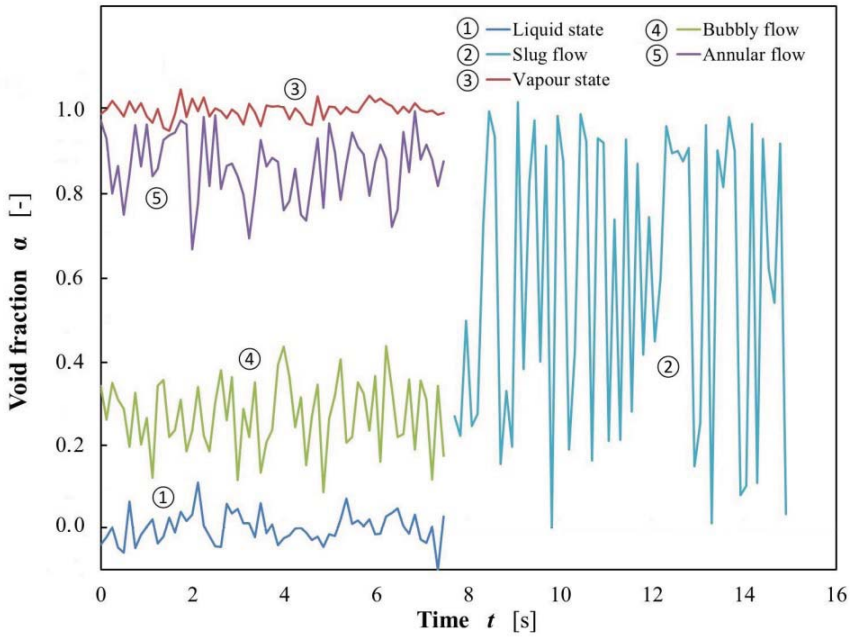

FIGURE 3.5: Void fraction time evolution for single-phase liquid and vapor flows and two-phase bubbly, slug and annular flows

Void fraction sensors: flow patterns can be determined from flow visualisations provided by the high-speed camera but also from the signal of the void fraction probes, as illustrated in Figure 3.5. Bubbly flows correspond to low void fraction close to the all-liquid level while annular flow data (with a vapor core) are observed for higher void fraction values near the all-vapor line. Slug flow is characterised by its intermittency, which is clearly visible on the signal oscillations between low and high void fraction values, even if spatial resolution and time resolution of the capacitance measurements do not allow to clearly see the slug passage.

However, the void fraction probes signals do not allow to distinguish transition flows from bubbly, slug and annular flows because of the poor space resolution of the measurements. Void fraction signals are therefore not used to determine flow patterns.

3.1.2 Effects of flow parameters on flow regimes

In this section, the parametric influence of the main flow parameters (mass flux G, wall heat flux q and vapor quality x) on the flow patterns is discussed. This analysis is valid under both normal gravity and microgravity conditions although experimental values corresponding to transitions between the main identified flow patterns may slightly change according to gravity level.

The vapor quality x is in fact the most relevant parameter needed to describe the evolution of flow patterns. The other flow parameters (such as the mass flux G, the inlet conditions or the wall heat flux q) affect the flow structure to the extent that they induce variations in the vapor quality:
− at fixed wall heat flux and inlet conditions, an increase of the mass flux leads to a decrease in the vapor quality and vice versa. As a result, bubbly flows can be observed for a large number of combinations of q and ΔT_{sub} at $G = 200$ kg.s^{-1}.m^{-2} while they only occur on very restricted ranges of flow parameters at $G = 50$ kg.s^{-1}.m^{-2};
− at fixed mass and heat fluxes, inlet conditions directly determine the local vapor quality. At high mass fluxes, setting a desired subcooling at the inlet of the test section almost always leads to the observation of bubbly flow along the whole tube, whereas a given inlet vapor quality causes the flow to be annular;
− at fixed mass flux and inlet conditions, an increase of the wall heat flux results in a increase of the vapor quality through further vaporisation.

An illustration of the influence of both the inlet conditions and the wall heat flux is presented in Figure 3.6 for $G = 200$ kg.s^{-1}.m^{-2}: flow visualisations are provided for various combinations of ΔT_{sub} (between 10°C and saturation conditions) / x_{in} (up to 25%) and q (up to 3 W.cm^{-2}) at a distance $z \simeq 12$cm from the inlet of the heated section. At this flow rate, the flow pattern can be considered as invariable along the tube since the test section is rather short and the wall heat fluxes limited.

At $G = 200$ kg.s^{-1}.m^{-2}, the available settings of wall heat flux and inlet conditions are enough to cover the whole range of flow pattern, from single-phase flow to smooth annular flow, including dispersed and dense bubbly flows, slug flow, transition flows and wavy-annular flow. On the graphic, the local vapor quality increases both with q and with x_{in}: the bottom right picture represents the flow pattern corresponding to the highest values of x with around 60% of vapor.

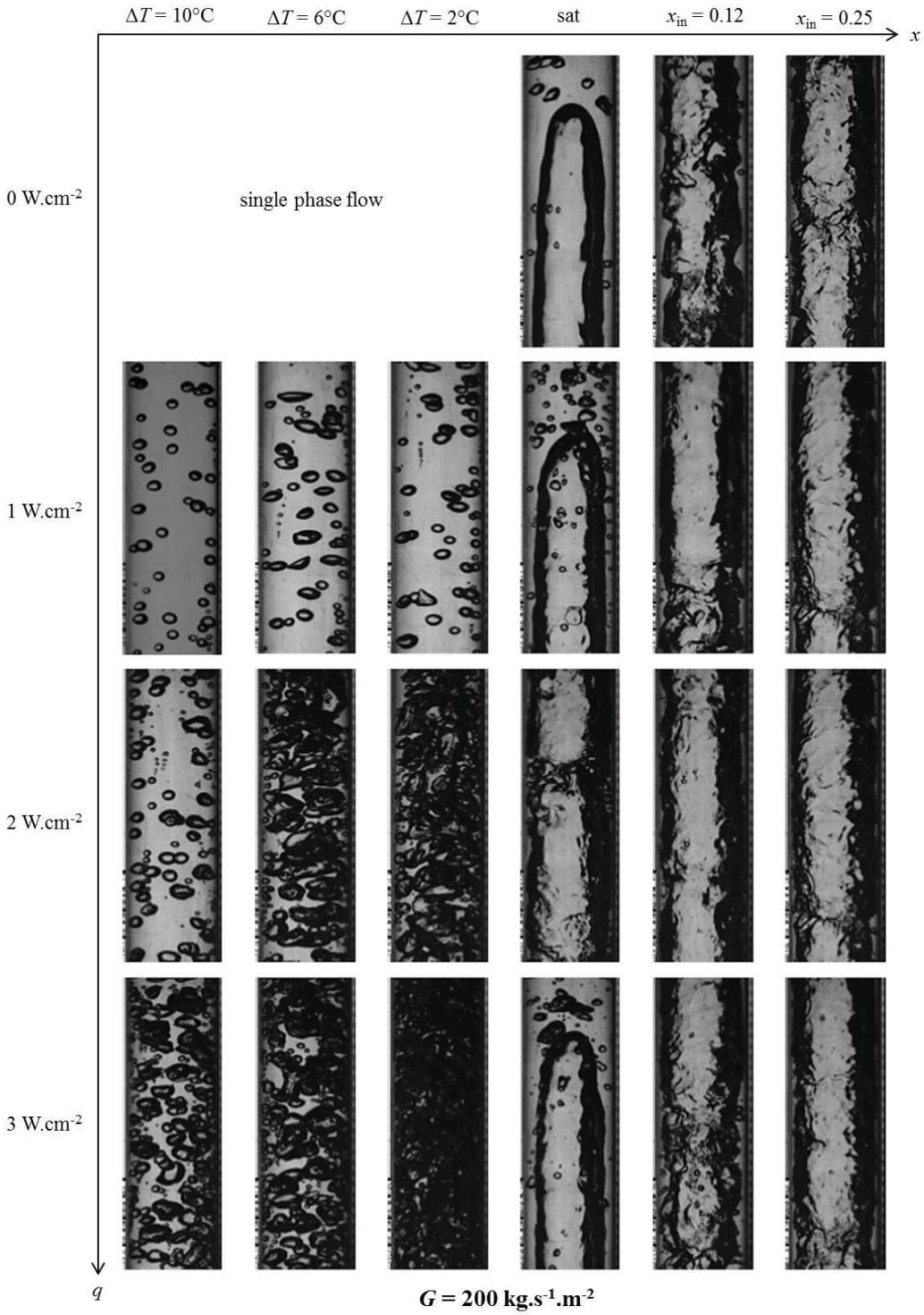

FIGURE 3.6: Influence of the inlet conditions and wall heat flux on flow patterns for $G = 200$ kg.s^{-1}.m^{-2} (lab tests, July 2012)

3.1.3 Evolution along the tube

Since this study focuses on two-phase boiling flow before the CHF, and because of safety reasons related to experiments during parabolic flight campaigns, dry out conditions are avoided. To achieve that, it is necessary to predict the structure of the flow at the outlet of the heated test section depending on the combinations of flow parameters that are

set. However, the high-speed camera allows to monitor only a restricted length of the sapphire tube in microgravity, and the flow pattern observed on the videos may not correspond to the flow pattern at the outlet of the test section, where measurements of void fraction, temperature and pressure drops are performed.

For that reason, one on-ground measurement campaign used a different high-speed camera to film the entire sapphire tube and appreciate the evolution of flow pattern along the test section according to various flow parameters settings. Some results are illustrated in Figure 3.7 for subcooled inlet conditions.

For high mass fluxes ($G = 200$ and 400 kg.s^{-1}.m^{-2}), the velocities are high enough and the heated length of the test section is short enough to prevent an important evolution of the vapor quality along the sapphire tube, for both subcooled (as illustrated in Figure 3.7(b)) and saturated inlet conditions. For almost any flow parameters combination, the same flow pattern can be observed between the inlet and outlet of the test section, with an increase in the bubble frequency for bubbly flows when the distance z increases, and a thinner liquid film at the wall near the outlet of the tube for annular flows. The maximal increase in the vapor quality along the tube (obtained with saturated inlet conditions and high wall heat fluxes) amounts to 10% for $G = 200$ kg.s^{-1}.m^{-2} and is even lower for $G = 400$ kg.s^{-1}.m^{-2}.

However, for low mass fluxes ($G = 50$ and 75 kg.s^{-1}.m^{-2}), the evolution of the vapor quality (and therefore of the flow pattern) along the sapphire is very significant, even at high subcoolings or low wall heat fluxes, as shown in Figure 3.7(a). The whole range of flow pattern can be observed with subcooled inlet conditions and high vapor qualities are reached at the outlet of the sapphire tube. For that reason, only subcooled tests were performed at low mass fluxes: runs where the fluid entered the test section in saturated conditions only lead to dry outs and malfunctioning in the cooling system. For these mass fluxes and the available heat fluxes, the increase in the vapor quality along the tube is typically between 10 and 40%.

Intermediate mass fluxes correspond to a less significant evolution of the flow pattern along the tube (generally with two different flow patterns observed between the inlet and outlet) and smaller increase in the vapor quality along the test section. Some experiments were performed at these mass fluxes with saturated inlet conditions, but only with low inlet vapor qualities, and low and moderate wall heat fluxes.

3.1.4 Flow pattern maps

Figures 3.8(a) and 3.8(b) present flow pattern maps for normal gravity and microgravity conditions; the liquid superficial velocity j_l is plotted according to the vapor superficial velocity j_v and isocurves of mass flux and vapor quality are added. The data selected for the flow pattern maps correspond to series with five different mass fluxes $G = 50$, 75, 100, 200 and 400 kg.s^{-1}.m^{-2}. Since the pressure variations induce small changes in the flow rate, especially during parabolic flights, the actual values of experimental mass fluxes range as follow: $47 < G < 53$, $70 < G < 80$, $90 < G < 110$, $190 < G < 210$, and $385 < G < 415$ kg.s^{-1}.m^{-2}.

$$j_l = \frac{G \cdot (1 - x)}{\rho_l} \qquad j_v = \frac{G \cdot x}{\rho_v} \tag{3.1}$$

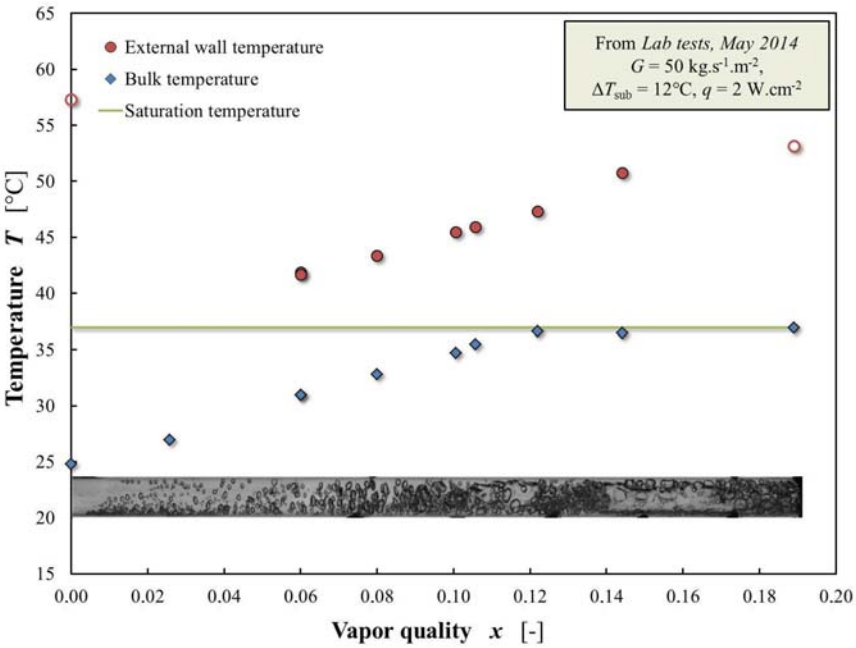

(a) $G = 50$ kg.s^{-1}.m^{-2}

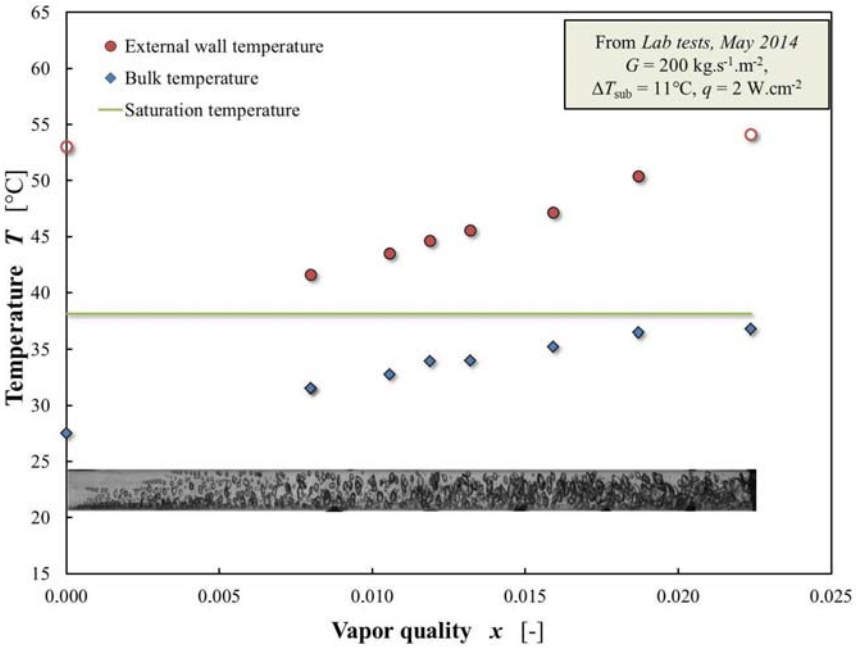

(b) $G = 200$ kg.s^{-1}.m^{-2}

FIGURE 3.7: Evolution of flow pattern along the heated test section according to the vapor quality, for $G = 50$ and 200 kg.s^{-1}.m^{-2}, $\Delta T_{sub} = 11$-12°C and $q = 2$ W.cm^{-2} (lab tests, May 2014)

Three main categories of flow patterns are identified in the flow pattern maps:
− bubbly flows include dispersed bubbly flows and regimes with dense distributions of bubbles or very small vapor plugs just before the transition from bubbly flow to slug flow. Experiments corresponding to vapor quality smaller than 0.01 have not been included in the maps since the error on the calculation of x at this order of magnitude leads to a significant uncertainty in the superficial velocities;

– since the distinction between slug and transition flows is sometimes difficult to make, and since slug flow only occurs for very restricted ranges of flow parameters, transition and slug flows have been regrouped in the maps. These points therefore include bubbly-slug, slug and frothy slug-annular flows, and undertemined transition flows;
– the third category corresponds to annular flows that regroup wavy annular flows and smooth annular flows.

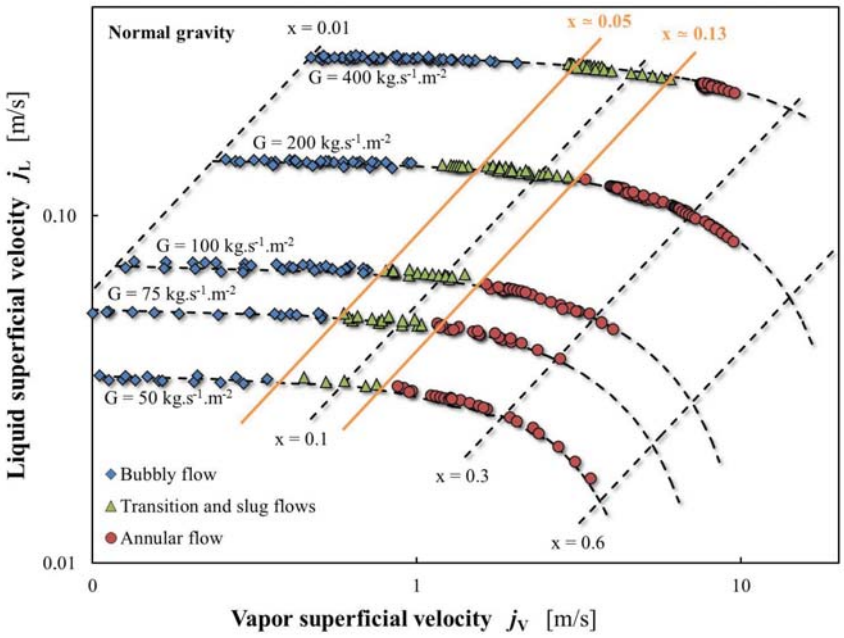

(a) Normal gravity conditions

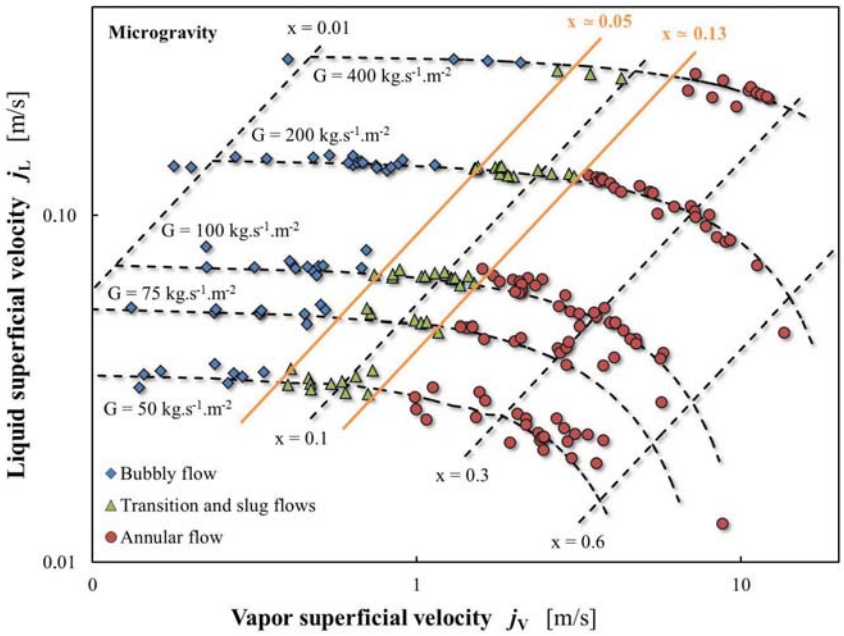

(b) Microgravity conditions

FIGURE 3.8: Flow pattern maps under normal and microgravity conditions (lab tests, 2014 and parabolic flight campaigns, 2012, 2013, and 2014)

Map in 1-g: Figure 3.8(a) presents parametric tests from a lab measurement campaign that took place in May 2014 and during which the whole sapphire tube was imaged. Experimental points in 1-g from parabolic flight campaigns cannot be processed for flow patterns investigation since the sapphire tube is not filmed during steady flight inbetween parabolas. This time interval is required for saving data acquired during the microgravity phase from the camera memory.

On-ground, flow parameters including working pressure are more easily controllable and steady mass fluxes at approximately 1.2 bar are achieved: the experimental points are concentrated on the isocurves of mass flux. Since the number of tests is not limited, numerous combinations of flow parameters are set in order to cover the whole range of vapor quality x. The vapor quality is calculated with an energy balance at a generic distance z from the inlet of the heated section and the corresponding flow pattern at the same location is indicated. With a visualisation of the entire tube in 1-g, it is possible to report five to six different locations (i.e. different vapor qualities) along the tube for a single run. As a result, almost 700 different experimental points are presented for more than 120 runs in the flow pattern under normal gravity conditions.

The distribution of the flow patterns according to the vapor quality clearly appears in the flow pattern map: bubbly flows always correspond to subcooled regimes at low vapor qualities with low vapor superficial velocities. From bubbly flows, an increase in x leads to transition and slug flows that occur on a small range of vapor quality; in particular, slug flow only occurs for very specific conditions around $x \simeq 0.08$ and can not be observed even in parametric runs without the appropriate settings. Finally, annular flow always correspond to saturated regimes at high vapor superficial velocities with moderate and high vapor qualities.

The transitions between the three main categories of flow patterns seem to occur at constant vapor quality, whatever the mass flux is. They are indicated with orange isocurves on the map. The flow tends to transition from bubbly to slug flow around $x \simeq 0.05$ while vapor qualities $x \gtrsim 0.13$ always correspond to annular flow. Transition criteria between different flow patterns are further discussed in terms of vapor quality and void fraction in the next sections.

Map in μ-g: experimental points presented in the flow pattern map under microgravity conditions were obtained during three parabolic flight campaigns in April 2012 (PFC 95), October 2013 (PFC 106) and April 2014 (PFC 110). Mass fluxes of 400 kg.s^{-1}.m^{-2} have only been investigated during PFC 95 while the series at 75 kg.s^{-1}.m^{-2} have mostly been provided by PFC 110, which explains the lack of points for this value of G.

During parabolas, the pressure is hardly controllable, which induces changes in the mass flux, especially for PFC 95 when no PID regulation of the pump was installed. For that reason, experimental data are more dispersed in the μ-g map and do not follow the isocurves of mass flux. Only the points near these isocurves were kept to plot the flow pattern map. The limitation in the number of parabolas does not allow to cover the entire range of vapor quality, and some parabolas are not usable because of encountered technical difficulties. Moreover, the field of view of the camera is smaller and only one or two different locations (i.e. vapor qualities) along the tube can be reported with their corresponding flow patterns for each test. As a result, about 250 experimental points corresponding to 190 - 200 runs are presented in the flow patterns map, for a total of 285 parabolas flown in three campaigns.

The flow pattern map under microgravity conditions looks very much alike the 1-g map: the same flow pattern are observed for the same superficial velocities. The transitions seem to occur at the same vapor quality as in normal gravity (the same isocurves of x are plotted on the two graphs). No significant difference can be seen in the flow pattern maps. As for the 1-g case, transition criteria are discussed in the next section.

However, due to difficulties in the characterisation of transition flow, it is not possible to clearly establish that the gravity level does not influence coalescence phenomenon near the transitions between distinct flow patterns, and dense bubbly flows / transition flows may exhibit small differences in the flow structure according to the gravity level, which would be difficult to be subjectively described and that may not appear near the transition lines plotted on the flow pattern maps.

Map indicating Reynolds numbers: limit values of liquid and vapor Reynolds number are indicated in Table 1.2 for ranges of flow parameters set for BRASIL experiments (with 50 kg.s^{-1}.m^{-2} $< G <$ 400 kg.s^{-1}.m^{-2} and $0.01 < x < 0.8$). Figure 3.9 presents the detail of the calculations for the liquid and vapor Reynolds numbers corresponding to 1-g data, with indications of flow patterns. Dotted lines represent critical values of Reynolds numbers for the transition from laminar to turbulent regimes. Notations defined by Lockhart and Martinelli [1949] are used to distinguish four different regions (as described in Table 1.3).

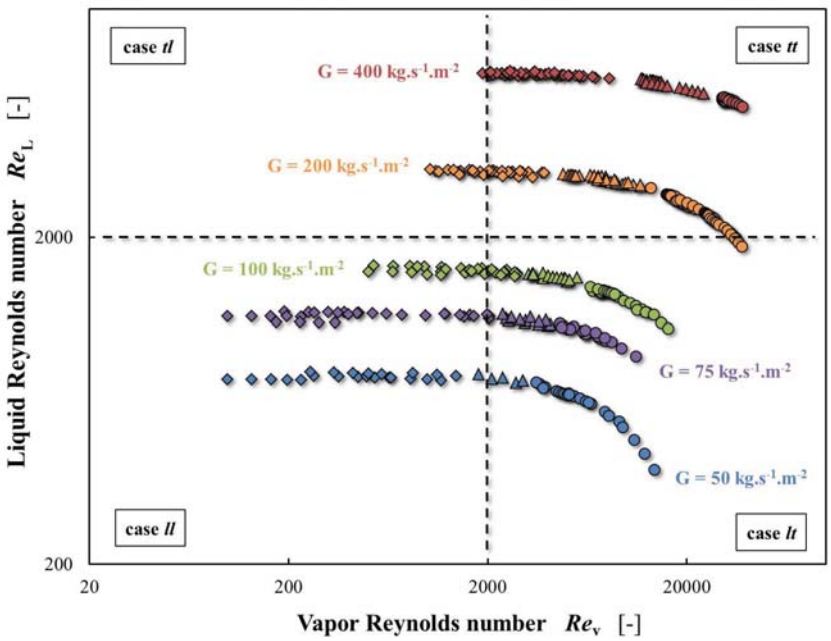

FIGURE 3.9: Flow pattern map for 1-g data according to liquid and vapor Reynolds numbers

As can be seen from the graphic, experimental data mainly cover three of the four regions. At high mass fluxes ($G = 400$ and 200 kg.s^{-1}.m^{-2}), almost all points correspond to turbulent liquid and vapor phases (case tt). At low mass fluxes ($G = 75$ and 50 kg.s^{-1}.m^{-2}), bubbly flow regimes are laminar flows (case ll), while at moderate G, they are near the transition from laminar to turbulent on each phase. Finally, flows at low and moderate G, and moderate and high x (corresponding to slug, transition and annular flows) exhibit a laminar behaviour for the liquid (and especially for the liquid film in annular flow) and a turbulent behaviour for the vapor (case lt).

3.1.5 Comparison with other microgravity datasets

The flow pattern data that are reported for the three mentioned microgravity datasets are presented in the flow pattern map of Figure 3.10. The two orange lines materialise transitions between bubbly and transition flows ($x \simeq 0.05$) and between transition and annular flows ($x \simeq 0.13$) that have been highlighted in the case of BRASIL experiment.

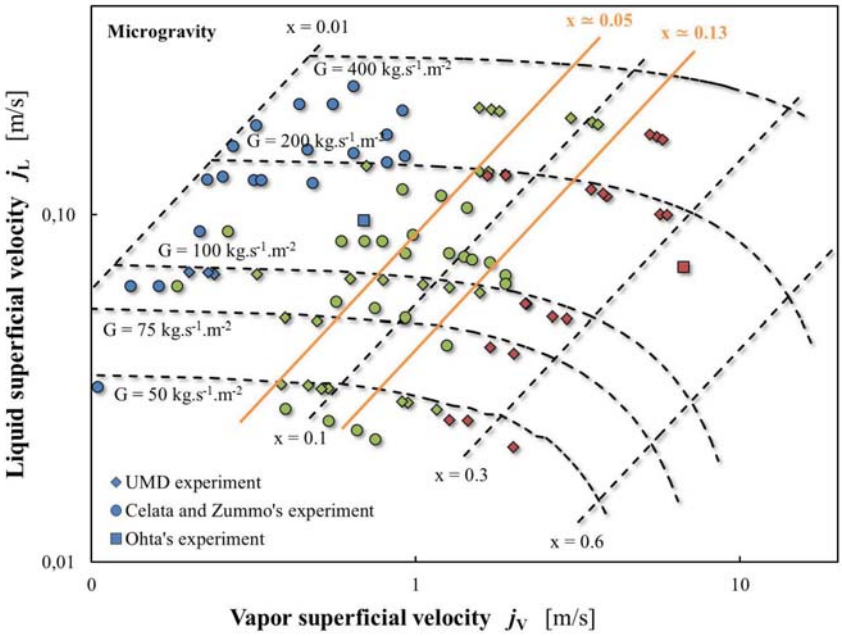

FIGURE 3.10: Flow pattern map in μ-g for different experiments - blue: bubbly flow, green: transition and slug flows, red: annular flow

Some considerations have to be taken into account before drawing a comparison between various flow visualisations:
− the identification of flow patterns is very subjective and various classifications were used by the different authors. In particular, the transition from bubbly to slug or intermittent flows is not very precisely determined. Celata and Zummo [2007] distinguished bubbly flows, bubbly-plug, plug and intermittent flows. The latter three were grouped together in the category "transition and slug flows";
− even though flow visualisations were provided for all set-ups, the different test sections do not always enable to obtain pictures suitable for precise identification of all features of the flow structure, especially in the case of the UMD experiment;
− ranges of superficial velocities are similar despite the differences in the working fluid and flow parameters settings. However, calculations of the vapor quality x may induce important variations in these velocity values. Indeed, some authors only used a thermodynamical vapor quality or do not characterise x as the vapor mass flow rate over the total mass flow rate in subcooled regimes, which can lead to significant differences in the indication of transitions between flow patterns.

All authors agree on the fact that the influence of gravity level can be neglected at very high mass flux, and the studies focus on G between 50 and 400 kg.s^{-1}.m^{-2}. Ohta illustrates the weak impact of gravity level on the flow structure by comparing bubbly flows (with moderate subcooling at the inlet of the heated test section) in 1-g and μ-g at $G = 600$ kg.s^{-1}.m^{-2}, as shown in Figure 3.11.

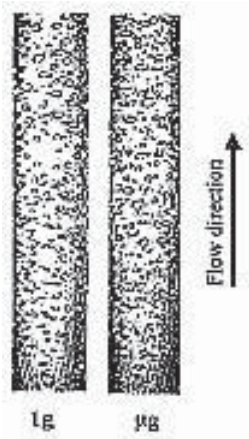

FIGURE 3.11: Bubbly flow in 1-g and μ-g at very high mass flux - $G = 600$ kg.s^{-1}.m^{-2}, $\Delta T_{sub} = 6.7°$C, $q = 4$ W.cm^{-2} [Ohta, 2003]

As can be seen from the flow pattern map, bubbly flow occurs at low x. The transition to slug and transition flows is rather blurry (mostly due to error on the calculation of the vapor quality) but it occurs between $x \simeq 0.03$ and $x \simeq 0.05$ depending on the dataset. At low and moderate mass fluxes, flow visualisations all highlight the same trend in the evolution of the flow structure with the gravity level: microgravity phases correspond to larger and more spherical bubbles compared to normal gravity conditions, which is illustrated in Figure 3.12. Celata and Zummo reported numerous points in bubbly flow while Ohta did not draw any flow pattern map and provided only one example of runs in bubbly flow. Even with low heat fluxes, very few points corresponding to this regime were obtained during the measurement campaign with UMD.

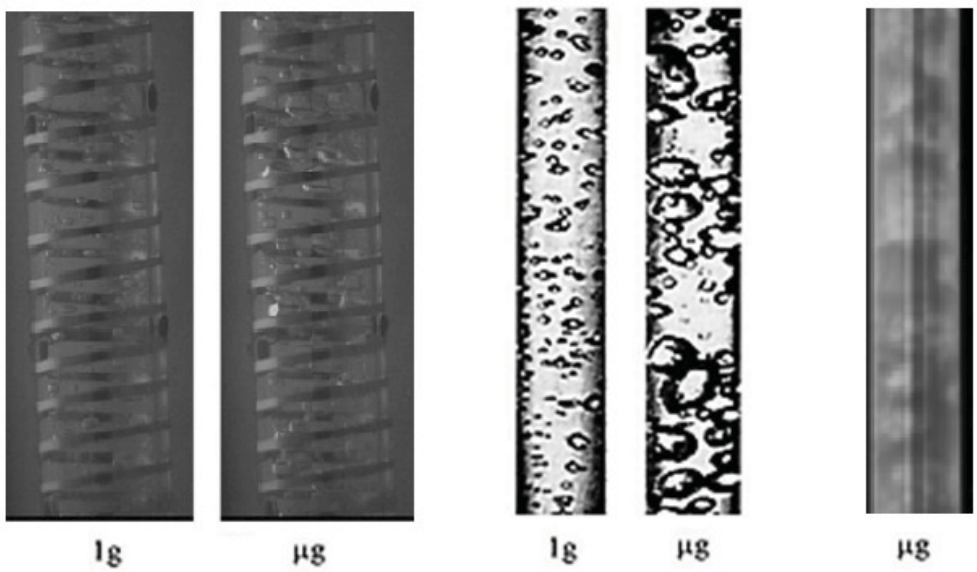

FIGURE 3.12: Bubbly flow visualisations in 1-g and μ-g at low mass fluxes from left to right:
[Baltis et al., 2012] $G = 50$ kg.s^{-1}.m^{-2} in 1-g and μ-g
[Ohta and Baba, 2013] $G = 150$ kg.s^{-1}.m^{-2}, $\Delta T_{sub} = 13°$C, $q = 2$ W.cm^{-2}
UMD experiment: $G = 50$ kg.s^{-1}.m^{-2}, $\Delta T_{sub} = 8°$C, $q = 6$ W.cm^{-2} in μ-g

As previously discussed, the category "transition and slug flows" regroups various regimes; most of them correspond to subcooled conditions. Celata and Zummo distinguished intermittent flows that are part of the category "transition flow" and plug flows that are

slug flows. Ohta did not report any data for these regimes. The flow pattern map shows that transition and slug flows from ENEA and UMD data are observed on the same range of x that the one highlighted in BRASIL experiments, with larger transitions from bubbly flows. The influence of the gravity level is hardly visible on these runs since it is very difficult to characterise corresponding flow structures and evolution.

No annular flow data were obtained by Celata and Zummo. Ohta only provided two illustrations of annular runs (with and without nucleation in the liquid film) while UMD set-up allowed to acquire several parabolas in saturated regimes. The transition from slug flow seems to occur approximately at the same vapor quality than the one observed in this thesis, even though UMD flow visualisations do not allow to identify it very precisely. An illustration of Ohta's and UMD annular flow observations is presented in Figure 3.13. As for BRASIL flow visualisations, the difference between the two gravity levels cannot be seen with the naked eye.

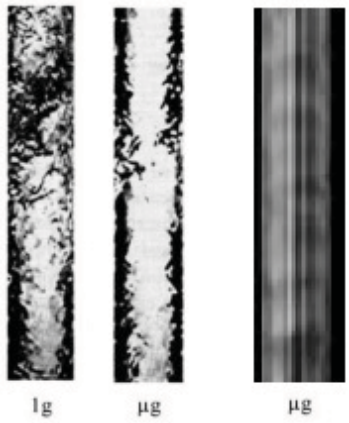

FIGURE 3.13: Annular flow visualisations in 1-g and μ-g at low mass fluxes from left to right:
[Ohta and Baba, 2013] $G = 150$ kg.s^{-1}.m^{-2}, $x_{in} = 0.28$, $q = 1$ W.cm^{-2} in 1-g and μ-g
UMD experiment: $G = 50$ kg.s^{-1}.m^{-2}, $x_{in} = 0.28$, $q = 0.9$ W.cm^{-2} in μ-g

3.2 Void fraction and film thickness

Void fraction measurements are performed at the inlet and outlet of the sapphire tube with capacitance sensors. While the inlet probe is only used in saturated conditions, the outlet sensor is very useful to provide data that can be correlated to the pressure drops that are obtained on the adiabatic part just after the heated section. The following section presents all processed runs both under normal gravity and microgravity conditions with error bars to characterise the uncertainty in the void fraction measurements. For the specific case of annular flow, liquid film thickness data are also reported.

3.2.1 Void fraction

The data that are presented thereafter were provided by experiments using three different designs of capacitance probe. Only the void fraction values acquired during PFC 2013 are not included in the graphics: despite the fact that they exhibit the exact same trend versus vapor quality than the other measurements between 1-g and μ-g, they are quantitatively not exactly consistent with these data; indeed, capacitance signals were acquired on the NI deck with the LabVIEW interface, which resulted in more important noises on the measurements compared to stand-alone acquisition programs.

As for the flow patterns, the most relevant parameter used to characterise the evolution of α is the vapor quality x. The other flow parameters or set values such as the mass flux G, the inlet conditions ΔT_{sub} / x_{in} or the wall heat flux q mainly affect the void fraction through their influence on the quality at the outlet of the sapphire tube.

Figure 3.14 presents the void fraction according to the vapor quality at the outlet of the heated test section for various mass fluxes G, both in 1-g and μ-g. Error bars are plotted on another figure for clarity purposes. High mass fluxes (Figure 3.14(a)) are separated from moderate and low mass fluxes(Figure 3.14(b)). Initial design and experiments focused on turbulent flow but they were extended to lower mass fluxes that were expected to correspond to different behaviours, strongly affected by the gravity level. Very high vapor qualities ($x > 0.7$) have not been investigated due to practical difficulties.

The general look of the void fraction curves is the same whatever the mass flux or the gravity level is: as can be seen, the void fraction depicts a growing trend with vapor quality, with a saturation at high qualities. Indeed, an increase of the vapor quality means that more mass is transported by the vapor phase, which requires a higher void fraction to accomodate the increased vapor mass flow in the tube. The rate of growth is very fast at low vapor qualities (typically up to $x \simeq 0.15$) and very slow at high vapor qualities (for $x \gtrsim 0.30$). Nevertheless, differences can be observed when the mass flux or the gravity level is varied.

The high mass fluxes that are presented in Figure 3.14(a) correspond to $G = 400$ and 200 kg.s^{-1}.m^{-2}. Only a few points are available in μ-g for $G = 400$ kg.s^{-1}.m^{-2} because this mass flux was only investigated during the first parabolic flight campaign. As can be seen, it is difficult to draw a comparison between different experiments at low vapor qualities. The rate of growth is rather similar for the two mass fluxes. However, differences can be noticed on the saturating part of the curve, for high vapor qualities:
– when G varies: both under 1-g and μ-g conditions, saturation levels are higher for G = 200 kg.s^{-1}.m^{-2} than for $G = 400$ kg.s^{-1}.m^{-2}, due to velocities differences;

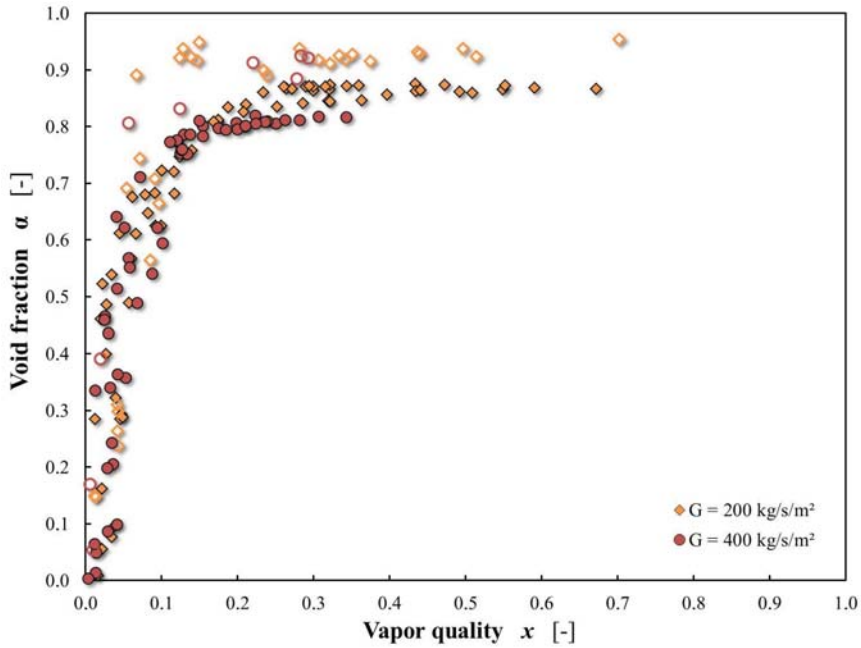

(a) $G = 400$ and 200 kg.s^{-1}.m^{-2}

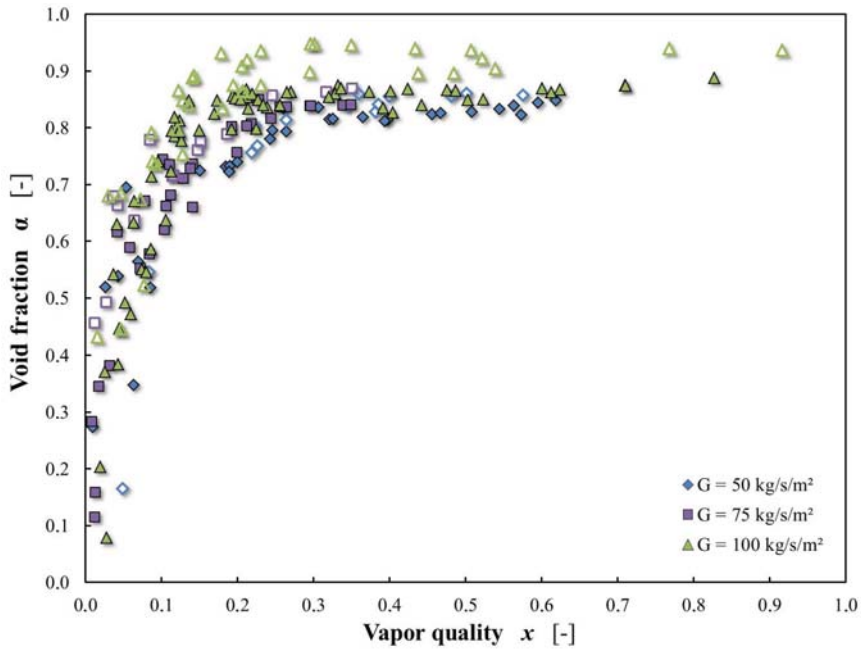

(b) $G = 100$, 75 and 50 kg.s^{-1}.m^{-2}

FIGURE 3.14: Void fraction according to vapor quality at the outlet of the heated test section, for various mass fluxes, in 1-g (closed symbols, lab tests 2012 and 2014, PFC 2014) and μ-g (open symbols, PFC 2012 and 2014)

– when the gravity level varies: the void fraction is significantly higher in microgravity than in normal gravity for the two mass fluxes. For $G = 200$ kg.s^{-1}.m^{-2} and $x > 0.30$, α is about 6% higher in μ-g than in 1-g. Borderline experimental points have confirmed the same trend for $G = 400$ kg.s^{-1}.m^{-2} between the two gravity levels.

The moderate and low mass fluxes in Figure 3.14(b) correspond to $G = 100$ kg.s^{-1}.m^{-2}, $G = 75$ and 50 kg.s^{-1}.m^{-2}. The two lowest were not investigated during the first parabolic flight campaign since the initial experimental facility was designed for higher ranges of G. Since x strongly evolves along the tube at these mass fluxes, most of the void fraction data at the outlet of the sapphire tube exhibit high vapor qualities. As for the high G, it is difficult to compare the few experiments at low vapor qualities. On this range of x, the void fraction rate of growth is similar for the three mass fluxes, and seems to be a bit lower than for $G = 400$ and 200 kg.s^{-1}.m^{-2}. Nevertheless, the observations made for moderate and high vapor qualities are different from high mass fluxes:

– when G varies: both under normal gravity and microgravity conditions, it can be seen that the saturation level slightly decreases as the mass flux decreases, even if the differences are small (they correspond to small steps of G). For a given vapor quality, the void fraction is slightly higher at $G = 100$ kg.s^{-1}.m^{-2} than at $G = 75$ kg.s^{-1}.m^{-2}. Same observation is made for $G = 50$ kg.s^{-1}.m^{-2};

– when the gravity level varies: the void fraction is higher in microgravity than in normal gravity, as for higher mass fluxes. However, flows at lower G seem to be less impacted by the gravity level than flow at intermediate $G = 100$ kg.s^{-1}.m^{-2}. While the difference on the void fraction between 1-g and μ-g is about 7% for this mass flux for $x > 0.30$, it amounts to only 3% for $G = 75$ and 50 kg.s^{-1}.m^{-2}.

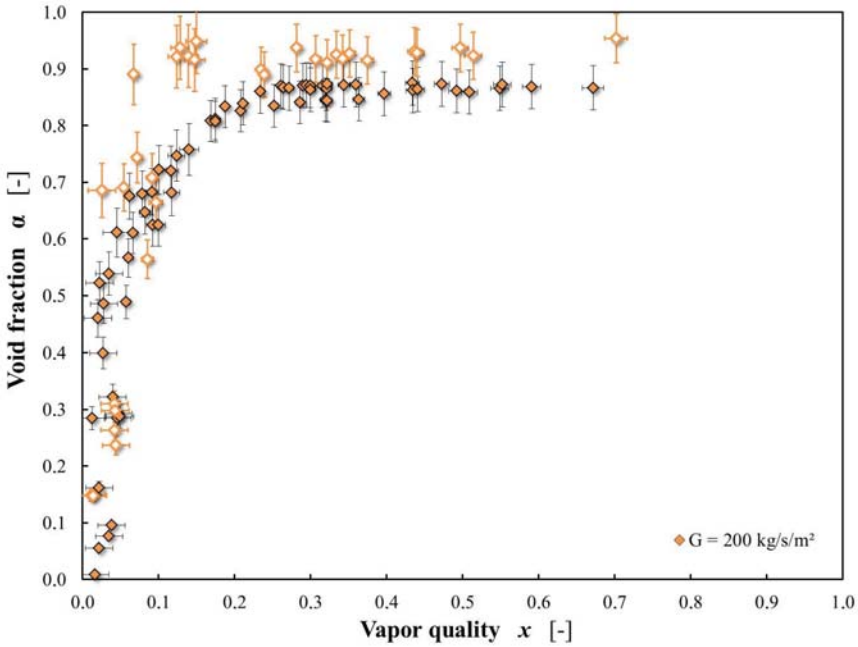

FIGURE 3.15: Void fraction according to vapor quality with experimental error bars, for $G = 200$ kg.s^{-1}.m^{-2}, in 1-g (closed symbols, lab tests 2012 and 2014, PFC 2014) and μ-g (open symbols, PFC 2012 and 2014)

3.2.2 Uncertainty in void fraction

As previously mentioned, data from Figure 3.14 were obtained with different probes during different measurement campaigns. These changes in the sensors and the fact that the working pressure cannot be strictly controled in μ-g induce small variations in the void fraction measurements for a given vapor quality. It is therefore necessary

to estimate the error made on the experimental values to confirm that the difference observed between the two gravity levels is really significant.

Figure 3.15 illustrates previous data at $G = 200$ kg.s^{-1}.m^{-2} with typical uncertainties in the vapor quality and the void fraction, under normal gravity and microgravity conditions. At low vapor qualities, the error on the void fraction measurements is rather small (around 2%) while there is a lack of precision on the calculation of x. The opposite trend is observed for moderate and high vapor qualities: the uncertainty in x in saturated (or near saturated) conditions is very small while the uncertainty in the void fraction ranges from 4% to 7% (due to lower measured capacitance levels and lack of experimental calibration points on this area).

Even though experimental error bars in 1-g and μ-g overlap a bit, the uncertainty in the void fraction is not important enough to explain the difference in the measurements for the two gravity levels at $G = 200$ kg.s^{-1}.m^{-2} and $G = 400$ kg.s^{-1}.m^{-2}. However, this trend is less obvious for low mass fluxes ($G = 75$ and 50 kg.s^{-1}.m^{-2}). Nonetheless, the fact that data from different campaigns are quantitatively consistent tends to promote a higher void fraction in microgravity even at these mass fluxes.

3.2.3 Flow pattern transitions

Since the void fraction is a strong function of the vapor quality at fixed densities ratio ρ_v/ρ_l, the transition criteria between flow patterns that are presented in the flow pattern maps (Figure 3.8) can be expressed in terms of void fraction.

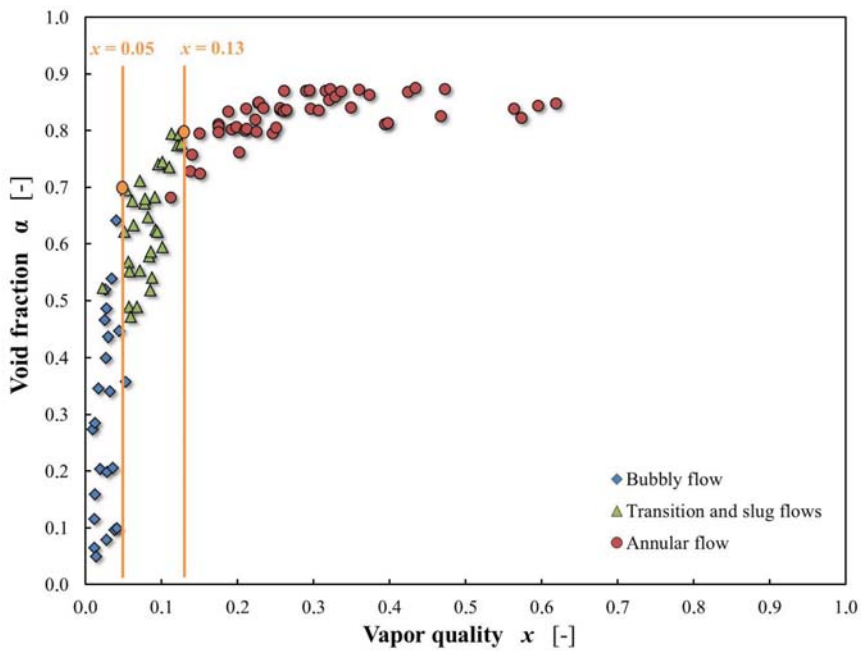

FIGURE 3.16: Void fraction according to vapor quality and flow patterns in 1-g (lab tests 2014)

Figure 3.16 shows void fraction data obtained during an on-ground measurement campaign for various mass fluxes according to the flow regime that are observed at the outlet of the heated sapphire tube. Transitions at constant vapor qualities are indicated in the same way as in the flow pattern maps. Bubbly flows occur at low void fraction ($\alpha <$ 0.45, which is more visible on the maps); undetermined transition flows are observed

for void fractions ranging from 0.5 to 0.7 where the flow transitions to actual slug flow. Finally, saturated regimes with annular flow correspond to void fraction $\alpha \gtrsim 0.8$.

3.2.4 Comparison with microgravity datasets

One of the key elements in the collaboration between IMFT and UMD was the design and integration of capacitance probes for void fraction measurements in the UMD rack. The sensors were build at IMFT on the model of the one designed for this thesis, with a good sensitivity and acquisition of data on LabVIEW.

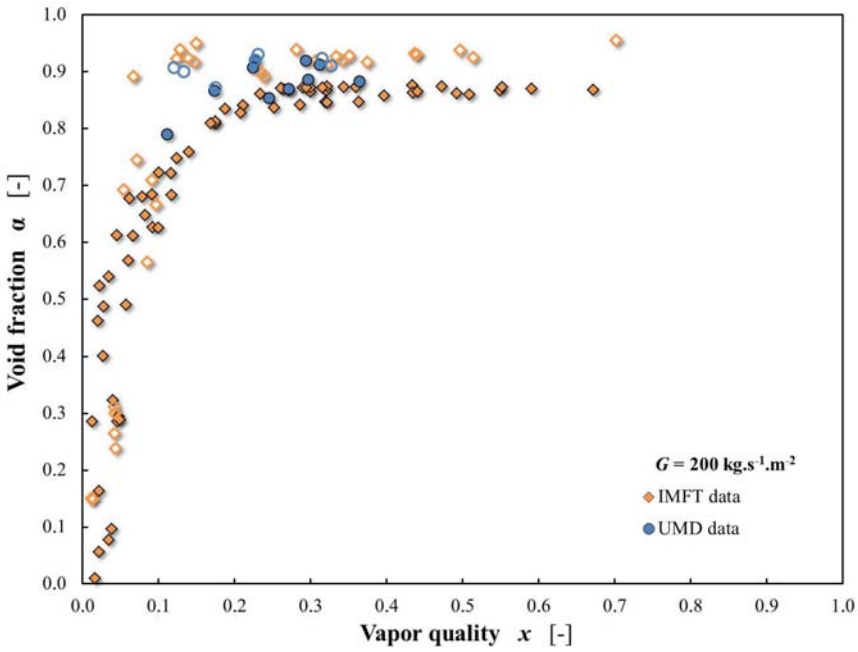

FIGURE 3.17: Void fraction measured by UMD et IMFT experimental set-ups at $G = 200$ kg.s^{-1}.m^{-2} in 1-g (closed symbols) and μ-g (open symbols, PFC 2013)

Figure 3.17 presents the few points that were acquired with UMD experiments during the parabolic flight campaign at $G = 200$ kg.s^{-1}.m^{-2} both under normal gravity (1-g phase during parabolic flight) and microgravity conditions, along with IMFT data. Considering the differences in the calibration and in experimental conditions (such as pressure differences or different working fluids), the data are in rather good agreement. 1-g data seem to be slightly higher in the case of UMD experiments compared to IMFT runs while μ-g data are consistent for the two datasets. As a consequence, the influence of gravity level is a bit less important on UMD data. Nevertheless, it is necessaray to obtain more experimental points to highlight actual trends.

Microgravity data at $G = 50$ and 100 kg.s^{-1}.m^{-2} are presented in Figure 3.18. The few points available in the UMD dataset are also consistent with the ones provided by BRASIL experiments, which gives similar results on the film thickness calculations (that are not shown here due to a lack of experimental points).

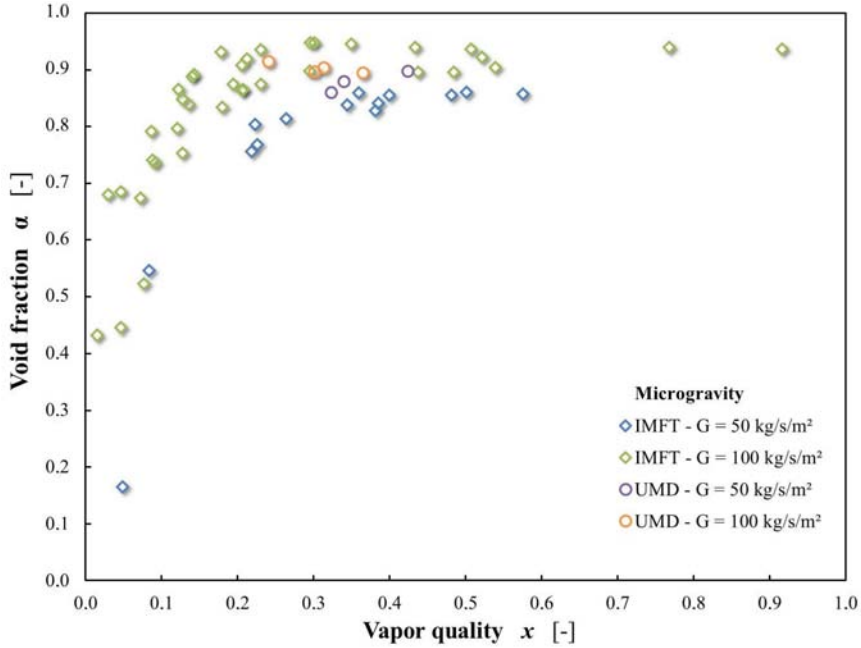

FIGURE 3.18: Void fraction measured by UMD et IMFT experimental set-ups at $G = 100$ and 50 kg.s^{-1}.m^{-2} in μ-g (PFC 2013)

3.2.5 Liquid film thickness in annular flow

In the case of annular flow with a vapor core and liquid flowing at the wall, it is interesting to translate void fraction data into liquid film thickness values since the heat transfer in convective boiling regimes occurs through the liquid film. The capacitance probes used in the experiment allow to measure an averaged void fraction, which means that the measured liquid fraction $1 - \alpha$ include the liquid flowing in the film at the wall plus liquid droplets in the vapor core in the case of annular flow with entrainment.

Figure 3.19 shows liquid film thicknesses for the runs where annular flow is observed at the outlet of the heated test section, for various mass fluxes. Calculations are made by considering that the entrainment is negligible, i.e. that all the liquid is flowing at the wall. Further analysis in Chapter 4 will show that droplet entrainement can be neglected for most of flow parameter combinations. Geometrical considerations allow to write a very simple expression of the film thickness δ:

$$\delta = \frac{D}{2} \cdot (1 - \sqrt{\alpha}) \tag{3.2}$$

Since the film thickness only depends on the void fraction when considering annular flow without entrainment, the observations on experimental values are the same as in the previous section for void fraction:
– at high mass fluxes, film thicknesses are more important for $G = 400$ kg.s^{-1}.m^{-2} than for $G = 200$ kg.s^{-1}.m^{-2}. However, for flow rates corresponding to transition and laminar flows, a decrease in the mass flux induces a increase in the liquid film thickness;
– for moderate values of the vapor quality ($0.13 < x < 0.25$), the difference in the film thickness between 1-g and μ-g is hardly quantifiable. However, for high vapor qualities and whatever the mass flux is, the higher level of void fraction in microgravity lead to smaller liquid film thicknesses in μ-g compared to normal gravity, and low mass fluxes seem to be less impacted by the changes in the gravity level.

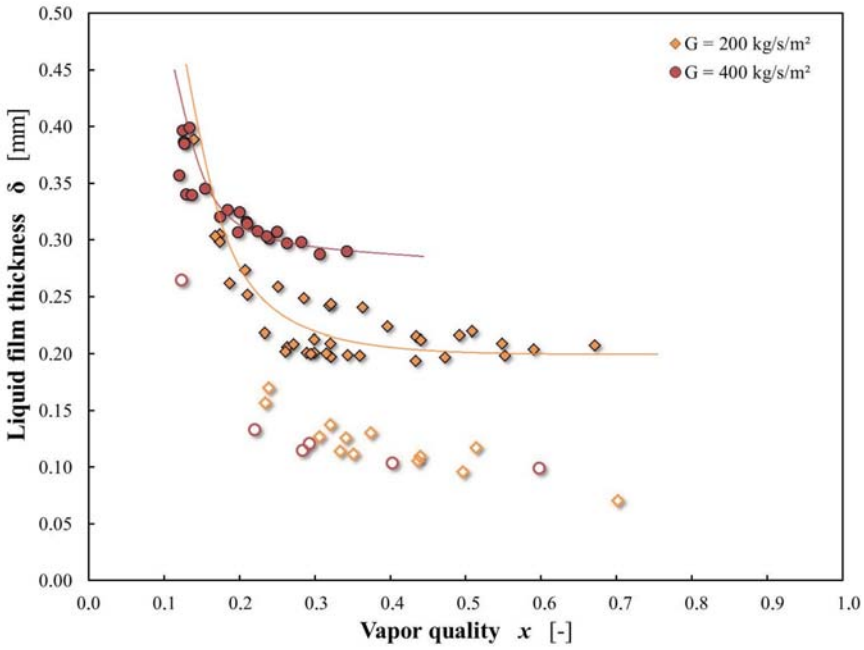

(a) Turbulent flow: $G = 200$ kg.s^{-1}.m^{-2} and $G = 400$ kg.s^{-1}.m^{-2}

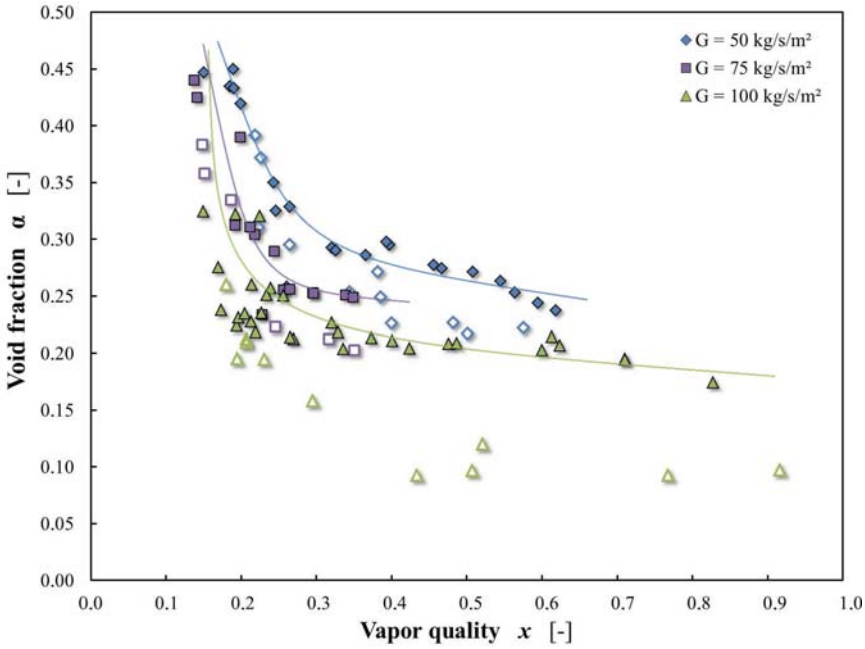

(b) Transition flow: $G = 100$ kg.s^{-1}.m^{-2} - laminar flow: $G = 50$ kg.s^{-1}.m^{-2} and $G = 75$ kg.s^{-1}.m^{-2}

FIGURE 3.19: Liquid film thickness according to vapor quality at the outlet of the heated test section, for various mass fluxes, in 1-g (closed symbols, lab tests 2012 and 2014, PFC 2014) and μ-g (open symbols, PFC 2012 and 2014)

Plotting δ in annular flow enables to better highlight the difference between normal gravity and microgravity situations for saturated conditions. However, these data correspond to important uncertainties that can be calculated with Equation (2.11). Figure 3.20 presents the film thickness measurements at $G = 200$ kg.s^{-1}.m^{-2} with error bars on δ and x. In annular flow, the error on the vapor quality is small (the maximal error on x is of 3% for vapor qualities higher than 0.25), but on this range the error on the

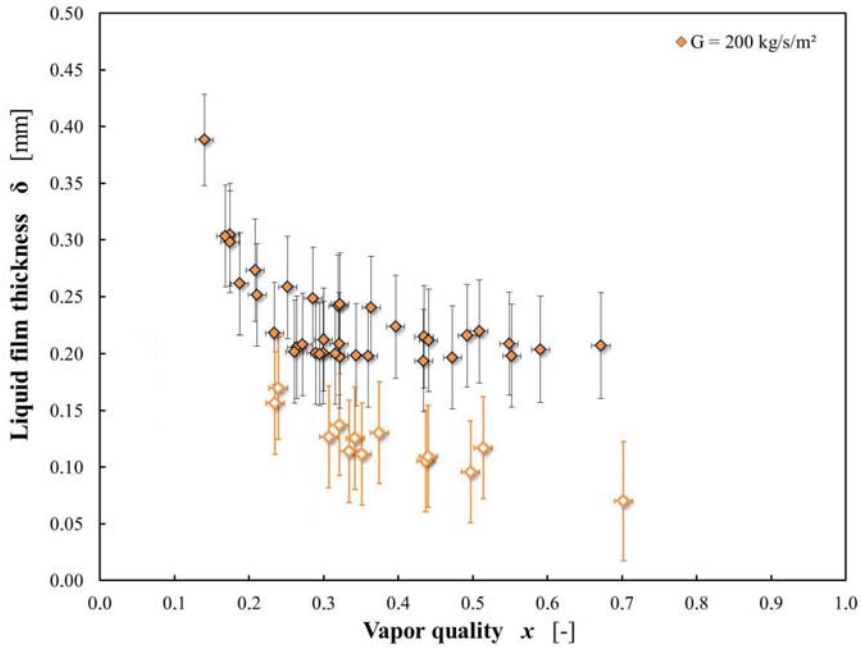

FIGURE 3.20: Liquid film thickness according to vapor quality with experimental error bars, for $G = 200$ kg.s^{-1}.m^{-2}, in 1-g (closed symbols, lab tests 2012 and 2014, PFC 2014) and μ-g (open symbols, PFC 2012 and 2014)

void fraction, and therefore on the film thickness that is a function of $-\sqrt{\alpha}$, is very important: the uncertainty ranges from $\pm$ 10% for experiments near the transition from slug flow to $\pm$ 90% at very high qualities. For example, for a film thickness $\delta = 60$ μm, the accuracy on the measurements is $\pm$ 55 μm.

The lack of precision on δ can induce small variations in the values that are presented in the previous graphics, but it cannot explain the smaller film thicknesses in μ-g by itself: even if it is difficult to precisely quantify the difference of δ between the two gravity levels, experimental data show that this difference is significant.

3.3 Pressure drops and shear stresses

Differential pressure drop measurements are performed along an adiabatic section just at the outlet of the sapphire tube. Temperature, vapor quality and void fraction are considered to be constant along this tube and equal to their values at the outlet of the heated part (corresponding to the location of the outlet void fraction probe). For the parabolic flight campaign that provided noisy measurements of capacitance, the actual void fraction was estimated using the experimental curves from previous section, which allowed to process all pressure drop measurements and add experimental points.

The following section presents the results on total pressure drop both under normal gravity and microgravity conditions. Special attention is paid to the investigation of wall shear stress in subcooled and saturated conditions, with error bars to characterise the uncertainty in the wall friction. For the specific case of annular flow, interfacial shear stress data are also discussed. Existing microgravity datasets do not include interfacial shear stress measurements in flow boiling; thus, it was not possible to draw any comparison.

3.3.1 Total pressure drop

For an upward flow in an adiabatic section, the total pressure drop along the tube can be written as the sum of a frictional term and a gravitational term (Equation (2.17)). The gravitational term can be neglected in microgravity but it is dominant in normal gravity, which induces important quantitative differences in the pressure drops between the two gravity levels. Figures 3.21 and 3.22 present the decomposition of the total pressure drop along the adiabatic section at low and high mass fluxes.

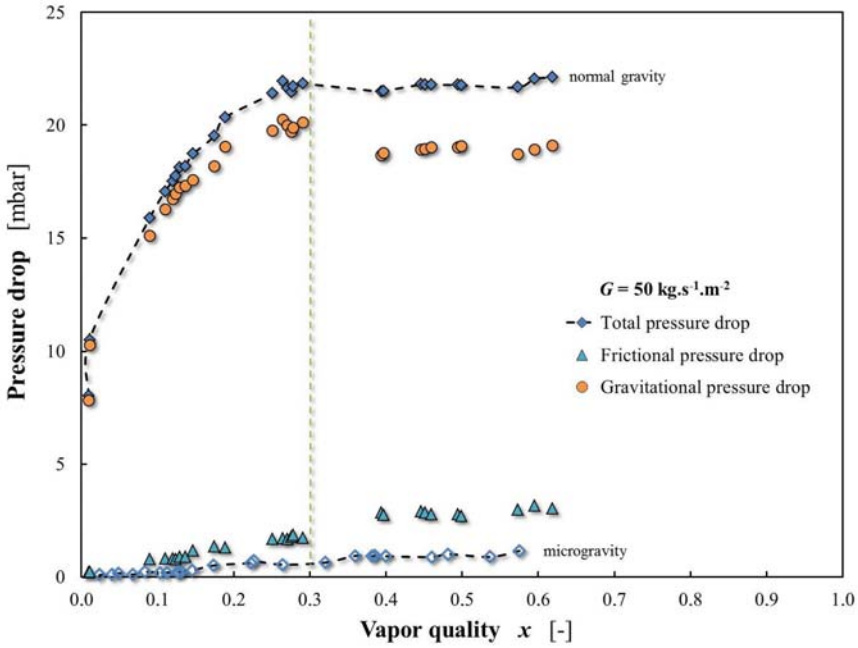

FIGURE 3.21: Total pressure drop decomposition, for $G = 50$ kg.s^{-1}.m^{-2}, in 1-g (closed symbols, lab tests 2014, PFC 2013 and 2014) and μ-g (open symbols, PFC 2013 and 2014)

Figure 3.21 shows the total pressure drop (Δp_{tot}) along the adiabatic section according to the vapor quality for $G = 50$ kg.s^{-1}.m^{-2}, in 1-g and μ-g, with the respective contributions of the friction component and the hydrostatic component. In microgravity, the total pressure drop that is plotted directly corresponds to the frictional pressure drop. The general trend of the curve corresponds to Δp_{tot} increasing with x until it reaches a saturation level at high vapor quality.

In normal gravity, at low and moderate vapor qualities ($x < 0.3$), the total pressure gradient is mostly due to the gravitational pressure loss that represents about 95% of Δp_{tot} against 5% for the frictional pressure drop, both increasing with x. However, at high vapor quality ($x > 0.3$), the pressure drops due to frictional and hydrostatic components both reach steady values. On this range of x that corresponds to annular flows, the contribution of the frictional pressure drop is still significantly lower than the one of the gravitational term, but it amounts to $\simeq$ 13% of Δp_{tot} (against 87% for the hydrostatic pressure loss).

In microgravity, the frictional pressure drop (and therefore the total pressure drop) evolves in the same way than in normal gravity. Nevertheless, a significant difference can be observed between the two gravity levels, with smaller frictional pressure drops in μ-g compared with 1-g. Further details on the frictional pressure drops are provided thereafter.

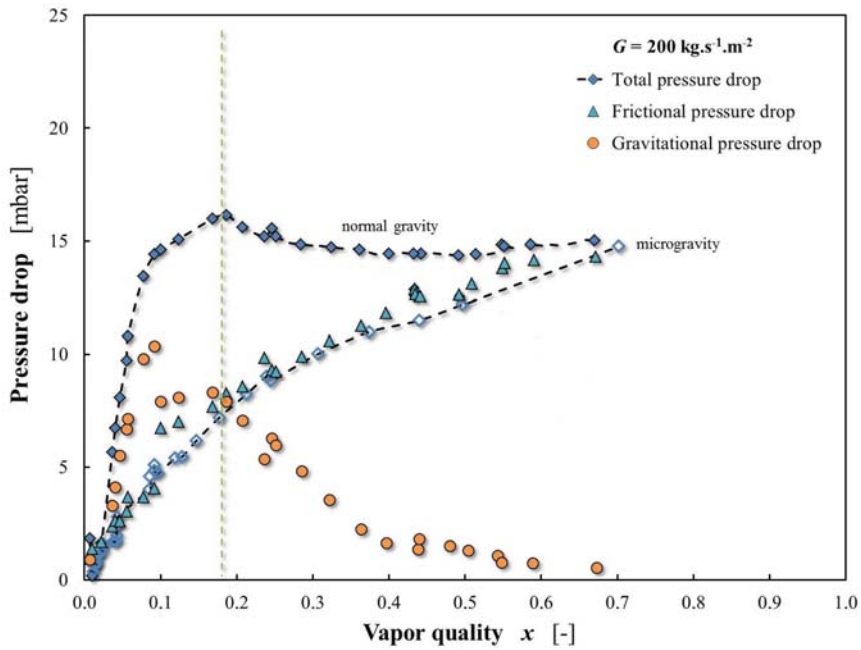

FIGURE 3.22: Total pressure drop decomposition, for $G = 200$ kg.s^{-1}.m^{-2}, in 1-g (closed symbols, lab tests 2012 and 2014, PFC 2013 and 2014) and μ-g (open symbols, PFC 2012, 2013 and 2014)

Figure 3.22 shows the total pressure drop (Δp_{tot}) along the adiabatic section according to the vapor quality for $G = 200$ kg.s^{-1}.m^{-2}, in 1-g and μ-g, with the respective contributions of the friction component and the hydrostatic component.

In normal gravity, the total pressure drop increases with the vapor quality until it reaches a maximum around $x \simeq 0.2$. Then, it slighly decreases and seems to tend towards a steady value at very high vapor quality. At low vapor qualities ($x < 0.05$), the flow is mostly driven by the gravitational term that represents 95% of Δp_{tot}. At moderate

vapor qualities ($0.05 < x < 0.2$), the rate of growth of the hydrostatic pressure drop decreases and the contribution of the frictional pressure drop increases to 46-48% of Δp_{tot}. Finally, for high vapor qualities ($x > 0.2$), the contribution of the hydrostatic component decreases until it becomes negligible compared to the frictional term, at very high vapor quality: for $x > 0.5$, the influence of the gravity is very small and the flow is mostly driven by the wall shear stress, which is further investigated thereafter.

In microgravity, the frictional pressure drop (and therefore the total pressure drop) increases with the vapor quality. However, since dry-out issues and vapor qualities higher than 0.7 are not studied in this thesis, no hypothesis on potential asymptotic behaviours has been validated. At this mass flux ($G = 200$ kg.s^{-1}.m^{-2}), the frictional pressure drops are almost the same under normal and microgravity conditions.

3.3.2 Wall shear stress

Characterising the wall shear stress through the frictional pressure drops is necessary to correctly describe boiling mechanisms. Figure 3.23 presents wall shear stress data under normal gravity and microgravity conditions from all lab and parabolic flight campaigns, according to vapor quality and classified by mass flux (shear stress scales are different for turbulent flows and laminar flows).

General trend: the general look of the wall shear stress curves is the same for all mass fluxes and gravity levels: as can be seen in the two figures, the wall shear stress depicts a growing trend with vapor quality, with a decrease in the rate of growth at high x, which seems to lead to a saturation at very high qualities. Nevertheless, significant quantitative differences can be observed when the mass flux or the gravity level is varied.

Influence of mass flux: whatever the gravity level is, an increase in the mass flux corresponds to a significant increase of the wall shear stress. Indeed, increasing the mass velocity results in a high flow inertia, which increases frictional pressure drops. For example, the wall shear stress at $G = 200$ kg.s^{-1}.m^{-2} represents 40% to 50% of the wall shear stress at $G = 400$ kg.s^{-1}.m^{-2}. The same difference is observed between $G = 50$ kg.s^{-1}.m^{-2} and $G = 100$ kg.s^{-1}.m^{-2}.

Influence of gravity level: turbulent flows are presented in Figure 3.23(a) for $G = 200$ and 400 kg.s^{-1}.m^{-2}. Very few points are available in microgravity for the highest investigated mass flux, and none of them was acquired at high vapor quality. 1-g data are nonetheless provided for comparison with lower mass flux. It is difficult to draw a comparison between different experiments at low vapor qualities, mostly because of the uncertainty in x. At higher qualities ($x > 0.20$), this is the uncertainty in the wall shear stress itself (Table 2.7) that prevents from confirming the influence of the gravity level: the wall shear stress seems to be slightly lower in μ-g than in 1-g, but this difference is not significant.

By contrast, the influence of the gravity level at low mass fluxes is clear (Figure 3.23(b)): the wall shear stress is significantly lower under microgravity conditions for $G = 50$, 75 and 100 kg.s^{-1}.m^{-2}. Another observation can be made for these mass fluxes: there seems to be a change in the rate of growth of the wall shear stress for the three mass fluxes and the two levels of gravity around $x \simeq 0.3$. For vapor qualities higher than 30%, the frictional pressure drops tend to increase slower than for low and moderate x, or even reach an almost steady value (for $G = 50$ kg.s^{-1}.m^{-2}); this change may be explained by a change in the flow pattern with a transition from wavy annular flow to

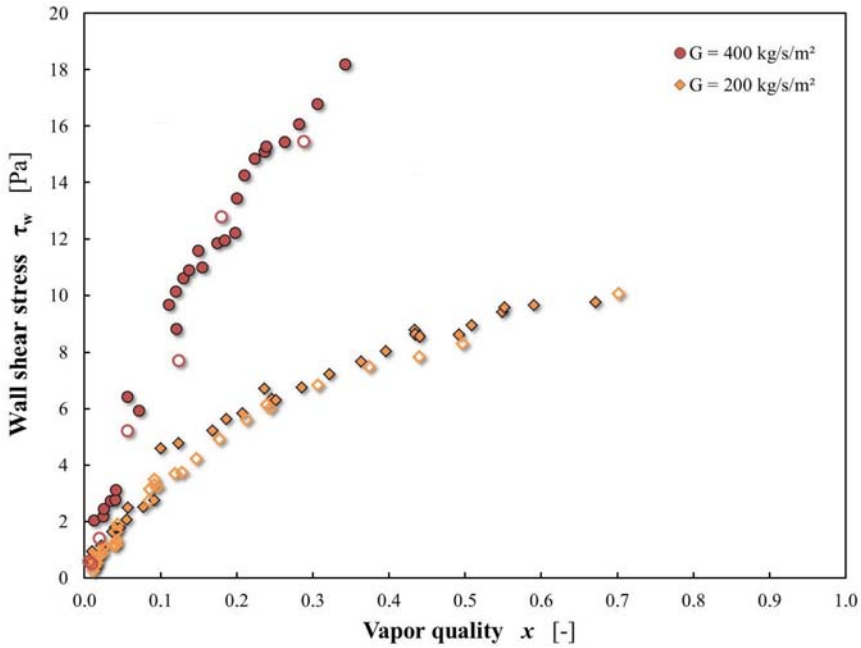

(a) Turbulent flow: $G = 200$ kg.s^{-1}.m^{-2} and $G = 400$ kg.s^{-1}.m^{-2}

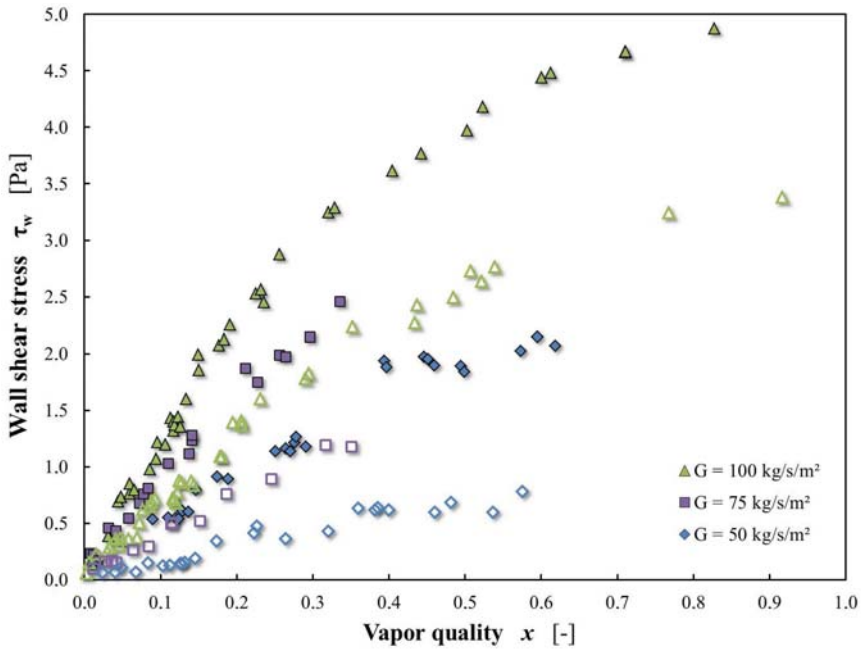

(b) Transition flow: $G = 100$ kg.s^{-1}.m^{-2} - laminar flow: $G = 50$ kg.s^{-1}.m^{-2} and $G = 75$ kg.s^{-1}.m^{-2}

FIGURE 3.23: Wall shear stress according to vapor quality on an adiabatic section, for various mass fluxes, in 1-g (closed symbols, lab tests 2012 and 2014, PFC 2013 and 2014) and μ-g (open symbols, PFC 2012, 2013 and 2014)

smooth annular flow, which can hardly be confirmed with flow visualisations given the restricted field of view of the camera and the strong evolution of flow pattern along the tube. Table 3.1 shows the averaged difference in the wall shear stress between normal gravity and microgravity according to the vapor quality.

	Low and moderate qualities $x < 0.3$	**High qualities** $x > 0.3$
G = **100 kg.s^{-1}.m^{-2}**	- 38%	- 30%
G = **75 kg.s^{-1}.m^{-2}**	- 50%	- 45%
G = **50 kg.s^{-1}.m^{-2}**	- 66%	- 63%

TABLE 3.1: Averaged difference in the wall shear stress in μ-g compared to 1-g for moderate and low mass fluxes

According to Table 3.1 and Figure 3.23(b), flows at lower mass fluxes are more influenced by the gravity level: the wall shear stress in microgravity represents 34% to 37% of the wall shear stress in normal gravity at $G = 50$ kg.s^{-1}.m^{-2} (i.e. a difference higher than 60%) while the difference between the two gravity levels only ranges from 30% to 38% for $G = 100$ kg.s^{-1}.m^{-2}.

Experimental uncertainty in the wall shear stress: the data presented in Figure 3.23 were acquired during various measurement campaigns with slightly different measuring systems. Thus, a summary of the wall shear stress data at $G = 100$ kg.s^{-1}.m^{-2} is provided in Figure 3.24 with error bars that take into account the different precisions on the void fraction and pressure drop measurements. Typical uncertainties in the vapor quality have not been plotted here since they were given in previous sections.

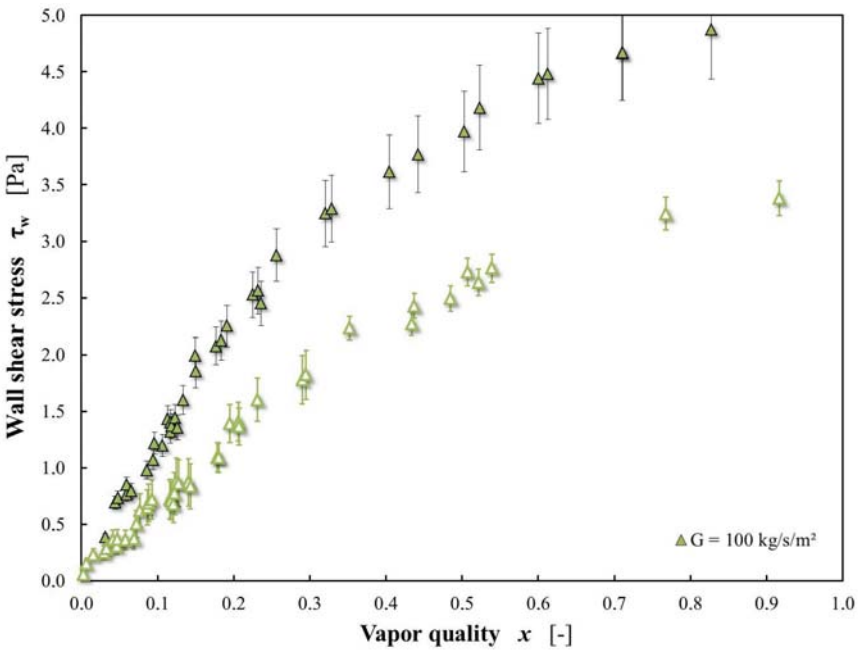

FIGURE 3.24: Wall shear stress according to vapor quality with experimental error bars, for $G = 100$ kg.s^{-1}.m^{-2}, in 1-g (closed symbols, lab tests 2012 and 2014, PFC 2013 and 2014) and μ-g (open symbols, PFC 2012, 2013 and 2014)

In microgravity, the void fraction is not needed to calculate τ_w, only the differential pressure data are used. Therefore, there is a lack of precision on the wall shear stress at low and moderate qualities ($\delta\tau_w \simeq \pm$ 20-30% because of small pressure drop measurements) while the uncertainty is rather small at high vapor qualities for higher measured pressure drops ($\simeq 5\%$). In normal gravity, the void fraction is necessary to substract the gravitational term from the total pressure gradient, which leads to higher experimental

errors; at low and moderate x, the precision on α is rather good, but small pressure drops make the error on the wall shear stress amounts to approximately 7-8%, whereas the lack of precision on the void fraction at high x leads to an uncertainty of $\pm$ 10-15% in higher values of τ_w.

According to these error bars, the difference of wall shear stress between 1-g and μ-g is significant for moderate and low mass fluxes while they do not allow to conclude on the influence of the gravity level for high mass fluxes.

Wall shear stress and flow patterns: Figure 3.25 presents wall shear stress data in 1-g and μ-g for $G = 200$ and 50 kg.s^{-1}.m^{-2} with corresponding flow patterns. As can be seen, the limit value $x \simeq 0.3$ that indicates a change in the rate of growth of the wall shear stress at low mass fluxes corresponds to annular flows. However, the transition between slug and annular flows occurs at lower quality ($x \simeq 0.13$). Since the current classification regroups wavy and smooth annular flows, a transition between these two regimes at $x \simeq 0.13$ is possible and might explain the variations in the wall friction.

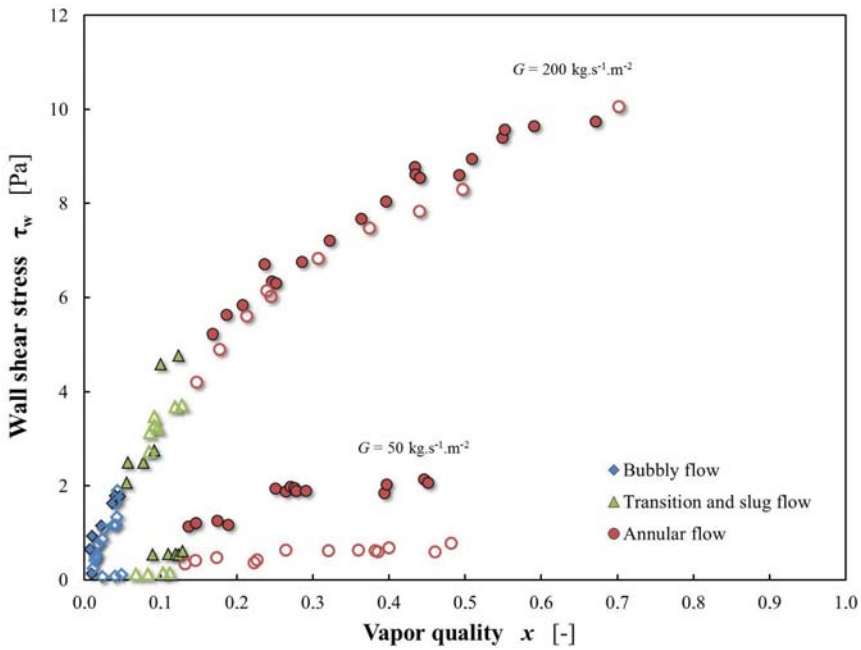

FIGURE 3.25: Wall shear stress according to vapor quality and flow patterns, for $G = 50$ and 200 kg.s^{-1}.m^{-2}, in 1-g (closed symbols, lab tests 2012 and 2014, PFC 2013 and 2014) and μ-g (open symbols, PFC 2012, 2013 and 2014)

3.3.3 Interfacial shear stress

At high quality, where annular flow is observed, the liquid film thickness and its structure are controlled by wall and interfacial shear stresses. It is therefore very important to determine τ_i. It can be deduced from the momentum balance on the vapor phase (Equation (1.26), that can be written by neglecting droplet entrainement in a first approximation. The impact of liquid entrainement will be discussed in the next chapter.

Figure 3.26 presents interfacial shear stress data under normal gravity and microgravity conditions from all lab and parabolic flight campaigns, according to vapor quality in saturated annular flow regimes and classified by mass flux.

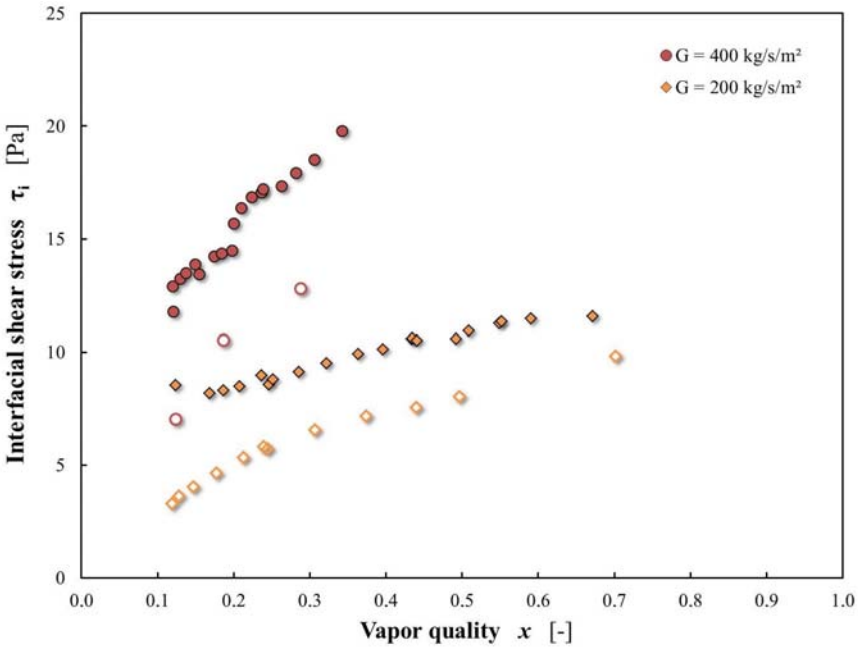

(a) Turbulent flow: $G = 200$ kg.s^{-1}.m^{-2} and $G = 400$ kg.s^{-1}.m^{-2}

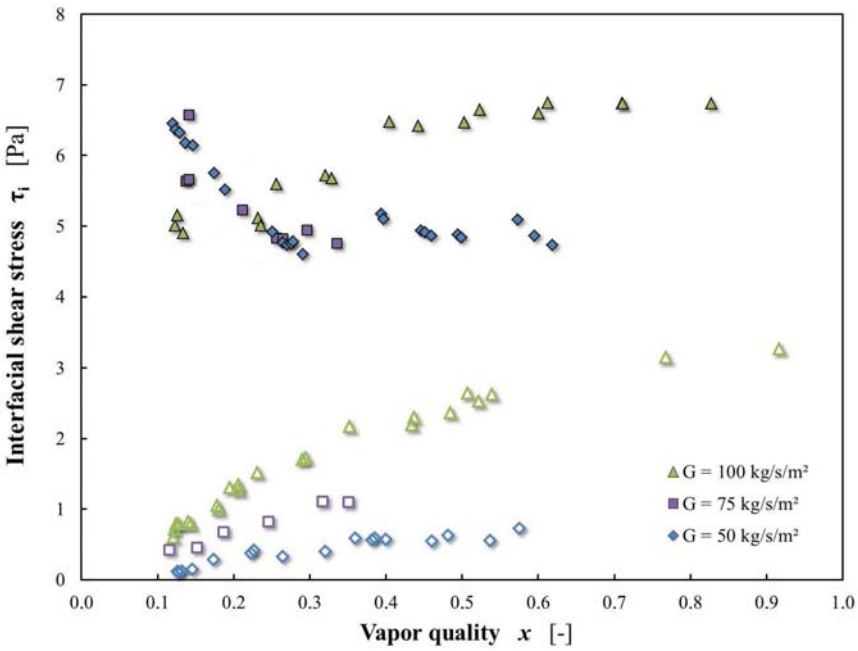

(b) Transition flow: $G = 100$ kg.s^{-1}.m^{-2} - laminar flow: $G = 50$ kg.s^{-1}.m^{-2} and $G = 75$ kg.s^{-1}.m^{-2}

FIGURE 3.26: Interfacial shear stress according to vapor quality on an adiabatic section, for various mass fluxes, in 1-g (closed symbols, lab tests 2012 and 2014, PFC 2013 and 2014) and μ-g (open symbols, PFC 2012, 2013 and 2014)

In microgravity, combining momentum balance equations for liquid and vapor yields $\tau_w.\sqrt{\alpha} = \tau_i$. Since the wall shear stress and the void fraction both are strong increasing functions of the vapor quality, the interfacial shear stress also depicts a growing trend with x in μ-g, whatever the mass flux is. At very high qualities, an asymptotic behaviour is observed: the interfacial friction tends to the wall friction (since α is close to one).

However, in normal gravity, the interfacial shear stress has to compensate both gravity and wall shear stress. A gravitational term is added to the calculation of τ_i in 1-g compared to the expression in μ-g. For moderate and high mass fluxes (G = 200 and 400 kg.s^{-1}.m^{-2} from Figure 3.26(a) and G = 100 kg.s^{-1}.m^{-2} from Figure 3.26(b)) corresponding to transition and turbulent flows, the interfacial shear stress increases when x increases. But at lower mass fluxes (G = 50 and 75 kg.s^{-1}.m^{-2} from Figure 3.26(b)), a decrease in the interfacial friction is observed with an increasing vapor quality; a saturation level seems to be reached for qualities higher than 0.5.

Nevertheless, the interfacial friction factor is significantly smaller under microgravity conditions compared to normal gravity, regardless of the evolution of τ_i in 1-g.

The data presented in Figure 3.26 depend on both the pressure drop and the void fraction measurements, that present non-negligible uncertainties. Thus, a summary of the interfacial shear stress data at G = 100 kg.s^{-1}.m^{-2} is provided in Figure 3.27 with error bars that take into account these uncertainties.

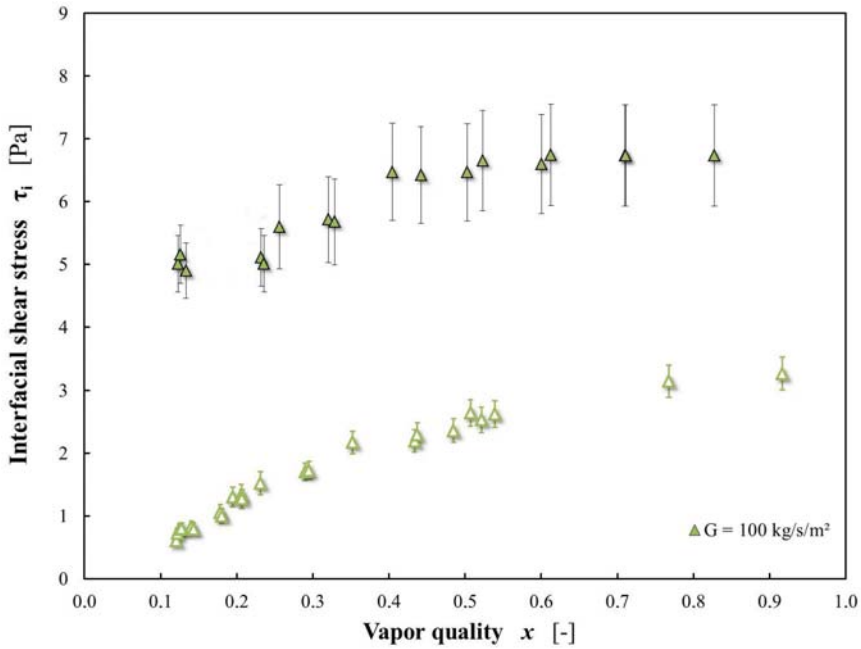

FIGURE 3.27: Interfacial shear stress according to vapor quality with experimental error bars, for G = 100 kg.s^{-1}.m^{-2}, in 1-g (closed symbols, lab tests 2012 and 2014, PFC 2013 and 2014) and μ-g (open symbols, PFC 2012, 2013 and 2014)

Interfacial data are reported for annular flow, thus for high vapor quality and high void fraction. Consequently, higher pressure drop measurements allow to obtain a rather good accuracy on the wall shear stress data. Combined with the experimental error on void fraction measurements, the uncertainty in τ_i ranges from 6% to 10% in microgravity. However, with the addition of the gravitational term that is a strong function of α in 1-g, the accuracy is worse in normal gravity: depending on the void fraction, error bars at $\pm$ 8 to 15% have been plotted.

Even with this lack of precision, the difference between normal gravity and microgravity on the interfacial shear stress is significant, regardless of the range of mass flux.

3.4 Heat transfer coefficient

Local measurements of the outer sapphire wall temperature at various locations of the heated test section are performed in order to characterise heat transfers mechanisms under normal gravity and microgravity conditions. As for the flow patterns, void fraction and shear stresses data, the vapor quality x is chosen to describe the evolution of heat transfer coefficients. A total of 270 points in μ-g and 350 points in 1-g is discussed thereafter.

The following section presents the experimental results on heat transfer coefficients both under normal gravity and microgravity conditions. The influence of the mass flux and wall heat flux are also investigated to determine the respective contributions of nucleate boiling and convective boiling in heat transfers. Error bars are plotted on some graphics to illustrate the uncertainty in the heat transfer coefficient. In addition, comparisons are drawn with experimental trends highlighted in existing microgravity datasets.

3.4.1 Characterisation of heat transfer coefficient measurements

The calculation of the heat transfer coefficient is presented in the data reduction section of Chapter 2. As demonstrated, h depends on the sapphire tube wall temperature, on the bulk temperature and on the wall heat flux q.

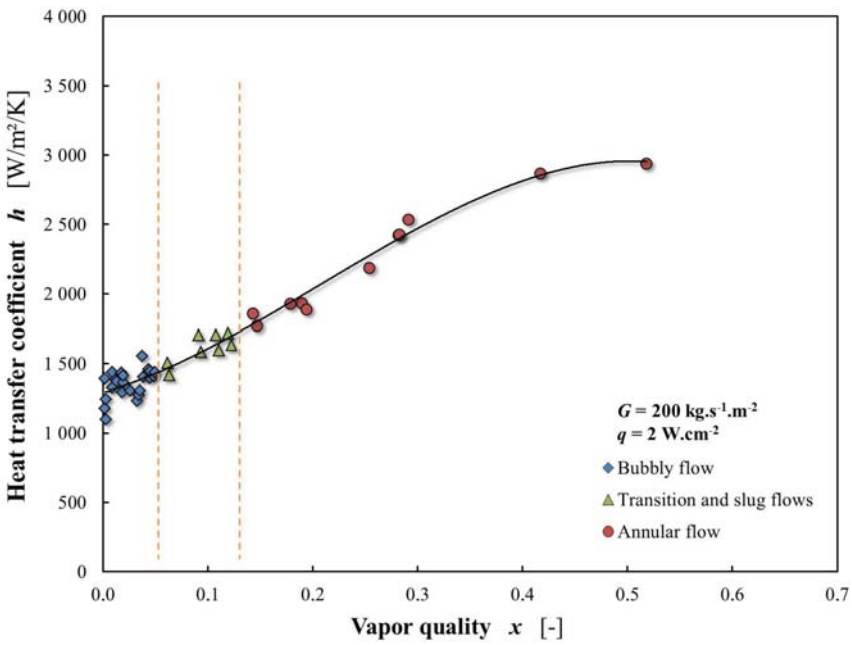

FIGURE 3.28: Heat transfer coefficient according to vapor quality and flow patterns, for $G = 200$ kg.s^{-1}.m^{-2}, in 1-g (lab tests 2012, PFC 2013 and 2014)

As previously mentioned, heat transfer coefficient data are plotted according to the vapor quality calculated at a distance z from the inlet of the heated sapphire tube, which corresponds to the location of the considered Pt probe. Since the vapor quality determines the flow pattern, various behaviours can be observed depending on x, due to completely different flow structures, as can be seen in Figure 3.28 for $G = 200$ kg.s^{-1}.m^{-2} and $q = 2$ W.cm^{-2}. In the following sections, it will be referred to subcooled regimes and saturated regimes: for clarity purposes, subcooled regimes correspond to bubbly flows

and transition / slug flows that occur at low and moderate qualities, while saturated regimes are considered to be annular flow at moderate and high qualities.

Experimental points are plotted in Figure 3.29 with error bars to illustrate the uncertainty in the heat transfer coefficient measurements. Since the calculations of h are the same whatever the gravity level is, only 1-g data are presented in this graphic. Examples of uncertainties are provided for $G = 200$ kg.s^{-1}.m^{-2} at $q = 2$ W.cm^{-2} and for $G = 50$ kg.s^{-1}.m^{-2} at $q = 1$ W.cm^{-2}.

The uncertainty in the heat transfer coefficient depends on the precision on the wall heat flux and the accuracy on the temperature measurements. Errors on the heat flux and liquid temperature are negligible compared to the uncertainty in the measurements of the outer wall temperature T_{ow} due to mechanical contact issues. An error of $\pm$ 2°C have been used for the error bars presented here, which corresponds to the maximal difference recorded between two probes diametrically opposed at the same distance z from the inlet of the sapphire tube.

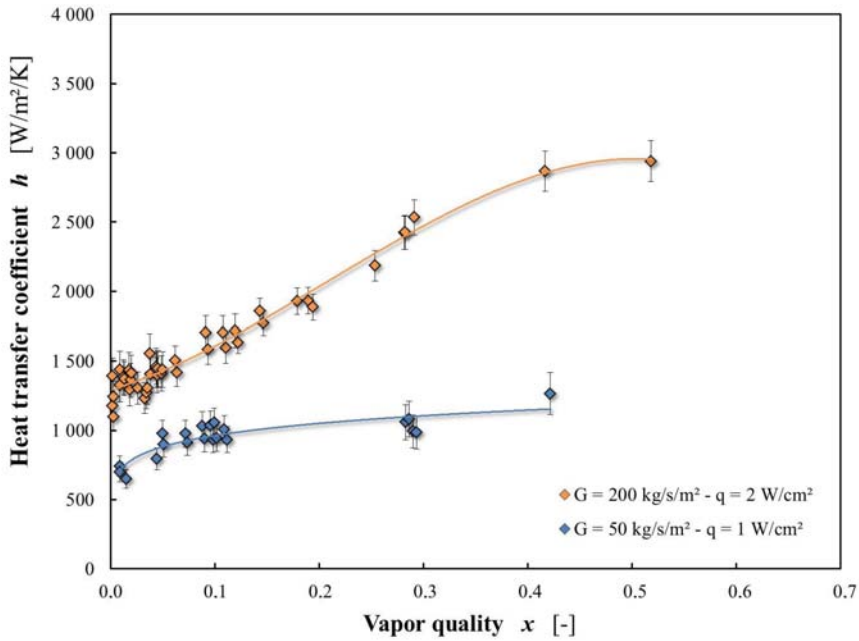

FIGURE 3.29: Heat transfer coefficient according to vapor quality with experimental error bars, for $G = 200$ and 50 kg.s^{-1}.m^{-2}, in 1-g (lab tests 2012, PFC 2013 and 2014)

The uncertainty in the heat transfer coefficient is therefore higher for subcooled regimes with smaller external wall temperature values, at fixed mass flux or wall heat flux (the error is $\pm$ 12% for $x < 0.1$ against $\pm$ 6% for $x > 0.3$ for $G = 50$ kg.s^{-1}.m^{-2} at $q = 1$ W.cm^{-2}). The uncertainty in h also slightly decreases as the wall heat flux increases (for example, for $G = 200$ kg.s^{-1}.m^{-2}, a increase of q from 1 to 2 W.cm^{-2} corresponds to a decrease in the error of 6,5% to 5.5%).

Heat transfer data are complicated to present in a single graphic since they exhibit various behaviours depending on the vapor quality x, the mass flux G and the wall heat flux q. Since CHF issues are not addressed, available heat fluxes are limited; they were categorised as follow in this study: high wall heat fluxes range from 3.5 to 3.8 W.cm^{-2}, moderate heat fluxes range from 1.9 to 2.1 W.cm^{-2} and low heat fluxes range from 0.9 to 1.1 W.cm^{-2}. Additional experiments were performed at $q \simeq 0.5$ W.cm^{-2} for the specific case of low mass fluxes.

3.4.2 Influence of mass flux

In the case of boiling experiments with BRASIL, the mass flux G is the flow parameter that affects the most strongly the heat transfer coefficient. In this section, the influence of G on h is investigated through 1-g data since a variation in the gravity level does not change the general trend of experimental curves. Thus, Figure 3.30 presents the evolution of h according to the vapor quality for various mass fluxes at $q = 2$ W.cm^{-2}, in 1-g. Trend curves are added to better visualise the evolution of h.

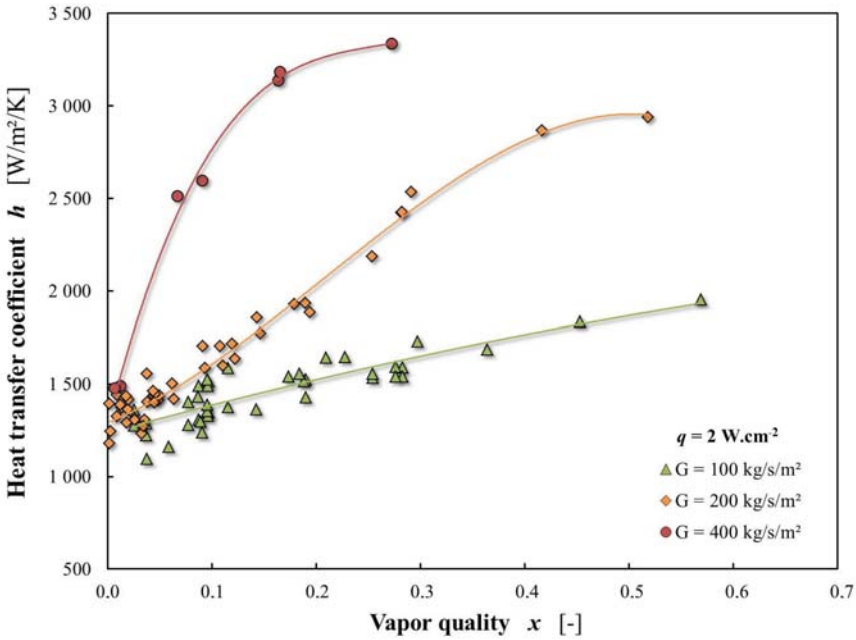

(a) $G = 400$, 200 and 100 kg.s^{-1}.m^{-2}

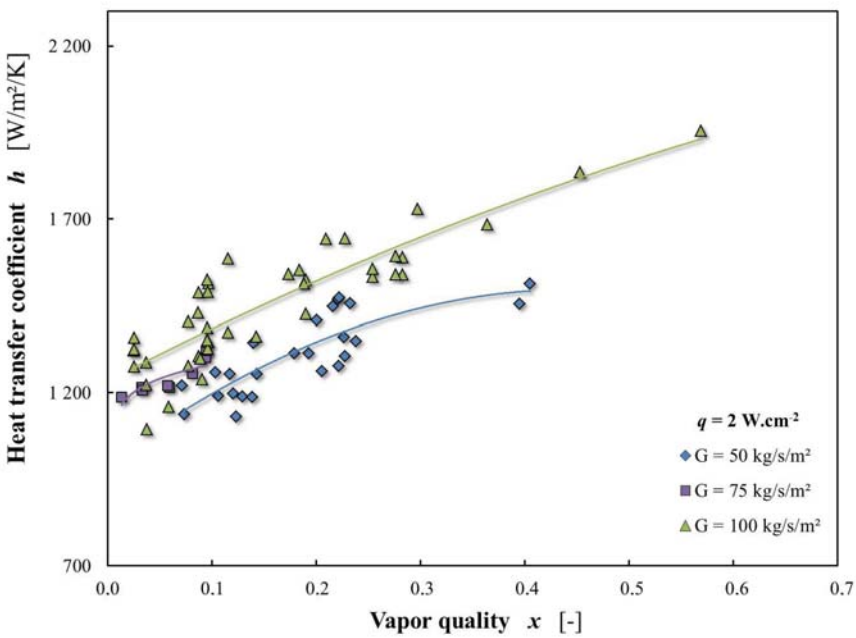

(b) $G = 100$, 75 and 50 kg.s^{-1}.m^{-2}

FIGURE 3.30: Influence of the mass flux on the heat transfer coefficient - heat transfer coefficient according to vapor quality, for various mass fluxes, in 1-g

As a first approximation, the graphics highlight the fact that the higher the mass flux, the larger the heat transfer coefficient. However, important disparities are observed between subcooled / saturated regimes and between high / low mass fluxes.

High mass fluxes are presented in Figure 3.30(a) with a transition flow at $G = 100$ kg.s^{-1}.m^{-2}. For very low vapor quality corresponding to bubbly flows, the heat transfer coefficient is almost independent of x and rather insensitive to the mass flux. This observation can be extended to transition and slug flows at low and moderate qualities (except for $G = 400$ kg.s^{-1}.m^{-2}). On these ranges of flow parameters corresponding to subcooled regimes, heat transfer mechanisms are dominated by nucleate boiling. On the opposite, the heat transfer coefficient sharply increases with x for moderate and high vapor qualities corresponding to annular flow. Moreover, the higher the mass flux, the larger the rate of growth. Convective boiling, that is promoted by higher mass fluxes, controls heat transfers in these conditions.

In Figure 3.30(b), at low mass fluxes, the respective contributions of nucleate boiling and convective boiling are more difficult to distinguish. The behaviour at low vapor quality is the same as for higher mass fluxes: the heat transfer coefficient is almost constant and quantitatively similar for the three presented mass fluxes; heat transfer mechanisms are still mostly controlled by the nucleation term. However, experimental points corresponding to annular flow do not exhibit a strong increase of h with x as for $G = 400$ and 200 kg.s^{-1}.m^{-2}. Especially at very low mass fluxes, the heat transfer coefficient only slightly increases with x in saturated regimes, which highlights a smaller contribution of convective boiling in heat transfer mechanisms.

3.4.3 Influence of wall heat flux

The effect of the wall heat flux on the heat transfer coefficient is presented in Figures 3.31, 3.32(a) and 3.32(b) for $G = 200$, 100 and 50 kg.s^{-1}.m^{-2}, corresponding to moderate / high, moderate and low mass fluxes, in normal gravity. Experimental points and trend curves for three different heat fluxes are plotted: $q = 1{,}2$ and 3.5 W.cm^{-2}. The same scales are used to illustrate h on the graphics.

The influence of the wall heat flux q on h is visible for all three mass fluxes: the higher the wall heat flux, the higher the heat transfer coefficient. However, significant differences in the evolution of h can be observed depending on G.

At $G = 200$ kg.s^{-1}.m^{-2}, the wall heat flux expecially affects the heat transfer coefficient in subcooled regimes corresponding to bubbly and transition flows in low vapor quality region. Then, as the vapor quality increases and the flow becomes annular, the influence of the wall heat flux on the heat transfer coefficient decreases and the trend curves tend to converge. A lack of experimental points at very high quality prevents from appreciating the actual behaviour for $x > 0.5$. Nevertheless, these observations highlight the fact that nucleate boiling is the dominant mode that drives heat transfer mechanisms in subcooled conditions; in saturated regimes, its contribution then gradually decreases as the vapor quality increases until it is suppressed, while convective boiling regime occurs.

At lower mass fluxes, the heat transfer coefficient is affected by the wall heat flux on the whole range of vapor qualities, as it can be seen from Figures 3.32(a) and 3.32(b). That indicates that the nucleate boiling contribution is still significant at high vapor quality.

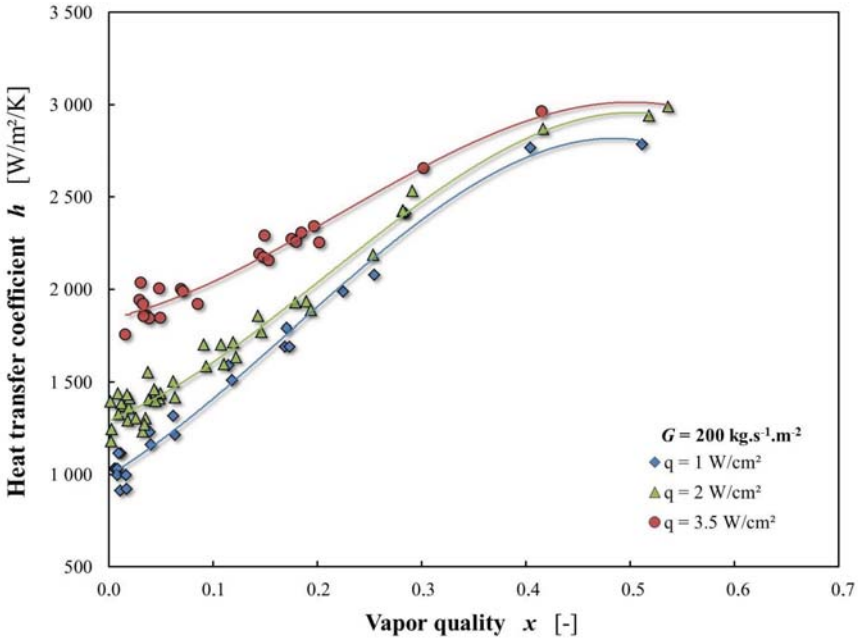

FIGURE 3.31: Influence of the wall heat flux on the heat transfer coefficient for $G = 200$ kg.s^{-1}.m^{-2}, in 1-g (lab tests 2012, PFC 2013 and 2014)

For $G = 100$ kg.s^{-1}.m^{-2}, subcooled flows are dominated by nucleate boiling as well. In saturated regimes, the heat transfer coefficient still slightly increases with the vapor quality, whatever the wall heat flux is, which means that convective boiling is still the dominant transfer mode even with a higher contribution of the nucleation term compared to high mass flux. As a result, h increases but the difference between different wall heat flux seems to be constant on the whole range of qualities.

For $G = 50$ kg.s^{-1}.m^{-2}, nucleate boiling seems to become the dominant mode in heat transfers for both the subcooled and the saturated regions: the influence of q on h is very significant for any vapor quality, and the heat transfer coefficient value is almost constant at moderate and high x, including annular flows at high qualities.

Table 3.2 summarises previous observations by indicating the respective contribution of nucleate boiling (NB and NBA in annular flow) and convective boiling (CB) in the heat transfer mechanisms in 1-g (the dominant mode is written in bold). The region that are affected by the wall heat flux are marked in red.

	Low x	**Moderate** x	**High** x
	$x < 0.13$	$0.13 < x < 0.25$	$x > 0.25$
$G = 200$, 400	**NB**	**CB**	**CB**
$G = 100$	**NB**	NB + **CB**	NBA + **CB**
$G = 50$, 75	**NB**	**NBA**	**NBA**

TABLE 3.2: Contributions of heat transfer modes depending on various flow parameters and influence of the wall heat flux on the heat transfer coefficient

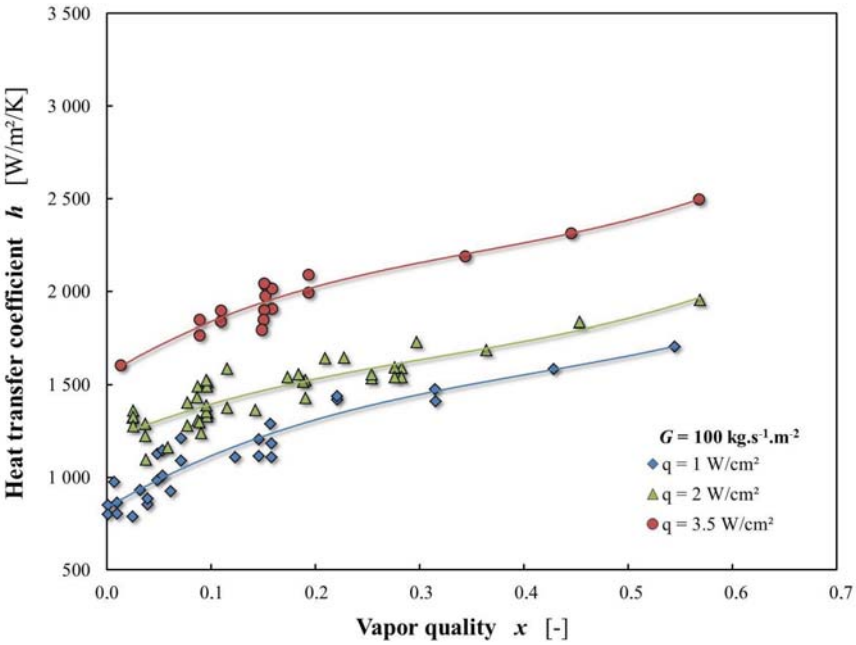

(a) $G = 100$ kg.s^{-1}.m^{-2}

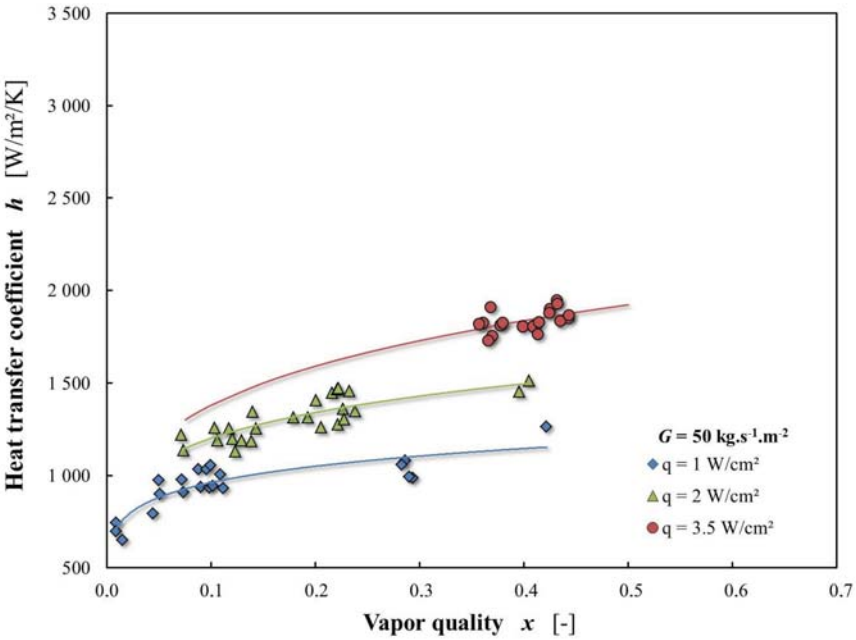

(b) $G = 50$ kg.s^{-1}.m^{-2}

FIGURE 3.32: Influence of the wall heat flux on the heat transfer coefficient for $G = 100$ and 50 kg.s^{-1}.m^{-2}, in 1-g (lab tests 2012, PFC 2013 and 2014)

3.4.4 Influence of gravity level

As for the other flow parameters, the gravity level affects the heat transfer coefficient in different ways depending on the flow features. Differences between 1-g and μ-g are discussed thereafter for various mass fluxes.

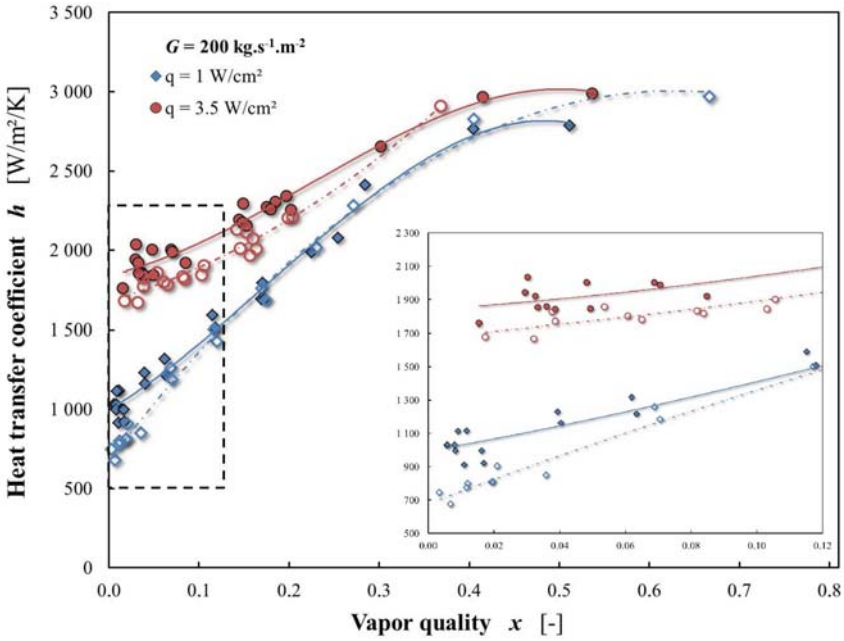

(a) $G = 200$ kg.s^{-1}.m^{-2}

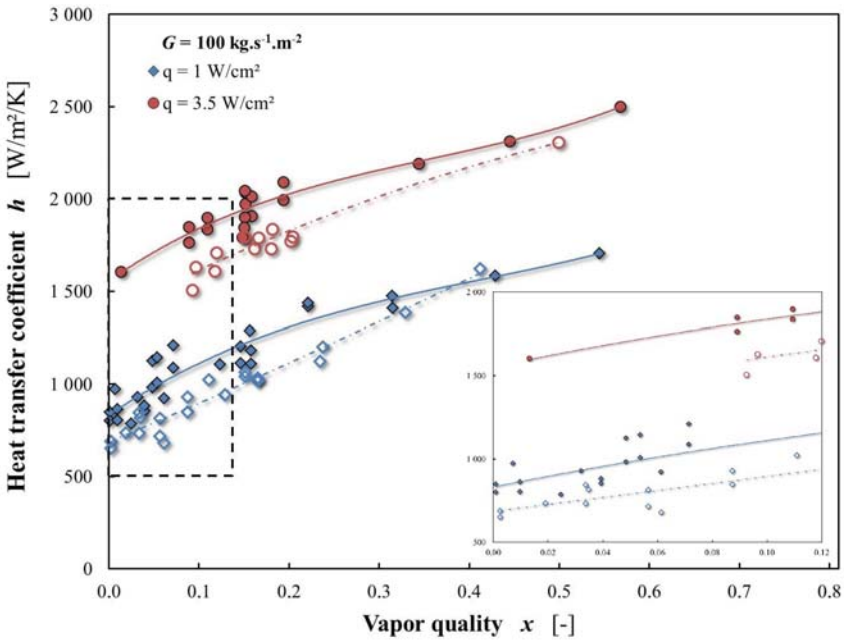

(b) $G = 100$ kg.s^{-1}.m^{-2}

FIGURE 3.33: Influence of the gravity level on the heat transfer coefficient for $G = 200$ and 100 kg.s^{-1}.m^{-2}, for two wall heat fluxes, in 1-g (closed symbols, lab tests 2012, PFC 2013 and 2014) and μ-g (open symbols, PFC 2012, 2013 and 2014)

Figures 3.33 and 3.34 present heat transfer coefficient data in 1-g (closed symbols and plain lines) and μ-g (open symbols and dotted lines) at two different wall heat fluxes (q = 1 and 3.5 W.cm^{-2}) for various mass fluxes G. A zoom on subcooled data is provided on each graphic.

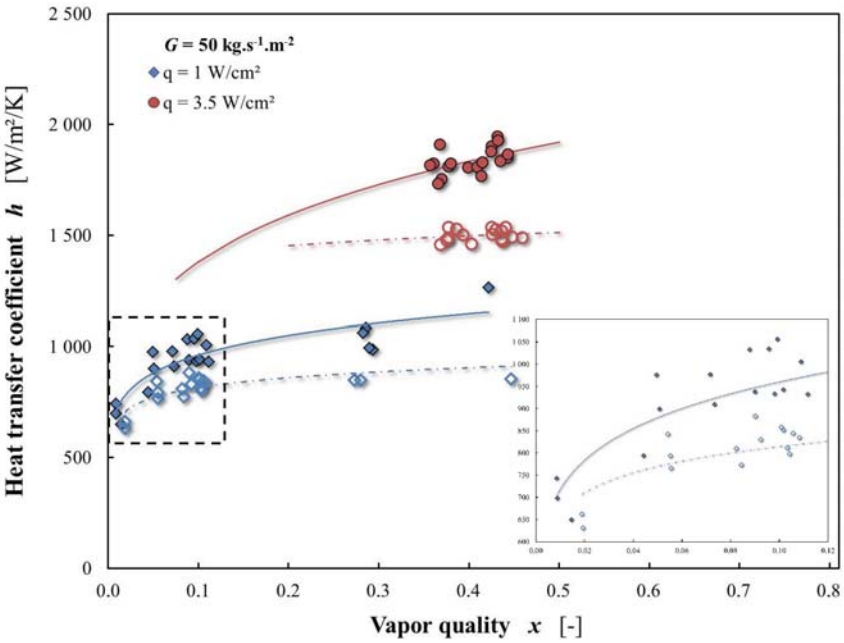

FIGURE 3.34: Influence of the gravity level on the heat transfer coefficient for G = 50 kg.s^{-1}.m^{-2}, for two wall heat fluxes, in 1-g (closed symbols, PFC 2013 and 2014) and μ-g (open symbols, PFC 2013 and 2014)

For G = 200 kg.s^{-1}.m^{-2}, subcooled regimes and saturated regimes are affected in different ways by the gravity level. In subcooled conditions, the heat transfer coefficient is systematically and significantly lower in μ-g than in 1-g, at any of the studied wall heat fluxes, while there is no obvious difference in h at high quality in saturated regimes. However, q seems to have an influence on the vapor quality that corresponds to a merging of the two gravity level curves: at low heat flux, the heat transfer coefficient values are already similar in 1-g and μ-g whereas the two trend curves only converge at high quality for high heat flux.

The trend curves are rather similar for G = 100 kg.s^{-1}.m^{-2}: at low vapor quality, a significant difference in the heat transfer coefficient can be observed between the two gravity levels, with smaller values of heat transfer coefficient h in microgravity, while no influence of the gravity can be noticed at very high quality in saturated regimes. Nevertheless, at moderate and high x where annular flows are first reported, the heat transfer coefficient is still higher in normal gravity than in microgravity: compared to higher mass flux, the transition between the region that is influenced by the gravity level and the one that is not occurs at higher quality, due to a more important contribution of the nucleate boiling on this range of x.

Heat transfers mechanisms are different at low mass fluxes, as shown in Figure 3.34: the heat transfer coefficient is almost constant on the whole range of vapor quality and the difference in h is therefore significant not only in subcooled conditions but for saturated regimes too; 1-g and μ-g curves do not converge. Contrary to higher values G, the influence of the gravity level on saturated regimes at this mass flux seems to be slightly less important at high heat flux.

Figure 3.35 presents trend curves of the ratio of the heat transfer coefficient in μ-g and 1-g in a qualitative form for an intermediate heat flux $q = 2$ W.cm^{-2} and for three mass fluxes according to the vapor quality.

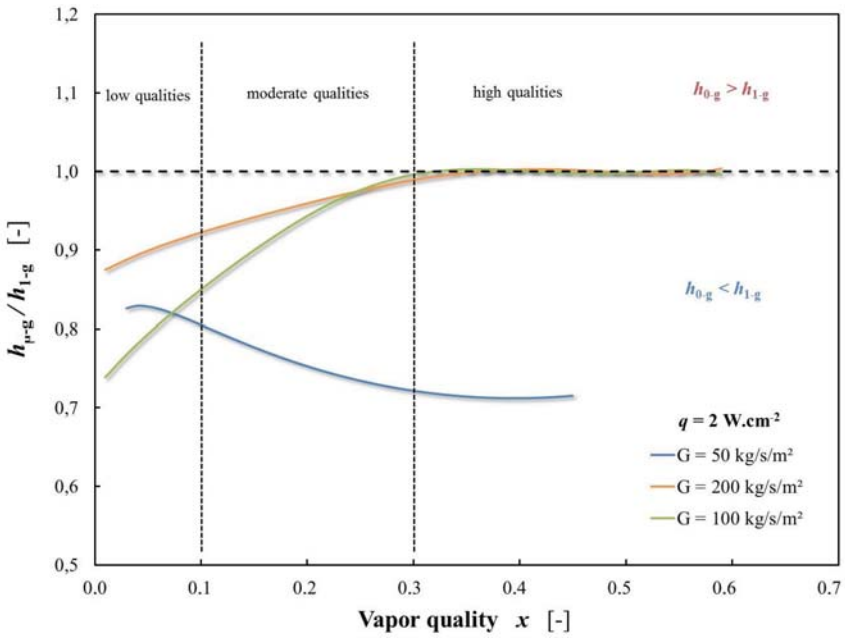

FIGURE 3.35: Ratio of the heat transfer coefficient in μ-g over the heat transfer coefficient in 1-g (trend curves) for $G = 200$, 100 and 50 kg.s^{-1}.m^{-2}, at $q = 2$ W.cm^{-2}

This graphic allows to see that the heat transfer coefficient is either smaller in μ-g or equal to the heat transfer coefficient in 1-g but never higher. For high and moderate G, h is 10 to 30% smaller at low vapor qualities; the difference then decreases as the vapor quality increases until no difference is visible for high vapor quality. However, on this range of subcooled regimes, the smaller the mass flux, the more influenced by the gravity level. At low mass flux, the heat transfer coefficient is still smaller in μ-g in subcooled conditions, but the difference between the two gravity levels increases with an increasing vapor quality; at high qualities, a constant difference of -30% in μ-g is reached.

Tables 3.3, 3.4 and 3.5 summarise the influence of the gravity level on the heat transfer coefficient depending on the heat flux and vapor quality for $G = 200$, 100 and 50 kg.s^{-1}.m^{-2} by indicating the mean difference in the value of $h_{\mu-g}$ compared to h_{1-g} in percentages on the considered range of vapor quality.

	Low x	**Moderate x**	**High x**
q **= 3.5 W.cm^{-2}**	-10%	-7%	-
q **= 2 W.cm^{-2}**	-10%	-5%	-
q **= 1 W.cm^{-2}**	-17%	-	-

TABLE 3.3: Influence of the gravity level on the heat transfer coefficient depending on the vapor quality and wall heat flux for $G = 200$ kg.s^{-1}.m^{-2} - mean difference in the value of $h_{\mu-g}$ compared to h_{1-g} [%]

Series at $G = 400$ and 75 kg.s^{-1}.m^{-2} have not been indicated here since they include less experimental points that for other values of G, and because they are similarly impacted

	Low x	**Moderate** x	**High** x
q **= 3.5 W.cm**$^{-2}$	-15%	-10%	-3%
q **= 2 W.cm**$^{-2}$	-20%	-8%	-
q **= 1 W.cm**$^{-2}$	-18	-6%	-

TABLE 3.4: Influence of the gravity level on the heat transfer coefficient depending on the vapor quality and wall heat flux for $G = 100$ kg.s^{-1}.m^{-2} - mean difference in the value of $h_{\mu-g}$ compared to h_{1-g} [%]

	Low x	**Moderate** x	**High** x
q **= 3.5 W.cm**$^{-2}$		-15%	-21%
q **= 2 W.cm**$^{-2}$	-18%	-23%	-28%
q **= 1 W.cm**$^{-2}$	-7%	-20%	-24%

TABLE 3.5: Influence of the gravity level on the heat transfer coefficient depending on the vapor quality and wall heat flux for $G = 50$ kg.s^{-1}.m^{-2} - mean difference in the value of $h_{\mu-g}$ compared to h_{1-g} [%]

by flow parameters: curves at $G = 200$ and 400 kg.s^{-1}.m^{-2} correspond to the same trends while data at $G = 75$ kg.s^{-1}.m^{-2} are very close from data at $G = 50$ kg.s^{-1}.m^{-2}.

3.4.5 Comparison with microgravity datasets

In available publications about boiling data in microgravity, authors mostly focus on the study of the evolution of heat transfer coefficient with the gravity level. The quality is chosen to describe the evolution of h. Two main datasets are used for comparison with BRASIL experimental data: data from ENEA (Italy) and data from the University of Kyushu (Japan).

ENEA data: Baltis et al. [2012] reported qualitative evolution of the heat transfer coefficient according to vapor quality by providing ratios $h_{\mu-g}$ over h_{1-g} for the MICROBO experiment with ENEA. Unfortunately, their experimental points cannot be plotted on the graphics displaying BRASIL data because the authors calculated a thermodynamical quality that does not characterise the actual fraction of vapor in subcooled regimes. Moreover, the dimensionless form they chose to present their results does not allow to appreciate the influence of the mass flux or heat flux on the heat transfer coefficient.

Figure 3.36 comes from the publication of Baltis et al. [2012]. The influence of the gravity level on the difference in the heat transfer coefficient between microgravity and normal gravity is presented according to the thermodynamical outlet vapor quality for various mass fluxes, in the 6mm tube. Wall heat flux settings are not indicated. Left graphic correspond to a thermocouple located near the inlet of the heated test section while the right one deals with measurements near the outlet of the tube.

For very low vapor qualities (near the entrance of the tube), heat transfer coefficients seem to be enhanced of up to 15% in microgravity compared to normal gravity, for $G < 200$ kg.s^{-1}.m^{-2}, which would be due, according to the authors, to the larger size of bubbles in μ-g. For higher mass fluxes, the heat transfer coefficient in microgravity either equals h in normal gravity or is slightly smaller. When increasing the vapor quality (near

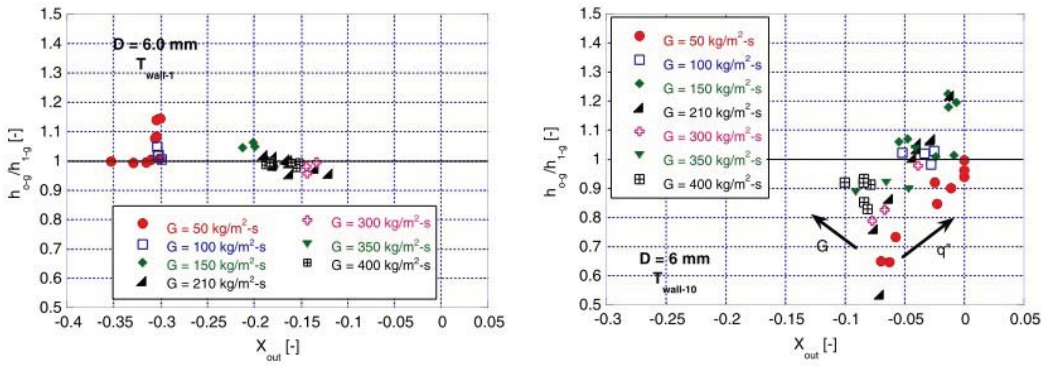

FIGURE 3.36: Ratio of heat transfer coefficients $h_{\mu-g}$ / h_{1-g} according to thermodynamical vapor quality at the outlet of the test section for various mass fluxes - (left) near the inlet of the tube, (right) near the outlet of the tube [Baltis et al., 2012]

the outlet of the tube, still in subcooled conditions), the influence of the gravity level on heat transfer mechanisms seems to change: the microgravity heat transfer coefficient, that is significantly smaller at low vapor quality compared to normal gravity, increases with x until it becomes higher than h in 1-g, up to 20%. According to the authors, the enhancement of h in microgravity corresponds to the transition from bubbly flow to intermittent flow. These data are in contradiction with BRASIL results that present heat transfer coefficients systematically smaller in μ-g than in 1-g in subcooled regimes. The influence of the mass flux on the difference between μ-g and 1-g is also not consistent between the two datasets.

Data from the University of Kyushu: Ohta and Baba [2013] recently published additional measurements of heat transfer coefficient with FC-72 in 4mm ID heated tube under microgravity conditions for very low mass fluxes $G = 40$, 60 and 150 kg.s^{-1}.m^{-2}, as presented in Figure 1.12. Quantitative values shown in this graphic are in good agreement with BRASIL experimental points. Figure 3.37 compare heat transfer coefficient in normal gravity and microgravity for IMFT data (at $q = 1$ W.cm^{-2} for $G = 50$ and 100 kg.s^{-1}.m^{-2}) and Ohta and Baba data (at $q = 0.86$ W.cm^{-2} for $G = 60$ and 150 kg.s^{-1}.m^{-2}).

1-g data from Ohta and Baba [2013] are in good agreement with 1-g data from this thesis. Even in subcooled regimes at these low G, an increase of the mass flux leads to an increase in the heat transfer coefficient. The influence of the wall heat flux on h is more difficult to appreciate in Ohta's dataset since no runs have been performed at the same vapor quality for various q.

Authors claim that the influence of gravity is negligible on h on these flow parameter ranges, but they use logarithmic scales to plot h and they regroup different mass and heat fluxes on the same graphic. In Figure 3.37, similar differences between the two gravity levels are observed with the two set-ups, with smaller heat transfer coefficients in microgravity in subcooled conditions and in saturated regimes at very low mass flux. In addition, Ohta [2003] stated that the gravity level does not significantly affect the heat transfer coefficient at high mass flux and high vapor quality, which is also consistent with BRASIL data.

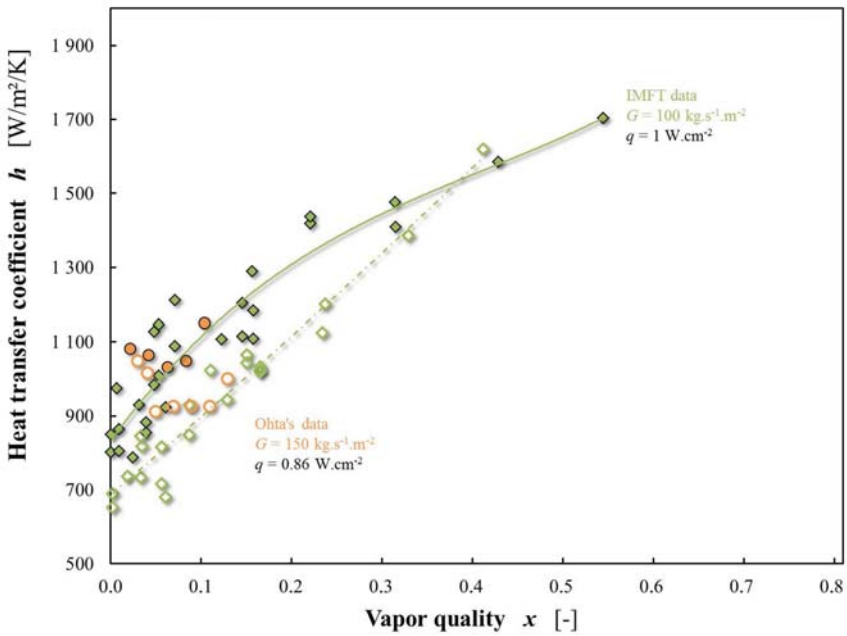

(a) Moderate mass fluxes

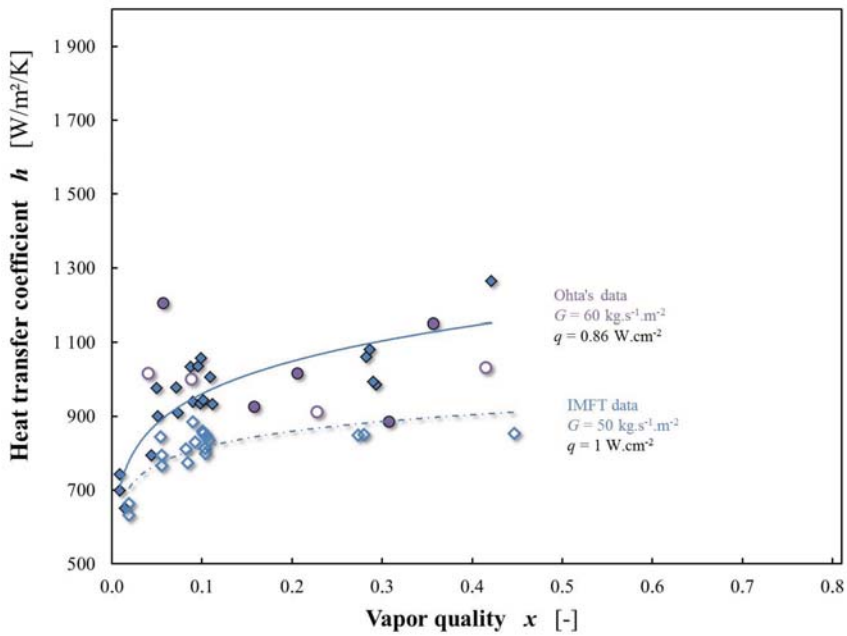

(b) $G = 100$ kg.s^{-1}.m^{-2}

FIGURE 3.37: Heat transfer coefficient according to vapor quality in 1-g (closed symbols) and μ-g (open symbols) for low mass and heat fluxes - IMFT data ($\diamond$), and Ohta and Baba data ($\circ$)

UMD data: experiments of the University of Maryland did not provide enough experimental points to plot trend curves at fixed mass flux or to study the influence of wall heat flux under microgravity conditions. However, they highlight the same trends as the ones presented in the experimental results of this thesis. In subcooled regimes, smaller heat transfer coefficients (up to 30%) are found in microgravity compared to normal gravity, as illustrated in Figure 3.38.

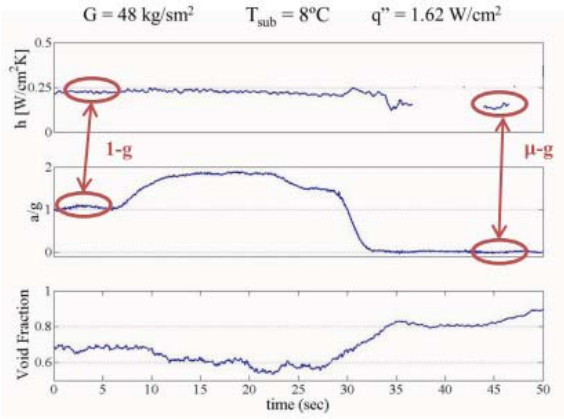

FIGURE 3.38: Time trace plot of heat transfer coefficient, gravity level and outlet void fraction for bubbly flow - UMD data

As for Ohta and Baba, and BRASIL experiments, they observed no visible influence of the gravity level on g for saturated regimes at high heat flux or high mass flux.

Conclusion

BRASIL experimental apparatus allowed to assess the influence of the gravity level on flow pattern, void fraction and film thickness, wall and interfacial shear stresses, and heat transfer coefficient data.

Void fraction measurements are clearly impacted by changes in the gravity level: while it is difficult to highlight trends in subcooled boiling (mostly because of the uncertainty in the vapor quality that is used to describe the evolution of α), the void fraction in saturated conditions is significantly higher in microgravity, whatever the mass flux is. However, the difference between 1-g and μ-g seems to decrease with decreasing G. As a result, the liquid film thickness calculated in annular flows exhibit higher values in normal gravity than in microgravity.

The wall shear stress is also affected by the mass flux and the gravity level. While an increase of G or x induces a increase in τ_w both under normal gravity and microgravity conditions, the influence of the gravity level on the wall shear stress also depends on the mass flux: at high mass fluxes, there is no clear difference between 1-g and μ-g points. On the contrary, for moderate and low values of G, τ_w is significantly lower in microgravity than in normal gravity.

The interfacial shear stress is calculated using pressure drop and void fraction data. τ_i increases with x, with a rate of growth that is proportionnal to G. On the whole range of mass fluxes, the interfacial shear stress is significantly lower in microgravity than in normal gravity.

As a general observation, the heat transfer coefficient increases both with G and with x. Experimental data also show that the wall heat flux plays an important role in heat transfers at fixed mass flux. The dependency on q in subcooled boiling and in saturated boiling at low mass fluxes highlights the important contribution of nucleate boiling in these conditions, whereas saturated flows at high G or very high x are controlled by the convective boiling term. The influence of the gravity level changes according to the dominant heat transfer mode: in subcooled boiling and in saturated boiling at low G, h is lower (of 10 to 30%) in microgravity than in normal gravity; in the regions driven by forced convection, there is no clear difference on h between the two gravity levels.

Comparisons drawn with fragmentary data available in microgravity underline consistent trends on void fraction and heat transfer coefficient when experimental conditions are clearly specified.

In order to be able to properly describe the influence of the gravity level on investigated physical quantities, it is necessary to compare experimental data with litterature correlations and models that express these quantities according to the main parameters and dimensionless numbers, with potential adjustments to fit data under microgravity conditions.

Chapter 4

Modelling of flow boiling under microgravity conditions

Experimental results concerning void fraction, wall and interfacial shear stresses, and heat transfer coefficient have been presented in Chapter 3. In order to model boiling mechanisms under microgravity conditions, measured data are compared to classical correlations and models, and the influence of the gravity level on these physical quantities is assessed.

Les données expérimentales caractérisant le taux de vide, les frottements pariétaux et interfaciaux ainsi que les coefficients d'échange de chaleur ont été présentées dans le Chapitre 3. Afin de modéliser les mécanismes de l'ébullition convective dans le but de prédire les évolutions de paramètres dans des conditions de microgravité, ces grandeurs mesurées sont comparées à des corrélations et des modèles de la littérature. L'influence du niveau de gravité est également évaluée à travers ces comparaisons.

Régimes d'écoulement et transitions
Les modèles prédisant les transitions entre régimes d'écoulement ont majoritairement été établis pour des écoulements gaz-liquide. Le critère de transition le plus utilisé correspond à une transition à taux de vide constant (donc à titre constant). Pour la transition entre écoulements à bulles et écoulements à poches-bouchons, un modèle à flux de dérive semi-empirique donne un accord raisonnable avec les données expérimentales. Cependant, la plus haute valeur de taux de vide trouvée expérimentalement ($\alpha_c > 0.45$) pour la transition semble indiquer que la coalescence est limitée, ce qui est confirmé par la valeur du nombre d'Ohnesorge.

La valeur critique de taux de vide pour la transition entre écoulements à poches-bouchons et écoulements annulaires est obtenue en égalisant les modèles décrivant α pour ces deux types d'écoulement. La valeur obtenue est cohérente avec les mesures. Au contraire, un critère de transition à nombre de Weber constant ne permet pas de prédire les données expérimentales.

Taux de vide et épaisseur de film
Pour les régimes sous-refroidis, correspondant majoritairement aux écoulements à bulles et écoulements à poches-bouchons, le taux de vide est relativement bien décrit par les corrélations dérivant des modèles à flux de dérive. Les valeurs de vitesse de dérive et de coefficient de distribution obtenues expérimentalement sont en bon accord avec les valeurs prédites pour les écoulements à bulles (le peu de points en écoulements à poches-bouchons ne permettant pas de conclure pour ces régimes).

En ébullition saturée, avec des écoulements annulaires, le modèle de Cioncolini et Thome décrit correctement l'évolution du taux de vide avec le titre. Il surestime néanmoins α de 10 à 20% en gravité normale, tandis que les points expérimentaux en microgravité sont un peu plus proches de la corrélation (en particulier à haut flux de masse, avec une différence inférieure à 5%).

Pour ces écoulements annulaires, une épaisseur de film liquide peut être calculée. Cette épaisseur de film n'est que très peu affectée par le taux d'entraînement liquide dans le cœur de vapeur et peut donc être écrite en fonction du diamètre du tube et du taux de vide total. La comparaison des données expérimentales au modèle de Cioncolini et Thome donne des résultats similaires aux observations faites sur le taux de vide : à haut flux de masse, en gravité normale, le film liquide est plus épais que prévu par la corrélation, alors que les points en microgravité sont en adéquation avec les valeurs prédites. La comparaison avec les données en écoulements à faibles flux de masse n'est pas pertinente, le film liquide n'étant pas turbulent à ces débits et la nucléation de bulles en paroi étant probable.

Frottements pariétaux et interfaciaux
Les résultats expérimentaux concernant le frottement pariétal sont confrontés à diverses corrélations qui fournissent une expression du multiplicateur diphasique en fonction du paramètre de Martinelli, et au modèle de Cioncolini et Thome qui donne une corrélation pour la vitesse de frottement dans le cas d'écoulements annulaires. En conclusion, il est montré qu'une corrélation classique du type Lockhart et Martinelli peut être adaptée pour prendre en compte l'influence du débit et du niveau de gravité, et mieux s'ajuster aux données expérimentales.

En écoulements annulaires, le frottement interfacial (qui est peu affecté par l'entraînement liquide) est relativement mal prédit par les corrélations usuellement utilisées en écoulement gaz-liquide. En revanche, l'influence de la gravité sur le coefficient de frottement interfacial expérimental est bien décrite par une corrélation proposée par Ohta en fonction de l'épaisseur de film et d'un nombre de Froude. Le tracé du frottement interfacial en gravité normale met en évidence une dépendance à l'épaisseur de film mais également au flux de masse (cette dernière étant modélisée par un nombre de Reynolds à la puissance -1.3), ce qui est typique d'un écoulement non pleinement rugueux. Une proposition de lissage de ces données en 1-g en fonction de δ et Re_v permet, combinée au modèle d'Ohta, d'obtenir une expression prédisant le frottement interfacial en microgravité. Cette expression reste néanmoins une proposition préliminaire à confronter à d'autres données expérimentales.

Coefficients d'échange de chaleur
Parmi les corrélations confrontées aux données expérimentales, certaines prennent en compte les contributions respectives de l'ébullition convective et de l'ébullition nucléée tandis que d'autres, comme le modèle de Cioncolini et Thome, ne considèrent que les transferts de chaleur par évaporation à travers le film liquide en écoulements annulaires. Le premier type de corrélation met en évidence l'importance du terme d'ébullition nucléée en régimes sous-refroidis, quelque soit le débit, et en régimes saturés pour les faibles débits, tandis que les écoulements à hauts flux de masse sont dominés par les transferts en ébullition convective dès que le titre en vapeur est assez important.

En ébullition sous-refroidie, toutes les corrélations testées surestiment les coefficients d'échange de chaleur en gravité normale. La différence entre valeurs prédites et valeurs mesurées est encore plus importante en microgravité, puisque h est significativement plus petit en microgravité qu'en gravité normale. Puisque l'ébullition nucléée domine les transferts de chaleur en régime sous-refroidi, ces disparités semblent liées à une surestimation de la contribution de l'ébullition nucléée dans les corrélations.

Pour les régimes saturés, la comparaison aux corrélations donne des résultats différents suivant les gammes de paramètres d'écoulement considérés, puisque la nature du terme dominant dans les échanges de chaleur change selon le flux de masse ou le titre. Les corrélations qui distinguent les contributions de l'ébullition nucléée et de l'ébullition convective fournissent cependant des prédictions raisonnables du coefficient d'échange de chaleur, excepté à très haut titre en vapeur, ce qui laisse penser que le terme convectif est sous-estimé.

En résumé, le coefficient d'échange de chaleur est relativement bien décrit par les corrélations distinguant terme de convection et terme de nucléation. Un ajustement de ces corrélations avec l'utilisation de facteur de suppression ou d'amélioration permettrait de rééquilibrer les contributions de ces deux termes pour mieux décrire les données expérimentales et rendre compte de l'influence de la gravité sur les transferts de chaleur.

4.1 Flow patterns and transition

As discussed in Section 1.3, several authors proposed various criteria for the prediction of transitions between flow patterns. In this section, experimental results are compared to these models. Three main flow patterns are observed in microgravity: bubbly flow, transition flow including slug and churn flows, and annular flow. Several models exist for the prediction of transitions from bubbly to slug flows and from slug to annular flows. The objective here is not to perform an extensive comparison of the flow pattern maps with models but only to focus on the one that are the most often used.

4.1.1 Transition between bubbly flow and slug flow:

Several authors [Colin et al., 1991, 1996, Dukler et al., 1988, Zhao et al., 2001] reported sets of experimental data for gas-liquid flow in μ-g, with models to predict flow pattern transitions. The most classical criterion used to predict the transition between bubbly and slug flows is based on a critical void fraction value α_c depending on a Ohnesorge number Oh.

$$Oh = \frac{\mu_l}{\sqrt{\rho_l.\sigma.D}} \tag{4.1}$$

Transition models: Dukler et al. [1988] assume that the local relative velocity between liquid and gas is negligible under microgravity conditions: $u_l = u_g$. Considering that $u_l = j_l/(1-\alpha)$ and $u_g = j_g/\alpha$, that corresponds to a transition criteria expressed by:

$$j_l = \frac{1-\alpha_c}{\alpha_c}.j_g \tag{4.2}$$

This transition can therefore be plotted on flow pattern map at $j_l = 1.22\ j_g$ for an experimental value $\alpha_c = 0.45$. By writing j_l and j_g according to the mass flux G and the critical vapor quality x_c, this transition criteria can be determined in terms of vapor quality:

$$x_c = \frac{1}{1 + \frac{1-\alpha_c}{\alpha_c}\frac{\rho_l}{\rho_g}} \tag{4.3}$$

Colin et al. [1991] made a different assumption by using a drift-flux model to determine the gas velocity according to the mixture velocity $j = j_l + j_v$ and a distribution parameter C_0:

$$u_g = C_0.(j_l + j_g) \tag{4.4}$$

wich leads to:

$$j_l = \frac{1-C_0.\alpha_c}{C_0.\alpha_c}.j_g \tag{4.5}$$

and

$$x_c = \frac{1}{1 + \frac{1-C_0.\alpha_c}{C_0.\alpha_c}\frac{\rho_l}{\rho_g}} \tag{4.6}$$

Experimental results provided a value of 1.2 for C_0 for their datasets in bubbly and slug flows. With a similar critical value of void fraction $\alpha_c = 0.45$, that corresponds to a transition at $j_l = 0.85\ j_g$ on a flow pattern map, for a diameter $D = 40$mm. By considering experiments performed with different diameter tubes and fluids, Colin et al.

[1996] highlighted two regimes of bubble coalescence leading to the transition to slug flow. If $Oh > 8.2\ 10^{-4}$, bubble coalescence is limited and $\alpha_c = 0.45$. If $Oh < 7.6\ 10^{-4}$, the rate of bubble coalescence is very high and $\alpha_c = 0.2$.

Comparison with models: in BRASIL experiments, transition between bubbly and slug flows is observed for a vapor quality $x_c \simeq 0.05$ and a void fraction $\alpha_c \simeq 0.7$, which is in agreement with the value of 0.74 found by Celata and Zummo [2007] for FC-72 runs in 4 and 6mm ID tubes.

The agreement between experimental data and model is reasonable with the drift-flux expression proposed by Colin et al. [1991] since it leads to a transition at $j_l = 0.140\ j_v$ and $x_c = 0.037$. However, this model still underpredicts the transition vapor quality of about 25%, despite similar values of distribution parameter (whose calculation is presented in the section about void fraction modelling) and drift velocity. Corresponding transitions are indicated in the flow pattern map of Figure 4.1.

A couple of potential causes is identified for this discrepancy in transition values between boiling flows and gas-liquid flows. First, the initial size of bubbles nucleated on the wall is very small. Second, the length of the heated test section is rather small in boiling experiment, with a ratio L/D close to 30 against 80 in the experiments of Colin et al. [1991], for example. The residence time of bubbles in the tube is therefore shorter and their probability of coalescence is also smaller. These reasons could explain that bubbly flow occurs at higher void fraction in boiling experiments.

In BRASIL experiment, the Ohnesorge number Oh approximately equals $1.14\ 10^{-3}$. According to Colin et al. [1996], bubble coalescence is limited, which is consistent with a critical value of void fraction $\alpha_c > 0.45$.

4.1.2 Transition between slug flow and annular flow:

Regarding the transition between slug flow and annular flow, some authors distinguish an intermediate region corresponding to frothy slug-annular flow with continuous appearence of frothy mixtures in the liquid slugs that travel at a velocity that is relatively higher than the liquid velocity at the wall.

Void fraction criteria: Dukler et al. [1988] only considered a direct transition from slug flow to annular flow. They speculated that it occurs when the void fractions, as described by two separate models for each type of flow, become equal:
− for the slug flow region, a semi-empirical drift-flux model is used. Through analysis of flow movies, values of C_0 between 1.0 and 1.3 were found, and the authors assumed it to be 1.25 in their calculations.

$$\alpha = \frac{1}{C_0} . \frac{j_v}{j_l + j_v} \tag{4.7}$$

− for the annular flow region, the momentum balance equations written for the liquid and the mixture yield $\tau_i = \tau_w \sqrt{\alpha}$ under microgravity conditions. By introducing the interfacial and wall friction factor f_i and f_w, the void fraction α can be calculated with the following equation:

$$\frac{\alpha^{5/2}}{(1-\alpha)^2} = \left(\frac{f_i}{f_w}\right) . \left(\frac{\rho_g}{\rho_l}\right) . \left(\frac{j_g}{j_l}\right)^2 \tag{4.8}$$

Wallis model is suggested to calculate the interfacial friction factor f_i, and the Blasius relation to obtain f_w at the wall. As the flow is expected to be a combination of slug and annular flows near the transition, Equations (4.7) and (4.8) can be combined to solve the superficial velocities at the boundary.

With the experimental datasets provided by the authors, a critical value $\alpha_c \simeq 0.80$ is found for the transition from slug flow to annular flow.

Weber number criteria: Zhao and Rezkallah [1993] reported a large set of experimental data on gas-liquid flow under microgravity conditions and suggested a model for the prediction of flow pattern transitions based on an analysis of the forces acting on the mixture. According to the authors, the Weber number, defined by the ratio between inertial forces over surface tension, plays an important role in μ-g when the buoyancy force is negligible. They therefore proposed a transition criteria based on a critical Weber number We_c calculated with the superficial gas velocity j_g and density ρ_g:
– bubbly and slug flow are observed for $We_c < 1$, where the surface tension force is higher than the inertial force;
– for $1 < We_c < 20$, comparable values of inertia and surface tension forces lead to a large transition with frothy slug-annular flow that correspond to the beginning of the transition from slug flow to annular flow;
– the last region is characterised by $We > 20$ and important inertial forces. It contains all the annular flow runs.

Comparison with models: in BRASIL experiments, transition between slug and annular flows is observed for a vapor quality $x_c \simeq 0.13$ and a void fraction $\alpha_c \simeq 0.8$, which is in agreement with Dukler et al. [1988].

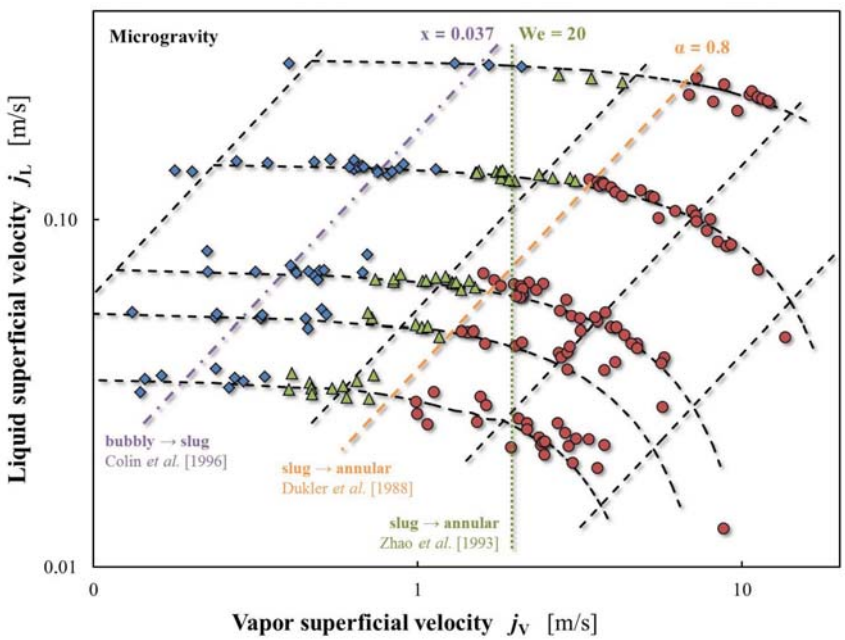

FIGURE 4.1: Flow pattern map in μ-g and transition between flow patterns as predicted by classical models

As discussed in the previous section, the drift-flux model provides a rather accurate prediction of the vapor velocity according to the mixture velocity in subcooled boiling. On the contrary, Equation (4.8) does not provide a description of friction factors and void fraction in agreement with experimental data: calculations of the ratio f_i/f_w for

measured values (with experimental void fraction measurements) and for Dukler's model highlight a systematic underprediction of about 70% under microgravity conditions (except for $G = 200$ and 400 kg.s^{-1}.m^{-2} at high vapor quality). This discrepancy was expected since Dukler et al. [1988] use Wallis model to predict interfacial friction factor and this correlations has proven to not fit experimental interfacial shear stress data.

Zhao and Rezkallah [1993]'s transition criteria does not correctly predict experimental trends. The transition is assumed to occur at a constant We_g value whatever the mass flux, whereas experimental results show that the value of the critical Weber number increases with the mass flux.

4.2 Void fraction and film thickness

In this section, void fraction measurements are compared to values provided by models and empirical correlations, for both subcooled and saturated boiling. In the specific case of annular flow, liquid entrainment is characterised and consistency of corresponding experimental liquid film thicknesses with models is discussed.

4.2.1 Void fraction

Most of literature correlations give an averaged surface or volumetric void fraction. In subcooled boiling, it therefore corresponds to the vapor fraction delimited by bubbles, while it characterises the vapor core (minus entrained liquid droplets) in annular flow. Proposed models are valid for a given flow pattern. Drift flux models [Zuber and Findlay, 1965] or the correlation of Steiner [1993] are relevant for the prediction of the void fraction in bubbly and slug flows corresponding to subcooled regimes. Other correlations (like the one of Cioncolini and Thome [2012b]) have been established over a wide range of vapor qualities corresponding to different flow patterns. Investigated correlations are presented in Figure 4.2 at $G = 200$ kg.s^{-1}.m^{-2} in 1-g and μ-g (when depending on the gravity level).

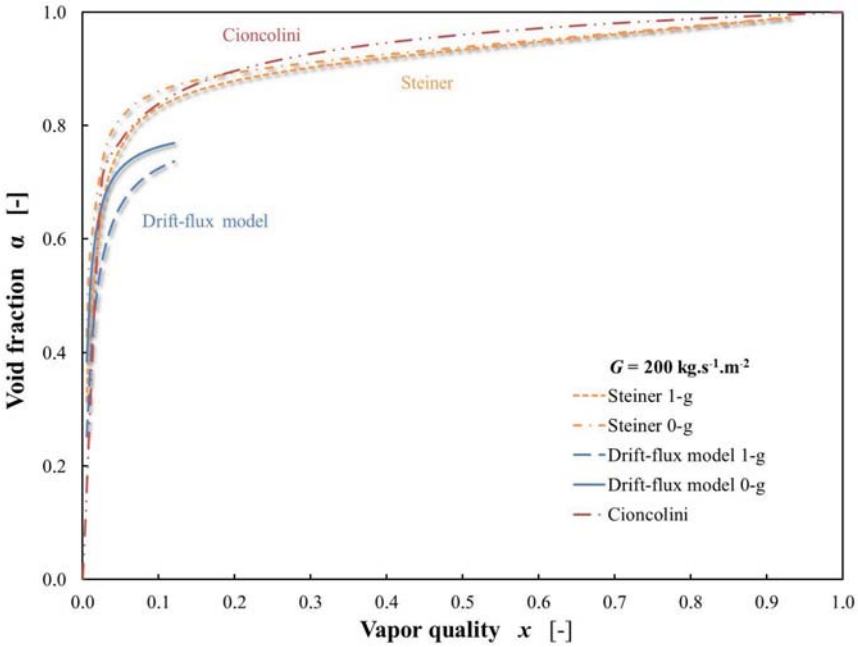

FIGURE 4.2: Predictions of void fraction according to various empirical correlations

In subcooled regimes: in subcooled boiling that mostly corresponds to bubbly and slug flows, void fraction values range from 0 to 0.6. Measurements at very low void fraction are not very accurate since the sensitivity of the capacitance probes is not good enough to properly distinguish them from the all-liquid state. Moreover, there is a lack of precision on the associated vapor quality, which makes it difficult to compare void fraction data to correlations given according to x. Nevertheless, some calculations can be made for subcooled conditions.

Experimental distribution parameter: the coefficient C_0 that characterises phase distribution in the drift-flux model can be determined with experimental results by plotting the vapor velocity u_v according to the mixture velocity for bubbly and slug flows.

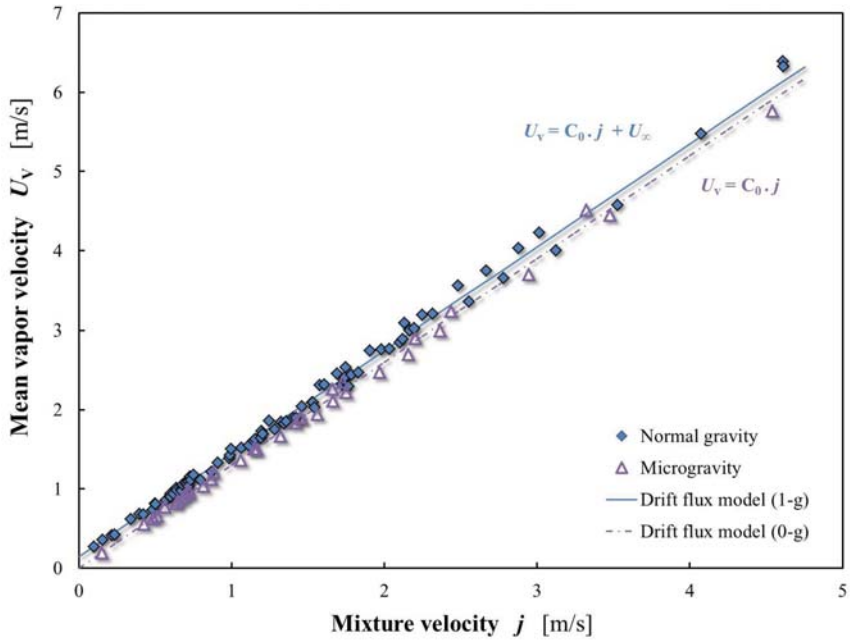

FIGURE 4.3: Mean vapor velocity for bubbly and slug flows un subcooled boiling, in 1-g (closed symbols) and μ-g (open symbols)
- comparisons with drift flux model for $C_0 = 1.25$

Figure 4.3 shows the vapor velocity in subcooled runs (bubbly and slug flows) in microgravity compared to the drift flux model $u_v = C_0.j$ with $C_0 = 1.25$. Despite the lower accuracy on measurements at low vapor quality, the agreement between experimental data and the relationship used by Colin et al. [1991] is good, and similar values of C_0 are found in μ-g. On-ground data are also plotted on Figure 4.3, with the same value of C_0 and by adding a drift velocity $u_\infty = 0.145$ m.s^{-1} corresponding to the theoretical value of Harmathy [1960] for bubbly flows (Equation (4.9)). In 1-g too, a drift-flux model provides a suitable description of the vapor velocity. Slug flow runs (that are not identified in the graphic, and correspond to higher mixture velocities) are too few and too scattered to highlight a specific velocity comparable with the theoretical value of 0.085 m.s^{-1} given for slug flows by $u_v = 0.35\sqrt{g.D}$.

$$u_\infty = 1.53 \cdot \left(g \cdot (\rho_l - \rho_v) \cdot \frac{\sigma}{\rho_l^2} \right)^{1/4} \tag{4.9}$$

Drift-flux model: the drift flux expression that is discussed in the flow pattern transition section can be written according to the mass flux and vapor quality to obtain α as a function of x. With a distribution coefficient C_0 and a drift velocity u_∞, the drift flux models in 1-g leads to:

$$\alpha = \frac{1/C_0}{1 + \left(\frac{\rho_v}{\rho_l} + \frac{u_\infty . \rho_v}{G} \right) \frac{1}{x} - \frac{\rho_v}{\rho_l}} \tag{4.10}$$

In Figure 4.4, experimental values of void fraction are compared to the ones predicted by the 1-g drift-flux model in the same conditions.

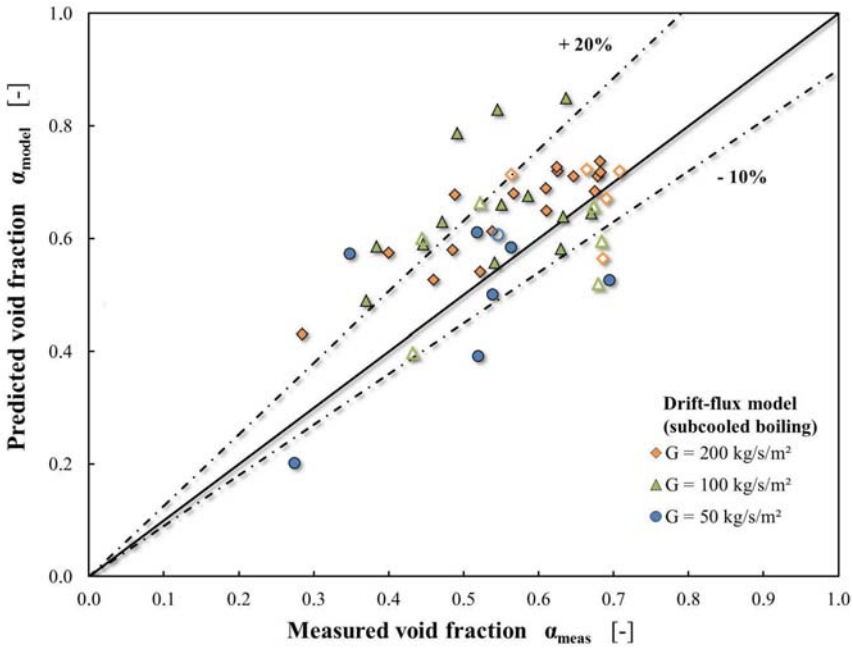

FIGURE 4.4: Comparison of measured void fraction and predicted void fraction in subcooled boiling, in 1-g (closed symbols) and μ-g (open symbols) using a drift flux model in 1-g with $C_0 = 1.25$ and $u_\infty = 0.145$ m.s^{-1}

In the region where α is very small (corresponding to dispersed bubbly flows), void fraction values cannot be compared with the model. Indeed, a small error on x leads to a significant error on α, according to Equation (4.10). However, near the transition from bubbly to slug flow and in transition and slug flows, most of the experimental points exhibit a difference of maximum $\pm$ 20% compared to Equation (4.10). The model predictions are in better agreement with 1-g data than with μ-g data.

Steiner correlation: Steiner [1993] developed a void fraction correlation derivated from the drift-flux model established by Rouhani and Axelsson [1970]. This correlation is described by Equation (1.46). As for the drift-flux relation presented above, this expression of α depends on the vapor quality but also on the mass flux G and the gravity level through the acceleration constant g. Neglecting the gravitational term yields a simplified correlation for microgravity cases that corresponds to higher void fraction than in normal gravity, as illustrated in Figure 4.5.

Even though this correlation was established with a drift flux model, authors claim it is suitable for boiling in subcooled and quality regions since it sucessfully predicted their experimental database. However, it is not quite adapted to annular flow at high vapor quality. Nevertheless, all experimental data are plotted in Figure 4.5 for $G = 200$ and 50 kg.s^{-1}.m^{-2}, with model trend curves in 1-g and μ-g. The same data are plotted in Figure 4.6 with additional experimental values at different mass fluxes, in order to draw a comparison between measurements and model calculations for the same flow features (fluid properties and flow parameters).

In dispersed bubbly flow, the error on the quality induces a large error on the predicted void fraction, making comparisons with the model of Steiner [1993] difficult. At vapor qualities corresponding to transition and slug flow, the difference between model and

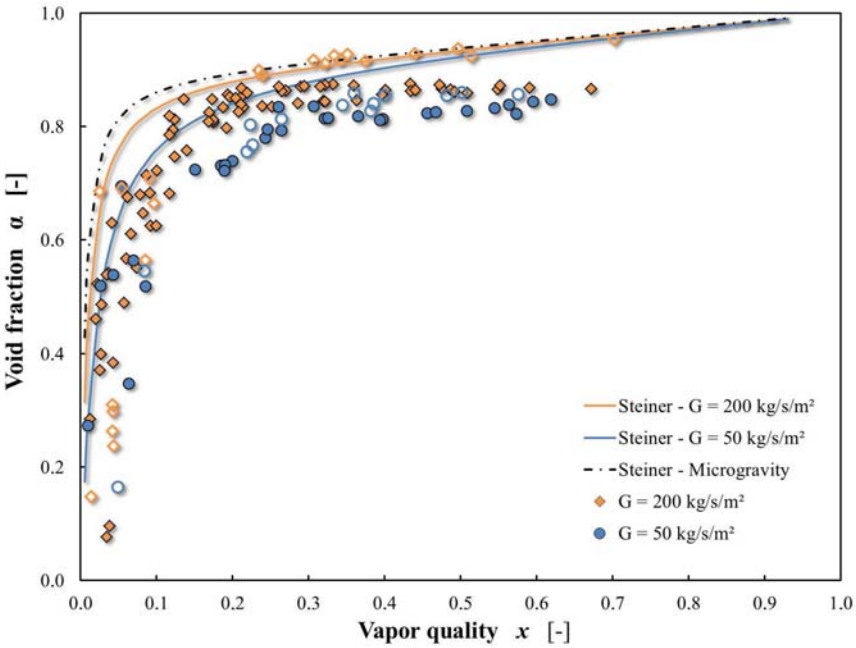

FIGURE 4.5: Void fraction in 1-g (closed symbols) and μ-g (open symbols) for two different mass fluxes - comparisons with the correlations proposed by Steiner [1993]

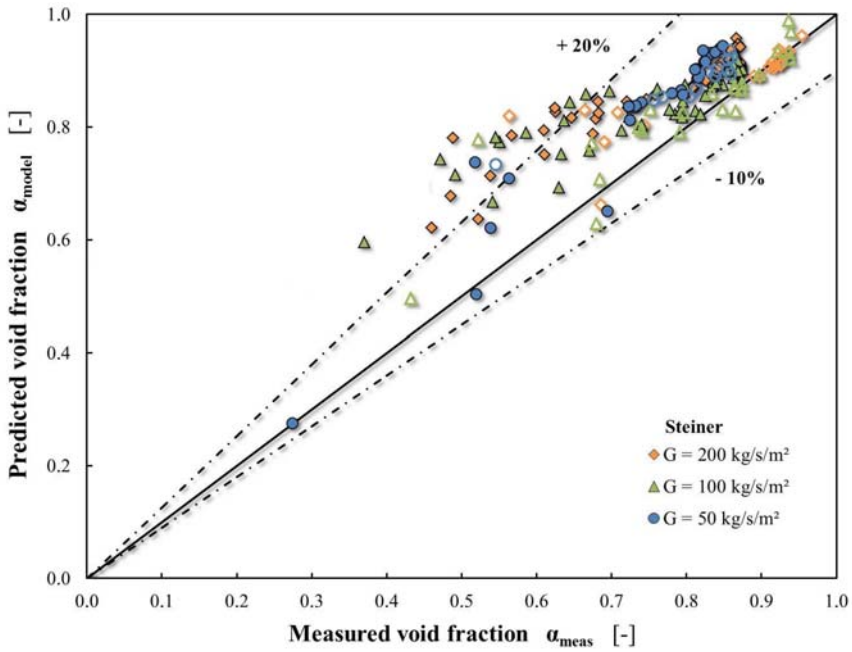

FIGURE 4.6: Comparison of measured void fraction and predicted values in 1-g (closed symbols) and μ-g (open symbols) using the correlation proposed by Steiner [1993]

measurements ranges from 10 to 40% and it is difficult to identify a trend for the influence of the gravity level. However, the results in saturated conditions ($\alpha > 0.8$) look alot like that of Cioncolini and Thome [2012b] model: trend curves at different mass fluxes and gravity levels merge at high vapor quality; high mass fluxes are better described by the correlation than experiments at lower G, whatever the gravity level is, and μ-g are in better agreement with the model than 1-g data. Corresponding Mean Absolute Errors (MAE) between experiments and models are presented for saturated boiling only

in Table 4.1, for each mass flux and gravity level.

$$\text{MAE} = \sum_{i=1}^{n} \left| \frac{\alpha_{n,meas} - \alpha_{n,theo}}{\alpha_{n,meas}} \right| \tag{4.11}$$

In saturated regimes: in their modelling of annular flow, Cioncolini and Thome [2012b] proposed a correlation for the void fraction that was presented in Equation (1.37). Unlike the drift-flux relation in subcooled regime, this expression is independent of the mass flux or the gravity level. It is plotted in Figure 4.7 for saturated runs at $G = 200$ and 50 kg.s^{-1}.m^{-2}, both under normal gravity and microgravity conditions, according to the vapor quality.

$$\alpha = \frac{m \cdot x^n}{1 + (m-1) \cdot x^n} \tag{4.12}$$

where

$$\begin{cases} m = a + (1-a) \cdot \left(\dfrac{\rho_v}{\rho_l}\right)^{a_1} & a = -2.129, a_1 = -0.2186 \\ n = b + (1-b) \cdot \left(\dfrac{\rho_v}{\rho_l}\right)^{b_1} & b = 0.3487, b_1 = 0.515 \end{cases} \tag{4.13}$$

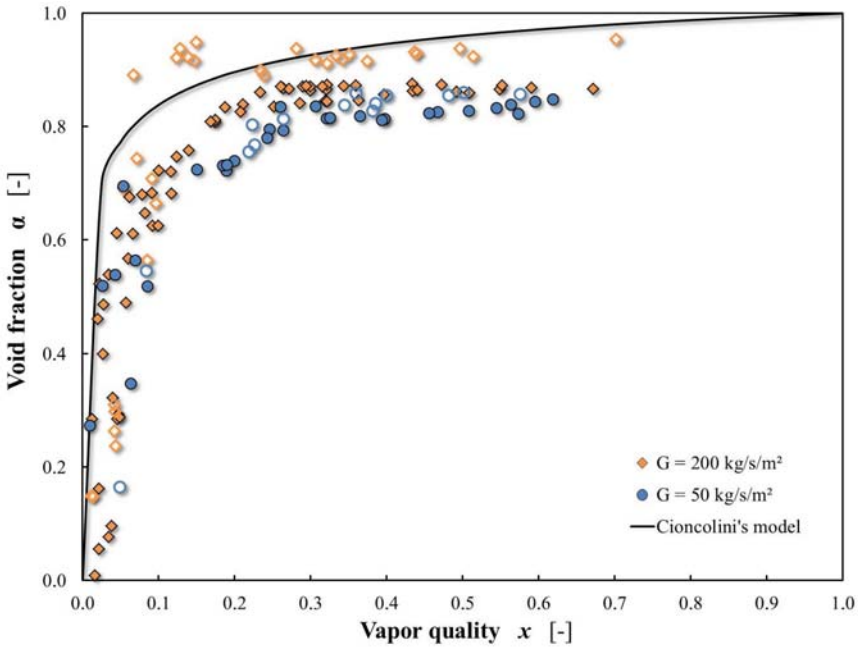

FIGURE 4.7: Void fraction in saturated boiling according to the vapor quality, in 1-g (closed symbols) and μ-g (open symbols) for two different mass fluxes - comparisons with the model proposed by Cioncolini and Thome [2012b]

In 1-g, the model clearly overpredicts the void fraction, whatever the mass flux is. However, in μ-g, void fraction data at high G are in good agreement with the correlation, while experimental values at low G are still overpredicted by the model (but slightly less than in normal gravity). Same trends can be observed in Figure 4.8 that draws a comparison between measured and predicted void fraction values in the same conditions. In a general way, these two graphics show that the model always overpredicts α.

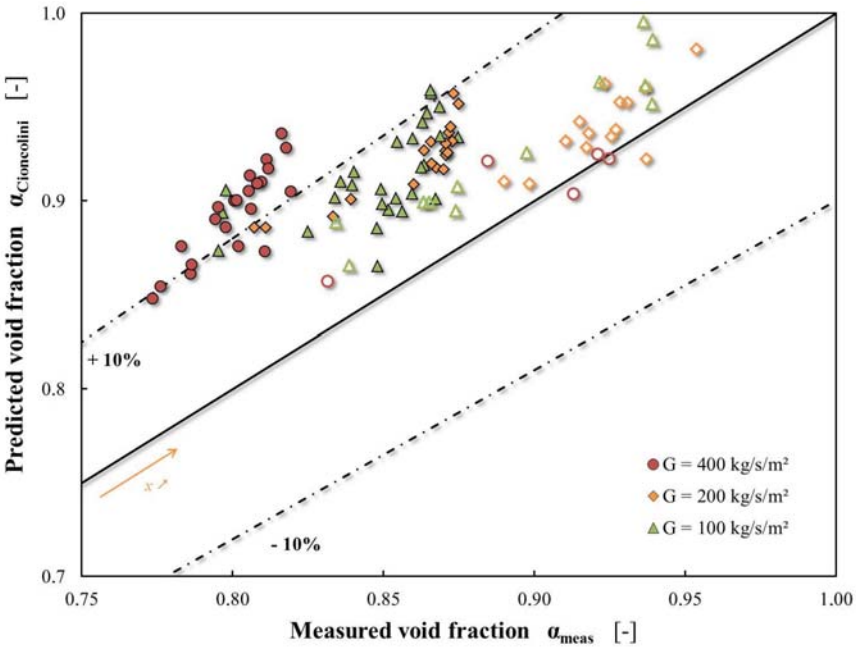

(a) High and intermediate mass fluxes

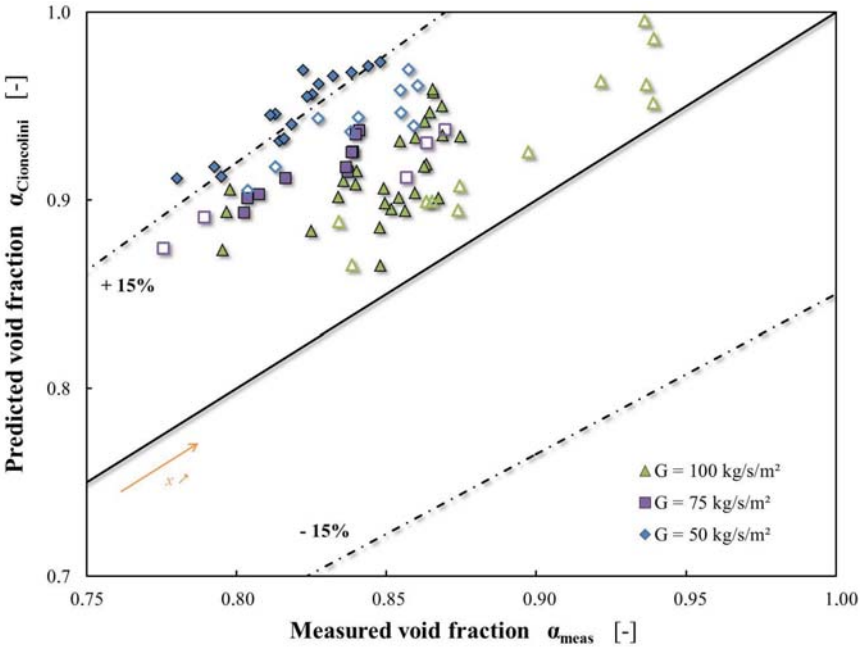

(b) Intermediate and low mass fluxes

FIGURE 4.8: Comparison of measured void fraction and predicted void fraction in saturated boiling, in 1-g (closed symbols) and μ-g (open symbols) using a prediction model proposed by Cioncolini and Thome [2012b]

As can be seen from Figure 4.8(a), void fraction data at high and moderate mass fluxes are rather well described by the correlation proposed by Cioncolini and Thome [2012b], especially in microgravity: while the difference between experimental and predicted values is between 5 and 15% in 1-g, a maximal difference of 5% is observed for the case of μ-g. The discrepancy between model and experiments is a bit higher for low mass fluxes, as shown in Figure 4.8(a): at $G = 50$ and 75 kg.s^{-1}.m^{-2}, this difference ranges

from 10 to 18% in 1-g and from 5 to 15% in μ-g. These observations are summarised in Table 4.1 devoted to saturated boiling.

Summary: comparisons previously drawn between void fraction experimental data and correlations are summarised in Table 4.1 (for saturated runs) with indications of MAE in % for each mass flux G and each gravity level. In this particular case, MAE correspond to - MRE (Mean Relative Error) since models systematically overpredict void fraction values. For each series of points, the correlation that better fits the dataset is indicated in bold, in blue (for 1-g data) or in purple (for μ-g data).

In bubbly and slug flows, none of the models correctly predicts void fraction at high mass flux, mostly due to the dispersion of experimental points and the lack of precision on the calculation of α and x for dispersed bubbly flows. At moderate and low mass fluxes, the mean error between model and experiments is smaller because these series mostly exhibit transition and slug flow runs, for which the accuracy on measurements is better (except for $G = 50$ kg.s^{-1}.m^{-2} in μ-g where only very few points are available in subcooled regimes). As a general observation, the classical drift flux model calculated with experimental distribution coefficient and drift velocity provides the better prediction of void fraction, for both 1-g and μ-g data.

In saturated conditions, the modified correlation of Steiner [1993], for the two gravity levels, and the model proposed by Cioncolini and Thome [2012b] are equivalent and provide a good prediction of the void fraction, even if experimental points are systematically a bit underpredicted. In 1-g, the correlation calculated with Steiner [1993] and $g = 9.81$ better fits BRASIL dataset, with MAE between 6 and 11% and smaller values for moderate mass fluxes ($G = 100$ and 200 kg.s^{-1}.m^{-2}). In μ-g, the three models are suitable for the prediction of α; at high mass fluxes ($G = 400$ and 200 kg.s^{-1}.m^{-2}), the correlation proposed by Cioncolini and Thome [2012b] exhibits a MAE of about 2%, while the Steiner [1993] version can be preferred at moderate and low mass fluxes with MAE ranging from 3 to 8%. Table 4.1 also highlights the fact that μ-g data are in better agreement with correlations than 1-g data are, since these correlations overpredict α that is slightly higher under microgravity conditions compared to normal gravity.

In conclusion, a drift-flux model can be used to describe void fraction data in bubbly and slug flows, with a precision that depends on flow parameters. In annular flow, α is controlled by the wall and interfacial shear stresses, τ_w and τ_i.

	$G = 400$		$G = 200$		$G = 100$		$G = 75$		$G = 50$	
	1-g	μ-g	1-g	μ-g	1-g	μ-g	1-g	μ-g	1-g	μ-g
Drift flux model (1-g)	-	-	-	-	-	-	-	-	-	-
Drift flux model (μ-g)	-	-	-	-	-	-	-	-	-	-
[Steiner, 1993] (1-g)	**10.8**	2.3	**6.0**	2.5	**7.8**	3.9	**9.2**	**5.6**	**10.9**	**7.7**
[Steiner, 1993] (μ-g)	11.5	2.4	6.7	**2.0**	9.4	**3.7**	12.2	8.6	13.7	10.2
[Cioncolini and Thome, 2012b]	11.9	**1.8**	8.5	3.2	11.4	4.0	18.3	11.6	16.6	13.2

TABLE 4.1: Mean absolute error (MAE, in %) between BRASIL experimental void fraction and void fraction predicted by various correlations and models in saturated boiling conditions

4.2.2 Liquid entrainment in annular flow

In the model they developed to describe thermodynamical mechanisms in annular flow, Cioncolini and Thome [2012a] propose an iterative correlation, presented in Equation (1.35), to estimate the liquid fraction e that is entrained in the vapor core under the form of liquid droplets. Since the entrainment is given according to a Weber number calculated with a superficial vapor velocity, it is expected to be higher at higher mass flux or higher vapor quality.

It is necessary to determine this flow parameter to correctly apprehend annular flow behaviour; indeed, if the liquid entrained fraction is significant, this could have an important influence on the wall liquid film thickness compared to the case where e can be neglected. Figure 4.9 presents the results of iterative calculations providing estimations of e for all mass fluxes and gravity levels.

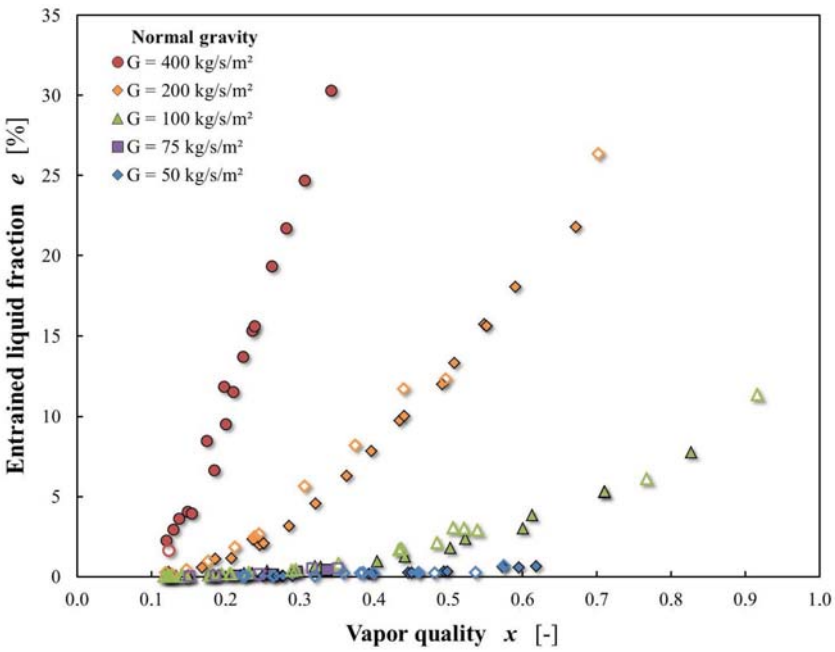

FIGURE 4.9: Liquid fraction (in %) of droplets entrained in the vapor core of annular flow, according to vapor quality and for various mass fluxes, in 1-g (closed symbols) and μ-g (open symbols)

Since the model does not take the gravity into account, the same observations can be made at fixed G for the two gravity levels. At low mass fluxes corresponding to low Weber numbers ($G = 50$ and 75 kg.s^{-1}.m^{-2}), the entrained liquid fraction can be neglected: even at high vapor quality, e does not exceed 1% of the total liquid fraction. At $G = 100$ kg.s^{-1}.m^{-2}), e is a bit higher but does not represent more than 5% of x_l (except at very high vapor quality $x > 0.7$ with very few available points), which is also negligible. However, at high mass fluxes, the entrained liquid fraction largely increases with the vapor quality due to larger relative velocity difference: at $G = 400$ kg.s^{-1}.m^{-2}), e goes up to 30% for $x = 0.4$; in the same way, the entrainement cannot be neglected at $G = 200$ kg.s^{-1}.m^{-2}) for vapor quality higher than 0.4.

All following experimental comparisons and calculations with models are made by taking this entrainement into account. Unfortunately, there is no way to correlate this calculated entrainment with experimental data from this study.

4.2.3 Film thickness in annular flow

In Chapter 3, experimental results on liquid film thickness in annular flow have been presented by neglecting the liquid entrainment in the vapor core according to preliminary calculations. However, Figure 4.9 shows that e cannot be neglected on all ranges of flow parameters (especially for combinaisons of high G and x). In this section, the influence of liquid entrainement on δ is discussed and corrected film thicknesses are compared to the one predicted by the model of Cioncolini and Thome [2012b].

Influence of liquid entrainement: as previously discussed, the liquid fraction that is entrained in the vapor core cannot be neglected at high mass fluxes, especially at high vapor quality. The wall liquid film thickness can therefore be recalculated using Equation (4.14) to account for the droplet entrainment.

$$\delta = \frac{D}{2}(1 - \sqrt{\alpha.(1 + \frac{\rho_v}{\rho_l} \cdot \frac{1-x}{x} \cdot e)} \tag{4.14}$$

However, the influence of the droplet entrainment on the liquid film thickness is negligible, mostly because e is weighted by the density ratio ρ_v/ρ_l. Indeed, the maximum error made by ignoring the liquid entrainment in the calculations of the liquid film thickness for BRASIL database is less than 3%.

Experimental data that are presented thereafter take into account the liquid fraction entrained in the vapor core, as calculated with the model developed by Cioncolini and Thome [2012a], but the difference with the case without droplet entrainment cannot be seen with the naked eye on the graphics.

Comparison to model: in their annular flow model, Cioncolini and Thome [2012a] proposed a correlation for the liquid film thickness by describing a velocity profile in the turbulent liquid film, which is presented in Equation (1.78). Contrary to void fraction data, this correlation depends on the mass flux G. Figure 4.10 draws a comparison between the model and experimental data for various mass fluxes both under normal gravity and microgravity conditions.

The general trends described by the correlation are in good agreement with experimental curves at high and moderate mass fluxes: the influence of G on δ is correctly illustrated, and film thicknesses are consistent at moderate vapor quality, in 1-g and μ-g. However, a quantitative difference can be observed at higher x for experimental values in 1-g: while microgravity data are rather close to the model on this range of quality, 1-g curves exhibit significantly larger film thicknesses.

At low mass fluxes, the qualitative evolution of δ is properly described by Cioncolini and Thome [2012a] correlation, but the latter systematically underpredicts δ compared to experiments, for the two gravity levels and even at moderate vapor quality near the transition from slug flow. Microgravity film thicknesses are still lower than 1-g values of δ but the influence of gravity level is less important than at higher mass fluxes. The difference between experimental data and model at these values of G can be explained by the fact that the liquid film is not turbulent anymore: at $G = 50$ kg.s^{-1}.m^{-2}, 300 $< Re_l <$ 850, and at $G = 75$ kg.s^{-1}.m^{-2}, 700 $< Re_l <$ 1000, with:

$$Re_l = \frac{j_l.D}{\nu_l} \tag{4.15}$$

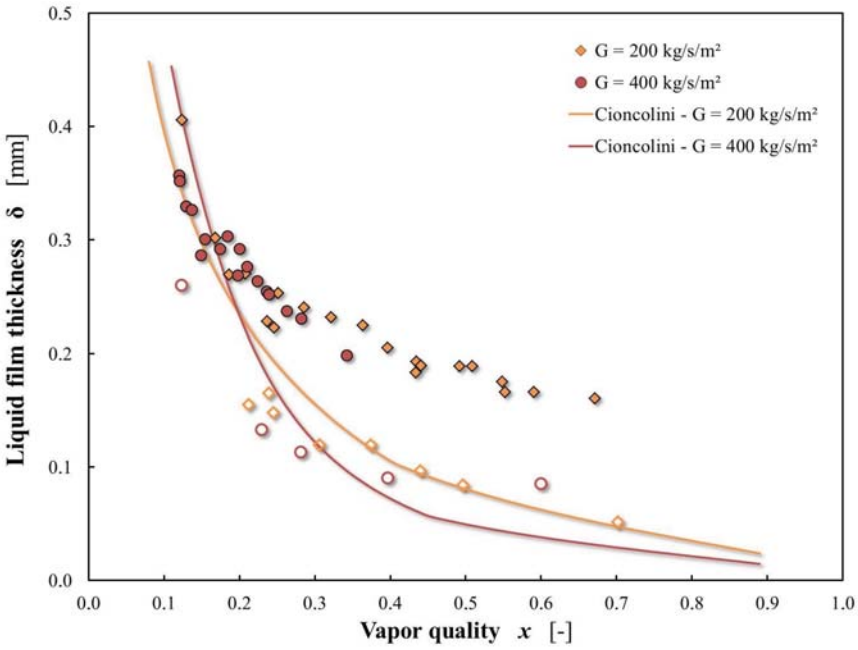

(a) High and intermediate mass fluxes

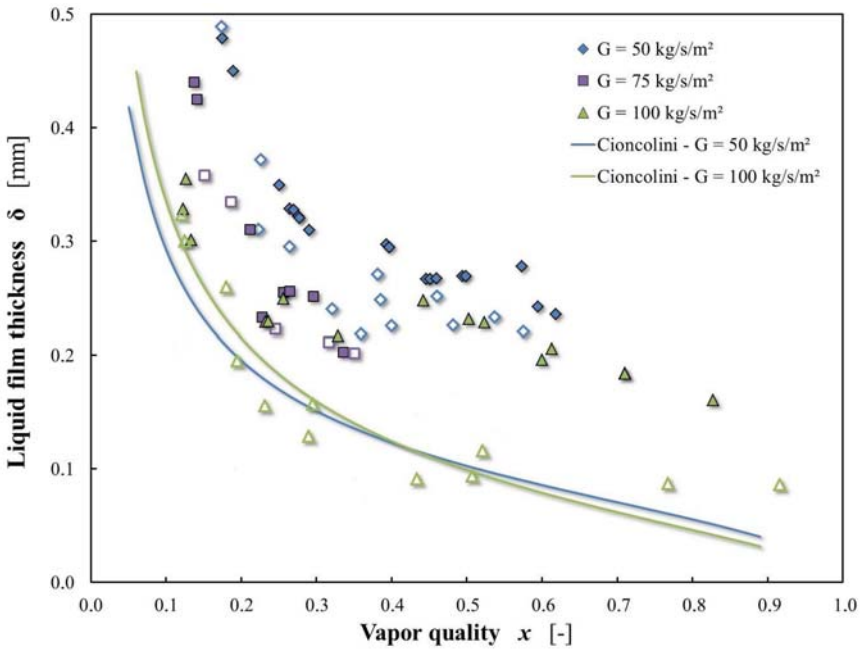

(b) Intermediate and low mass fluxes

FIGURE 4.10: Liquid film thickness in saturated boiling according to the vapor quality, in 1-g (closed symbols) and μ-g (open symbols) for various mass fluxes - comparisons with the model proposed by Cioncolini and Thome [2012a]

These observations are summarised in Figures 4.11 and 4.12 that show a comparison of predicted and experimental values of the liquid film thickness in normal gravity and microgravity for all investigated mass fluxes, including those where the liquid film is laminar. The MAE corresponding to these graphics are indicated in Tables 4.2 and 4.3.

Tables 4.2 and 4.3 presents the MAE in % between experimental data and the prediction correlation proposed by Cioncolini and Thome [2012a] for each mass flux and each

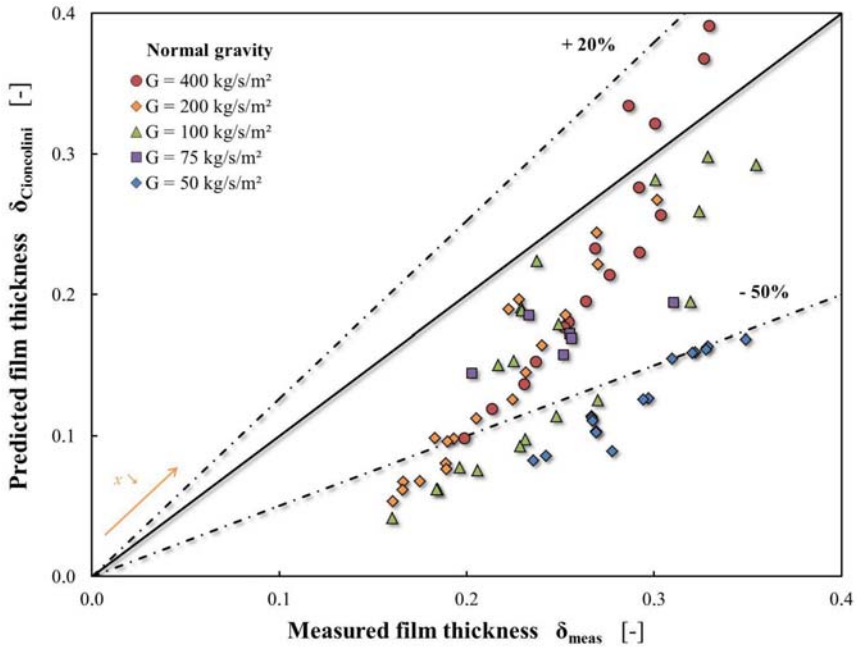

FIGURE 4.11: Comparison of measured liquid film thickness and predicted liquid film thickness in saturated boiling, in 1-g using a prediction model proposed by Cioncolini and Thome [2012a]

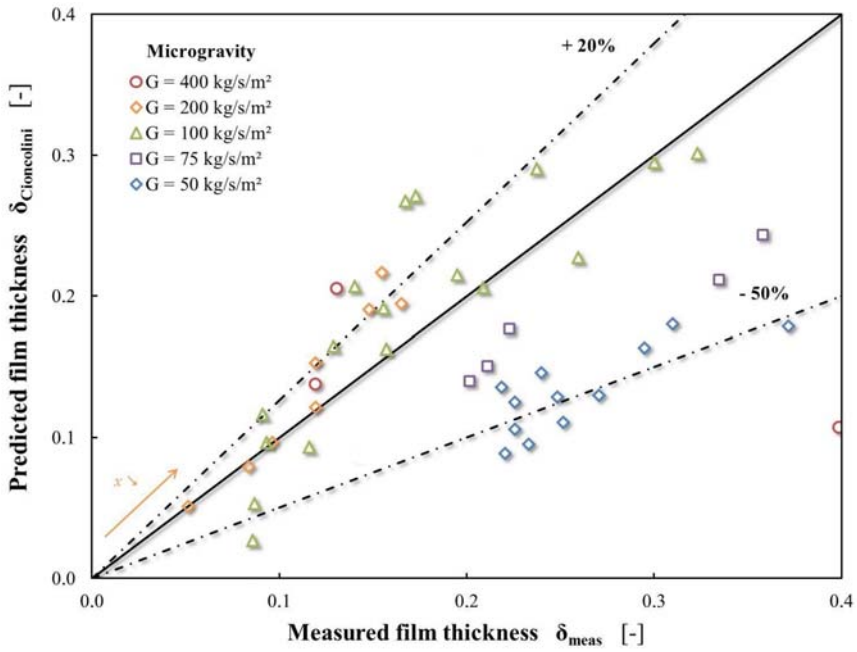

FIGURE 4.12: Comparison of measured liquid film thickness and predicted liquid film thickness in saturated boiling, in μ-g using a prediction model proposed by Cioncolini and Thome [2012a]

gravity level. Moderate and high vapor quality regions have arbitrary been distinguished to separate data near the transition from slug flow with strong evolution of the film thickness and data that are less sensitive to the quality.

In normal gravity, experimental data at high mass flux are in rather good agreement with the correlation near the transition from slug flow with MAE smaller than 20% whereas the model largely underpredicts δ (of about 40 - 50%) at higher vapor qualities. At low mass fluxes, liquid films are laminar and the comparison with the model is not relevant anymore: the correlation underpredicts the film thickness even at moderate x.

	Moderate vapor quality $0.13 \leqslant x \leqslant 0.25$	**High vapor quality** $0.25 < x$
$G = 400$	16.4	38.3
$G = 200$	13.7	49.9
$G = 100$	27.6	53.9
$G = 75$	-	-
$G = 50$	-	-

TABLE 4.2: Mean absolute error (MAE, in %) between BRASIL experimental liquid film thicknesses and liquid film thicknesses predicted by the model of Cioncolini and Thome [2012a] in 1-g in saturated boiling conditions

Since experimental curves highlight a clear influence of the gravity level on liquid film thickness, the comparison between Cioncolini and Thome [2012a] relation and experimental data exhibit different trends in μ-g. At low mass flux, the correlation still underpredicts the film thickness, but to a lesser extent than in 1-g since δ is smaller in μ-g. This difference due to change in the gravity level also explains that experimental values of δ at high vapor quality better fit the model in microgravity than in normal gravity (with a MAE of 8% for $G = 200$ kg.s^{-1}.m^{-2} at high x in μ-g against 50% in 1-g, for example).

	Moderate vapor quality $0.13 \leqslant x \leqslant 0.25$	**High vapor quality** $0.25 < x$
$G = 400$	57.9	15.9
$G = 200$	28.6	7.3
$G = 100$	24.2	27.1
$G = 75$	-	-
$G = 50$	-	-

TABLE 4.3: Mean absolute error (MAE, in %) between BRASIL experimental liquid film thicknesses and liquid film thicknesses predicted by the model of Cioncolini and Thome [2012a] in μ-g in saturated boiling conditions

Cioncolini and Thome [2012a] film thickness model can therefore be used to fit experimental data (1) in 1-g, at high and moderate mass fluxes, and at moderate vapor quality, (2) in μ-g, at high and moderate mass fluxes, at moderate / high and high vapor quality. On other flow parameter ranges, a correction is needed since δ is underpredicted of 30 to 60% (3) in 1-g, at high and moderate mass fluxes, and at high vapor quality, (4) in 1-g and μ-g, at low mass fluxes.

4.3 Wall and interfacial shear stresses

In this section, the experimental database obtained with BRASIL experiment in 1-g and μ-g is compared to the prediction of various correlations in order to model wall and interfacial shear stresses. The influence of the gravity level is also discussed.

4.3.1 Wall shear stress

Most of the correlations used for the prediction of pressure drops in two-phase flow are valid for both subcooled and saturated conditions. These correlations are therefore evaluated in the whole range of flow parameters, but subcooled and saturated regimes are nonetheless distinguished in the comparisons. An additional model that is valid only in annular flow is also assessed.

Investigated correlations: the consistency of experimental data with empirical predictions has been evaluated for various correlations that are presented in Chapter 1, i.e the correlations of Lockhart and Martinelli [1949] (Equation (1.53)), Awad and Muzychka [2010] (Equation (1.81)), Friedel [1979] (Equation (1.58)), and Müller-Steinhagen and Heck [1986] (Equation (1.60)) that give an expression of the two-phase multiplier ϕ_l^2 according to Martinelli parameter X. All assessed correlations are shown in Figure 4.13 for HFE-7000 at atmospheric pressure and saturation temperature.

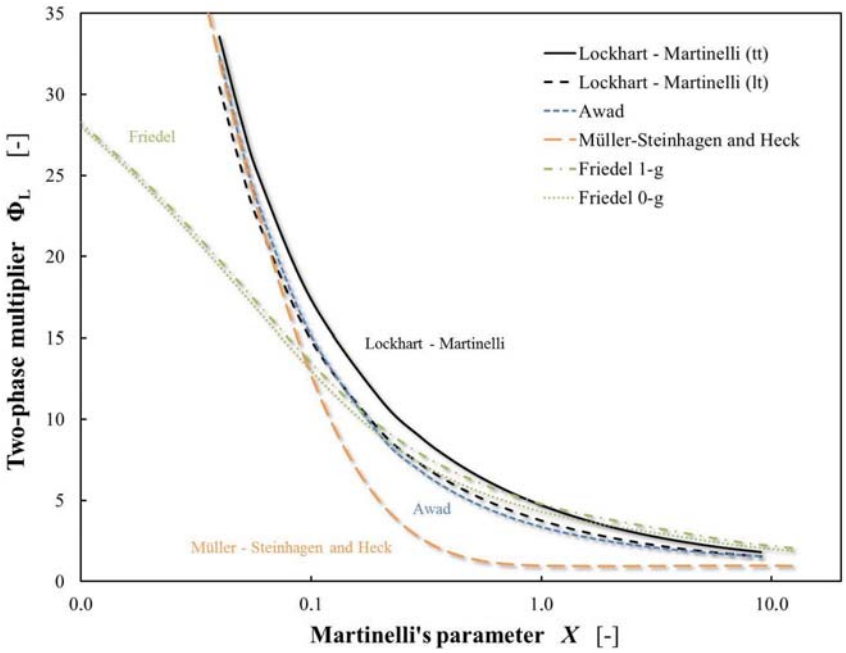

FIGURE 4.13: Predictions of two-phase multiplier according to various empirical correlations, for HFE-7000 at atmospheric pressure and saturation temperature

Lockhart and Martinelli [1949] correlation can be calculated with different coefficients depending on whether each phase exhibits turbulent or laminar behaviour (Equation (1.53)). Two situations are investigated here: the case where both phases are turbulent (Re_v and $Re_l > 2000$, referred to as tt) and the case were only the vapor phase is considered to be turbulent ($Re_v > 2000$ and $Re_l < 2000$, referred to as lt). There are also two possible calculations for the pressure drop predicted by Friedel [1979] (Equation

(1.58)) since it includes a Froude number taking the gravity into account. Two different curves corresponding to 1-g and μ-g are therefore presented.

In subcooled conditions corresponding to $X \gtrsim 1.0$ (low values of x), the four correlations are rather equivalent (except for the version of Müller-Steinhagen and Heck [1986] that predicts slightly lower values), especially when considering that the uncertainty in the measurements is maximal on this particular range of flow parameters. At moderate / high quality, Müller-Steinhagen and Heck [1986] (Equation (1.60)) clearly underpredicts ϕ_l compared to the other curves that are very close. On the contrary, at very high x (lowest values of X), the curves merge but the one predicted by Friedel [1979] that exhibits a different behaviour at the limit.

The prediction method proposed by Awad is equivalent to the one of Lockhart and Martinelli [1949] since it consists in a recent modification of the two-phase multiplier to fit microgravity data. Regarding predictions by Friedel [1979], the influence of the gravity level induces no significant variation in the two-phase multiplier.

Comparison with correlations: for clarity purposes, the experimental two-phase multiplier is presented with the sole correlation of Lockhart and Martinelli [1949] according to X in 1-g (Figure 4.14) and in μ-g (Figure 4.15).

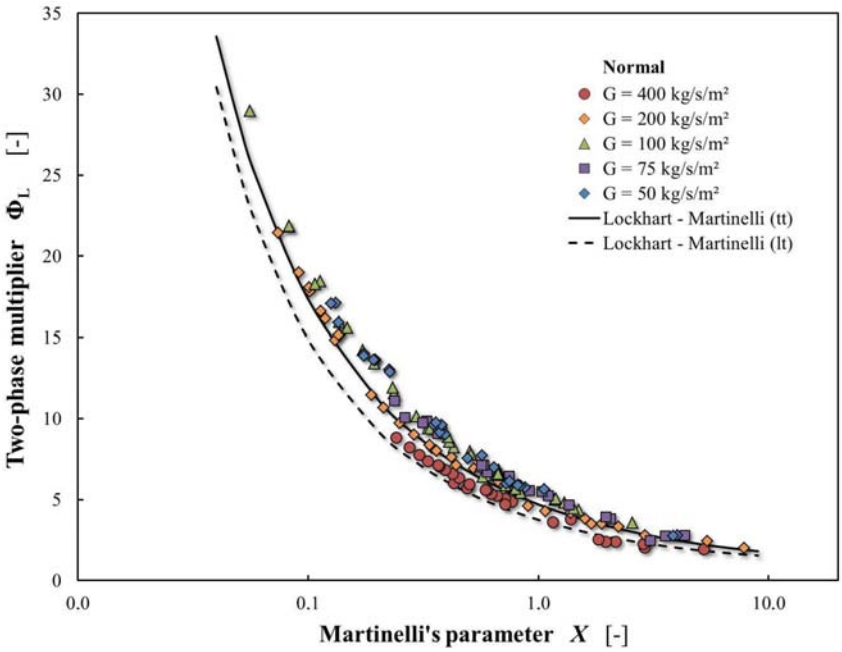

FIGURE 4.14: Experimental two-phase multiplier according to Martinelli parameter for all investigated mass fluxes in 1-g - comparisons with two correlations proposed by Lockhart and Martinelli [1949]

In normal gravity, ϕ_l is rather well described by the correlation at high mass fluxes, with a intermediate coefficient between lt and tt cases. The same observation can be made in microgravity: the influence of the gravity level at $G = 200$ and 400 kg.s^{-1}.m^{-2} is not clearly visible in these graphics. On the other side, behaviours at moderate and low mass fluxes are different according to gravity conditions: in μ-g, where the total pressure gradient only depends on the frictional term, the experimental curve at fixed G shifts down to the lt region predicted by Lockhart and Martinelli [1949] as the mass flux decreases. On the contrary, the additional gravitational contribution plays an important role in 1-g, especially at low mass fluxes, which explains an increase in the two-phase

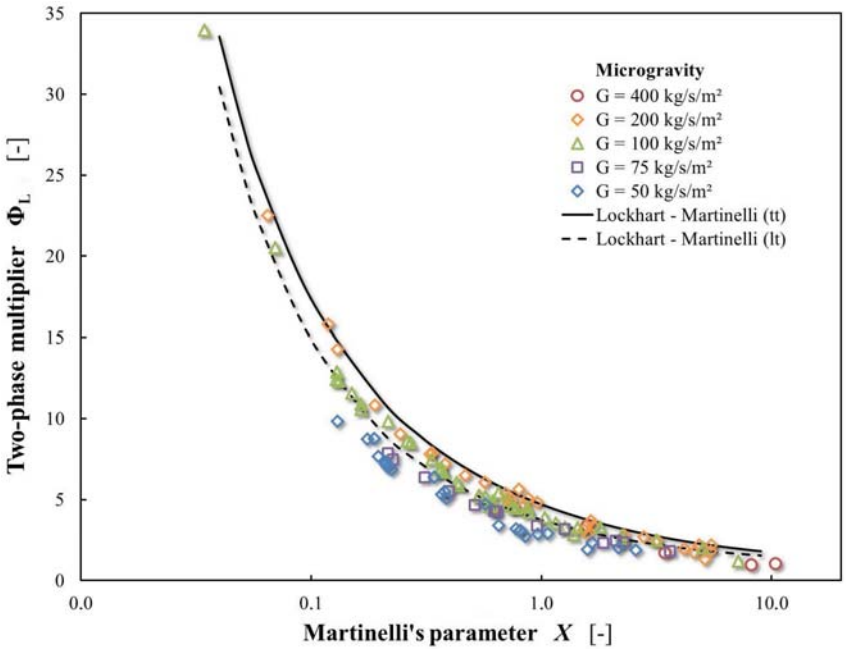

FIGURE 4.15: Experimental two-phase multiplier according to Martinelli parameter for all investigated mass fluxes in μ-g - comparisons with two correlations proposed by Lockhart and Martinelli [1949]

multiplier with a decrease of G in normal gravity. Trends can hardly be distinguished at very low vapor quality (highest values of X) to characterise the influence of G or g.

Whatever the flow parameter range is, the general trend followed by ϕ_l is well described by the correlation of Lockhart and Martinelli [1949], and a simple adjustment of the coefficient C used in the model would allow to properly fit experimental data depending on the mass flux and gravity level.

Further comparisons with correlations are provided thereafter for microgravity and normal gravity conditions, in Figures 4.16 to 4.20, along with corresponding MAE.

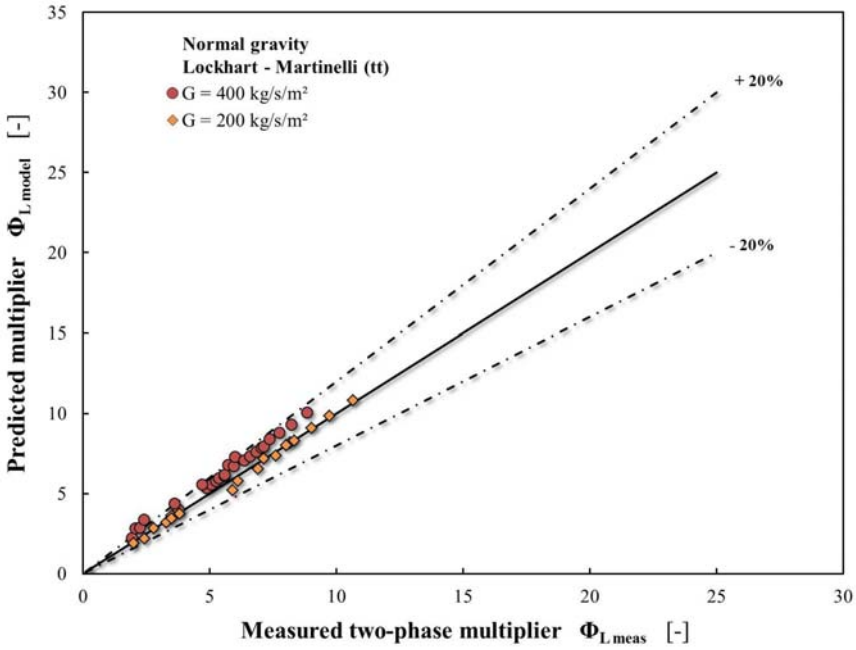

(a) in 1-g, tt case

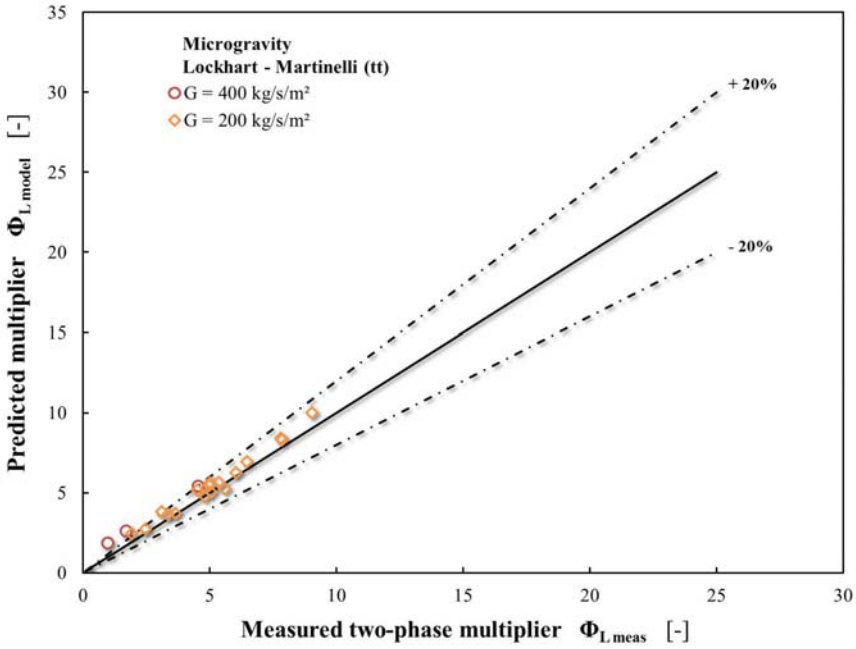

(b) in μ-g, tt case

FIGURE 4.16: Comparison of measured two-phase multiplier and predicted two-phase multiplier using an empirical correlation proposed by Lockhart and Martinelli [1949]

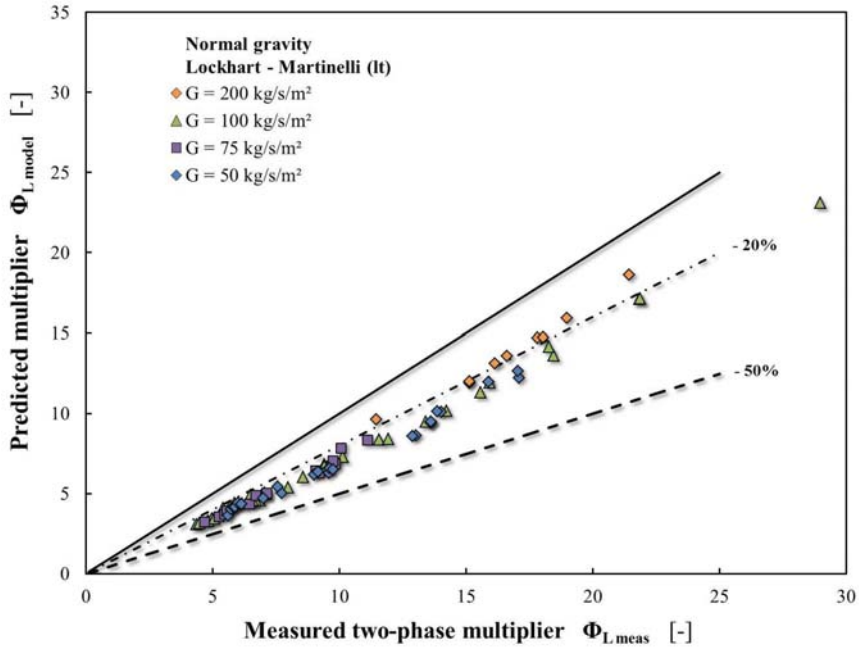

(a) in 1-g, lt case

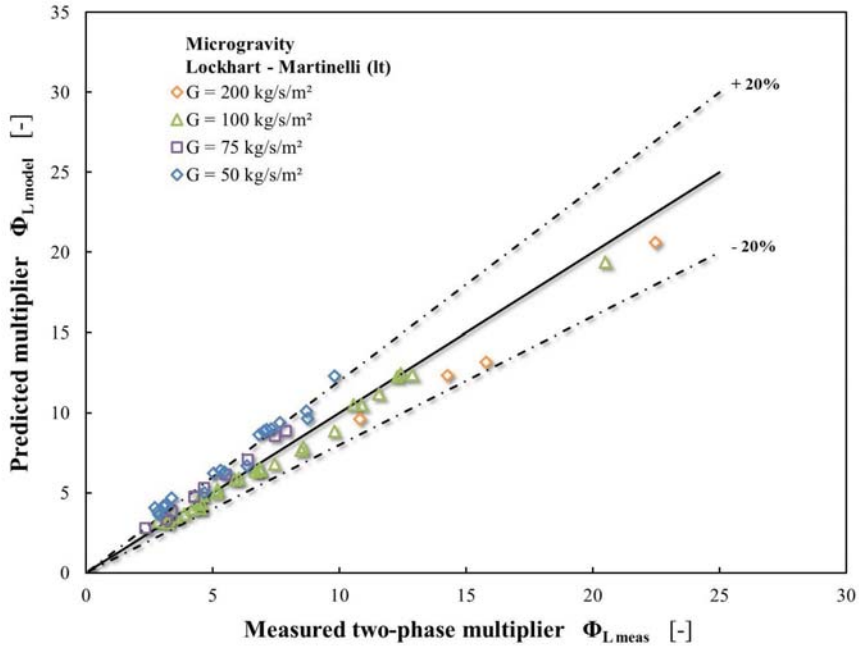

(b) in μ-g, lt case

FIGURE 4.17: Comparison of measured two-phase multiplier and predicted two-phase multiplier using an empirical correlation proposed by Lockhart and Martinelli [1949]

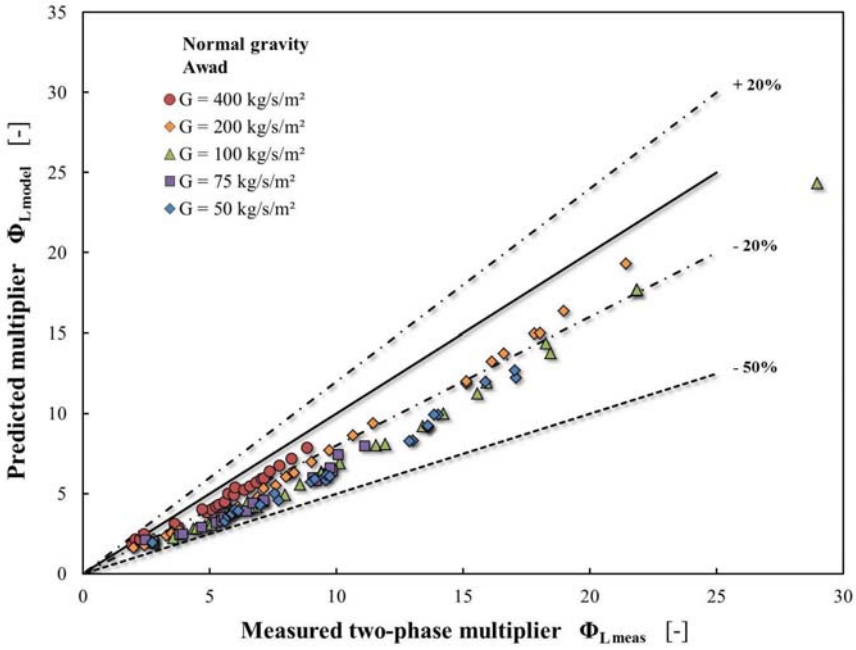

(a) in 1-g

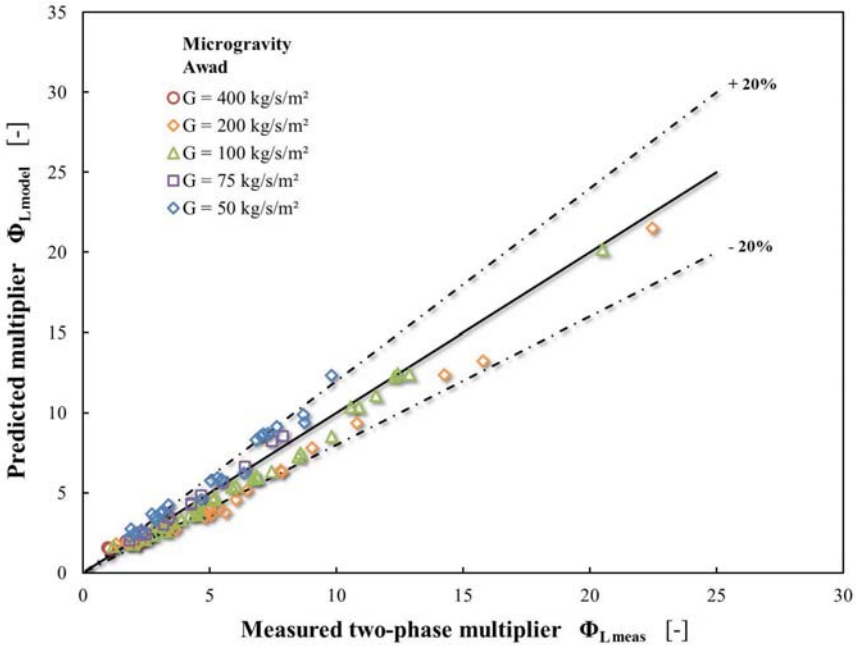

(b) in μ-g

FIGURE 4.18: Comparison of measured two-phase multiplier and predicted two-phase multiplier using an empirical correlation proposed by Awad and Muzychka [2010]

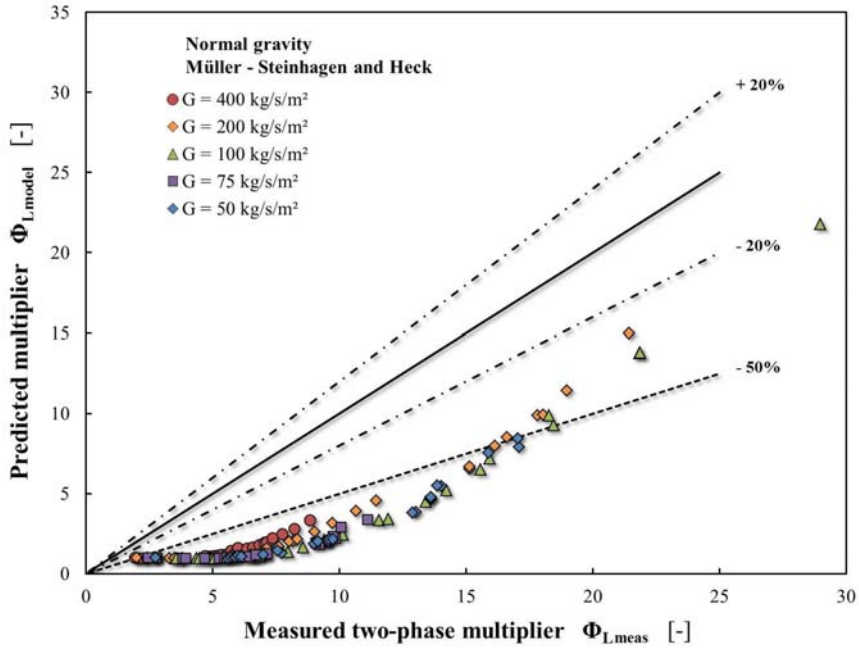

(a) in 1-g

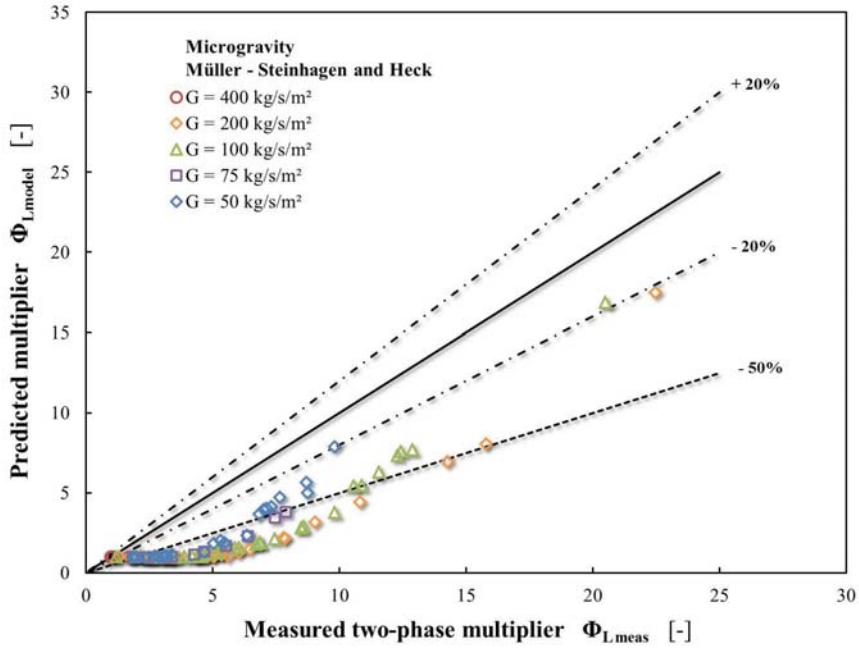

(b) in μ-g

FIGURE 4.19: Comparison of measured two-phase multiplier and predicted two-phase multiplier using a correlation proposed by Müller-Steinhagen and Heck [1986]

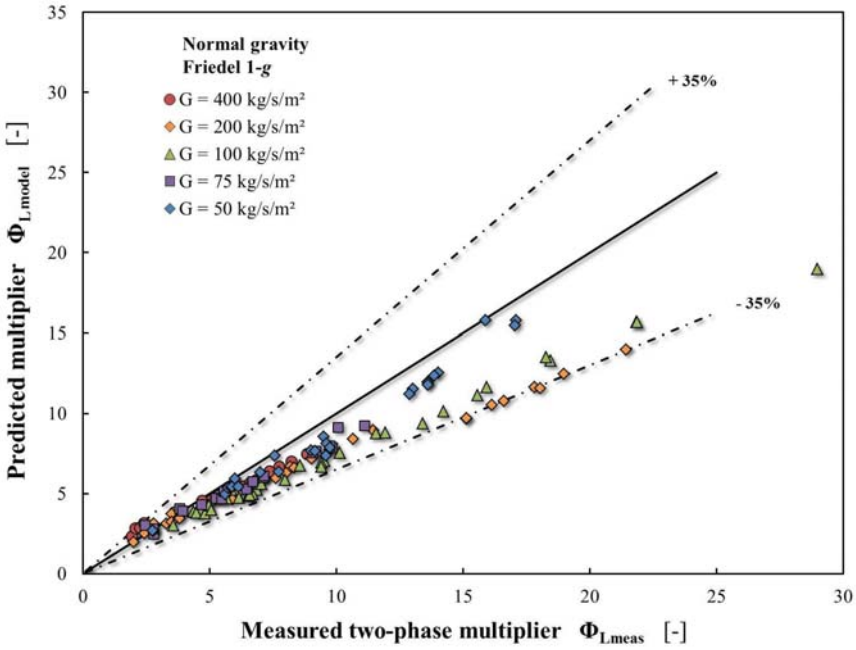

(a) in 1-g, 1-g correlation

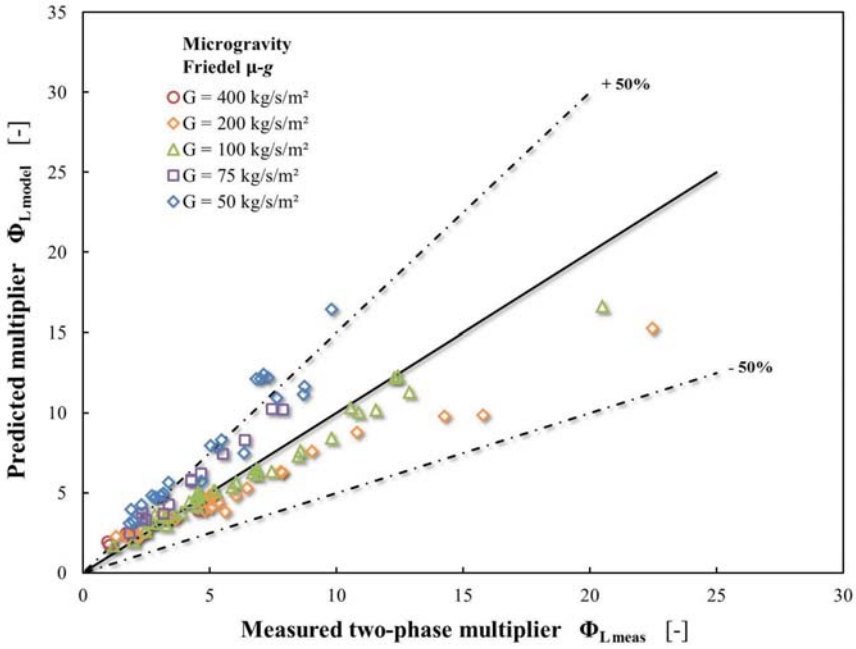

(b) in μ-g, μ-g correlation

FIGURE 4.20: Comparison of measured two-phase multiplier and predicted two-phase multiplier using an empirical correlation proposed by Friedel [1979]

Cioncolini model: the annular flow model that has been developed by Cioncolini and Thome [2009] includes a method to predict two-phase frictional pressure drop in this kind of regime, as presented in Equation (1.61) (as a matter of fact, this expression of the wall shear stress is necessary to calculate the liquid film thickness previously investigated through the same model). Figures 4.21 and 4.22 show a comparison between experimental friction velocity $u^* = \sqrt{\tau_w/\rho_l}$ and values predicted by the correlation in saturated boiling, both under normal gravity and microgravity conditions. Mass fluxes corresponding to turbulent films and errors bars are indicated.

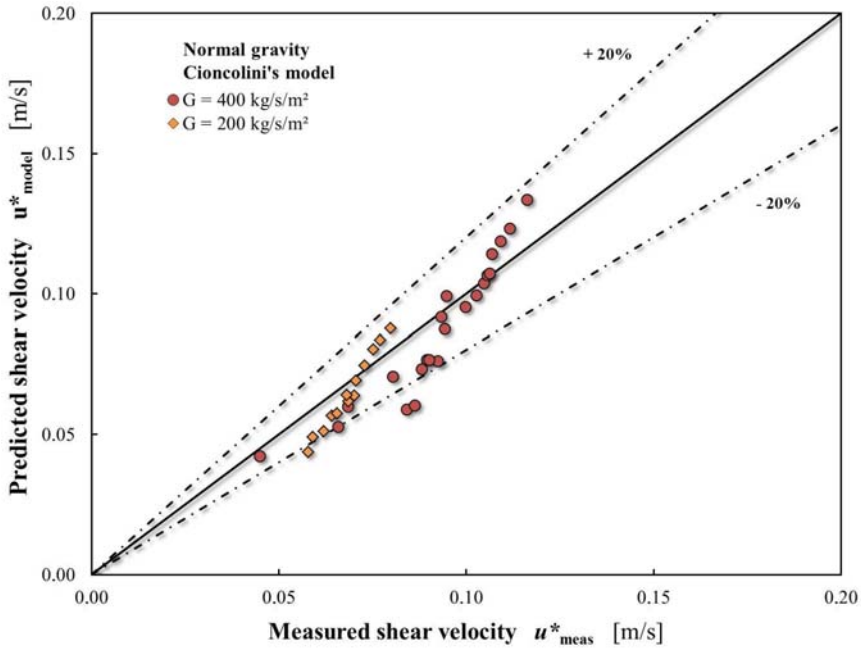

FIGURE 4.21: Comparison of measured friction velocity and predicted friction velocity in 1-g using a model proposed by Cioncolini and Thome [2009]

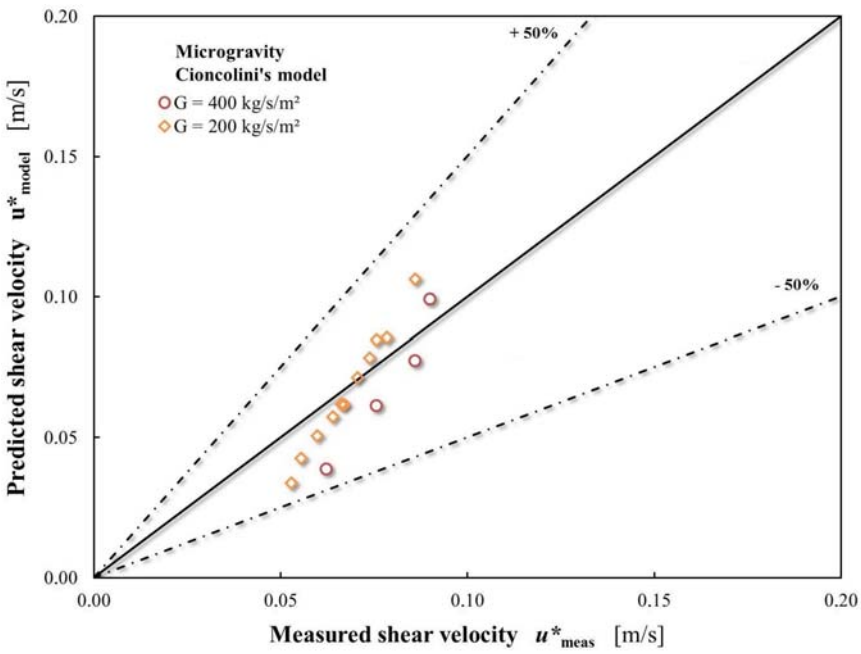

FIGURE 4.22: Comparison of measured friction velocity and predicted friction velocity in μ-g using a model proposed by Cioncolini and Thome [2009]

In normal gravity, all mass fluxes exhibit the same trend (with quantitative differences due to changes in the velocities): at moderate quality, near the transition from slug flow, the model underpredicts u^*, and the discrepancy between model and experiments gets smaller as G decreases (it is about -20% at G = 400 kg.s^{-1}.m^{-2}, and only -12% at G = 200 kg.s^{-1}.m^{-2}). At moderate and high x, the correlation is in very good agreement with experimental points (with errors lower than 10%). Finally, as the vapor quality increases towards very high x, the difference between the model and experimental u^* increases, but still in reasonable extent. As a general observation, the friction velocity u^* in 1-g is well predicted by Cioncolini's model, with a maximal error of 25% on the whole range of vapor quality.

In microgravity, the evolution of u^* is the same than in 1-g but with slightly smaller values of measured friction velocity at low vapor quality. As a consequence, the prediction of the model on this range of quality is not as good as in 1-g, with errors up to 40%. For high values of x, similar observations can be made for the two gravity levels.

The model established by Cioncolini and Thome [2009] can therefore be used to predict the friction velocity u^* for flow regimes corresponding to turbulent liquid films with a rather good accuracy, both under normal gravity and microgravity conditions (since τ_w is similar in the two gravity levels at high mass fluxes).

Summary: comparisons previously drawn between two-phase experimental pressure drop data and correlations are summarised in Tables 4.4 (for subcooled runs) and 4.5 (for saturated runs) with indications of MAE in % for each mass flux G and each gravity level. For each series of points, the correlation that better fits the dataset is indicated in bold, in blue (for 1-g data) or in purple (for μ-g data).

In subcooled boiling, the accuracy on measurements and the differences in various models are not important enough to enable the validation of one correlation over the others. The correlation proposed by Lockhart and Martinelli [1949] seems nonetheless in good agreement with experimental μ-g data (with MAE between 5 and 20%), especially at moderate and low G for lt cases (except for the series at $G = 50$ kg.s^{-1}.m^{-2} that exhibits less subcooled runs than for other G). For 1-g data, Lockhart and Martinelli [1949] in tt case rather well fits data at high, while Friedel [1979] version can be chosen over other correlations for low G. Whatever the gravity level is, the expression proposed by Müller-Steinhagen and Heck [1986] significantly underpredicts the friction, with MAE higher than 50%.

In saturated boiling, the uncertainty in measurements is smaller but the influence of the mass flux or the gravity level makes hardly possible to chose a general correlation over the others. For example, in 1-g, the expression established by Lockhart and Martinelli [1949] or the one of Friedel [1979] with $g = 9.81$ m.s^{-1} can be used depending on the range of vapor quality or mass flux, with MAE around 5%. The modified correlation of Awad and Muzychka [2010] provides a suitable prediction of μ-g data for any flow parameter setting but the original correlation of Lockhart and Martinelli [1949] in the turbulent / turbulent case may be preferred as high mass fluxes. Finally, Müller-Steinhagen and Heck [1986] model gives the worst predictions at moderate and high vapor qualities by significantly underpredicting the pressure drop.

As previously mentioned, a correlation in the form of the expression determined by Lockhart and Martinelli [1949] would enable to fit 1-g and μ-g data, and describe the influence of the mass flux by using a coefficient C depending on G and g (which may be done through a Froude number, for example).

	$G = 400$		$G = 200$		$G = 100$		$G = 75$		$G = 50$	
	1-g	μ-g	1-g	μ-g	1-g	μ-g	1-g	μ-g	1-g	μ-g
Lockhart and Martinelli [1949], *tt* case	22.3	**16.4**	**5.3**	**14.9**	-	-	-	-	-	-
Lockhart and Martinelli [1949], *lt* case	-	-	-	-	28.8	**8.2**	28.2	**11.0**	29.3	**35.9**
Awad and Muzychka [2010]	**11.1**	36.7	27.4	18.7	35.7	14.1	34.1	13.4	35.2	23.1
Friedel [1979], 1-g	18.1	66.1	20.3	21.5	**18.0**	16.7	**10.2**	50.4	**6.2**	89.1
Friedel [1979], μ-g	15.3	56.3	24.5	16.5	26.0	10.0	15.7	35.5	15.2	70.4
Müller-Steinhagen and Heck [1986]	66.7	30.3	71.8	64.8	80.9	60.9	74.7	64.0	77.2	59.3
Cioncolini and Thome [2009]	-	-	-	-	-	-	-	-	-	-

TABLE 4.4: Mean absolute error (MAE, in %) between BRASIL experimental two-phase multiplier and two-phase multiplier predicted by various correlations and models in subcooled boiling conditions

	$G = 400$		$G = 200$		$G = 100$		$G = 75$		$G = 50$	
	1-g	μ-g	1-g	μ-g	1-g	μ-g	1-g	μ-g	1-g	μ-g
Lockhart and Martinelli [1949], tt case	12.9	19.1	**2.6**	**5.7**	**12.4**	15.9	**11.2**	38.4	15.3	48.0
Lockhart and Martinelli [1949], lt case	**8.9**	**4.9**	18.5	13.1	27.5	**4.3**	28.2	12.6	30.7	20.9
Awad and Muzychka [2010]	15.7	14.3	20.6	16.5	29.9	8.4	33.2	**5.9**	34.1	**15.3**
Friedel [1979], 1-g	12.5	5.7	30.5	18.3	26.7	7.0	15.9	43.0	**12.2**	61.6
Friedel [1979], μ-g	19.0	14.2	34.4	23.3	31.1	9.9	22.4	32.9	17.4	51.7
Müller-Steinhagen and Heck [1986]	73.0	76.5	60.5	62.5	65.8	56.5	77.9	62.2	70.9	51.8
Cioncolini and Thome [2009]	7.4	16.2	13.2	11.5	-	-	-	-	-	-

TABLE 4.5: Mean absolute error (MAE, in %) between BRASIL experimental two-phase multiplier and two-phase multiplier predicted by various correlations and models in saturated boiling conditions

4.3.2 Interfacial shear stress

In saturated boiling corresponding to annular flow, the main features of the liquid film flowing at the wall are controlled by interfacial and wall shear stresses. Modelling the interfacial friction is therefore necessary to apprehend boiling mechanisms in these regimes.

Influence of liquid entrainement: since the calculation of τ_i is made using the momentum balance equation for the vapor phase, the liquid fraction entrained in the vapor core has to be evaluated. As discussed in previous sections, even if the entrainment rate e cannot be neglected on all flow parameter ranges, droplet entrainment has almost no influence on the liquid film thickness.

In the same way, the liquid entrainment does not induce a significant change in the calculations of τ_i, neither in 1-g nor in μ-g, since the entrained liquid fraction α_{le} that appears in the calculation of the interfacial shear stress (Equation (1.27)) is very small compared to α. In the two gravity levels, the difference in τ_i between the case with entrainement and the case without entrainement is lower than 2%, whatever the mass flux or vapor quality is, which can be neglected since it is significantly smaller than the uncertainty in τ_i itself.

Comparisons with model: the interfacial shear stress can be plotted according to different flow parameters. Several two-phase correlations provide an expression of the interfacial friction factor f_i according to the liquid film thickness δ or void fraction α, such as the Wallis correlation that is given by:

$$f_i = 0.005 \cdot \left(1 + 300 \cdot \frac{\delta}{D}\right) \tag{4.16}$$

To provide a better description of interfacial shear stress in annular gas-liquid flow under microgravity conditions, Bousman and Dukler [1993] proposed a expression of f_i/f_v according to the void fraction, f_v being the single phase gas flow friction factor calculated versus $Re_v = j_v.D/\nu_v$ (Equation (1.41)):

$$\frac{f_i}{f_v} = 211.4 - 245.9\alpha \tag{4.17}$$

However, this linear trend was fitted from experimental data corresponding to annular and slug-annular flows exhibiting void fraction values between 0.7 and 0.85, and authors claim it not to be able to predict interfacial shear stress at higher α.

Figure 4.23 presents experimental 1-g and μ-g interfacial shear stress data according to liquid film thickness at various mass fluxes, with comparisons with the correlations of Wallis [1969] and Bousman and Dukler [1993] (the latter being plotted in its validity range $0.7 < \alpha < 0.85$). In 1-g, the Wallis correlation is not well-suited for the description of experimental interfacial friction factor, whatever the mass flux is. For this gravity level, the expression of Bousman and Dukler [1993] provides a good qualitative prediction of the evolution of f_i/f_v according to δ on the range of α determined by the authors, with a good agreement with quantitative values at $G = 200$ kg.s^{-1}.m^{-2}. This clearly shows that the ratio f_i/f_v not only depends on δ but also on the mass flux G. In μ-g, the Wallis correlation largely overpredicts the experimental values, whatever the mass flux is. A larger discrepancy with Bousman and Dukler [1993] correlation is observed compared to 1-g conditions.

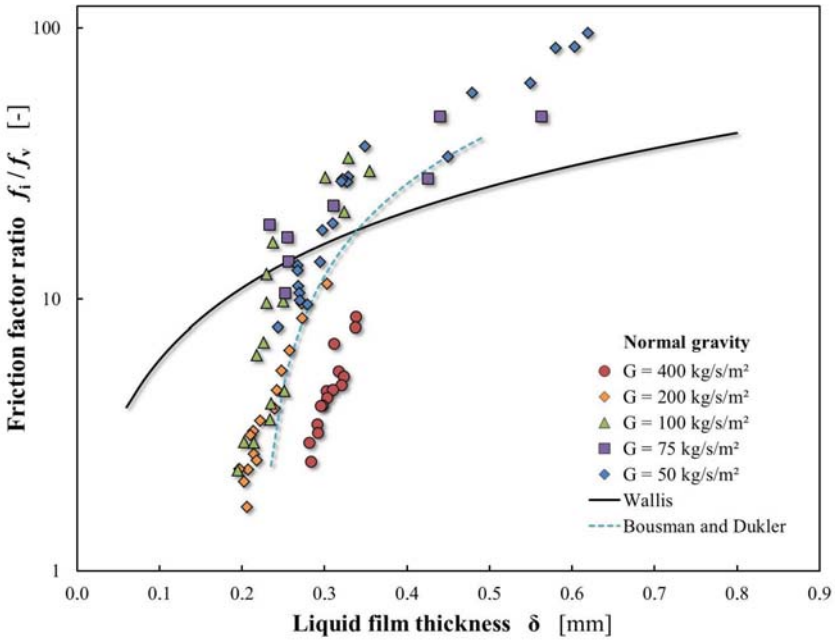

(a) in 1-g

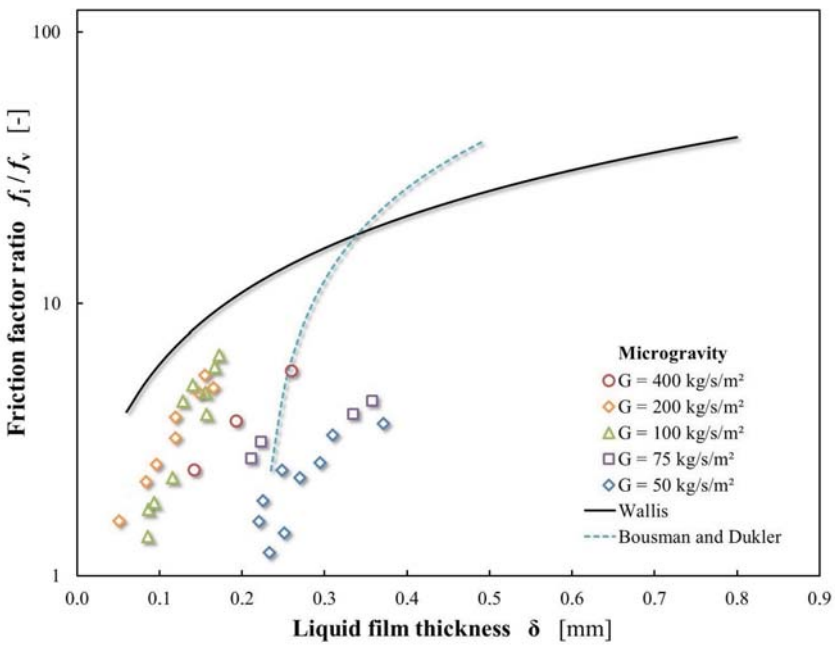

(b) in μ-g

FIGURE 4.23: Interfacial friction factor for various mass fluxes according to the liquid film thickness - comparisons with two empirical correlations

In Figure 4.24, the experimental values of f_i/f_v are plotted versus the vapor Reynolds number Re_v based on the superficial vapor velocity and the diameter of the vapor core, for all investigated mass fluxes under normal gravity and microgravity conditions. In the two gravity levels, f_i/f_v is a decreasing power function of Re_v. In 1-g, the ratio $f_i/f_v \sim Re_v^{-1.3}$ and seems to be almost not impacted by the mass flux at low and moderate mass fluxes, while in μ-g the power seems to slightly evolve with the mass flux. The dependency of f_i/f_v with Re_v proves that the turbulent regimes of the vapor core is not fully rough. Moreover, for a given value of Re_v, the dimensionless interfacial

friction factor is lower in μ-g than in 1-g, with a difference that increases as the mass flux decreases.

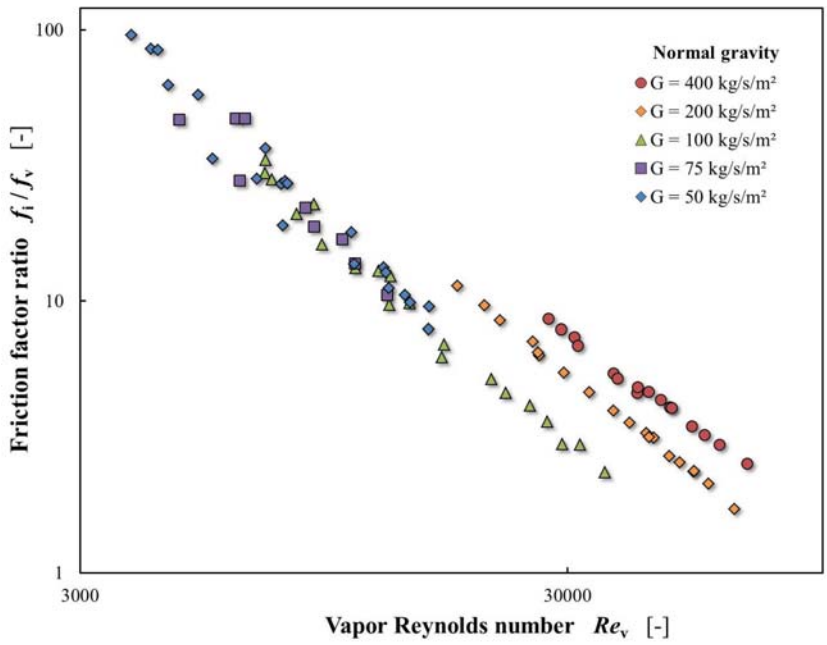

(a) in 1-g

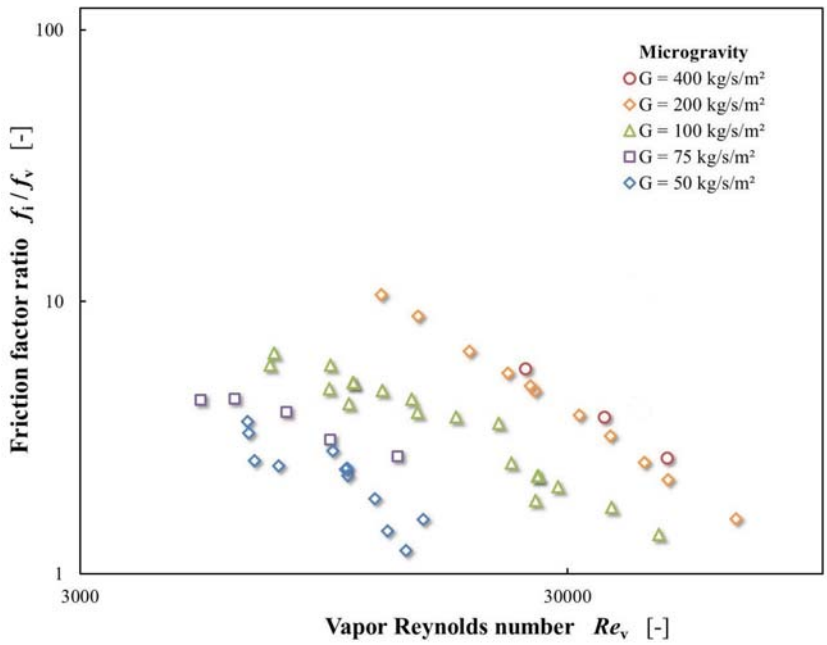

(b) in μ-g

FIGURE 4.24: Interfacial friction factor for various mass fluxes according to the vapor Reynolds number

Influence of the gravity level: experimental results highlight the fact that the interfacial shear stress is clearly affected by changes in the gravity level. Ohta [2003] proposed a correlation to predict the behaviour of the interfacial friction term in microgravity compared to normal gravity, as presented in Equation (1.83):

$$\frac{f_{i,1g}}{f_{i,\mu g}} = 1 + 0.08 \cdot \left(\frac{1-x}{x}\right)^{0.9} \cdot Fr^{-1} \tag{4.18}$$

According to the authors, the ratio $f_{i,1g}/f_{i,\mu g}$ depends on the vapor quality x and on a Froude number Fr calculated with the superficial liquid velocity. This expression is confronted with experimental data in Figure 4.25. It must be noted that the accuracy on the friction factor ratios that are plotted here is not as good as on other experimental results on τ_i or f_i since it requires to find 1-g and μ-g runs in the exact same conditions (of pressure, mass flux, vapor quality...); averaged ratios have been calculated with experimental points exhibiting differences $\Delta p < 0.2$ bar, $\Delta G < 10$ kg.s^{-1}.m^{-2} and $\Delta x < 0.01$.

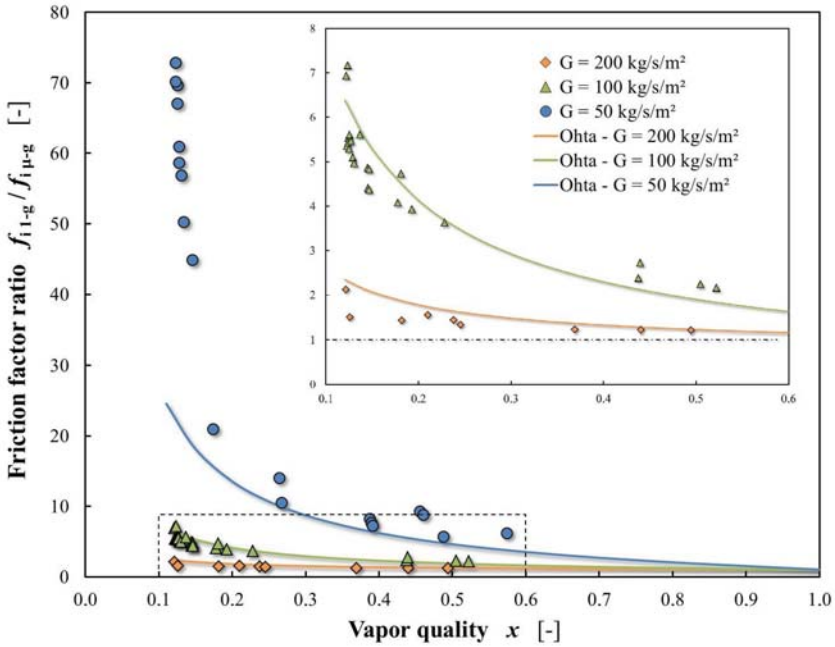

FIGURE 4.25: Ratio of 1-g interfacial friction factor over μ-g interfacial friction factor according to vapor quality - comparison with a model proposed by Ohta [2003]

According to Figure 4.25, the correlation proposed by Ohta provides a rather accurate description of the influence of microgravity conditions on interfacial friction factor: at high and moderate mass fluxes, experimental data are in good agreement with the correlation on the whole range of vapor quality. At low mass flux, Equation (1.83) can be used to predict $f_{i,1g}/f_{i,\mu g}$ at high x. However, at these mass fluxes, the model clearly underpredicts the friction factor ratio near the transition from slug flow ($0.13 < x < 0.16$). It can nonetheless be stated that the model proposed by Ohta [2003] is well-suited for describing the influence of the gravity level on the interfacial shear stress.

Attempt of experimental data fitting: as suggested by Lopez and Dukler [1986], the dependency on both roughness and Reynolds number is characteristic of a transition between smooth and fully rough turbulent regimes. For this partly rough turbulent regime, Fore et al. [2000] proposed a correction of the Wallis correlation introducing a function of the vapor Reynolds number as $1 + A/Re_v$.

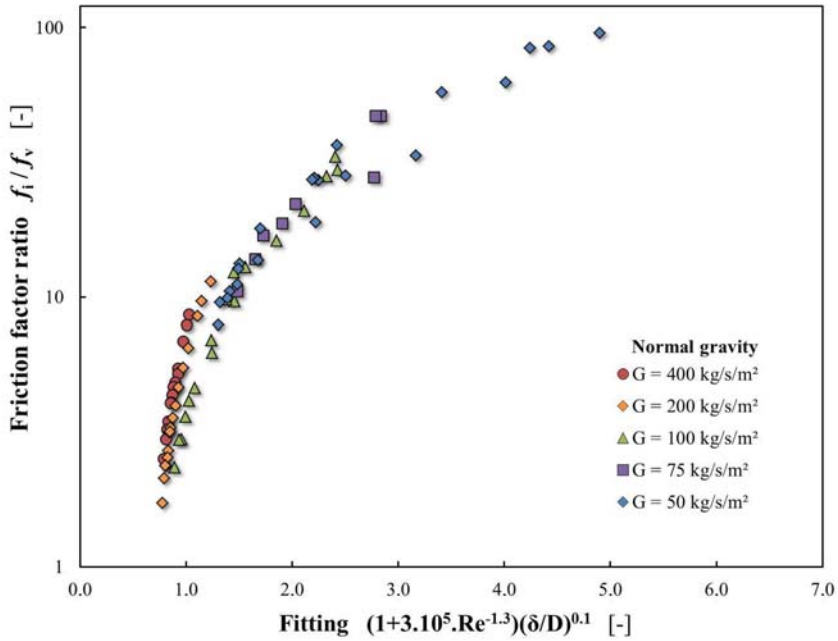

FIGURE 4.26: Attempted fitting of experimental interfacial friction factor in 1-g according to the liquid film thickness and the vapor Reynolds number

Following this approach, a relation between f_i/f_v, Re_v and δ is proposed. In Figure 4.26, f_i/f_v is plotted in normal gravity versus $(1+3.10^5.Re_v^{-1.3})(\delta/D)^{0.1}$. The power of the vapor Reynolds number is equal to -1.3, and the power of the dimensionless liquid film thickness is much smaller than in the Wallis correlation. This expression allows to gather the experimental points around the curve corresponding to Equation (4.19).

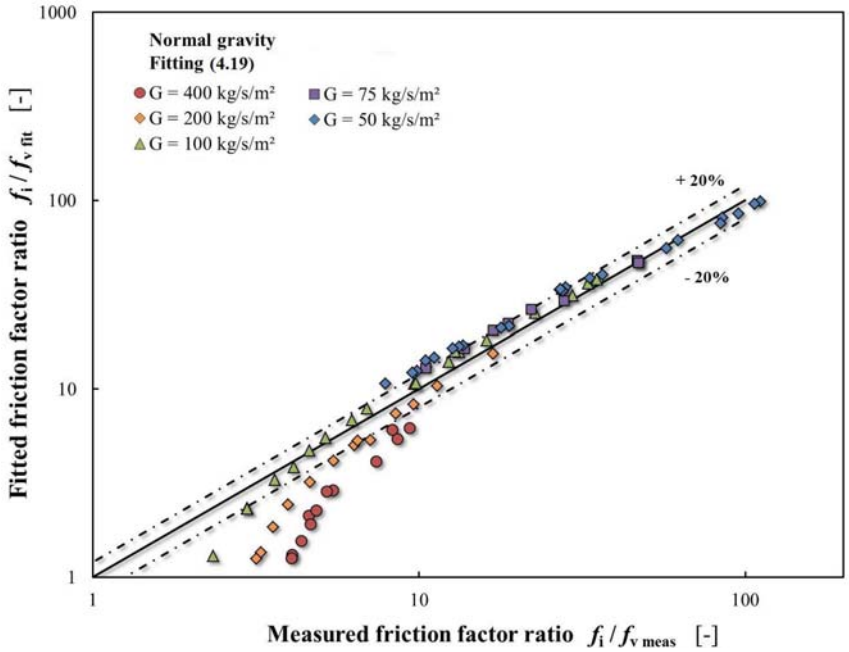

FIGURE 4.27: Comparison between experimental friction factor and predictions provided by the fitting for various mass fluxes in 1-g

$$\frac{f_i}{f_v} = 1 + 18.3\left[\left(1 + \frac{3.10^5}{Re_v^{1.3}}\right) \cdot \left(\frac{\delta}{D}\right)^{0.1} - 0.89\right] \tag{4.19}$$

In 1-g, Equation (4.19) provides a reasonable prediction of the interfacial friction fractor at moderate and low mass fluxes on the whole range of vapor quality corresponding to annular flow, as can be seen from Figure 4.27 with error bars at ± 20%. However, it overestimates the interfacial shear stress at high G and very high x. For this particular range of flow parameters, an adjustment of the coefficients is necessary to fit experimental data.

For the prediction of f_i/f_v in microgravity, another approach can be chosen: since the fitting of f_i/f_v (Equation (4.19)) provides a suitable description of interfacial friction factors in 1-g and since the model proposed by Ohta (Equation (4.18)) correctly assesses the influence of the gravity level on f_i, it is possible to determine a general expression of the dimensionless interfacial friction factor under microgravity conditions by combining Equations (4.19) and (4.18).

Results of this combination are presented in Figure 4.28, with error bars at ± 20%. Since the fitting of 1-g values was determined on data corresponding to moderate mass fluxes at moderate and high x, the combination of the two equations is not in a very good agreement with data at high mass fluxes and high vapor quality ($G = 200$ and 400 kg.s^{-1}.m^{-2} at $x > 0.25$) or at low mass flux and very high quality ($G = 100$ kg.s^{-1}.m^{-2} and $x > 0.5$). Nevertheless, for intermediate ranges of flow parameters, the prediction of the correlation is rather good: the predicted dimensionless friction factor at $G = 100$ kg.s^{-1}.m^{-2} is in good agreement with experimental values on the whole range of investigated quality, with a maximal error of 21%.

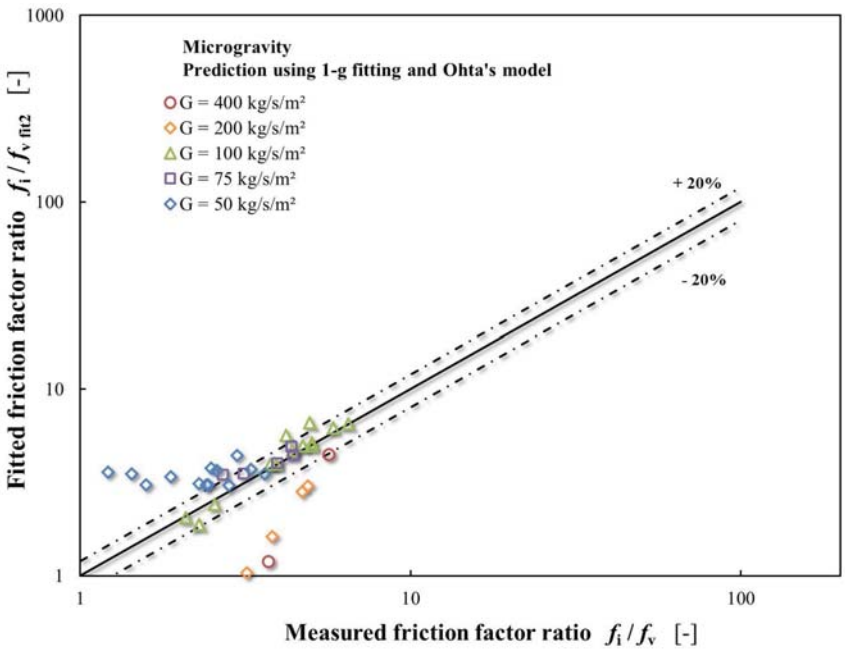

FIGURE 4.28: Comparison between experimental friction factor in microgravity and predictions provided by combining 1-g data fitting and Ohta's model

Evolution of physical quantities: by eliminating the pressure gradient between the momentum balance equations written for the two phases and neglecting the acceleration term, a relation between the void fraction, the wall shear stress and the interfacial shear stress is obtained:

$$-\tau_w.\sqrt{\alpha} + \tau_i - (\rho_l - \rho_v).g.\sqrt{\alpha}.(1-\alpha)\frac{D}{4} = 0 \tag{4.20}$$

where τ_w, τ_i and the gravity acceleration g are positive.

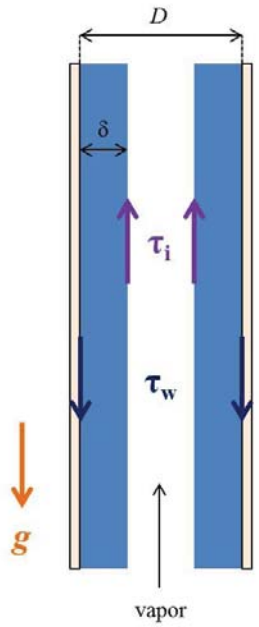

FIGURE 4.29: Schematic representation of shear stresses and gravity terms in annular flow

Then, the first term of Equation (4.20) is negative, the second one positive and the third one negative. In vertical upward flow in normal gravity, the interfacial shear stress has to compensate both gravity and wall shear stress. At high and moderate mass fluxes, τ_i is a little bit larger in normal gravity than in microgravity, but this larger value cannot compensate the gravity term on its own. The first term of Equation (4.20) has therefore to be lower in normal gravity. Since the wall shear stress is about the same in 1-g and μ-g for these values of G, it means that the void fraction has to be lower and the film thickness larger in 1-g, which is in agreement with experimental results. The evolution of the shear stresses and void fraction is also consistent at low mass flux: the increase in τ_i under normal gravity conditions is associated with a significant increase in τ_w.

4.4 Heat transfer coefficient

The heat transfer coefficients in saturated and subcooled boiling under normal gravity and microgravity conditions are deduced from the wall heat flux, and wall and liquid bulk temperatures. Experimental results presented in the previous chapter are thereafter compared to classical correlations. The respective contributions of convective and nucleate boiling are discussed along with the influence of the liquid film thickness on heat transfer coefficients in annular flow.

4.4.1 Comparison with correlations

Some of the correlations used for the prediction of heat transfer coefficient in two-phase flow are not valid for both subcooled and saturated conditions. These two regions are therefore considered separately in the next sections, with saturated regimes mostly corresponding to annular flow. An additional model for the specific case of annular flow is also assessed.

The consistency of experimental data with empirical predictions has been evaluated for five different correlations presented in Chapter 1 or recalled below, i.e. the correlations of Chen [1966] (Equation (1.69)), Kandlikar [1990] (Equation (1.73)), Kim and Mudawar [2013] (Equation (4.21)), Kew and Cornwell [1997] (Equation (1.77)) and Sun and Mishima [2009] (Equation (1.76)). The model proposed by Cioncolini and Thome [2011] for annular flow is also presented.

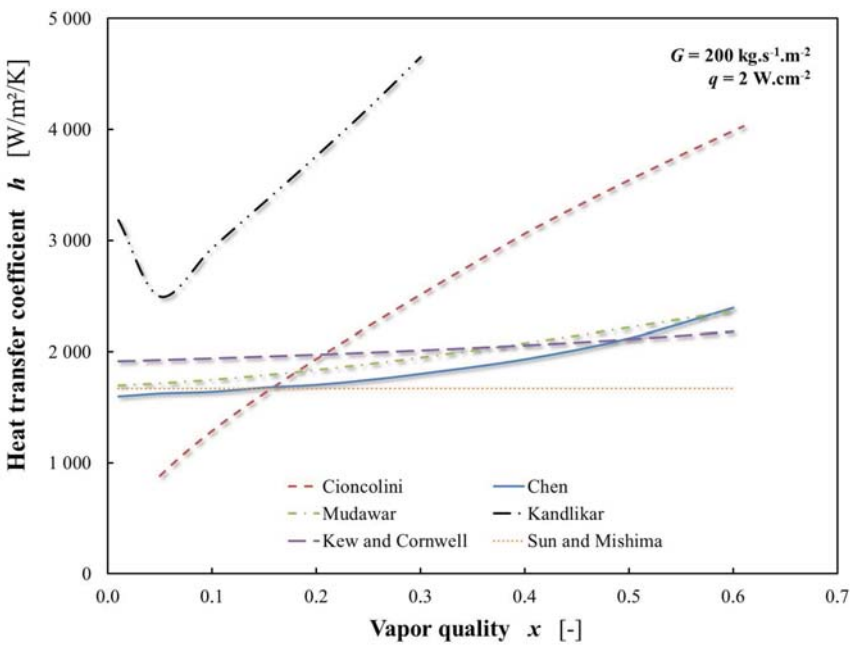

FIGURE 4.30: Predictions of heat transfer coefficient according to various empirical correlations at $G = 200$ kg.s^{-1}.m^{-2} and $q = 2$ W.cm^{-2}

Figures 4.30 and 4.31 show the corresponding predictions of h at $q = 2$ W.cm^{-2} for two different mass fluxes $G = 200$ and 50 kg.s^{-1}.m^{-2}. The Kandlikar correlation always overpredicts the heat transfer coefficient compared to the four other correlations that are consistent, especially at high vapor quality and whatever the mass flux is. The difference between the model proposed by Cioncolini and Thome [2011] and other correlations

depends on G: at $G = 200$ kg.s^{-1}.m^{-2}, it significantly overpredicts h at high x compared to other expressions while it is consistent with predicted values at $G = 50$ kg.s^{-1}.m^{-2} for vapor qualities larger than 0.4.

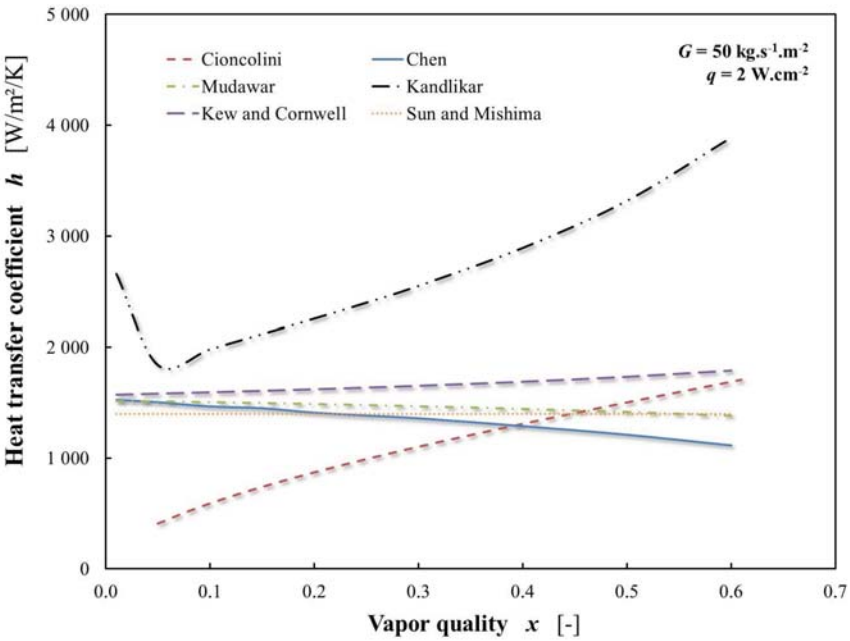

FIGURE 4.31: Predictions of heat transfer coefficient according to various empirical correlations at $G = 50$ kg.s^{-1}.m^{-2} and $q = 2$ W.cm^{-2}

Experimental heat transfer coefficients at $q = 2$ W.cm^{-2} are plotted according to the vapor quality with comparisons to the Kim and Mudawar [2013] and Cioncolini and Thome [2011] correlations, for three different mass fluxes $G = 200$, 100 and 50 kg.s^{-1}.m^{-2} in normal gravity (Figure 4.32) and microgravity (Figure 4.33).

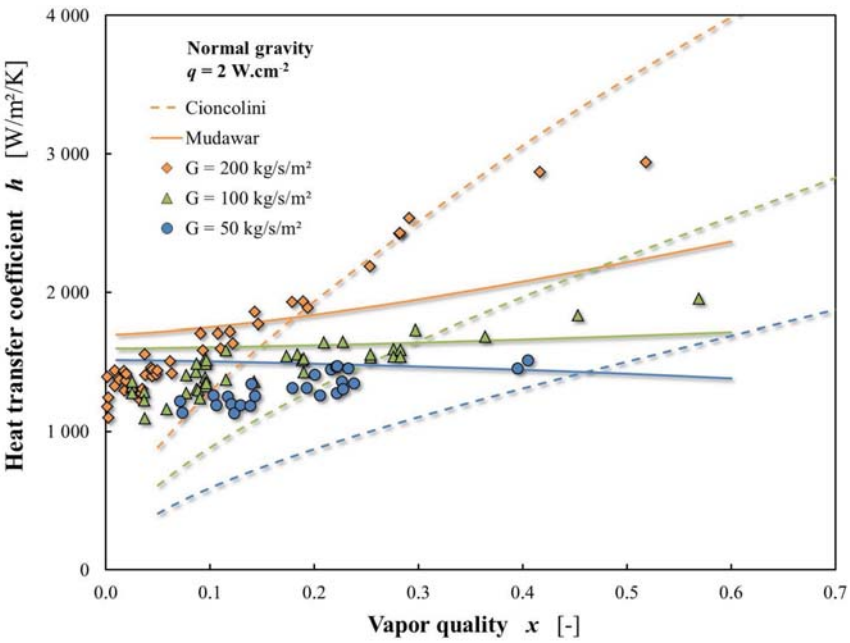

FIGURE 4.32: Experimental heat transfer coefficient according to the vapor quality for three mass fluxes at $q = 2$ W.cm^{-2} in 1-g - comparisons with two empirical correlations

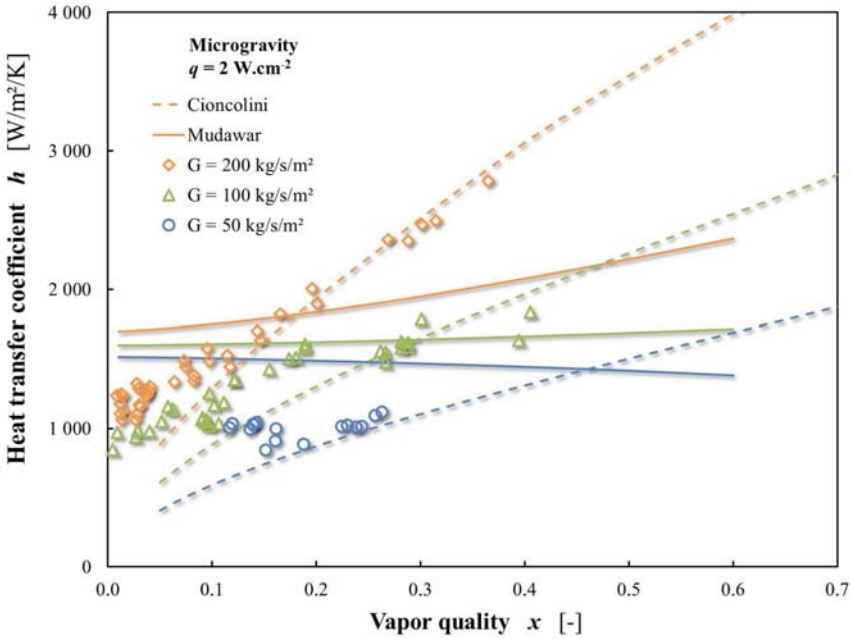

FIGURE 4.33: Experimental heat transfer coefficient according to the vapor quality for three mass fluxes at $q = 2$ W.cm^{-2} in μ-g - comparisons with two empirical correlations

The influence of mass flux or gravity level on h has already been discussed in Chapter 3. In order to evaluate the consistency of predictions with experimental data, each correlation is studied separetely since the gravity level, mass flux, wall heat flux or saturated / subcooled conditions strongly impact the heat transfer coefficient, as shown in Figures 4.32 and 4.33.

4.4.2 Contributions of nucleate and convective boiling

Among the investigated correlations, both Chen and Kim and Mudawar correlations express the heat transfer coefficient h as a combination of a nucleate boiling term and a convective boiling term, referred to as h_{nb} and h_{cb}, respectively. Since the contributions of these terms have been a bit discussed in the presentation of experimental results, it is interesting to compare their evolution.

The calculations have been made with the relation proposed by Kim and Mudawar [2013] because it results in a better agreement with experimental data than the Chen correlation. Corresponding expression is recalled in Equation (4.21):

$$\begin{aligned} h &= \sqrt{h_{nb}^2 + h_{cb}^2} \\ h_{nb} &= h_l.\left[2345.Bo^{0.7}.\frac{p}{p_{crit}}^{0.38}.(1-x)^{-0.51}\right] \\ h_{cb} &= h_l.\left[5.2Bo^{0.08}.We_{lo}^{-0.54} + 3.5\cdot\left(\frac{1}{X}\right)^{0.94}\cdot\left(\frac{\rho_v}{\rho_l}\right)^{0.25}\right] \end{aligned} \tag{4.21}$$

Figure 4.34 shows the total heat transfer coefficient and the convective and nucleate boiling contributions calculated with this empirical correlation for values of vapor quality,

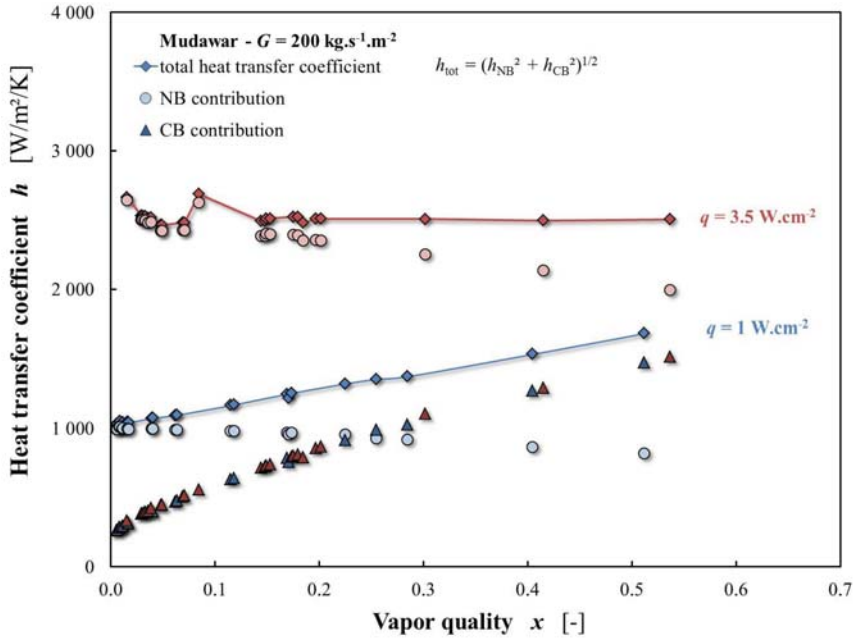

(a) $G = 200$ kg.s^{-1}.m^{-2}

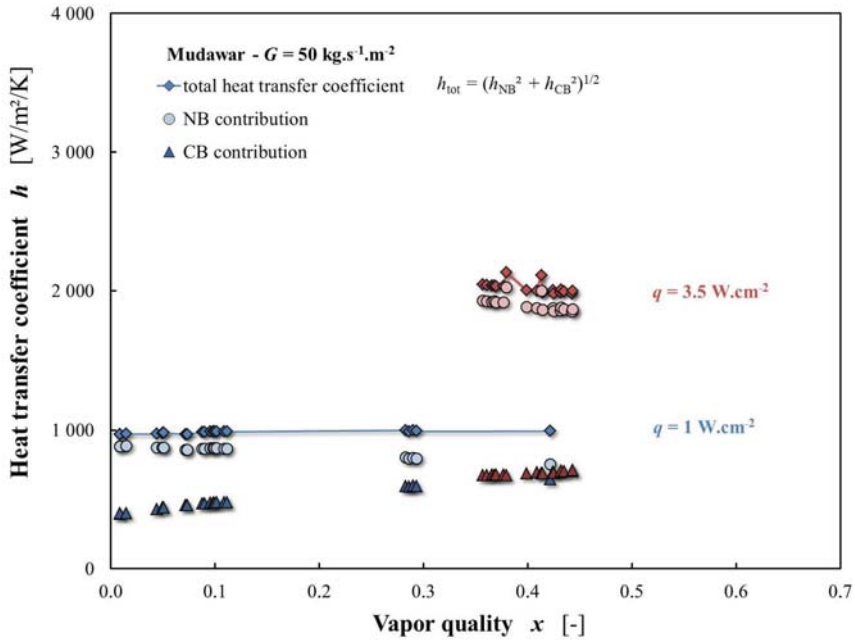

(b) $G = 50$ kg.s^{-1}.m^{-2}

FIGURE 4.34: Contributions of nucleate and convective boiling in the calculations of the heat transfer coefficient as proposed by Kim and Mudawar [2013], according to vapor quality, for two mass fluxes and two wall heat fluxes, in 1-g

velocity and flux corresponding to experimental runs in normal gravity (points corresponding to microgravity conditions are not reported in the graphic; they exhibit the exact same trend than 1-g data since the correlation does not depend on the gravity level). Limit behaviours are illustrated with two different mass fluxes ($G = 200$ and 50 kg.s^{-1}.m^{-2}) and two wall heat fluxes for each G ($q = 1$ and 3.5 W.cm^{-2}).

Despite the fact that the boiling number Bo appears in h_{cb}, the convective term of h is almost independent of the wall heat flux q. It increases with the mass flux, and with the vapor quality. The first term in the bracket in the expression of h_{cb} remains small for the low Boiling numbers of BRASIL experiments; plus, the power on the Boiling number is low (0.08). Opposite trends are observed for the nucleate boiling term: dependency with q, decrease with x and no impact of G.

At $G = 200$ kg.s^{-1}.m^{-2}, the nucleate boiling contribution is clearly dominant in h in subcooled regimes, at any wall heat flux. Despite the strong increase of the convective term with the vapor quality, nucleate boiling is still the main heat transfer mode in saturated regimes at high quality for $q = 3.5$ W.cm^{-2}, according to the correlation. However, at $q = 1$ W.cm^{-2}, the increase of h_{cb} and the decrease of h_{nb} makes the two terms equivalent at moderate x. And for this heat flux, the convective boiling contribution prevails over the nucleate one at high vapor quality. For the two values of q, the combination of the nucleate and convective terms corresponds to an increase of the heat transfer coefficient with the vapor quality.

At $G = 50$ kg.s^{-1}.m^{-2}, h_{nb} is the same than at $G = 200$ kg.s^{-1}.m^{-2}, but the convective term is much smaller (except at very low vapor quality). As a result, the convective boiling contribution is never more important than the one of nucleate boiling. At $q = 3.5$ W.cm^{-2}, h_{nb} is more than two times larger than h_{cb} at very high quality. At $q = 1$ W.cm^{-2}, the two terms are equivalent at high vapor quality. Combining h_{nb} and h_{cb} leads to a heat transfer coefficient that is almost constant on the whole range of x.

The general evolution of the terms due to the two heat transfer modes is in rather good agreement with the observations made on experimental results. However, the contribution of the nucleate boiling term seems to be a bit overpredicted by the correlation proposed by Kim and Mudawar [2013], as discussed thereafter.

4.4.3 Subcooled boiling

Subcooled regimes mostly correspond to bubbly flows, and transition and slug flows. The correlations proposed by Chen [1966] and Kim and Mudawar [2013] can be used to predict the heat transfer coefficient in subcooled conditions since they evaluate a convective boiling and a nucleate boiling term, the latter being dominant in these regimes. The Sun and Mishima [2009] expression of h can also be plotted in this region since it is an empirical correlation independent of x, based on experimental conditions where nucleate boiling is predominant.

Figures 4.35, 4.36 and 4.37 show experimental data compared to heat transfer coefficients predicted by these three correlations, under normal gravity and microgravity conditions, with error bars at $\pm$ 50%. More detailed results can be found in Table 4.6 that presents the mean absolute error between experiment and predictions for each mass flux and each gravity level. In this table, the correlation that suits the best h_{meas} is indicated in bold, in blue for 1-g data and in purple for μ-g data.

In subcooled conditions, the correlation proposed by Kim and Mudawar [2013] provides the best description of the heat transfer coefficient, both under normal gravity and microgravity conditions and for all investigated mass fluxes. The Sun and Mishima [2009] expression gives similar predicted values, which is consistent with the fact that nucleate boiling is predominant at these vapor qualities and that the latter correlation was developed for this kind of regimes.

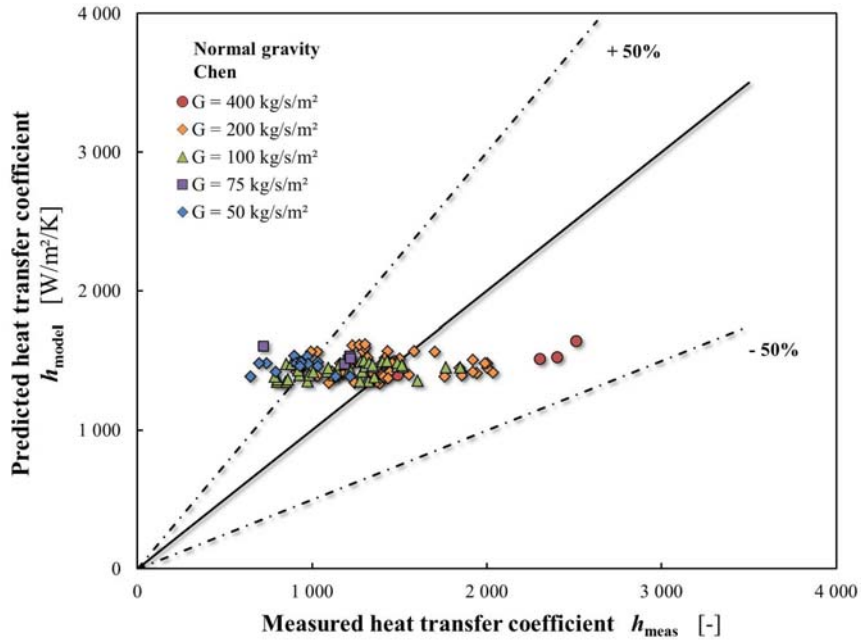

(a) in 1-g

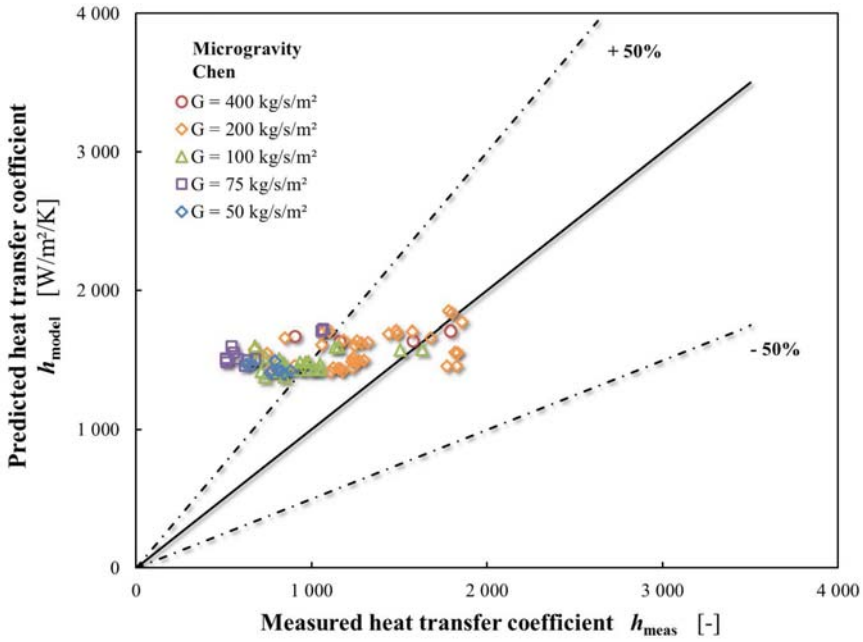

(b) in μ-g

FIGURE 4.35: Comparison of measured heat transfer coefficient and predicted heat transfer coefficient in subcooled boiling using a correlation proposed by Chen [1966]

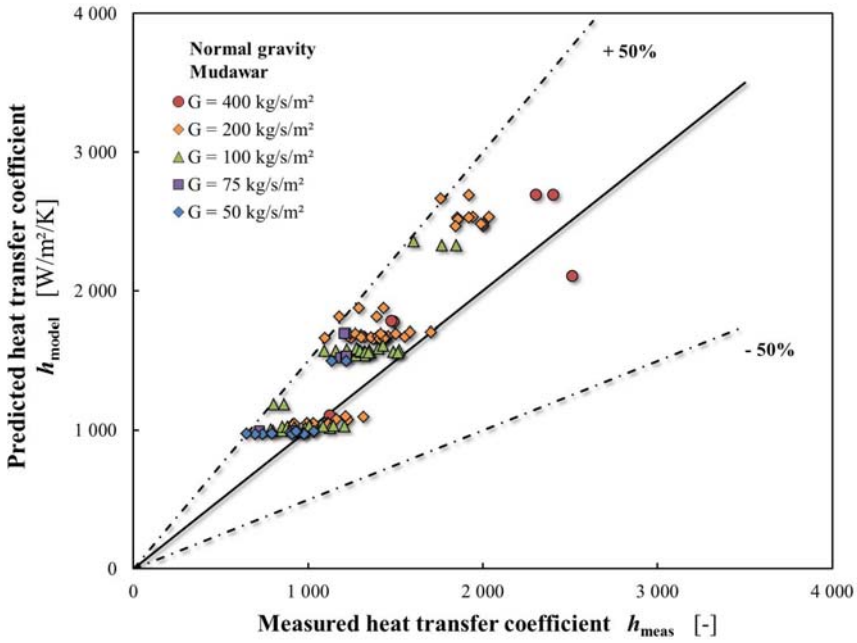

(a) in 1-g

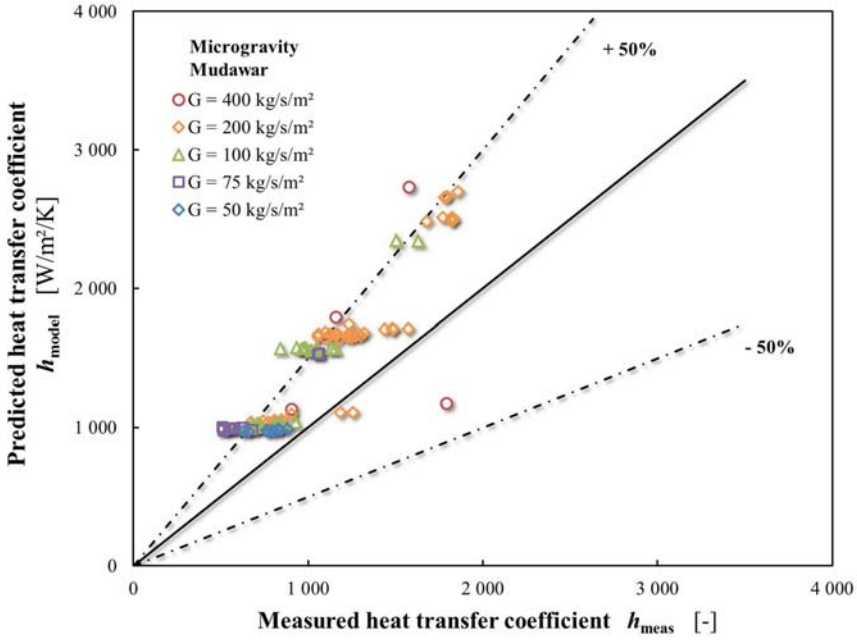

(b) in μ-g

FIGURE 4.36: Comparison of measured heat transfer coefficient and predicted heat transfer coefficient in subcooled boiling using a correlation proposed by Kim and Mudawar [2013]

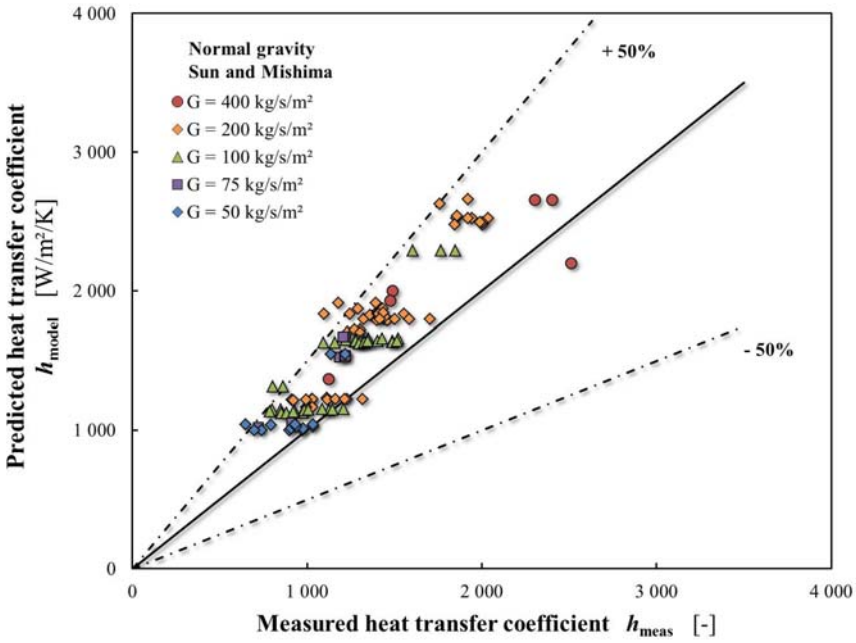

(a) in 1-g

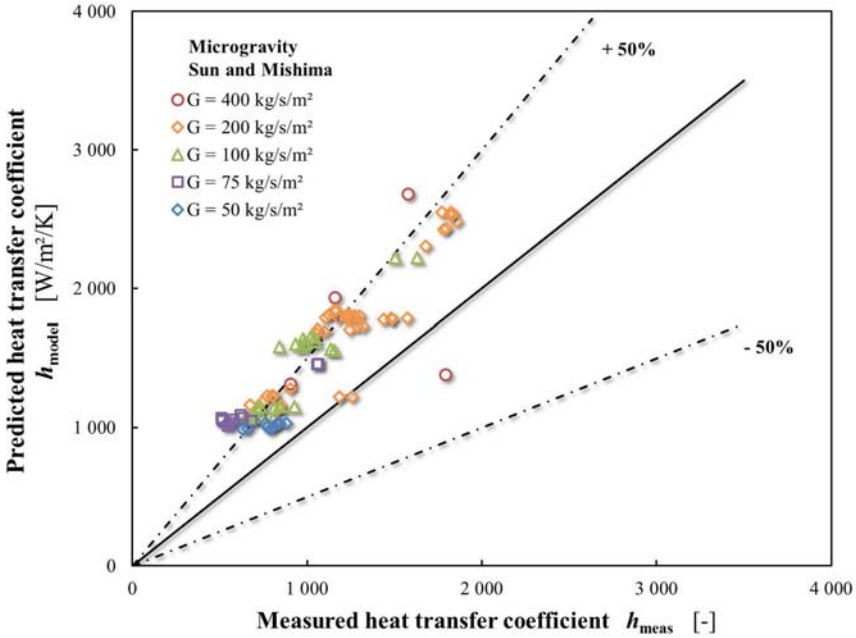

(b) in μ-g

FIGURE 4.37: Comparison of measured heat transfer coefficient and predicted heat transfer coefficient in subcooled boiling using a correlation proposed by Sun and Mishima [2009]

	$G = 400$		$G = 200$		$G = 100$		$G = 75$		$G = 50$	
	1-g	μ-g	1-g	μ-g	1-g	μ-g	1-g	μ-g	1-g	μ-g
Chen [1966]	22.7	48.5	29.2	36.1	26.7	65.6	44.2	148.1	70.4	87.2
Sun and Mishima [2009]	20.8	51.2	27.4	41.8	24.8	51.8	30.3	76.8	18.2	31.0
Kim and Mudawar [2013]	**14.5**	**46.7**	**21.3**	**34.8**	**18.4**	**44.7**	**29.6**	**69.4**	**14.9**	**26.8**

TABLE 4.6: Mean absolute error (MAE, in %) between BRASIL experimental heat transfer coefficients and heat transfer coefficients predicted by various correlations and models in subcooled boiling conditions

Nevertheless, the Kim and Mudawar correlation always overpredicts the heat transfer coefficient. In 1-g, the overestimation amounts to 15 to 25% while predicted h are 30 to 70% larger than experimental data in μ-g. This is due to the fact that heat transfer coefficients in microgravity are significantly lower than in normal gravity in subcooled conditions: in μ-g, bubble diameter at detachment is larger for $G < 400$ kg.s^{-1}.m^{-2} and the frequency of bubble formation is lower. The relative motion of bubble is also smaller than in 1-g, which could explain lower values of h. Since the model used by Kim and Mudawar establishes that nucleate boiling controls the heat transfer coefficient in subcooled regimes (especially at high wall heat flux), it can be deduced than the calculation of h_{nb} presented in Equation (4.21) corresponds to overestimated values. A correction factor may be added in order to reduce the contribution of nucleate boiling.

4.4.4 Saturated boiling

Some correlations relevant for the prediction of heat transfer coefficient in saturated boiling involve both convective boiling and nucleate boiling heat transfer (such as Sun and Mishima [2009], Kew and Cornwell [1997], Kim and Mudawar [2013], Chen [1966], Kandlikar [1990]). Other correlations (Cioncolini and Thome [2011]) only consider the heat transfered by evaporation through the turbulent liquid film in annular flow.

Heat transfer with convective and nucleate boiling: in Figures 4.38 to 4.42, the heat transfer coefficient predicted by the first kind of correlations is plotted according to experimental data, with various error bars. A summary with MAE by mass flux and gravity level is given in Table 4.7. In this table, the correlation that suits the best h_{meas} is indicated in bold, in blue for 1-g data and in purple for μ-g data.

High mass fluxes: at the highest mass flux value ($G = 400$ kg.s^{-1}.m^{-2}), the Kandlikar correlation can be used to predict h in 1-g. However, it clearly overestimates the heat transfer coefficient at lower values of G. On the contrary, the Kim and Mudawar correlation strongly underestimates h at $G = 200$ and 400 kg.s^{-1}.m^{-2}, especially at high vapor quality, which may lead to assume that the contribution of the convective term is underpredicted by the expression of Equation (4.21).

Moderate and low mass fluxes: at $G = 100$, 75 and 50 kg.s^{-1}.m^{-2}, the contribution of the nucleate boiling is significant even in saturated conditions. The correlations that assess the h_{nb} term are therefore more relevant to describe the heat transfer coefficient at these values of G, as can be seen in Table 4.7. 1-g experimental data are in good agreement with the correlations given by Kim and Mudawar [2013] and Sun and Mishima [2009] at moderate and low mass fluxes, except at very high quality where differences of about 25% are observed. The Chen correlation gives similar results. The overestimation of h is a bit more consequent in microgravity (since smaller heat transfer coefficient are exhibited for these mass fluxes in μ-g on the whole range of vapor quality).

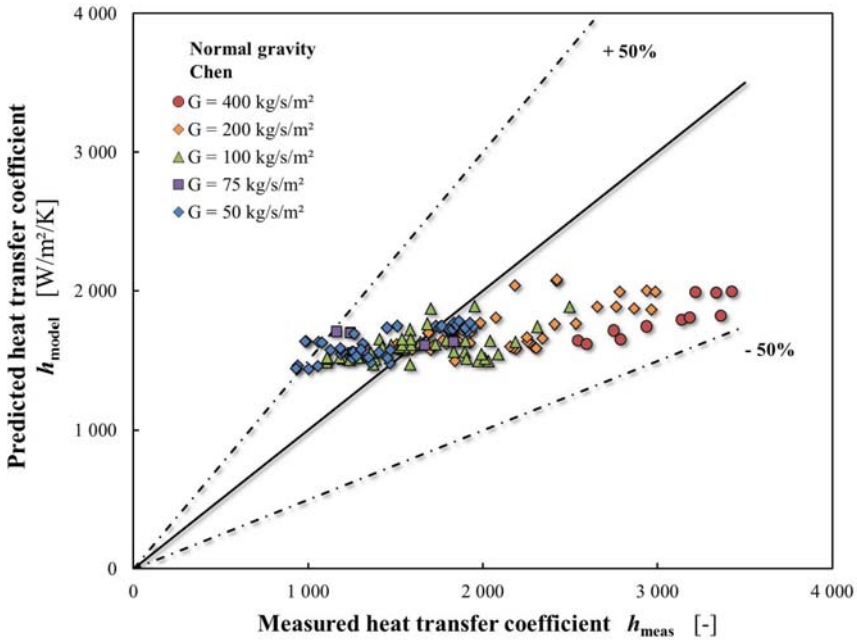

(a) in 1-g

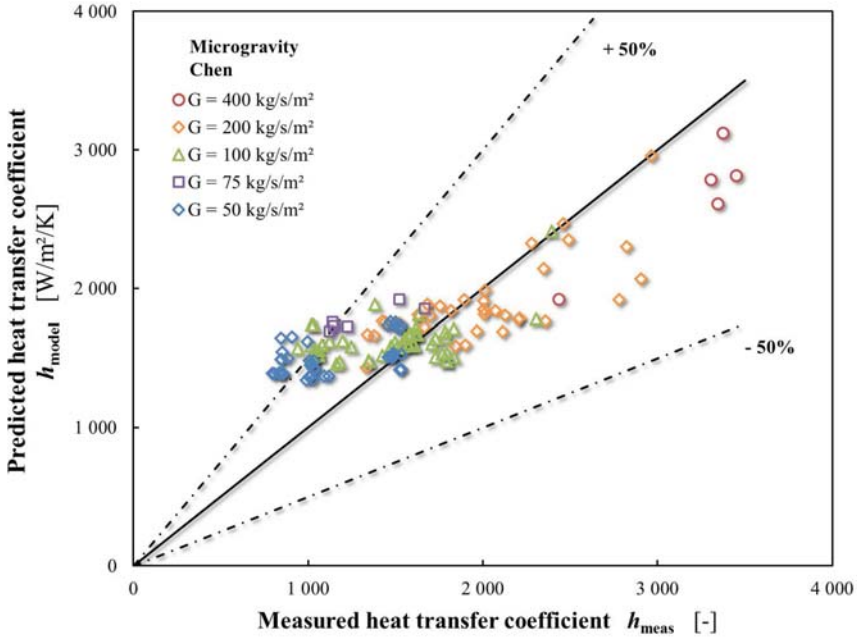

(b) in μ-g

FIGURE 4.38: Comparison of measured heat transfer coefficient and predicted heat transfer coefficient in saturated boiling using a correlation proposed by Chen [1966]

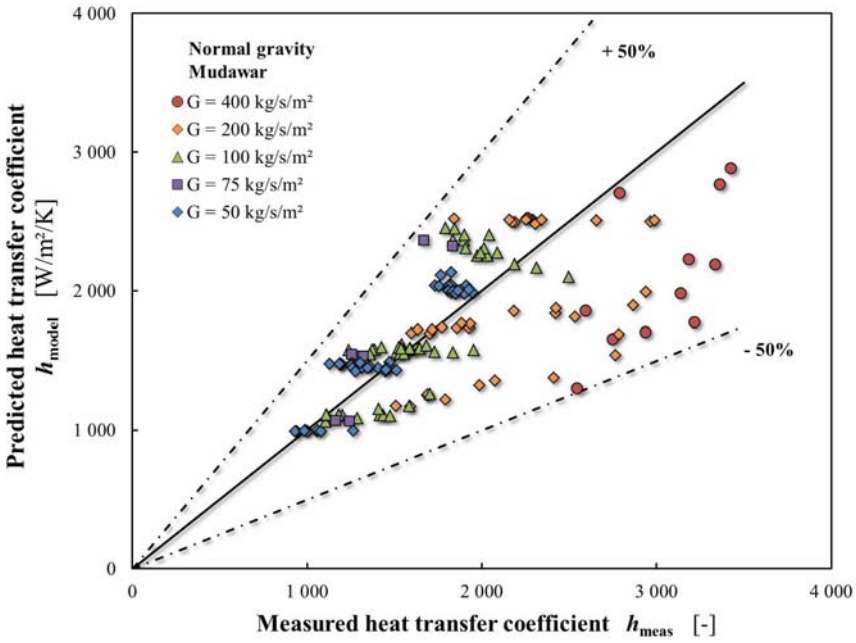

(a) in 1-g

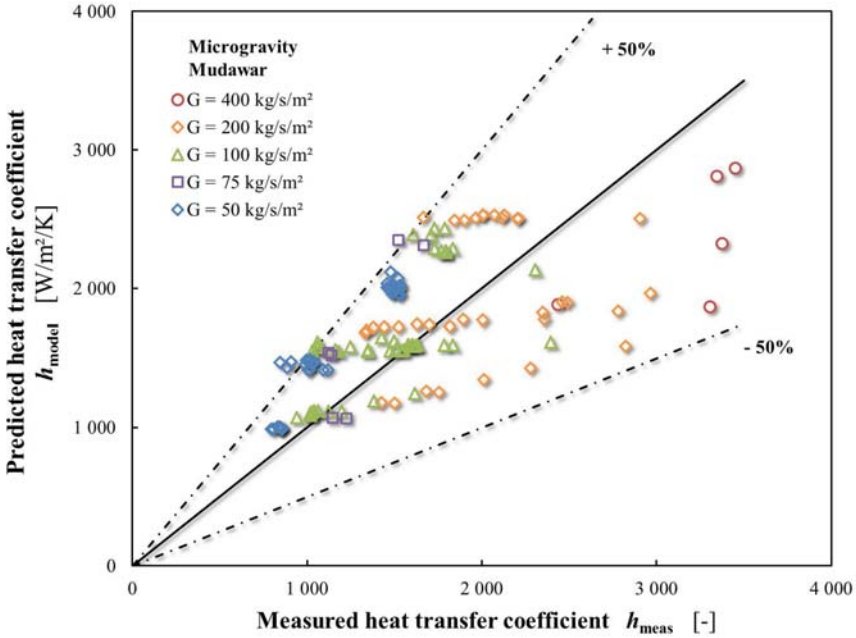

(b) in μ-g

FIGURE 4.39: Comparison of measured heat transfer coefficient and predicted heat transfer coefficient in saturated boiling using a correlation proposed by Kim and Mudawar [2013]

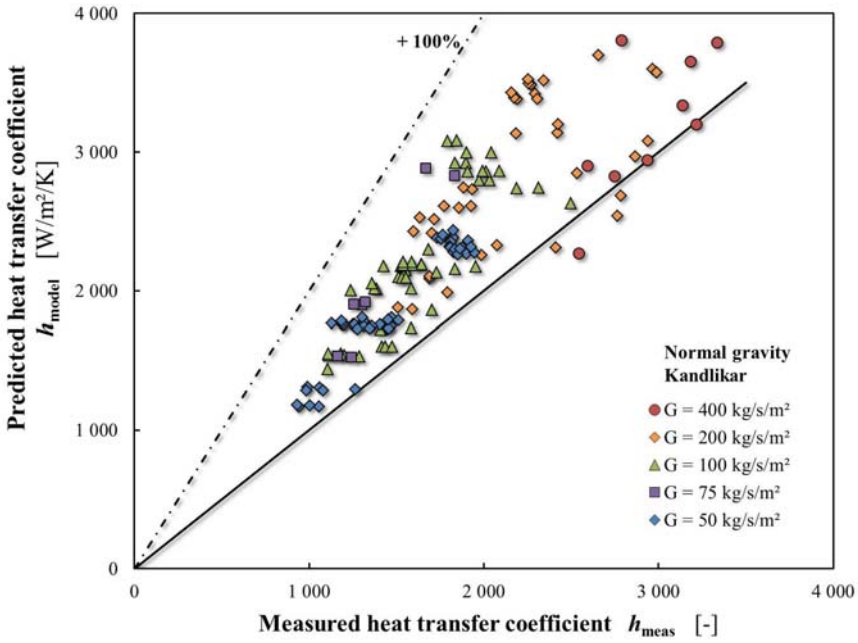

(a) in 1-g

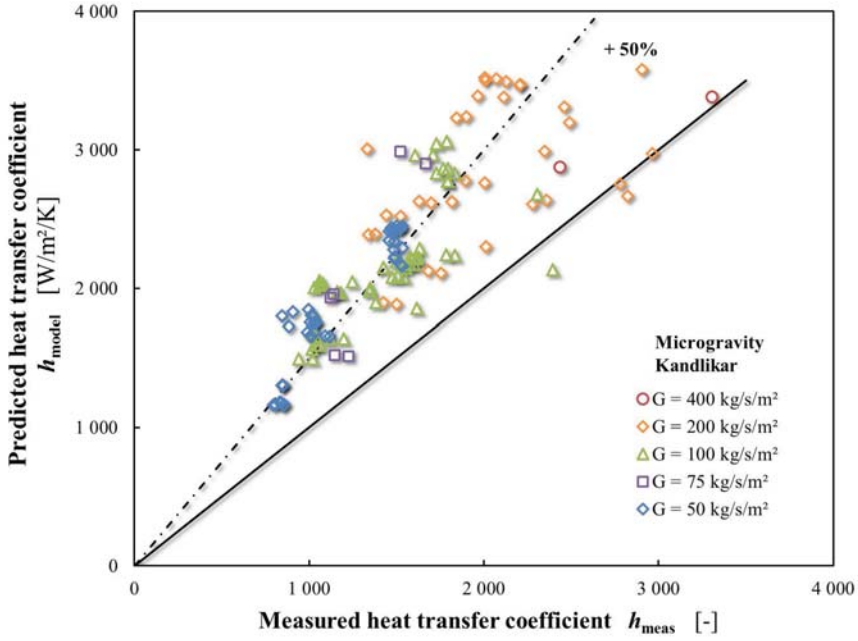

(b) in μ-g

FIGURE 4.40: Comparison of measured heat transfer coefficient and predicted heat transfer coefficient in saturated boiling using a correlation proposed by Kandlikar [1990]

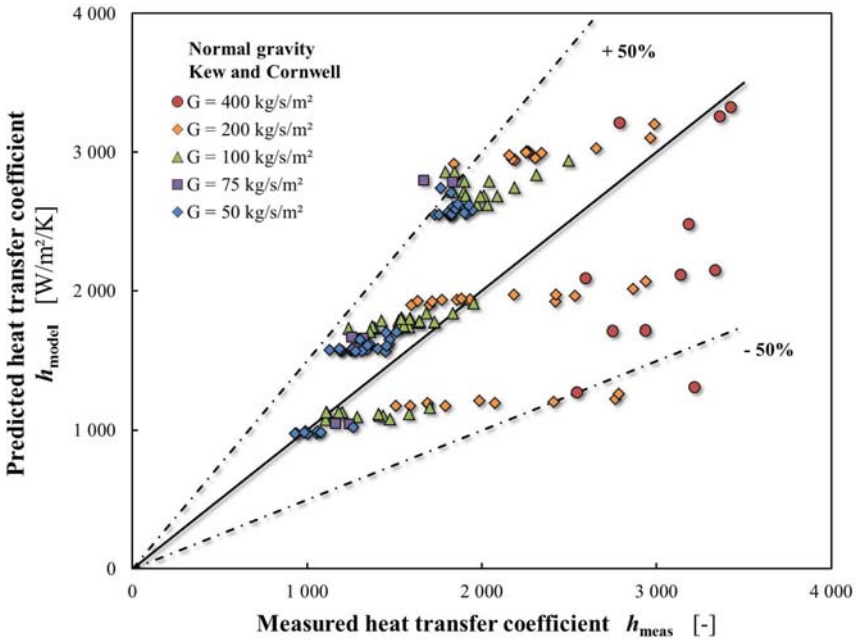

(a) in 1-g

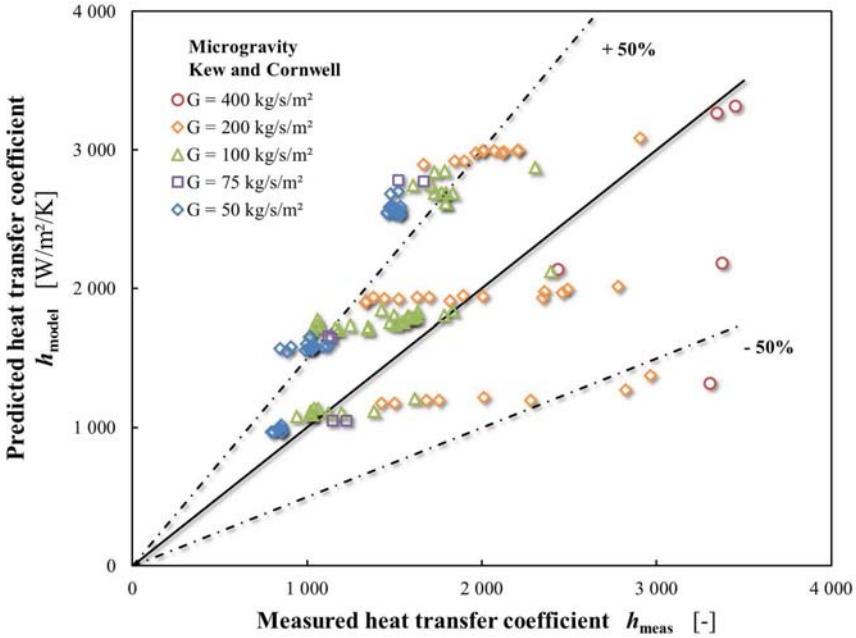

(b) in μ-g

FIGURE 4.41: Comparison of measured heat transfer coefficient and predicted heat transfer coefficient in saturated boiling using a correlation proposed by Kew and Cornwell [1997]

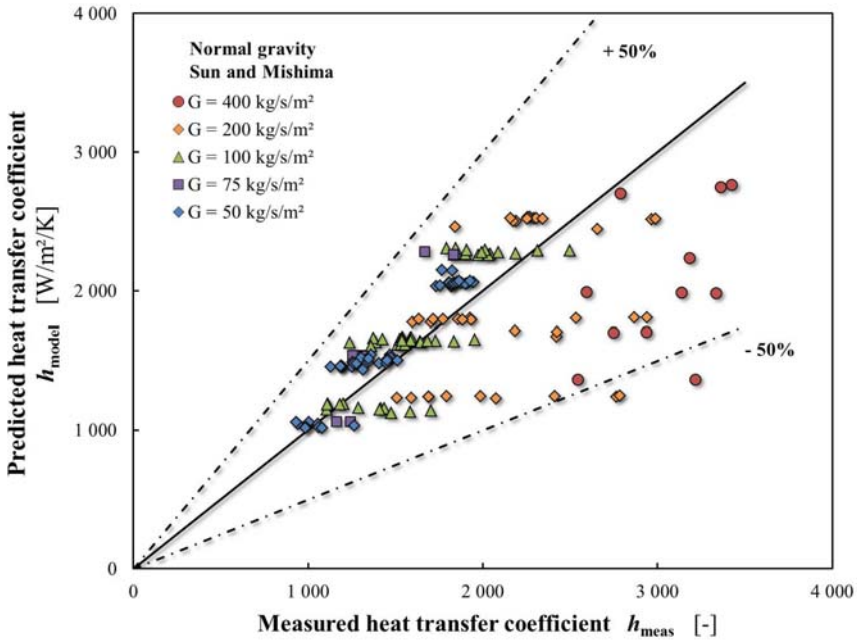

(a) in 1-g

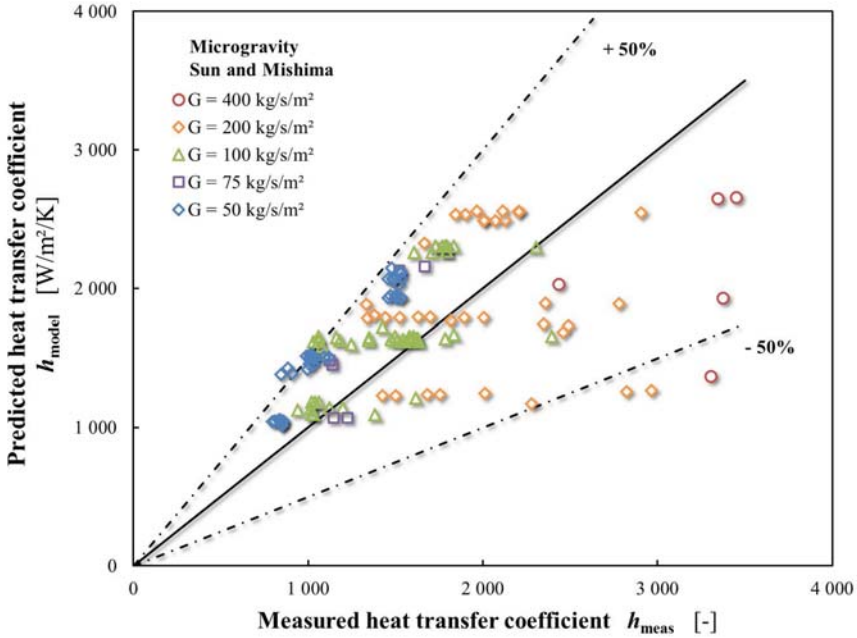

(b) in μ-g

FIGURE 4.42: Comparison of measured heat transfer coefficient and predicted heat transfer coefficient in saturated boiling using a correlation proposed by Sun and Mishima [2009]

Heat transfer by evaporation through the liquid film in annular flow: the annular flow model developed by Cioncolini and Thome [2011] includes a correlation for the prediction of the heat transfer coefficient according to the liquid film thickness and the wall shear stress, as presented in Chapter 1:

$$h = \frac{\lambda_l}{\delta} 0.0776.(\delta^+)^{0.9}.Pr^{0.52} \qquad \text{with } \delta^+ = \frac{\delta}{y^*} = \frac{\delta.u^*}{\nu_l} \qquad \text{for } 10 < \delta^+ < 800 \quad \text{and} \quad 0.86 < Pr < 6.1 \tag{4.22}$$

Figure 4.43 presents the heat transfer coefficient calculated with the values of δ and u^* predicted by the correlations in Cioncolini and Thome annular flow model, under normal gravity and microgravity conditions, while experimental values of δ and τ_w are used to plot h in Figure 4.44 (MAE presented in Table 4.7 are calculated with the expression of h of the model and the experimental values of film thickness and wall shear stress).

In Figures 4.43(a) and 4.43(b), the agreement on heat transfer coefficient is better than 30% on most of the experimental points for 1-g data at high mass flux, despite the large discrepancy between the model and data on film thickness in normal gravity. It may be explained by the small dependency of h to the liquid film thickness in Equation (4.22): $h \sim \delta^{0.1}$.

For calculations using experimental values of δ and u^* (Figures 4.44(a) and 4.44(b), heat transfer data are less scattered than with the complete model of Cioncolini and Thome [2011], both under normal gravity and microgravity conditions. Despite an overprediction of about 20% in 1-g, the agreement between the model and the experiments in 1-g and μ-g is rather good.

An explanation for the low sensitivity of the heat transfer coefficient to gravity can be found by looking at the velocity profiles provided by Cioncolini for thick turbulent liquid films: both temperature and velocity gradients are concentrated near the wall on a range of dimensionless distance from the wall $0 < y^+ < 30$. Yet experimental dimensionless liquid film thickness in 1-g for $G > 100$ kg.s^{-1}.m^{-2} correspond to $\delta^+ > 55$.

It can therefore be assumed that a change in the film thickness due to changes in the gravity level does not consequently affect the velocity and temperature profiles near the wall as long as the liquid film is thick enough ($\delta^+ > 30$). This could explain the low sensitivity $\sim \delta^{0.1}$ in the modelling of heat transfer coefficient for $G > 100$ kg.s^{-1}.m^{-2}. Furthermore, for $G = 400$ and 200 kg.s^{-1}.m^{-2}, the wall shear stress is almost not affected by gravity; thus, no effect of the gravity level on heat transfer is expected.

Conclusion on heat transfer correlations: comparisons with empirical correlations have shown that various expressions can be used depending on the flow parameters. However, the correlation proposed by Kim and Mudawar [2013] is interesting because it assesses both nucleate and convective boiling contributions. It may be adjusted in order to fit BRASIL experimental heat transfer coefficient in normal gravity: by using an enhancement factor for h_{cb} and a suppression factor for h_{nb} (as in the Chen correlation), it may be possible to fit 1-g data on the whole range of flow parameters. The influence of the gravity level on each term would then be assessable.

At high mass fluxes and qualities, when the heat transfer is mainly due to evaporation through the liquid film, Cioncolini and Thome [2011] correlation is well adapted. Nevertheless, the modelling of the wall friction that appears in Equation (4.22) has to be improved.

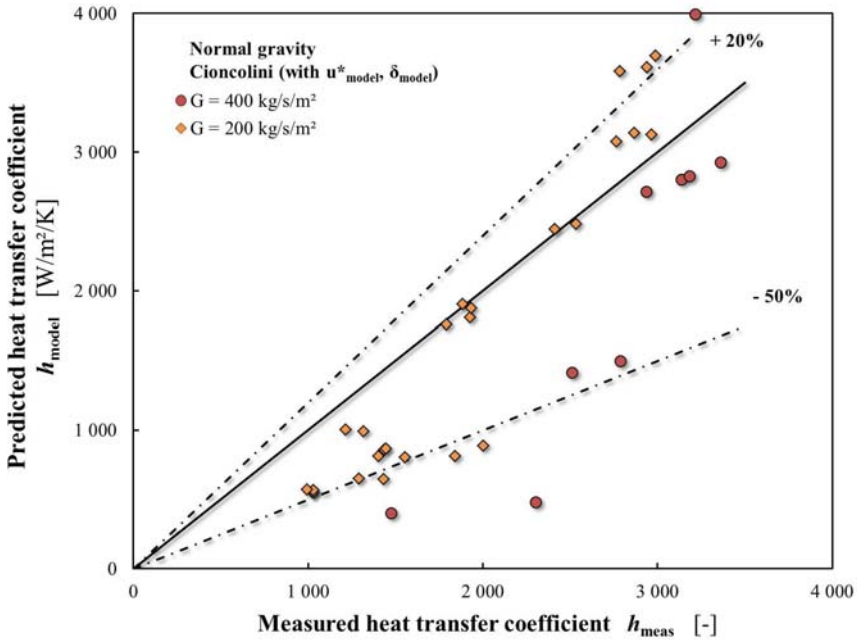

(a) in 1-g

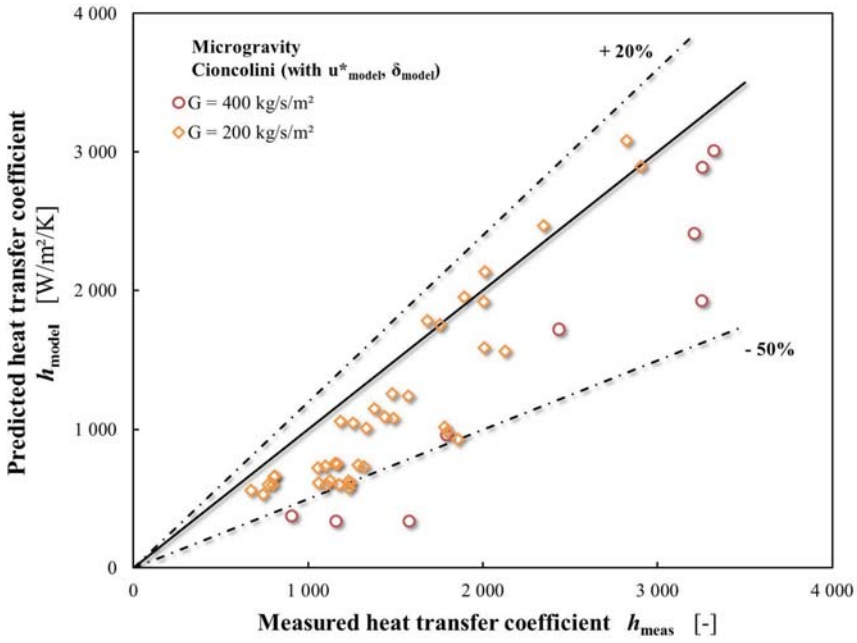

(b) in μ-g

FIGURE 4.43: Experimental heat transfer coefficient compared with the correlation of Cioncolini and Thome [2011] using liquid film thickness and wall shear stress values from their model, for turbulent liquid films

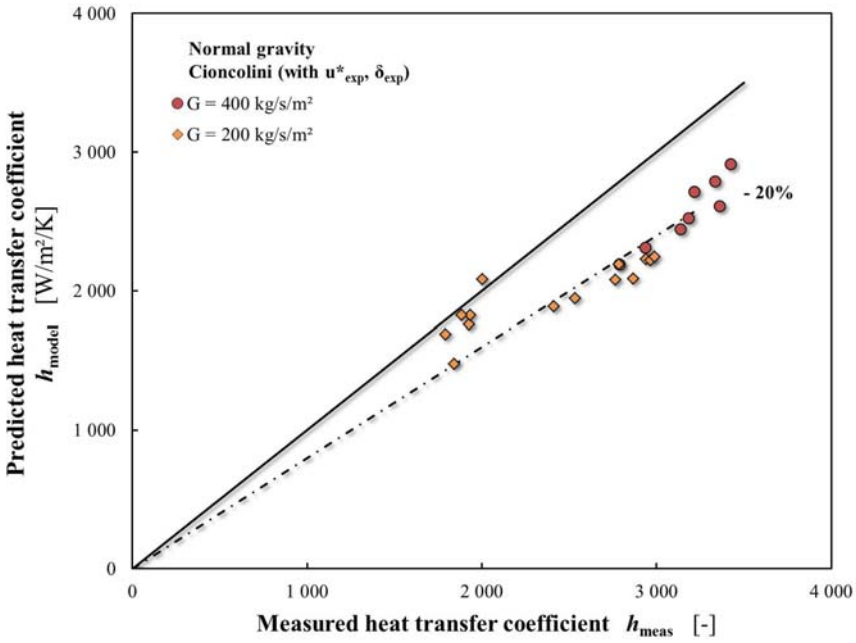

(a) in 1-g

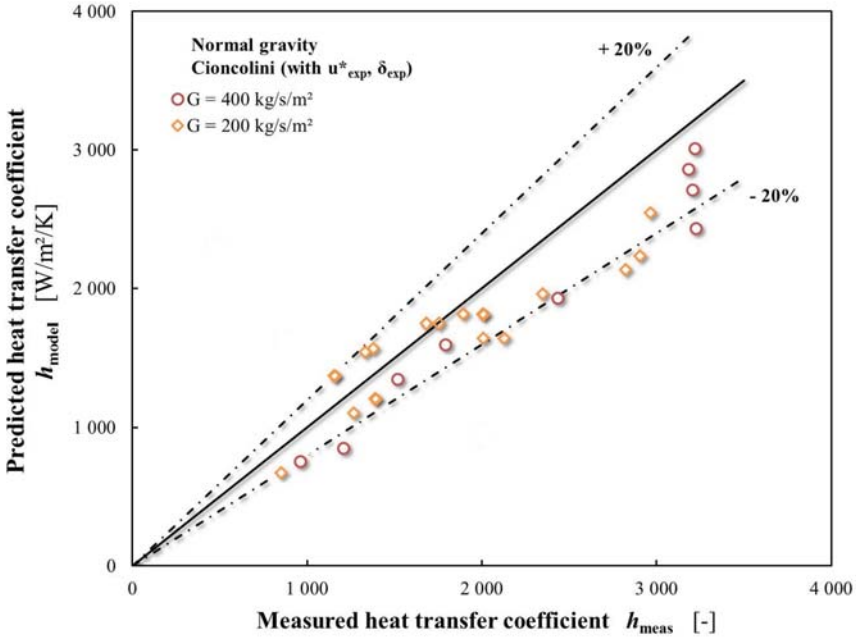

(b) in μ-g

FIGURE 4.44: Experimental heat transfer coefficient compared with the correlation of Cioncolini and Thome [2011] using liquid film thickness and wall shear stress values from BRASIL experiments, for turbulent liquid films

	$G = 400$		$G = 200$		$G = 100$		$G = 75$		$G = 50$	
	1-g	μ-g	1-g	μ-g	1-g	μ-g	1-g	μ-g	1-g	μ-g
Chen [1966]	40.3	**17.0**	18.6	**12.7**	13.9	21.6	22.9	38.9	20.0	36.8
Kew and Cornwell [1997]	29.0	22.8	25.4	33.2	21.8	28.4	33.1	43.9	25.7	54.5
Sun and Mishima [2009]	32.3	32.4	20.6	25.6	**12.2**	**19.7**	**20.1**	**24.7**	**11.7**	**37.3**
Kandlikar [1990]	**14.5**	24.5	36.3	50.6	35.7	51.6	46.4	61.6	29.1	60.6
Kim and Mudawar [2013]	31.0	26.1	18.6	23.0	**12.4**	**18.1**	**21.1**	30.6	**10.3**	**35.1**
Cioncolini and Thome [2011]	19.4	20.9	**18.2**	13.6	-	-	-	-	-	-

TABLE 4.7: Mean absolute error (MAE, in %) between BRASIL experimental heat transfer coefficients and heat transfer coefficients predicted by various correlations and models in saturated boiling conditions

Conclusion

Experimental results obtained in normal gravity and microgravity have been compared to classical correlations of the literature in order to provide a preliminary modelling of flow pattern transitions, void fraction and film thickness, wall and interfacial shear stresses, and heat transfer coefficients.

Flow pattern maps show that transitions between flow patterns occur at a constant value of vapor quality. A transition criteria based on a critical value of α is therefore the most relevant criteria to predict flow regimes. The transition from bubbly to slug flows is well described by a semi-empirical drift-flux model with a distribution coefficient $C_0 \simeq 1.25$ considering that coalescence is limited, while the transition from slug to annular flows is also in good agreement with the critical value of α predicted for gas-liquid flows.

Thus, the same drift-flux model is used to predict the void fraction in subcooled boiling. In saturated regimes, the void fraction tends to be overestimated by the correlations in normal gravity, whereas microgravity data are in rather good agreement with the correlation developed by Cioncolini and Thome in turbulent annular flows (since α is larger in microgravity than in normal gravity). Similar observations can be made on the evolution of the liquid film thickness in annular flows.

Wall shear stress data are compared with classical correlations which show that the two-phase multiplier is well predicted by an expression like the one established by Lockhart and Martinelli according to the Martinelli parameter, with potential adjustments of the coefficient to account for the influence of the mass flux and / or the gravity level. The interfacial shear stress is not well described by usual correlations. However, a combination of a preliminary fitting characteristic of a transition from smooth to fully rough flow in normal gravity and the correlation established by Ohta to assess the influence of gravity on the interfacial friction factor allows to propose an expression to predict f_i with a reasonable agreement in microgravity.

Comparisons of heat transfer coefficient data with empirical correlations highlight the fact that the expressions which assess the respective contributions of nucleate and convective boiling provide a rather good description of h on the whole range of flow parameters. Additional adjustments may allow to balance the two terms and fit experimental measurements. The correlation of Cioncolini and Thome for heat transfer by evaporation through a turbulent liquid film is in good agreement with experimental data in both normal gravity and microgravity at high mass fluxes and high qualities.

The comparisons drawn with empirical correlations and the observations made on the modelling of flow boiling in normal gravity and microgravity are summarised in the section "Conclusions and Perspectives".

Conclusions and Perspectives

This section provides a concise overview of the main observations and results obtained during this PhD work that consisted in an experimental investigation of upward flow boiling of HFE-7000 in a 6mm ID heated tube under normal gravity and microgravity conditions. Recommendations and relevant perspectives for the continuation of this project are put forward in the last part.

Synthesis

Objective of the thesis and experimental facility

Despite the fact that it is of great interest for space applications, the influence of the gravity level (and especially of near-weightlessness conditions) on flow boiling mechanisms is almost not assessed in fundamental research, mostly due to practical difficulties. Indeed, a brief state-of-the-art review points out the lack of experimental data on flow boiling under microgravity conditions. Moreover, the few available datasets are not always consistent, and they generally focus on the study of flow patterns or heat transfer coefficients only.

In order to fill the gap observed in the literature and to provide a more global description of flow boiling under microgravity conditions, a new experimental set-up called BRASIL was built at the Institute of Fluid Mechanics of Toulouse (IMFT) to investigate flow boiling of HFE-7000 in a 6mm ID vertical sapphire tube coated with ITO and heated by Joule effect. This test section and an additional adiabatic section were instrumented with temperature and pressure sensors, a camera and specifically designed void fraction probes to characterise flow patterns, void fraction, wall and interfacial shear stresses, and heat transfer coefficients.

A wide range of flow parameters was investigated: the values of vapor quality cover subcooled and saturated boiling regimes, while set mass fluxes corresponds to both laminar and turbulent behaviours of liquid and vapor phases. However, the chosen wall heat fluxes remain small: critical heat flux issues are not addressed in this thesis. Experimental data under microgravity conditions were acquired during three parabolic flight campaigns, each campaign providing 93 parabolas with a 22s microgravity phase. Measurements in laboratory were performed to complete BRASIL database with parametric runs.

Flow patterns

Three main flow patterns are observed in upward flow boiling below the critical heat flux: bubbly flows, transition flows including slug and churn flows, and annular flows. The same types of regimes are observed under normal gravity and microgravity conditions. For mass fluxes lower than 400 $kg.s^{-1}.m^{-2}$, the difference between the two gravity levels is visible on the shape and size of bubbles (that are bigger and more spherical in microgravity) in bubbly flows, whereas flow visualisations in transition and annular flow regimes do not exhibit changes with the gravity.

Despite the fact that coalescence phenomenon seems to be enhanced in microgravity, it is hardly possible to assess the influence of the gravity level on the transition between flow patterns, because the identification of transition flows is very subjective. Flow patterns maps plotted versus superficial liquid and vapor velocities therefore shows similar transitions between flow patterns in normal gravity and microgravity. These transitions occur at constant vapor quality (i.e. constant void fraction), at $x \simeq 0.05$ ($\alpha \simeq 0.7$) for the transition from bubbly to slug flows, and at $x \simeq 0.13$ ($\alpha \simeq 0.8$) for the one from slug to annular flows. The first transition is rather well described by a semi-empirical drift-flux model with a distribution coefficient $C_0 \simeq 1.25$ [Colin et al., 1996], while the latter one is in good agreement with the prediction of Dukler et al. [1988].

The flow pattern map in microgravity is consistent with the few experimental points that were reported in similar conditions for flow boiling of refrigerants during parabolic flight campaigns.

Void fraction and liquid film thickness

New capacitance probes were designed to acquire void fraction data. This physical value is rarely reported in two-phase flow experiments under microgravity conditions, which explains a lack of results characterising the interfacial shear stress, for example. Measurements point out that the void fraction is a strong function of the vapor quality, but it is also influenced by the mass flux. Comparisons drawn between normal gravity and microgravity conditions show a significant difference in the void fraction depending on the gravity level, with larger values of void fraction in microgravity.

In subcooled regimes, a semi-empirical drift-flux model provides a reasonable description of the void fraction, as mentioned in the flow pattern section. In saturated boiling, the few assessed correlations tend to overestimate the void fraction in normal gravity. However, microgravity data for turbulent flow are in rather good agreement with the correlation developed by Cioncolini and Thome [2011] in their model of annular flow with evaporation through the liquid film, since the void fraction is larger than in normal gravity.

In the specific case of annular flow, a liquid film thickness can be calculated from the void fraction and the diameter of the tube (the entrainment and deposition of liquid droplets in the vapor core do almost not affect the calculations of the film thickness). Thicker liquid films are consequently observed in normal gravity compared to microgravity, on the whole range of vapor quality or mass flux, and

similar comparisons as for the void fraction are drawn with Cioncolini and Thome [2011] model in turbulent flows: in normal gravity, the liquid film is thicker than expected from the correlation, but experimental points in microgravity are in good agreement with predicted values.

Designing and adding void fraction probes in a new experimental facility was the subject of a collaboration with the University of Maryland. A common parabolic flight campaign provided similar results on void fraction and liquid film thickness for flow boiling of HFE-7100.

Wall and interfacial shear stresses

Measurements of pressure drops were performed on an adiabatic section at the outlet of the sapphire tube. In microgravity, these measurements are enough to calculate the wall shear stress, whereas the void fraction is needed in normal gravity to express the frictional pressure gradient. Experimental results show that the influence of the gravity level on the wall shear stress depends on the mass flux: at high mass flux, there is no clear difference between normal gravity and microgravity data. On the contrary, for moderate and low values of mass flux, the wall shear stress is significantly lower than in normal gravity.

Comparison with classical correlations point out that experimental values of the two-phase multiplier is well predicted by an expression like the one established by Lockhart and Martinelli [1949] that distinguish turbulent and laminar flows. An adjustment may be done to better fit BRASIL data by using a coefficient accounting for the mass flux and / or the gravity level, through a Froude number, for example.

In the case of annular flows, the interfacial shear stress is calculated using pressure drop and void fraction data. As for the liquid film thickness, the interfacial friction factor is almost not influenced by the rate of liquid entrainment in the vapor core. On the whole range of mass flux, the interfacial shear stress is significantly lower in microgravity than in normal gravity.

The correlations that are usually compared to microgravity data do not provide a suitable description of the interfacial shear stress, whatever the gravity level. However, the dependency on the mass flux highlights the fact the interfacial friction factor does not only depend on the film thickness but also on the vapor Reynolds number, which is characteristic of a transition between smooth and fully rough turbulent regimes. According to this observation, a preliminary fitting written according to the film thickness and the vapor Reynolds number at the power -1.3 is proposed for normal gravity data. Combined with the model developed by Ohta [2003] that provides a reasonable prediction of the interfacial friction factor in microgravity compared to normal gravity, it allows to obtain an expression for the prediction of interfacial shear stress under microgravity conditions.

Heat transfer coefficients

Heat transfer coefficients are calculated according to the outer wall temperature and the liquid bulk temperature on various locations along the sapphire tube. Experimental data show that the mass and wall heat fluxes play an important role in heat transfers, whatever the gravity level is. The dependency on the wall heat flux highlights the important contribution of nucleate boiling in subcooled regimes and in saturated boiling at low mass flux, whereas saturated flows at high mass flux or very high vapor quality are controlled by convective boiling.

The influence of the gravity level changes according to the dominant heat transfer mode: in subcooled regimes and saturated regimes at low mass flux, where nucleate boiling prevails, the heat transfer coefficient is lower in microgravity than in normal gravity, due to larger bubble diameter at detachment and smaller relative motion of bubbles in microgravity. However, in the regions driven by forced convection, there is no cleear difference on the heat transfer coefficient between the two gravity levels. This observation has been already made in the literature for microgravity datasets where experimental conditions were clearly specified.

Comparisons with empirical correlations from the literature show that various expressions can be used to predict the heat transfer coefficient depending on the flow parameters. Nevertheless, correlations that assess both nucleate and convective boiling contributions such as the correlation of Kim and Mudawar [2013] may provide a reasonable description of the heat transfer coefficient on the whole range of flow parameters with adjustments to balance the two terms and fit BRASIL data.

The correlation proposed by Cioncolini and Thome [2011] to predict heat transfer coefficient in their turbulent annular flow model highlights a small dependency of the heat transfer coefficient on the liquid film thickness. This low sensitivity may be explained by the fact that the liquid film thickness is much larger than the distance from the wall where both temperature and velocity gradients are concentrated. As a result, a variation in the film thickness due to changes in the gravity level is not expected to induce changes in the heat transfer coefficient in saturated boiling at high mass flux. The correlation is able to predict with a good agreement the heat transfer due to liquid film evaporation in both normal gravity and microgravity providing that a relevant modelling of the friction velocity has been used.

Perspectives

Flow boiling mechanisms are complex and require the investigation of numerous physical values for their description. Unfortunately, the study of this phenomenon is even more complicated under microgravity conditions due to limitations in experimental apparatuses and available points related to parabolic flight campaigns. For that reason, further experiments are needed to complete the analysis and modelling of flow boiling under microgravity conditions. For future work on the subject, priority should be given to:

– **complete the database in microgravity:** additional points are needed to confirm experimental trends and calculations made in this thesis. Moreover, a more complete database is required to properly model experimental results. The main regions of interest have already been distinguished in this work, they only need to be further investigated.

– **improve measurements techniques:** the transition between two parabolic flight campaigns represents an opportunity to further improve the measurements techniques that are often limited due to the restrictions in the design of the experiment. In particular, the capacitance probes can easily be modified to provide better sensitivity and acquisition frequency. The fixation of the platinium probes on the outer surface of the sapphire tube can also be changed to improve the measurements of heat transfer coefficients.

– **process camera images:** the use of flow visualisations is not limited to the identification of flow patterns. Better settings and new data reduction protocols would allow to process experimental data on bubble velocity (that could be correlated to void fraction or vapor quality) or on waves frequency.

– **complete the preliminary modelling of flow boiling:** with additional experimental points to better describe void fraction, heat transfer coefficient, wall and interfacial shear stress, it would be possible to propose a more general and complete model of flow boiling, both in normal gravity and microgravity.

Cette section résume de manière concise les principaux résultats et observations obtenus lors de cette thèse qui consistait en l'étude expérimentale de l'ébullition convective de HFE-7000 dans un tube vertical et chauffé de 6 millimètres de diamètre intérieur, dans des conditions de gravité normale et de microgravité. Les recommandations et perspectives relatives à la poursuite de ce projet sont exposées dans la dernière partie.

Synthèse

Objectif de la thèse et installation expérimentale

Malgré le fait que cela soit d'un grand intérêt pour de potentielles applications dans le domaine spatial, l'influence de la gravité (et tout particulière des conditions d'apesanteur presque totales) sur les mécanismes de l'ébullition convective est très peu évaluée dans les travaux de recherche fondamentale, principalement à cause de difficultés techniques. En effet, un rapide état de l'art met en évidence un manque de données expérimentales concernant l'ébullition convective en microgravité. De plus, les quelques jeux de données déjà existants ne s'accordent pas toujours sur les tendances générales dégagées, et la plupart du temps, ils ne traitent que d'un aspect du problème, comme les régimes d'écoulement ou les coefficients d'échange de chaleur.

Afin de pallier cette insuffisance de résultats dans la littérature et de fournir une description plus générale de l'ébullition convective en microgravité, un nouveau banc d'essai a été dimensionné et construit à l'IMFT (Institut de Mécanique des Fluides de Toulouse) pour permettre l'étude de l'ébullition convective de HFE-7000 dans un tube de saphir vertical, recouvert d'un dépôt d'ITO et chauffé par effet Joule. Cette section d'essai et une portion supplémentaire de tube correspondant à des conditions d'adiabaticité ont été instrumentées avec des capteurs de température, de pression et de taux de vide, ainsi qu'avec une caméra rapide, afin de caractériser les régimes d'écoulement, le taux de vide, les frottements pariétaux et interfaciaux, et les coefficients d'échange de chaleur.

Une large gamme de paramètres d'écoulement a été parcourue lors des expériences : les valeurs de titre massique en vapeur couvrent les régimes d'ébullition sous-refroidie et d'ébullition saturée, tandis que les flux de masse choisis correspondent à la fois à des comportements laminaires et turbulents des phases liquide et vapeur. Toutefois, les flux de chaleur appliqués en paroi restent faibles : les problèmes de flux critique ne sont pas abordés dans cette thèse. Les données expérimentales en microgravité ont été obtenues lors de trois campagnes de vol paraboliques qui assurent chacune 93 paraboles correspondant à une phase de microgravité de 22s. Des mesures en laboratoire ont été réalisées afin de compléter les données fournies par BRASIL avec des essais paramétriques.

Régimes d'écoulement

Trois principaux régimes d'écoulement sont observés en ébullition convective ascendante en-dessous du flux critique: écoulements à bulles, écoulements de transition incluant les écoulements à poches-bouchons et les écoulements churn, et écoulements annulaires. Les mêmes types de régimes sont observés dans des conditions de gravité normale et de microgravité. Pour des flux de masse inférieurs à 400 kg.s^{-1}.m^{-2}, la différence entre les deux niveaux de gravité est visible sur la taille et la forme des bulles (qui sont plus grosses et plus sphériques en microgravité) en écoulements à bulles, alors que les visualisations d'écoulement en écoulement de transition et écoulements annulaires ne sont pas distinctement affectées par la gravité.

Bien que le phénomène de coalescence semble être stimulé en microgravité, il est difficile d'évaluer l'influence du niveau de gravité sur les transitions entre régimes d'écoulement, car l'identification des régimes de transition est un processus très subjectif. Les cartes de configuration d'écoulements tracées en fonction des vitesses superficielles de la vapeur et du liquide montrent donc des transitions similaires en gravité normale et en microgravité. Ces transitions se font à titre constant (c'est-à-dire à taux de vide constant), à $x \simeq 0{,}05$ ($\alpha \simeq 0{,}7$) pour la transition des écoulements à bulles vers les écoulements à poches-bouchons, et à $x \simeq 0{,}13$ ($\alpha \simeq 0{,}8$) pour la transition des écoulements à poches-bouchons vers les écoulements annulaires. La première transition est plutôt bien décrite par un modèle semi-empirique à flux de dérive, avec un coefficient de répartition de phase $C_0 \simeq 1{,}25$ Colin et al. [1996], tandis que la deuxième transition est en accord avec la prédiction de Dukler et al. [1988].

La carte de configuration d'écoulements en microgravité est cohérente avec les quelques points expérimentaux rapportés dans des conditions similaires pour l'ébullition de réfrigérants durant des campagnes de vols paraboliques.

Taux de vide et épaisseur de film liquide

De nouvelles sondes capacitives ont été construites afin de réaliser des mesures de taux de vide. Cette grandeur est rarement renseignée dans les expériences en écoulement diphasiques dans des conditions de microgravité, ce qui explique en partie le manque de résultats pour la caractérisation du frottement interfacial, par exemple. Les mesures montrent que le taux de vide est fonction du titre massique en vapeur mais qu'il est également influencé par le flux de masse. Les comparaisons entre gravité normale et microgravité montrent une différence significative sur le taux de vide selon le niveau de gravité, avec des valeurs de taux de vide plus importantes en microgravité.

Pour les régimes sous-refroidis, un modèle semi-empirique à flux de dérive permet de décrire raisonnablement bien le taux de vide, comme mentionné dans la section sur les régimes d'écoulement. En ébullition saturée, les quelques corrélations évaluées tendent à surestimer le taux de vide en gravité normale. Cependant, les données en microgravité pour des écoulements turbulents sont en bon accord avec la corrélation développée par Cioncolini and Thome [2011] dans leur modèle d'écoulement annulaire avec évaporation à travers le film liquide, puisque le taux de vide est plus important en microgravité.

Dans le cas particulier des écoulements annulaires, une épaisseur de film liquide peut être calculée à partir du taux de vide et du diamètre du tube (l'arrachage et la redéposition de gouttelettes n'affectent presque pas les calculs d'épaisseur de film), ce qui résulte en l'observation de films liquides plus épais en gravité normale, comparé aux conditions de microgravité, sur toute la gamme de titre et de débits. Des remarques similaires à celles pour le taux de vide peuvent être faites quant aux comparaisons avec le modèle de Cioncolini and Thome [2011] en écoulement turbulent : en gravité normale, le film de liquide est plus épais que ce que prédit la corrélation, alors que les points en microgravité sont en bon accord avec les valeurs prédites.

Le dimensionnement et l'ajout de sondes de taux de vide sur une nouvelle installation expérimentale a été le sujet d'une collaboration avec l'Université du Maryland. Une campagne de vols paraboliques commune a permis d'obtenir des résultats similaires à ceux fournis par BRASIL sur le taux de vide et les épaisseurs de film liquide pour l'ébullition convective de HFE-7100.

Frottements pariétaux et interfaciaux

Des mesures de pertes de pression ont été réalisées sur une section adiabatique à la sortie du tube de saphir. En microgravité, cette grandeur est suffisante pour calculer le frottement pariétal, alors que le taux de vide est nécessaire en gravité normale pour exprimer la perte de pression par frottement. Les résultats expérimentaux montrent que l'influence du niveau de gravité sur le frottement pariétal varie selon le flux de masse : à haut débit, il n'y a aucune différence significative entre les données en gravité normale et en microgravité. Au contraire, pour des valeurs de flux de masse faibles ou modérées, le frottement pariétal est clairement plus faible en microgravité.

Des comparaisons avec les corrélations de la littérature classiquement utilisées montrent que le multiplicateur diphasique est bien prédit par une expression du type de celle établie par Lockhart and Martinelli [1949] qui distingue les écoulements laminaires des écoulements turbulents. Néanmoins, l'utilisation d'un coefficient prenant en compte l'influence du flux de masse et / ou de la gravité (à travers un nombre de Froude, par exemple) permettrait de mieux aprocher les données expérimentales.

Dans le cas des écoulements annulaires, le frottement interfacial est calculé à partir des mesures de pertes de pression et de taux de vide. Comme pour l'épaisseur de film liquide, le frottement interfacial est très peu impacté par l'arrachage liquide dans le cœur de vapeur. Sur toute la gamme de flux de masse, le frottement interfacial est significativement plus petit en microgravité, comparé à la gravité normale.

Les corrélations qui sont usuellement utilisées pour des comparaisons aux données en microgravité ne permettent pas de prédire correctement le frottement interfacial, quelque soit le niveau de gravité. En effet, la dépendance au flux de masse met en lumière le fait que le coefficient de frottement interfacial ne dépend pas seulement de l'épaisseur de film, mais également d'un nombre de Reynolds vapeur, ce qui est caractéristique d'une transition entre écoulement lisse et écoulement pleinement rugueux. Un lissage préliminaire est donc proposé pour prédire les données en gravité normale en fonction de l'épaisseur de film et d'un nombre de Reynolds à la puissance -1,3. Combiné à la corrélation proposée par Ohta [2003] qui décrit raisonnablement bien l'influence de la gravité sur le coefficient de frottement interfacial, il est possible d'obtenir une

expression pour la prédiction du frottement interfacial dans des conditions de microgravité.

Coefficient d'échange de chaleur

Les coefficients d'échange de chaleur sont calculés à partir des mesures de temperature de la paroi externe du tube de saphir et de température du liquide dans l'écoulement, en diverses positions le long de la section d'essai chauffée. Les données expérimentales montrent que les flux de masse et de chaleur jouent un rôle important dans les transferts de chaleur, quelque soit le niveau de gravité. La dépendance en flux pariétal met en évidence l'importance de la contribution de l'ébullition nucléée en régimes sous-refroidis et en régimes-saturés à faible débit, alors que les écoulements saturés à fort titre et / ou fort débit sont contrôlés par l'ébullition convective.

L'influence du niveau de gravité sur le coefficient d'échange de chaleur change selon le mode dominant de transfert de chaleur : lorsque l'ébullition nucléée prévaut, le coefficient d'échange de chaleur est plus faible en microgravité qu'en gravité normale, à cause d'un diamètre plus large au détachement et d'une plus petite vitesse relative des bulles en microgravité. Cependant, dans les régions dominées par l'ébullition convective, il n'y a pas de différence visible sur le coefficient d'échange de chaleur selon les niveaux de gravité. Ces observations avaient déjà été faites dans la littérature pour des séries de mesures pour lesquelles les conditions expérimentales étaient clairement spécifiées.

Les comparaisons avec les corrélations empiriques de la littérature montrent que différentes expressions peuvent être utilisées en fonction des paramètres d'écoulement considérés. Néanmoins, les corrélations qui évaluent les contributions respectives de l'ébullition nucléée et de l'ébullition convective, telles que la corrélation de Kim and Mudawar [2013], peuvent fournir une bonne description du coefficient d'échange de chaleur sur la gamme complète de paramètres étudiés, avec des ajustements destinés à équilibrer les deux termes pour mieux approcher les données de BRASIL.

La corrélation proposée par Cioncolini and Thome [2011] pour prédire le coefficient d'échange de chaleur dans leur modèle d'écoulement annulaire turbulent met en évidence une faible dépendance du coefficient d'échange à l'épaisseur de film liquide. Cette faible sensibilité peut être expliquée par le fait que le film liquide est bien plus épais que la zone proche de la paroi dans laquelle sont concentrés les gradients de vitesse et de température. En conséquence, une diminution de l'épaisseur de film due aux conditions de microgravité n'influe pas sur le coefficient d'échange de chaleur en régime saturé à haut flux, tant que le film reste assez épais. La corrélation de Cioncolini and Thome permet donc de prédire avec un bon accord le coefficient d'échange de chaleur en gravité normale et en microgravité, à condition d'utiliser un modèle pertinent pour la vitesse de frottement.

Perspectives

Les mécanismes de l'ébullition convective sont complexes et requièrent une étude approfondie de différentes grandeurs physiques en fonction de nombreux paramètres. Malheureusement, cette étude est encore plus compliquée à réaliser pour des conditions de microgravité à cause des restrictions au niveau de l'installation expérimentale et du nombre limité de points de mesure, tout ceci étant lié à la tenue des campagnes de vols paraboliques. Pour cette raison, des expériences supplémentaires sont nécessaires, afin de complète l'analyse et la modélisation de l'ébullition convective dans des conditions de microgravité. Pour de futurs travaux sur le sujet, la priorité devrait être donnée à :

– **compléter les séries de mesures en microgravité :** des points supplémentaires sont nécessaires pour confirmer les tendances expérimentales et les calculs réalisés dans cette thèse. De plus, une base de données plus complète est requise pour correctement modéliser les résultats obtenus. Les principales régions d'intérêt ont déjà été dégagées lors de ce travail, il reste surtout à compléter cette étude.

– **améliorer les techniques de mesure :** la période de transition entre deux campagnes de vols paraboliques représente une opportunité d'améliorer les techniques de mesure qui sont souvent sujettes à restrictions. En particulier, le dessin actuel des sondes capacitives pour la mesure de taux de vide peut facilement être modifié pour fournir une meilleure dynamique du signal et une meilleure fréquence d'acquisition. De même, la méthode de fixation des sondes platine à la surface du tube de saphir peut être changée pour améliorer les mesures de coefficients d'échange de chaleur.

– **traiter les images de la caméra rapide :** l'utilisation des vidéos d'écoulement ne se limite pas à l'identification des régimes d'écoulement. De meilleurs réglages et de nouveaux protocoles de traitement de données utilisant les images de la caméra rapide permettraient d'obtenir des résultats expérimentaux sur la vitesse des bulles (qui est corrélée au taux de vide ou au titre) ou la fréquence des vagues en écoulements annulaires.

– **compléter les modélisations préliminaires de l'ébullition convective :** avec des points expérimentaux supplémentaires pour mieux caractériser le taux de vide, les coefficients d'échange de chaleur et les frottements pariétaux et interfaciaux, il serait possible de proposer une modélisation plus complète et plus générale des mécanismes de l'ébullition convective dans des conditions de gravité normale et de microgravité.

Appendix A

Validyne calibration curves

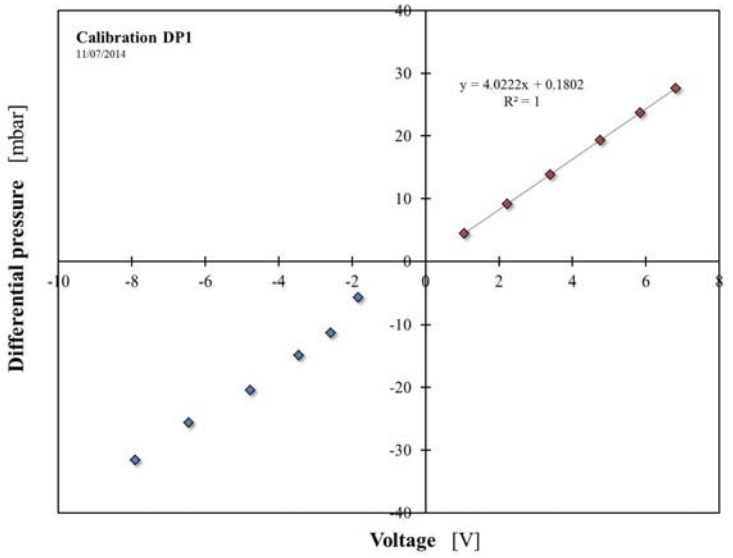

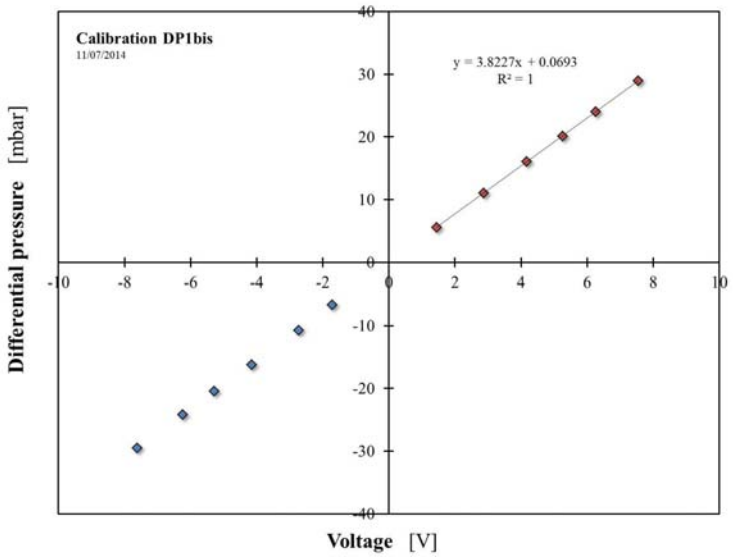

FIGURE A.1: Calibration curves for differential pressure transducers

Appendix B

Selected publications

A journal publication and a conference item are presented in this Appendix.

The paper article was published in the *International Journal of Multiphase Flow (IJMF)* [Narcy et al., 2014]. It deals with experimental results obtained during the parabolic flight campaign of April 2012 and the corresponding preliminary data reduction.

The conference item was written in collaboration with Scammell and Kim from the University of Maryland following the common parabolic flight campaign of March 2013, and can be found in the proceedings of the *15th International Heat Transfer Conference (IHTC)*.

International Journal of Multiphase Flow 60 (2014) 50–63

Contents lists available at ScienceDirect

International Journal of Multiphase Flow

journal homepage: www.elsevier.com/locate/ijmulflow

Flow boiling in tube under normal gravity and microgravity conditions

Marine Narcy, Erik de Malmazet, Catherine Colin *

IMFT, University of Toulouse, CNRS, Allée Camille Soula, 31400 Toulouse, France

ARTICLE INFO

Article history:
Received 5 September 2013
Received in revised form 26 November 2013
Accepted 28 November 2013
Available online 8 December 2013

Keywords:
Two-phase flow
Microgravity
Heat transfer
Wall friction

ABSTRACT

Forced convective boiling experiments of HFE-7000 were conducted in earth gravity and under microgravity conditions. The experiment mainly consists in the study of a two-phase flow through a 6 mm diameter sapphire tube uniformly heated by an ITO coating. The parameters of the hydraulic system are set by the conditioning system and measurements of pressure drops, void fraction and wall temperatures are provided. High-speed movies of the flow were also taken. The data were collected in normal gravity and during a series of parabolic trajectories flown onboard an airplane. Flow visualisations, temperature and pressure measurements are analysed to obtain flow pattern, heat transfer and wall friction data.

© 2013 Elsevier Ltd. All rights reserved.

1. Introduction

Two-phase thermal systems are broadly used in various industrial applications and engineering fields. Flow boiling heat transfer is common in power plants (energy production or conversion), transport of cryogenic liquids and other chemical or petrochemical processes. Thus, the understanding of boiling mechanisms is of importance for accidental off-design situations. These systems take advantage of latent heat transportation, which generally enables a good efficiency in heat exchanges. For that reason, two-phase thermal management systems are considered as extremely beneficial for space applications. Indeed, in satellites or space-platforms, the major thermal problem is currently to remove the heat generated by devices from the inside into space, in order to ensure suitable environmental and working conditions. Moreover, the growing interest for space applications such as communication satellites and the increasing power requirements of on-board devices require sophisticated management systems capable to deal with larger heat loads. Since the heat transfer capacity associated with phase change is typically large and with a relatively little increase in temperature, this solution could mean decreased size and weight of thermal systems. But boiling is a complex phenomenon which combines heat and mass transfers, hydrodynamics and interfacial phenomena. Furthermore, gravity affects the fluid dynamics and may lead to unpredictable performances of thermal management systems. It is thus necessary to perform experiments directly in (near) weightless environments. Besides the ISS, microgravity conditions can be simulated by means of a drop-tower, parabolic flights on board an aircraft or a sounding-rocket.

Although flow boiling is of great interest for space applications under microgravity conditions, few experiments have been conducted in low gravity. These experiments provided a partial understanding of boiling phenomena and have been mostly performed for engineering purposes such as the evaluation of ISS ("International Space Station") hardware or two-phase loop stability. Moreover, flow boiling heat transfer experiments in microgravity (referred to as $\mu - g$) require large heat loads and available space. They are subject to severe restrictions in the test apparatus, do not last long and offer few opportunities to repeat measurements, which could explain the lack of data and of coherence between existing measurements. Nevertheless, several two-phase flow (gas–liquid flow and boiling flow) experiments have been conducted in the past forty years and enabled to gather data about flow patterns, pressure drops, heat transfers including critical heat flux and void fraction in thermohydraulic systems. Previous state of the art and data can be found in the papers of Colin et al. (1996), Ohta (2003), and Celata and Zummo (2009). Several studies have been carried out under microgravity conditions in order to classify adiabatic two-phase flows by various patterns through observation and visualisations of the flow. Various flow patterns have been identified at different superficial velocities of liquid $j_l$and gas j_g, for both adiabatic gas–liquid flows and boiling flows: bubbly flow, slug flow and annular flow. Transitions between these flow patterns have been studied too: transition between bubbly and slug flow, and transition between slug and annular flow or frothy slug-annular flow. The determination of these transitions is of importance because the wall friction and wall heat transfer are very sensitive to the flow pattern. Colin et al. (1991) and Dukler

* Corresponding author.
E-mail address: colin@imft.fr (C. Colin).

0301-9322/$ - see front matter © 2013 Elsevier Ltd. All rights reserved.
http://dx.doi.org/10.1016/j.ijmultiphaseflow.2013.11.011

et al. (1988) drew a map based on void fraction transition criteria to predict patterns in liquid–gas flows. These patterns were also observed in flow boiling for heat transfer below the critical heat flux by Ohta (2003), Reinarts (1993) and more recently by Celata and Zummo (2009). The transition between bubbly and slug flows occurs from coalescence mechanisms. Coalescence can be promoted or inhibited depending on the value of the Ohnesorge number. A general flow pattern map for bubbly and slug flows based on the value of the *Oh* number was proposed by Colin et al. (1996) for air–water flow and also for boiling refrigerants. The Ohnesorge number $Oh = (\rho\nu^2/\sigma D)^{1/2}$ is based on the pipe diameter D and on the fluid properties: ν, ρ, σ, the kinematic viscosity, density and surface tension of the liquid, respectively. A criterion based on the Ohnesorge number was also established by Jayawardena et al. (1997). The transition between slug and annular flows has also been investigated by several authors, who proposed criteria based on transition void fraction value as Dukler et al. (1988), critical value of a vapour Weber number as Zhao and Rezkallah (1993), balance between gas inertia and surface tension according to Reinarts (1993) and Zhao and Hu (2000).

The estimation of cross-sectional averaged void fraction α or mean gas velocity U_g is a key-point for the calculation of wall and interfacial frictions. It has been shown that the mean gas velocity $U_g = j_g/\alpha$ is well predicted by a drift flux model $U_g = C_0 \cdot j$ for bubbly and slug flow (Dukler et al., 1988), $j = j_l + j_g$ being the mixture velocity and C_0 a coefficient depending on the local void fraction and gas velocity distributions. Very few experimental data on film thickness in microgravity is available, and only for gas–liquid annular flows (Bousman et al., 1996; de Jong and Gabriel, 2003). Different experimental technics have been used to determine the cross-sectional averaged void fraction: capacitance probes (Elkow and Rezkallah, 1997), conductance probes (Colin et al., 1991) and optical techniques.

Regarding the measurements of the wall shear stress, most of the studies performed under microgravity conditions concern gas–liquid flow without phase change (Zhao and Rezkallah, 1995; Colin and Fabre, 1995; Colin et al., 1996). Some results also exist for liquid–vapour flow (Chen et al., 1991), but in an adiabatic test section. The frictional pressure drop has been compared (Zhao and Rezkallah, 1995; Chen et al., 1991) to different empirical models (homogeneous model, Lockhart and Martinelli's model Lockhart and Martinelli, 1949). Recently, Awad and Muzychka (2010) and Fang et al. (2012) proposed a modified expression of the correlation of Lockhart and Martinelli and found good agreement with the experimental data. Very few studies reported data on the interfacial shear stress in annular flow (Dukler et al., 1988). This can be explained by the difficulty of measuring simultaneously pressure drops and film thickness.

Little research on flow boiling heat transfer in microgravity has been conducted, mainly because of the restrictive experimental conditions. Lui et al. (1994) carried out heat transfer experiments in subcooled flow boiling with R113 through a tubular test Section (12 mm internal diameter, 914.4 mm length). Heat transfer coefficients were approximately 5–20% higher in microgravity, generally increasing with higher qualities, which was believed to be caused by the greater movement of vapour bubbles on the heater surface. Ohta (1997, 2003) studied flow boiling of R113 in a 8 mm internal diameter vertical transparent tube, internally coated with a gold film, both on ground and during parabolic flight campaigns, and for the preparation of a future experiment on board the International Space Station. The authors examined various flow patterns and the influence of gravity levels on heat transfer coefficients for flow boiling. They found that, in bubbly flow, heat transfer is similar in normal and microgravity conditions, despite different bubble sizes at low mass fluxes. In annular flow, heat transfer coefficients are smaller in microgravity at low heat flux. The difference in the heat transfer coefficient in annular flow between normal and microgravity conditions disappears at high flux in the nucleate boiling regime. Celata and Zummo (2009) performed subcooled flow boiling experiments with FC-72 in Pyrex tubes (2, 4 and 6 mm internal diameters). They found that in bubbly and slug flow the influence of gravity is not evident for liquid velocities larger than 0.25 m/s or qualities larger than 0.3. Recently, a new technique for the measurement of heat transfer distributions has also been developed by Kim et al. (2012). They used an IR camera to determine the temperature distribution within a multilayer consisting of a silicon substrate coated with a thin insulator. They have not quantified the difference between microgravity and normal gravity yet. No clear conclusion on the influence of the buoyancy force on the heat transfer can be pointed out from these experiments. It seems to be strongly dependent on the mass flux and quality values. Work is still needed to confirm and give coherence to the previous results of the literature on flow boiling and to compare the data sets obtained by the different authors.

The objective of the present work is to collect, analyse and compare flow boiling data in normal gravity and under microgravity conditions. A refrigerant circulates in a heated tube of 6 mm inner diameter coated by a conductive film heated by the Joule effect. Its outer diameter is 8 mm. Flow patterns, void fraction, film thickness, wall and interfacial shear stresses, and heat transfer are investigated. This paper presents the main results of the measurement campaigns. The first section describes the experimental apparatus and the measurement techniques. The data reduction to obtain the mass quality, gas velocity, wall shear stress and heat transfer coefficient is described in a second section. Finally the experimental results obtained in $\mu - g$ and $1 - g$ experiments are presented and discussed.

2. Experimental set-up and measurement techniques

2.1. Hydraulic loop

The experimental set-up used to study vapour-liquid flows in $1 - g$ and $\mu - g$ mainly consists of a hydraulic loop represented in Fig. 1. In this pressurised circuit, the working fluid is the refrigerant 1-methoxyheptafluoropropane ($C_3F_7OCH_3$), commonly referred to as HFE-7000. This fluid has been chosen for safety reasons due to restrictions in $\mu - g$ experiments and because of its low saturation temperature at atmospheric pressure (34 °C at 1 bar), and its low latent heat of vapourization (142 kJ/kg against 2257 kJ/kg for water). In the circuit, the HFE-7000 may be in a liquid or a liquid–vapour state depending on the portion of the hydraulic loop, but it is never in a pure vapour state. The HFE-7000 is first pumped at liquid state by a gear pump while the liquid flow rate is measured by a Coriolis flowmeter. Then the fluid circulates through two serial preheaters. Its temperature can be adjusted below the saturation temperature (subcooled conditions) or the fluid can be preheated to its boiling point and partially vapourised (saturated conditions). It then enters a 22 cm long vertical stainless steel tube just upstream the test section, which enables the flow to fully develop. In the test section, the HFE-7000 (upward flow) is further vapourised in a sapphire tube heated by Joule effect through an outside ITO coating. The fluid exiting the test section is then condensed and cooled 10 °C below its saturation temperature by four cold plates containing Peltier modules and fans before it enters the pump again. The pressure is adjusted in the circuit via a volume compensator, whose bellows can be pressurised by air.

The loop pressure is set from 1 to 2 bars and the fluid circulates with mass fluxes G between 100 and 1200 kg/m^2/s. A wide range of flow boiling regimes is studied, from subcooled flow boiling to

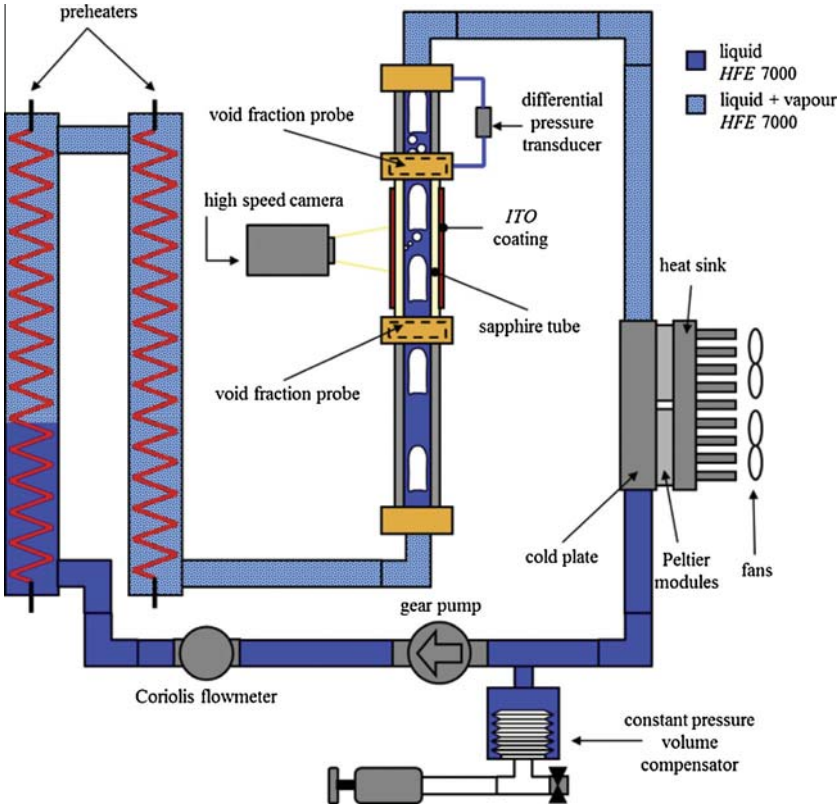

Fig. 1. Experimental set-up.

saturated flow boiling, by adjusting the power input of the heaters (vapour mass qualities x up to 0.8) and the power through the ITO coating (wall heat flux q_{ow} up to 4.5 W/cm^2). The total vapour quality at the outlet of the test section can be set up to 0.9.

The test section mainly consists of a 20 cm long sapphire tube with a 6 mm inner diameter D and a 1 mm thickness. The outer surface is coated on a length of 16.4 cm with ITO, an electrical conductive and transparent coating that enables a uniformly heating by Joule effect and a visual display of the flow.

2.2. Measurement technique

Various measurement instruments provide experimental data for the calculation of the wall shear stress, heat transfer coefficient, gas velocity or film thickness.

2.2.1. Pressure drop

Two P305D Valydine differential pressure transducers (to cross-check) measure the pressure drops along an adiabatic section of 20 cm long at the outlet of the test section (see Fig. 1), with a precision of 0.5 mbar; they are calibrated at IMFT using two manometers with different ranges.

2.2.2. Absolute pressure

Two Omega pressure transmitters 24 V DC are used to calculate the saturation temperature at the inlet and outlet of the sapphire tube. No differential pressure measurement is performed on this section.

2.2.3. Temperature

Type K thermocouples measure the flow temperature at the test section inlet and outlet, with a precision of ±0.2 °C. Two type T thermocouples are also used to measure the temperature difference between a hot junction and a cold junction located at the inlet and outlet of the test section, respectively. This differential thermocouple allows a very accurate measurement of the fluid temperature difference between both ends of the sapphire tube. Pt100 probes measure the ambient temperature and the external surface temperature of the sapphire tube at four different positions (at a distance of 45, 73, 106, 133 mm from the beginning of the heated length), with a precision of ±0.1 °C. We used Pt100 probes that are specifically designed for wall temperature measurements. They are flat and mechanically squeezed against the ITO coating by an O-ring in order to reduce thermal resistance. The measurement technique for the heat flux is validated in single-phase flow by comparison of the measurements with classical correlations in the next section. Both thermocouples and Pt100 probes are calibrated using a silicone oil bath and a reference Pt100 probe (±0.01 °C with calibration certificate).

2.2.4. Flow visualisations

A high-speed camera PCO 1200 HS with the associated backlight provides movies of the flow through the transparent ITO coating on the sapphire tube. The camera field of view is $1000 * 350$ pixels^2 and the acquisition frequency is 1000 or 1500 images per second depending on the flow regime. The spatial resolution of the images is 33.3 pixels/mm. Only a short length of 30 mm is imaged by the camera. It is located between the 2nd and 3rd Pt100 probes.

2.2.5. Void fraction

Specific void fraction probes were designed and built at IMFT to provide accurate data of the volume fraction of the vapour phase at the inlet and outlet of the test section. These sensors are made of two copper electrodes (and four guard electrodes) of around 1

cm^2 placed on both sides of the two-phase flow as can be seen in Fig. 2a.

The capacitance measured between the electrodes depends on the permittivity of the considered volume and can be related to the void fraction after calibration. Liquid HFE-7000 and Teflon rods whose permittivity is close to the one of HFE-7000 vapour are used to mimic the annular flow configuration for the calibration. For each void fraction value, the reduced capacitance $C^* = (C - C_v)/(C_l - C_v)$ is measured and plotted on a calibration curve (Fig. 2b). C, C_v and C_l are the measured capacitance for the liquid–vapour mixture, for the vapour alone and for the liquid alone, respectively. The geometry of the sensor has been designed to minimise the sensitivity of the measurement to the void fraction distribution and thus to the flow pattern. Nevertheless a direct calibration measuring the bubble velocities from image processing is recommended for bubbly flows. A numerical model of capacitances in series and parallel has also been developed to combine both flow regimes in a single calibration curve (Fig. 2b). The signal sensibility (corresponding to the capacitance difference between liquid state and vapour state $C_l - C_v$) is around 0.3 pF. The accuracy on the measurement is 0.001 pF, which gives an uncertainty less than 1% on the capacitance data. The uncertainty on the void fraction itself depends on the precision of the calibration and is estimated at 2%.

The acquisition system consists of a 36 channels National Instrument deck, two laptops with LabVIEW interfaces and a computer for the acquisition of camera images using Cameware software.

2.3. Measurement campaigns

Experiments were conducted both on ground and under microgravity conditions. A near-weightless situation is simulated during a parabolic flight campaign which consists of three flights with 31 parabolas per flight. Each parabola provides up to 22 s of microgravity with a gravity level smaller than ± 0.03 g, with $g = 9.81$ m/s^2. Parabolic flight campaigns are the only sub-orbital opportunity for experimenters to work directly on their experimental apparatus under microgravity conditions without too severe restrictions on the size of their set-up and the available power on board. Two parabolic flight campaigns (May 2011 and April 2012) provided data for the results presented in this article. The liquid mass flux is imposed by a gear pump. During one parabola, the gravity level drastically changes between $1-g$, $1.8-g$ and $\mu-g$, leading to pressure variations in the test section. Since no PID regulation of the rotating speed of the pump was used, a variation of the mass flux was observed between the different phases of a parabola. The mass flux is steady during $1-g$ phases between two parabolas (G =100, 200 or 400 kg/s/m^2), but it drops a little bit during the $1.8-g$ period and then increases in microgravity (as can be seen in Fig. 3). This is the reason why experimental points do not exactly fit the G isocurves on the flow pattern map in microgravity. Nevertheless, after a short transient period, the flow rate stabilises in microgravity and a steady state is reached.

During the on-ground measurement campaign, relevant parabolas were reproduced in order to compare data obtained in normal gravity and under microgravity conditions. A series of parametric runs has also been conducted to complete the dataset.

3. Data reduction

In the next sections, the experimental results on wall and interfacial shear stresses, quality, vapour velocity, film thickness and heat transfer coefficients will be presented. These values are deduced from the measurements of wall and liquid temperatures, heat flux, pressure drop and void fraction by using mass, momentum and enthalpy balance equations, which are detailed in this section. The measurement techniques are validated in single-phase flow by comparison of the experimental results with classical correlations of the literature.

3.1. Wall friction

The momentum balance equation for the liquid–vapour mixture in steady state enables to write the wall friction along a heated test section according to the pressure drop, the void fraction, the mass flux and the vapour quality:

$$\frac{dP}{dz} = \frac{4}{D}\tau_w - \frac{d}{dz}\left[\frac{G^2x^2}{\rho_v\alpha} + \frac{G^2(1-x)^2}{\rho_l(1-\alpha)}\right] - g\left[\rho_v\alpha + \rho_l(1-\alpha)\right] \quad (1)$$

where P, G, x, α, g, ρ_l, ρ_v are the pressure, mass flux, quality, void fraction, acceleration of gravity, density of liquid and vapour, respectively. τ_w is the wall friction, which is negative. The second term of the Right Hand Side (RHS) is an acceleration term, that has to be taken into account when quality and void fraction evolve along the test section. Since the pressure drop measurements were performed along an adiabatic test section in our experiment, this term is equal to zero. The last term of the RHS is the hydrostatic

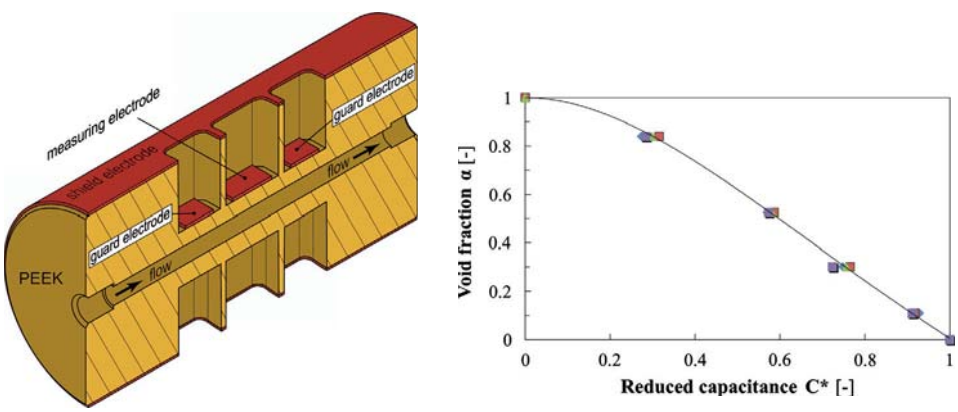

(a) *Schematic of the void fraction probe.* (b) *Calibration curve.*

Fig. 2. Void fraction probe.

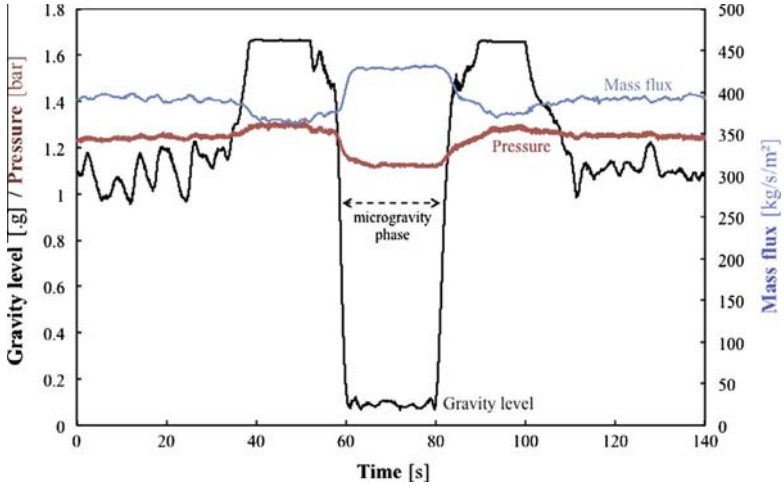

Fig. 3. Pressure and mass flux evolutions during one parabola.

pressure gradient that is negligible in microgravity. On ground, in upward flow, this last term is dominant, thus the accuracy of the wall shear stress measurement is directly linked to the accuracy of the void fraction measurement itself. An averaged value of the wall shear stress is deduced from the pressure drop and void fraction measurements by integration of Eq. (1). Measurements for single-phase liquid flows have enabled to validate the measurement technique by comparing the data to Blasius's correlation:

$$f_w = \frac{\tau_w}{1/2\rho_l j_l^2} = 0.079Re^{-0.25} \tag{2}$$

where Re is the Reynolds number of the liquid flow. Fig. 4 shows the measurements obtained with the two differential transducers for single-phase liquid flows at various mass fluxes and Blasius's correlation. The dashed lines correspond to Blasius's correlation at ±10%. The agreement is good considering that the measurement range of the transducers is adapted to two-phase flow with much larger pressure drops.

3.2. Wall heat transfer

The heat transfer coefficient is measured at the inner wall of the sapphire tube. A cross-section of the sapphire tube is represented in Fig. 5. T_{iw} and T_{ow} are the inner and outer temperatures of the sapphire tube wall, respectively. $T_{e\infty}$ is the temperature of the ambient air far from the tube (measured by a Pt100 probe) and

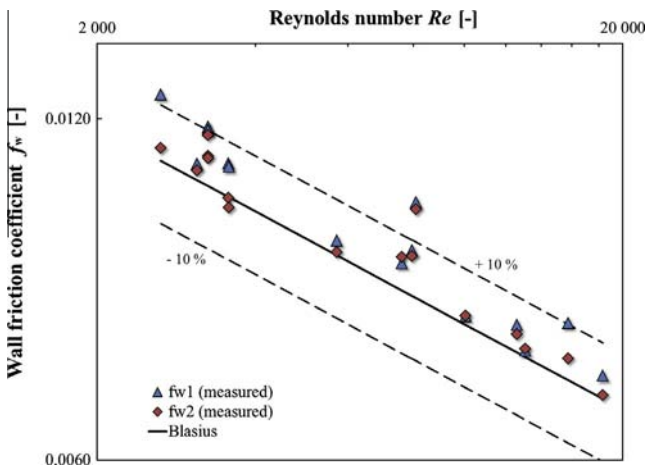

Fig. 4. Wall friction coefficient and Blasius correlation in single-phase flow.

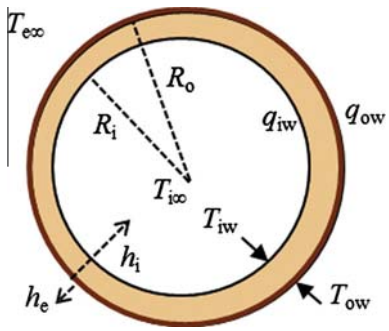

Fig. 5. Scheme of the heated test section.

$T_{i\infty,}$ is the liquid bulk temperature in the tube. T_{in} and T_{out} are the liquid bulk temperatures at the inlet and outlet of the sapphire tube. The inner and outer radii of the sapphire tube are denoted by R_i and R_o, respectively. The sapphire thermal conductivity is denoted by k and is equal to 22 W/m/K. The ITO coating on the external surface of the test section provides a heat flux q_{ow}. The heat flux q_{iw} delivered to the fluid is considered as equal to q_{ow} corrected by the radii ratio R_o/R_i. The heat transfer between the flow and the internal wall of the sapphire tube is characterised by the heat transfer coefficient h_i. The heat transfer between the environment and the external wall of the sapphire tube (thermal losses) is characterised by the heat transfer coefficient h_e.

In order to estimate the heat transfer coefficient at the inner wall h_i the following hypotheses are made: (1) temperature profiles are axisymmetric. (2) axial conduction is neglected. (3) heat transfer by radiation is neglected.

By using a conduction equation, the temperature at the inner wall T_{iw} can be deduced from the measurements of the temperature at the outer wall T_{ow} and the heat flux q_{ow} applied by Joule effect through the ITO coating:

$$T_{ow} - T_{iw} = [q_{ow} - h_e(T_{ow} - T_{ew})] \cdot ln\left(\frac{R_o}{R_i}\right) \cdot \frac{R_o}{k} \tag{3}$$

The temperature T_{ow} is measured by the previously described Pt100 probes. The heat transfer coefficient at the inner wall h_i and the Nusselt number $Nu = 2h_iR_i/k_l$ (k_l being the thermal conductivity of the liquid) is deduced from an energy balance through the tube:

$$h_i \cdot (T_{iw} - T_{i\infty}) = \frac{R_o}{R_i}[q_{ow} - h_e(T_{ow} - T_{e\infty})] \tag{4}$$

The temperature evolution between T_{in} and T_{out} can be considered as linear or parabolic, which enables to calculate $T_{i\infty}$ all along the sapphire tube. A series of experiments has been conducted in order to evaluate the thermal losses given by the coefficient h_e. In particular, it can be locally estimated in normal gravity with the local measurement of T_{ow} and the measurement of $T_{e\infty}$ for single or two-phase flow without heating by using a known correlation to estimate h_i. In this configuration, thermal losses have been estimated for single and two-phase flows with different correlations. The maximal heat transfer coefficient h_e that was obtained in normal gravity represents 6% of heat transfer coefficient h_i. Experiments with single-phase flows characterised by very low mass fluxes G and high temperatures have allowed us to conclude through a global energy balance about the nature of thermal losses that are considered as negligible. In order to validate the heat transfer measurements, experiments are performed in single-phase flow and the results are compared to the classical correlations in the literature. It is important to notice that the heated length is short and the heat transfer regime is not fully established. Then the entrance effect correction has to be taken into account in order to compare measurements and correlations. For a fully developed turbulent single-phase flow, the Nusselt number Nu_∞ can be calculated with Gnielinski's correlation (5) (Gnielinski, 1976) valid for fully developed turbulent flow in a wide range of Reynolds numbers $2500 < Re < 5.10^6$ and Prandtl numbers $0.5 < Pr < 2000$:

$$Nu_\infty = \frac{(f_w/2)\cdot(Re-1000)\cdot Pr}{1+12.7(f_w/2)^{1/2}\cdot(Pr^{2/3}-1)} \tag{5}$$

where f_w is the wall friction coefficient. In Fig. 6a the measured values of the Nusselt number $Nu_m = h_i \cdot D/k$ are plotted versus the Reynolds number. Since the flow is not thermally developed, these values of the Nusselt number are larger than the values measured in thermally developed flow Nu_∞. The deviation from the correlation is in inverse proportion to the distance between the temperature sensors and the inlet of the heated section. In order to compare the measurements with the preceding correlations, the measured values of the Nusselt number have been corrected by the entrance effect using Al-Arabi's correlation (Al-Arabi, 1982):

$$\frac{Nu_m}{Nu_\infty} = 1 + \frac{\frac{(z/D)^{0.1}}{Pr^{1/6}}\left(0.68+\frac{3000}{Re^{0.81}}\right)}{z/D} \tag{6}$$

Fig. 6b shows the measurements corrected with Al-Arabi's correlation according to the sensor position z and the comparison to Gnielinski's correlation. The experimental data meet the correlations with a maximal error of ±17%. The precision between measurements and correlations is satisfying for the whole set of experiments in single-phase flow. It also confirms the weak impact of external thermal heat losses on the measurements.

3.3. Vapour quality

The vapour quality can be calculated by using the enthalpy balance equation in steady state. q_{iw} is the inner wall heat flux delivered to the fluid and it will be noted q in the following. D is the inner diameter of the sapphire tube, z is the distance from the inlet of the heated test section, x is the quality at z, x_0 is the quality at $z = 0$. The enthalpy balance equation can be written versus the enthalpies of the liquid phase h_l and the vapour phase at saturation temperature $h_{v,sat}$:

$$\frac{4qz}{D} = G([xh_{v,sat}(z) + (1-x)h_l(z)] - [x_0h_{v,sat}(0) + (1-x_0)h_l(0)]) \tag{7}$$

The pressure drop along the test section is low then it does not induce a significant change of the saturation temperature and fluid properties, which will be considered as constant between 0 and z. For saturated boiling regimes, the liquid temperature T_l is equal to the saturation temperature T_{sat}. The local mass quality x at a distance z from the inlet of the heated section is equal to:

$$x = x_0 + \frac{4z\cdot q}{G\cdot D\cdot h_{lv}} \tag{8}$$

where h_{lv} is the latent heat of vapourisation, x_0 is the quality at the inlet of the test section, equal to the quality at the outlet of the preheater and calculated from an enthalpy balance in the preheaters. For subcooled boiling regimes, $x_0 = 0, T_l$ is smaller than T_{sat} and the vapour temperature is assumed to be equal to the saturation temperature. The quality $x(z)$ can be deduced from Eq. (7):

$$x(z) = \frac{\frac{4qz}{GD} - [h_l(z) - h_l(0)]}{h_{lv} + h_{l,sat}(z) - h_l(z)} = \frac{\frac{4qz}{GD} - C_{pl}(T_l(z) - T_l(0))}{h_{lv} + C_{pl}(T_{sat} - T_l(z))} \tag{9}$$

where C_{pl} is the specific heat of the liquid at constant pressure. The wall heat flux leads to an increase of the total enthalpy of the mixture, both by phase change and by increasing the liquid temperature. The fluid temperature is measured at the inlet and outlet of the test section and the temperature evolution between these two points is considered as linear or parabolic. Note that in Eq. (9), quality x is not the thermodynamical quality. The calculation of vapour quality in subcooled boiling is tricky because of the order of magnitude of x and of measurement uncertainties. We can define

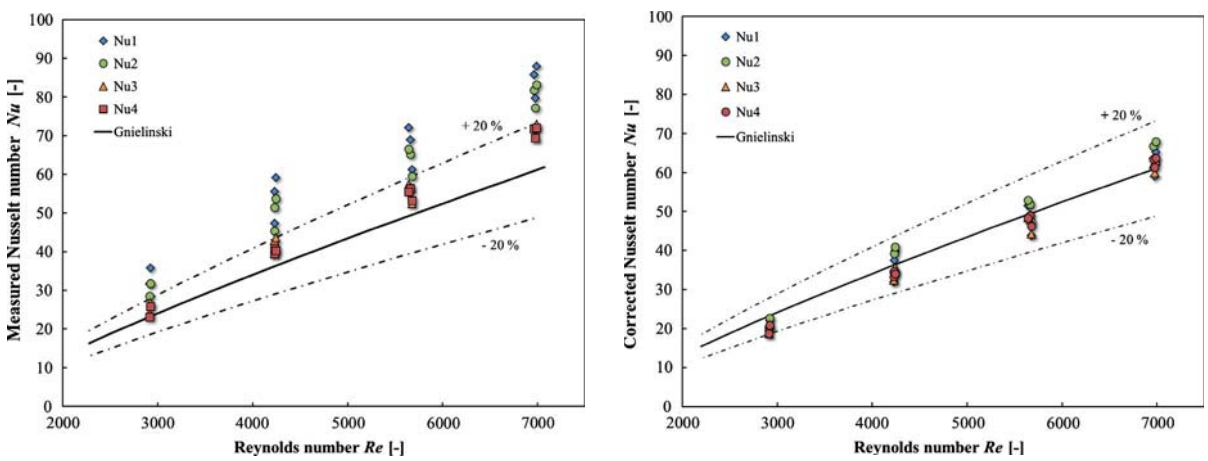

(a) *Without any correction.* (b) *With Al'Arabi's correction.*

Fig. 6. Nusselt number versus Reynolds number in single-phase flow.

measurement errors $\Delta q = 1000\ \mathrm{W/m^2}$ on the measured wall heat flux and $\Delta T_l = 0.2$ K on the measured liquid temperature. Measurement errors on mass flux G, and geometrical and physical properties are neglected. The error on the vapour quality is $2 \cdot 10^{-3}$, which is the order of magnitude of x itself for subcooled regimes at low vapour qualities. This error was confirmed by an analysis of flow videos that compared the mean bubble velocity measured from image processing and those calculated using the void fraction and the quality values.

4. Results and discussion

Experimental results concerning flow regimes, void fraction, film thickness, wall and interfacial shear stresses and finally heat transfer coefficient are presented in this section and compared to classical models of the literature.

4.1. Flow pattern

The high speed camera enables us to visualise flow patterns for various mass fluxes G, vapour qualities x at the inlet of the test section and heat fluxes q through the ITO coating. Three main flow patterns have been observed under both normal gravity and microgravity conditions: bubbly flow, slug flow and annular flow. The relevant parameter used to study the evolution of flow patterns is the vapour quality. At low vapour qualities corresponding to subcooled regimes ($T_l < T_{sat}$), bubbly flows occur. Bubbles are nucleated on the heated wall, they slide along the wall and detach. Bubbles grow due to phase change and also by coalescence. Fig. 7 shows a comparison between bubbly flows in $1-g$ and $\mu-g$ for the same parameters (G, x and q) and a liquid subcooling $\Delta T_{sub} = T_{sat} - T_l = 20\ ^\circ\mathrm{C}$. The impact of gravity level on the bubble size and shape is not significant in the videos for a high mass flux of 540 kg/m^2/s, but it can be clearly seen for a lower mass flux of 200 kg/m^2/s. At this low mass flux, under microgravity conditions, bubbles are larger than in normal gravity and are not deformed, because they have a very small relative velocity compared to the liquid velocity. The larger bubble size in microgravity can be explained by both the larger bubble diameter at detachment and the higher rate of coalescence due to the small relative motion of the bubbles.

In saturated flow boiling, annular flow regime is mostly observed for quality above 0.1 (Fig. 8). The liquid is flowing at the wall around a vapour core. The liquid film can become very thin and wavy because of the strong interfacial shear stress induced by the vapour core flow. Roll waves at the vapour-liquid interface are visible on the videos. At the highest qualities and mass fluxes, some liquid droplets are also detached from the film surface and entrained into the vapour core.

Several intermediate regimes are observed between bubbly and annular flow regimes which are themselves clearly described: slug flows (Fig. 9), churn flows and other transition flows that are difficult to identify. These regimes occur for low liquid subcoolings or for saturated boiling at low qualities. From bubbly flow, as quality increases, dense bubble distributions including a few Taylor bubbles can be observed. Coalescence phenomenon then leads to slug flow with Taylor bubbles, whose length increases with vapour quality. Once the gas core is no longer interrupted by liquid plugs, annular flow is observed.

The flow pattern can be determined from flow visualisations but also from the signal of the void fraction sensors (Fig. 10). Bubbly flows correspond to low void fractions while annular flows data (with the vapour core) are observed for higher void fraction values. Slug flow is characterised by its intermittency, which is clearly visible on the signal oscillating between low and high void fraction values, even if spatial resolution and time resolution of the capacitance measurement do not allow to clearly see the slug passage.

The evolution of flow patterns according to the liquid and vapour superficial velocities can be plotted on flow patterns maps that illustrate all the runs that were performed on-ground (Fig. 11) and during parabolic flight campaigns (Fig. 12). Regimes are indicated according to the superficial vapour velocity j_v and superficial liquid velocity j_l, and iso-curves for mass flux G and vapour quality $x$are also plotted on these figures. The same flow patterns are observed in $1-g$ and $\mu-g$ conditions for about the same flow conditions j_l and j_v.

4.2. Wall and interfacial friction factors

The wall shear stress τ_w can be deduced from the pressure drop and void fraction measurements using Eq. (1). The second term of the RHS is equal to zero since the pressure drop measurements are

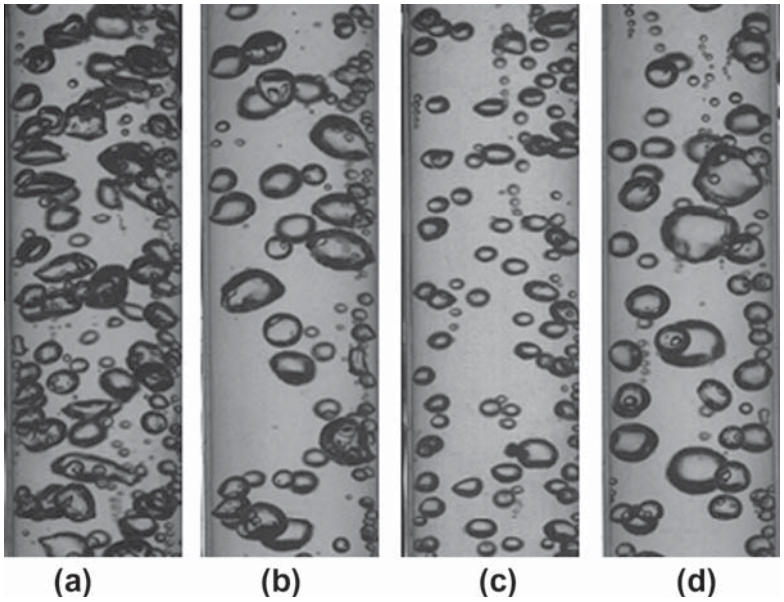

Fig. 7. Flow visualisations for bubbly flows, $\Delta T_{sub} = 12\ ^\circ\mathrm{C}$, $q = 2\ \mathrm{W/cm^2}$, (a) $G = 540\ \mathrm{kg/m^2/s}$ in $1-g$, (b) in $\mu-g$ and (c) $G = 220\ \mathrm{kg/m^2/s}$ in $1-g$, (d) in $\mu-g$.

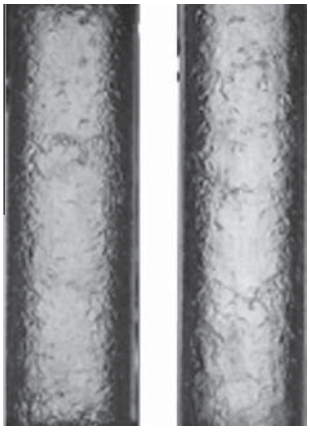

Fig. 8. Flow visualisation for annular flow $G = 200\ \mathrm{kg/m^2/s}$ and $x = 0.20$: left in $1-g$, right in $\mu-g$.

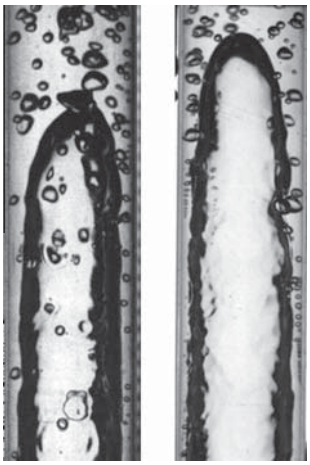

Fig. 9. Flow visualisation for slug flow at $G = 220\ \mathrm{kg/m^2/s}$ and $x = 0.05$: left in $1-g$, right in $\mu-g$.

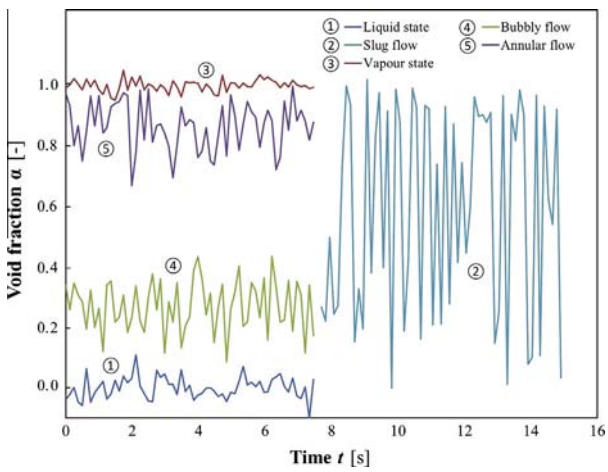

Fig. 10. Void fraction time evolution in single-phase liquid and vapour flows and in two-phase bubbly, slug and annular flows.

performed on an adiabatic part of the test section. In microgravity, the last term of the RHS is negligible and the measured pressure drop is directly proportional to the wall shear stress. In normal gravity (vertical upward flow), the hydrostatic pressure drop has to be deduced from total measurement. A good estimation of the

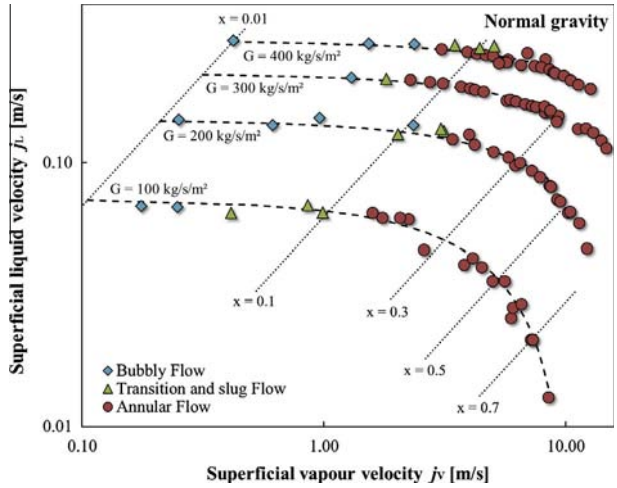

Fig. 11. Flow pattern map for normal gravity experiments.

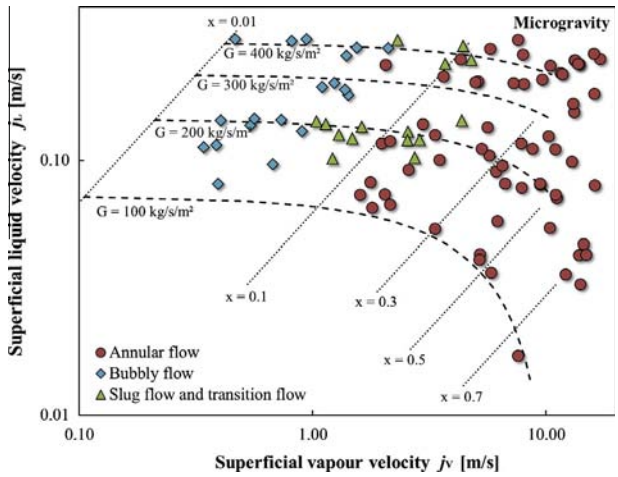

Fig. 12. Flow pattern map for microgravity experiments.

wall shear stress in this configuration requires an accurate measurement of the void fraction.

The experimental data are compared to the prediction of Lockhart and Martinelli's correlation (Lockhart and Martinelli, 1949), that gives an expression of the two-phase multiplier ϕ_L versus the Martinelli parameter X:

$$\left(\frac{dP}{dz}\right)_{fr} = \phi_L^2 \cdot \left(\frac{dP}{dz}\right)_l \quad \text{with} \quad \phi_L^2 = 1 + \frac{C}{X} + \frac{1}{X^2} \quad \text{and}$$
$$X^2 = \left(\frac{dP}{dz}\right)_l \Big/ \left(\frac{dP}{dz}\right)_v \tag{10}$$

where $\left(\frac{dP}{dz}\right)_l$ and $\left(\frac{dP}{dz}\right)_v$ would be the frictional pressure drops if the liquid or vapour were flowing alone in the tube. The constant C is equal to 20 if liquid and vapour Reynolds numbers are above 2000 (turbulent flow referred as LM_{tt} in Fig. 13) and C is equal to 10 if liquid Reynolds number is below 2000 (laminar regime) and vapour Reynolds number above 2000 (referred as LM_{lt}). Fig. 13 represents the experimental two-phase multiplier ϕ_L under normal gravity and microgravity conditions, compared to the one predicted by Lockhart and Martinelli's correlation.

A good agreement is obtained especially in annular flow regimes. The discrepancy between experiments and the model for bubbly flow in normal gravity may be attributed to a significant error on the superficial vapour velocity for low vapour qualities

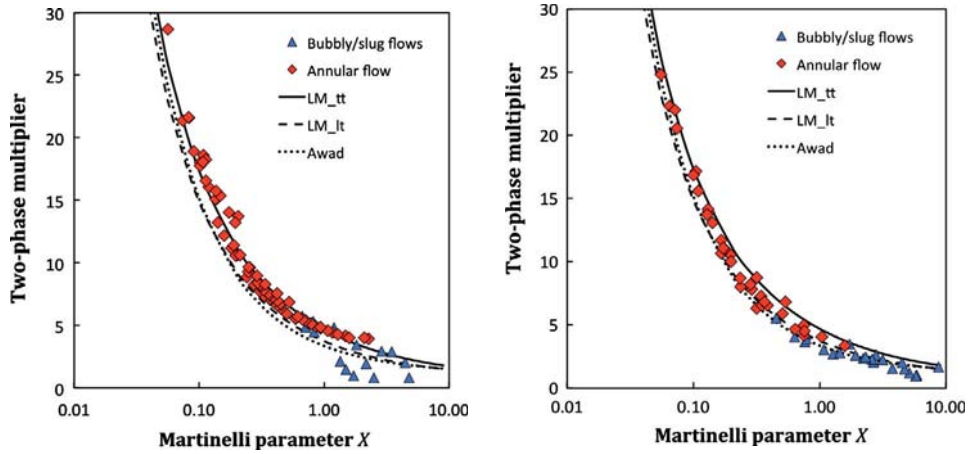

(a) *Normal gravity* (b) *Microgravity conditions.*

Fig. 13. Frictional pressure drop: two-phase multiplier.

and also to larger measurement errors on the pressure drop for bubbly flows. For microgravity experiments, an improvement of the two-phase multiplier model has been proposed by (Awad and Muzychka, 2010) and is also in very good agreement with experimental data:

$$\phi_L^2 = \left[1 + \left(\frac{1}{X^2}\right)^{2/7}\right]^{7/2} \tag{11}$$

From the measurement of the pressure drop and the void fraction or the film thickness, it is possible to determine the interfacial shear stress τ_i from the momentum balance equation for the vapour core (Wallis, 1969):

$$-\alpha\frac{dP}{dz} - \frac{4\tau_i\sqrt{\alpha}}{D} - \rho_v\alpha g = 0 \tag{12}$$

Eq. (12) is written for an annular flow without liquid droplet entrainment, assumption that will be justified in the next section. The interfacial friction factor f_i can be calculated according to τ_i:

$$f_i = \frac{\tau_i}{0.5\rho_v(U_v - U_l)^2} \simeq \frac{\tau_i}{0.5\rho_v U_v^2} \tag{13}$$

and compared to the wall friction factor of a vapour flow on the smooth wall f_v:

$$f_v = 0.079Re_v^{-1/4} \quad \text{with} \quad Re_v = \frac{U_v D}{\nu_v} \tag{14}$$

In annular flow, the vapour velocity U_v is most of the time much higher than the liquid velocity U_l. This high velocity difference leads to a destabilisation of the interface of the liquid film, which becomes wavy. For annular wavy liquid films, Wallis (1969) proposed an expression of the interfacial friction factor linked to the roughness of the liquid film that is assumed to equal the film thickness:

$$\frac{f_i}{f_v} = 1 + 300\frac{\delta}{D} \tag{15}$$

This correlation was developed for two-phase flow in large tubes (diameters around 50 mm). In this configuration, f_v is equal to about 0.005 and almost independent of Re_v corresponding to a fully-rough turbulent flow. Very few measurements of the interfacial shear stress have been performed in millimetric diameter tubes and almost no measurements exist in microgravity conditions. A data set is reported in 12.7 mm diameter tube in microgravity by Bousman and Dukler (1993), who provided a correlation for the prediction of f_i/f_v:

$$\frac{f_i}{f_v} = 211.4 - 245.9\alpha \tag{16}$$

The interfacial friction factor is calculated from our experiments. f_i/f_v is plotted versus the dimensionless film thickness δ/D characterising the film roughness in Fig. 14a and compared to the correlations of Wallis (1969) and Bousman and Dukler (1993). The Wallis's correlation largely overpredicts the interfacial friction factor and the Bousman and Dukler's correlation seems to be in reasonable agreement with the $1-g$ data. In Fig. 14b, the values of f_i/f_v are plotted versus the vapour Reynolds number Re_v based on the vapour velocity and on the diameter of the vapour core $D\sqrt{\alpha}$. f_i/f_v is a decreasing power function of $Re_v : f_i/f_v \sim Re_v^{-1.3}$. The dependency of f_i/f_v with Re_v proves that the turbulent regime of the vapour core is not fully rough. For a given value of Re_v, the dimensionless interfacial friction factor f_i/f_v seems to be lower in $\mu-g$ than in $1-g$, difference that increases while the mass flux decreases. Nevertheless it is important to remark that the friction factor also depends on the film thickness that is different in $\mu-g$ and in $1-g$.

As suggested by Lopez and Dukler (1986), the dependency on both roughness and Reynolds number is characteristic of a transition between smooth and fully rough turbulent regimes. For this partly rough turbulent regime, Fore et al. (2000) proposed a correction to the Wallis's correlation introducing a function of the vapour Reynolds number as $1 + A/Re_v$. Following this approach, a relation between $f_i/f_v, Re_v$ and δ/D is proposed. f_i/f_v is plotted versus $(1 + 3.10^5/Re_v^{1.3})(\delta/D)^{0.1}$ in Fig. 15. The power of the vapour Reynolds number is equal to -1.3 as shown in Fig. 14. The power of (δ/D) is much smaller than in the Wallis correlation. The following equation provides a reasonable prediction of the interfacial friction factor for the highest mass fluxes (Fig. 15). However large discrepancies are found the lowest mass flux $G = 100$ kg/m^2/s, especially in microgravity. Specific experiments at low mass fluxes will be performed in the future.

$$\frac{f_i}{f_v} = 1 + 28\left[\left(1 + \frac{3\cdot 10^5}{Re_v^{1.3}}\right)\left(\frac{\delta}{D}\right)^{0.1} - 0.82\right] \tag{17}$$

4.3. Void fraction and film thickness

For bubbly and slug flows, it is possible to calculate the value of the mean vapour velocity from the void fraction measurements. In Fig. 16, the mean vapour velocity U_v is plotted versus the mixture velocity j and compared to the classical drift flux model of Zuber and Findlay (1965):

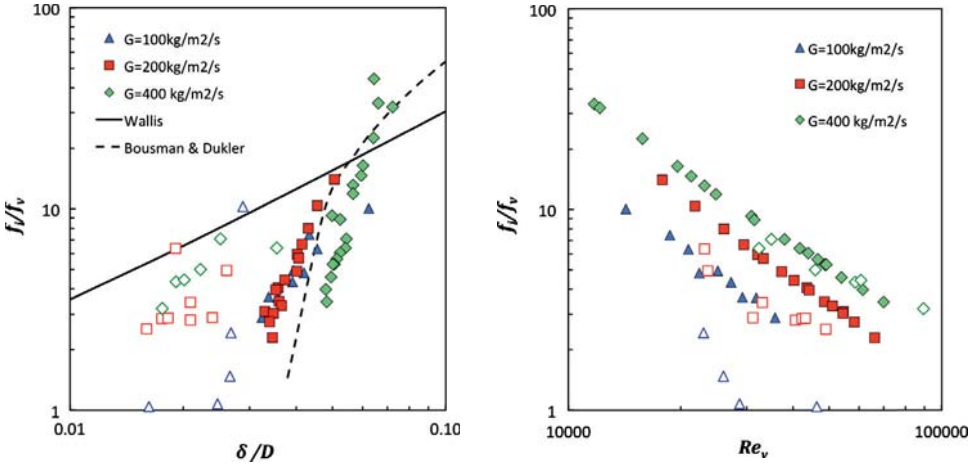

(a) f_i/f_v *versus film thickness* (b) f_i/f_v *versus vapor Reynolds number.*

Fig. 14. Interfacial friction factor in $1-g$ (closed symbol) and in $\mu-g$ (open symbols) experiments.

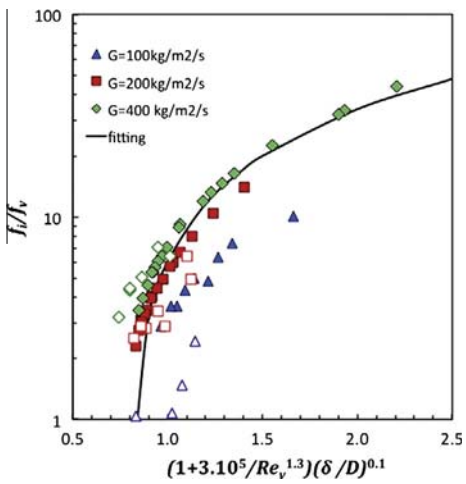

Fig. 15. prediction of interfacial friction factor in $1-g$ (closed symbols) and $\mu-g$ conditions (open symbols), solid line Eq. (17).

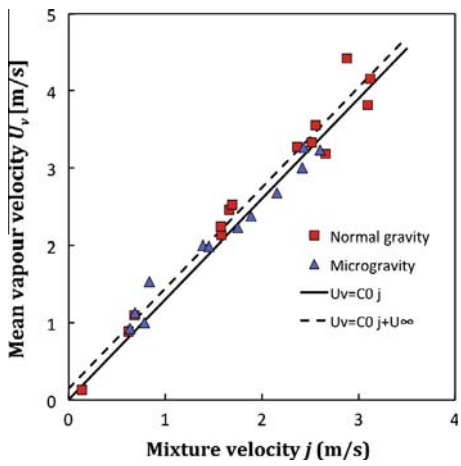

Fig. 16. Mean gas velocity for bubbly and slug flows in subcooled boiling. Comparison with the drift flux model for $C_0 = 1.3$.

$$U_v = \frac{j_v}{\alpha} = C_0 \cdot j + U_\infty = C_0 \cdot (j_l + j_v) + U_\infty \tag{18}$$

where the drift velocity U_∞ has different expressions for bubbly and slug flows: $U_\infty = 1.53(g(\rho_l - \rho_v)\sigma/\rho_l^2)^{1/4}$ (Harmathy, 1960) for bubbly flows and $U_\infty = 0.35\sqrt{gD}$ (Niklin et al., 1962) for Taylor bubbles in slug flow. These values are around 0.1 m/s in our experiments. In microgravity, U_∞ is equal to zero and a good agreement with Eq. (18) is found for a value of C_0 equal to 1.3.

This confirms the results previously obtained by Colin et al. (1991, 1996) for air–water flows in tubes of different diameters. The data on ground are compared to Eq. (18) for the same value of C_0 and a drift velocity for a bubbly flow $U_\infty = 0.15$ m/s. The scattering of the experimental data around the predicted values may be explained by the lower accuracy on the measurements for the very low quality values.

In the annular flow regime, the liquid film thickness δ can be deduced from the void fraction measurement by geometrical considerations. If there is no liquid droplet entrainment in the gas core, all the liquid flows at the wall and $\delta = D/2(1-\sqrt{\alpha})$. The accuracy on the film thickness measurement is linked to the capacitance measurement accuracy and the calibration procedure. For an accuracy of 2% on the void fraction value, the relative error on the film thickness is about 7%. A film thickness of 300 μm is evaluated with an accuracy of 20 μm. If there is an entrainment rate e, it has to be taken into account in the calculation of the film thickness (Cioncolini et al., 2009):

$$\delta = \frac{D}{2}\left(1 - \sqrt{\alpha\frac{\rho_l x + \rho_v(1-x)e}{\rho_l x}}\right) \tag{19}$$

Since the void fraction sensor provides a void fraction measurement almost independent of the phase distribution, only a global measurement of the liquid holdup, including both liquid film and droplets is obtained. In order to evaluate the rate of entrainment in our experiments and its influence on the film thickness measurement, it has been evaluated by using the correlation of Cioncolini and Thome (2012):

$$e = (1 + 279.6We_c^{-0.8395})^{-2.209} \tag{20}$$

where We_c is the Weber number of the vapour core based on the superficial vapour velocity and on the density ρ_c of the vapour core carrying droplets:

$$We_c = \frac{\rho_c j_v^2 D}{\sigma} \quad \text{with} \quad \rho_c = \frac{x + e(1-x)}{\frac{x}{\rho_g} + \frac{e(1-x)}{\rho_l}} \tag{21}$$

The Weber number We_c ranges between 10 and 10^5. From Eq. (19), it is possible to estimate the absolute error made by neglecting entrainment on the film thickness evaluation. This error is about equal to $(\rho_g(1-x)e)/(2\rho_l x)$. For the range of our experimental parameters G between 100 and 400 kg/m^2/s and x up to 0.8, e has been estimated from Eq. (20). The highest value found for the absolute error is 5%. Nevertheless, entrainment has been taken into account in the calculations for a better estimation of the film thickness.

In Fig. 17, the film thickness is plotted versus quality for three mass fluxes G in normal gravity and microgravity conditions. The accuracy on the film thickness measurement is about 20 μm. It can clearly be seen that for qualities larger than 0.2, the film thickness is larger in normal gravity than in microgravity. It can be explained from the momentum balance equations for the liquid film and the gas core. By eliminating the pressure gradient between these two equations and neglecting the acceleration term, a relation between the void fraction, the wall shear stress τ_w and the interfacial shear stress τ_i is obtained:

$$-\tau_w \cdot \sqrt{\alpha} + \tau_i - (\rho_l - \rho_g)g \cdot \sqrt{\alpha}(1-\alpha)D/4 = 0 \tag{22}$$

τ_w, τ_i and g the gravity acceleration are positive in this equation. Then the first term is negative, the second one positive and the third one negative. In microgravity, this equation reduces to $\tau_w \cdot \sqrt{\alpha} = \tau_i$. In vertical upward flow in normal gravity, the interfacial shear stress has to compensate both gravity and wall shear stress. Even if the interfacial shear stress is a little bit larger in normal gravity than in microgravity, this larger value cannot compensate the gravity term. The first term of Eq. (22) has to be lower in normal gravity. Since the wall shear stress is about the same in $1-g$ and $\mu-g$, it means that the void fraction has to be lower and the film thickness larger, which is in agreement with the experimental results. In Fig. 17, the measured film thickness values are also compared to the theoretical film thickness values calculated by Cioncolini and Thome (2011) using an algebraic eddy viscosity model for describing the velocity profile in the turbulent liquid film of an annular flow:

$$\delta = y_\star \cdot max\left[\sqrt{\frac{2\Gamma^+_{lf}}{R^+}}; 0.0066\frac{\Gamma^+_{lf}}{R^+}\right] \tag{23}$$

where $y_\star = \nu_l/u_\star$ is the viscous length scale, $R^+ = D/2y_\star$ is the dimensionless pipe radius and Γ^+_{lf} the dimensionless mass flow rate in the liquid film:

$$\Gamma^+_{lf} = \frac{(1-e)(1-x)G\pi \cdot D^2}{8\pi\rho_l u_\star y_\star^2} \tag{24}$$

In Eqs. (23) and (24), the friction velocity $u_\star = \sqrt{\tau_w/\rho_l}$ is evaluated according to Cioncolini et al. (2009):

$$\tau_w = \frac{1}{2}f_{wl}\rho_c V_c^2 \quad \text{with} \quad f_{wl} = 0.172We_c^2 \tag{25}$$

where the Weber number We_c is based on the core density ρ_c, core mean velocity V_c and core diameter d_c. In these calculations, the following expression has been used for the estimation of the void fraction in annular flow:

$$\alpha = \frac{f \cdot x^n}{1+(f-1)\cdot x^n} \quad \text{with} \quad f = a + (1-a)\left(\frac{\rho_v}{\rho_l}\right)^{a_1} \quad \text{and} \quad n = b + (1-b)\left(\frac{\rho_v}{\rho_l}\right)^{b_1} \tag{26}$$

with $a = -2.129$, $b = 0.3487$, $a_1 = -0.2186$, $b_1 = 0.515$. The measurements of the void fraction in microgravity are in reasonable agreement with the prediction of Eq. (26), whereas this equation largely overpredicts the measurement in $1-g$ conditions. Then, the measurements of the liquid film thickness are in good agreement with the prediction of Eq. (23) in microgravity. In normal gravity, the model largely underpredicts the measured values, because of the overestimation of the void fraction, as can be seen in Fig. 18.

4.4. Heat Transfer Coefficient

The heat transfer coefficients in saturated and subcooled boiling in $1-g$ and $\mu-g$ are deduced from the wall heat flux measurements q and the wall (given by the second probe near the imaged part of the tube) and liquid bulk temperatures using Eq. (4). By using a linear evolution of the temperature in the heated section and by considering uncertainties Δq and ΔT on the heat flux and temperature difference, respectively, heat transfer coefficients can be calculated with an error of ±14%. In saturated boiling corresponding to annular flow, the heat transfer coefficients are plotted in Fig. 19a and compared to the classical correlations of Kandlikar (1990) and Chen (1966). For vertical flows, Kandlikar' s correlation gives the value of the heat transfer coefficient:

$$h = h_l\left[C_1 Co^{C_2} + C_3 Bo^{C_4} F_K\right] \tag{27}$$

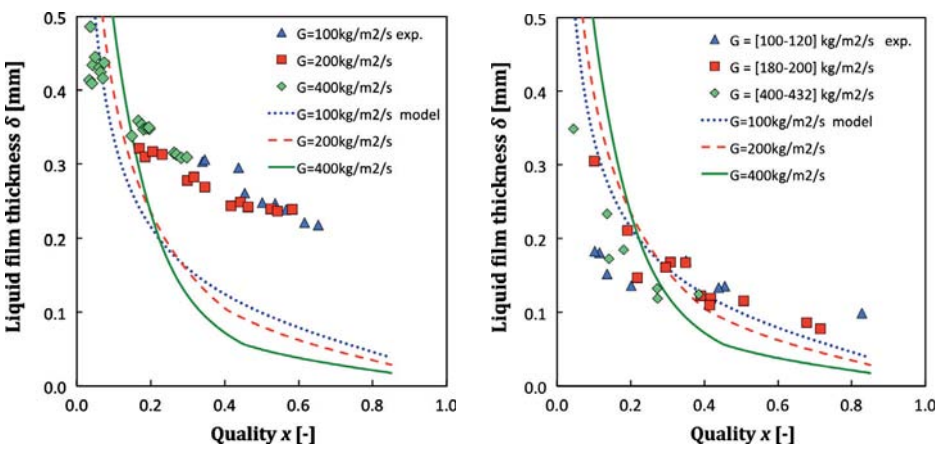

(a) *Normal gravity* (b) *Microgravity conditions.*

Fig. 17. Liquid film thickness in annular flow – symbols: experiments – lines: Eq. (23).

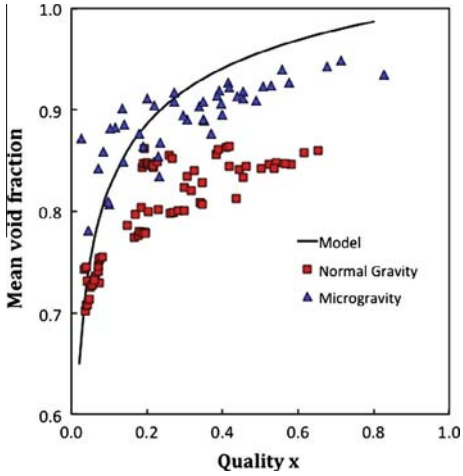

Fig. 18. Void fraction versus quality in $1-g$ (squares) and $\mu-g$ conditions (triangles), solid line Eq. (26).

where h_l is the heat transfer coefficient for a liquid single-phase flow at velocity j_l, $Bo = \frac{q}{Gh_{lv}}$ is the Boiling number and $Co = \left(\frac{1-x}{x}\right)^{0.8}\sqrt{\frac{\rho_g}{\rho_l}}$ a convection number. The values of the constants are for $Co < 0.65$, $C_1 = 1.136$, $C_2 = -0.9$, $C_3 = 667.2$, $C_4 = 0.7$ and for $Co > 0.65$, $C_1 = 0.6683$, $C_2 = -0.2$, $C_3 = 1058$, $C_4 = 0.7$. The value of F_K has been taken equal to 1.3, close to those of similar refrigerants.

The heat transfer coefficient can also be calculated using Chen's correlation:

$$h = F \cdot h_l + S \cdot h_{nb} \tag{28}$$

where h_{nb} is the heat transfer coefficient in pool boiling:

$$h_{nb} = 0.00122\left[\frac{k_l^{0.79}Cp_l^{0.45}\rho_l^{0.49}}{\sigma^{0.5}\mu_l^{0.29}h_{lv}0.24\rho_v^{0.24}}\right]\cdot(T_w - T_{sat})^{0.24} \cdot (P_{sat}(T_w) - P_{sat})^{0.75} \tag{29}$$

and F and S are amplification and suppression factors, function of Martinelli's parameter X:

$$F(X) = 2.35\left(0.213 + \frac{1}{X}\right)^{0.736} \quad \text{if} \quad \frac{1}{X} > 0.1 \quad \text{else} \quad F(X) = 1 \tag{30}$$

$$S(X) = \frac{1}{1 + 2.53\cdot 10^{-6}\cdot\left(\frac{GD(1-x)F(x)^{1.25}}{\mu_l}\right)^{1.17}} \tag{31}$$

Experimental data correspond with wall heat fluxes $q = 1$, 2, 4 W/cm^2. Indeed, the wall heat flux has a rather small influence on the heat transfer coefficient and was therefore not distinctly plotted, for clarity reasons. Chen's and Kandlikar's correlations are given for $q = 2$ W/cm^2.

Chen's correlation seems to underpredict the experimental data, especially at high quality, whereas Kandlikar's correlation gives a better prediction of the data. Nevertheless, it overpredicts the data for lower mass fluxes and lower qualities.

The experimental data are also compared to the heat transfer coefficient (HTC) estimated by Cioncolini and Thome (2011), according to the film thickness and wall friction in Fig. 19b:

$$h = \frac{k_l}{\delta}0.0776\cdot\delta^{+0.9}Pr_l^{0.52} \quad \delta^+ = \frac{\delta}{y_\star} \tag{32}$$

This expression is valid for $10 < \delta^+ < 800$ and $0.86 < Pr_l < 6.1$. This model seems able to reproduce the experimental trend, except for the highest high flux $G = 400$ kg/m^2/s and the lowest qualities $x < 0.2$. In order to better check the accuracy of the model, the predicted value of heat transfer coefficients by Eq. (32) is plotted versus the measured ones in Fig. 20. In Fig. 20a, the values of δ and $u_\star$ are calculated using Eqs. (23) and (25), whereas in Fig. 20b, the experimental values of δ and $u_\star$ are used for the calculations.

In Fig. 20a, the agreement is better than ±20% for most of the data, except for $1-g$ data at high heat flux. Despite the large discrepancy of the model and the data on the film thickness in $1-g$ (see Fig. 17), a reasonable agreement in found on the heat transfer coefficient. It may be explained by the small dependency of the heat transfer coefficient to the film thickness in Eq. (32): $h \propto \delta^{0.1}$. A significant difference is also found between the measured values of the wall shear stress τ_w and the prediction of Eq. (25). Then experimental data have finally be compared to the prediction of Eq. (32) using the experimental values for δ and $u_\star$. A much better agreement is found in this case, with most of the data predicted in a range of accuracy of ±15%, except for a few data at the lowest mass flux in microgravity.

An explanation for the low sensitivity of the heat transfer coefficient to gravity can be found by looking at the temperature and velocity profiles provided by Cioncolini for thick turbulent liquid films: both temperature and velocity gradients are concentrated

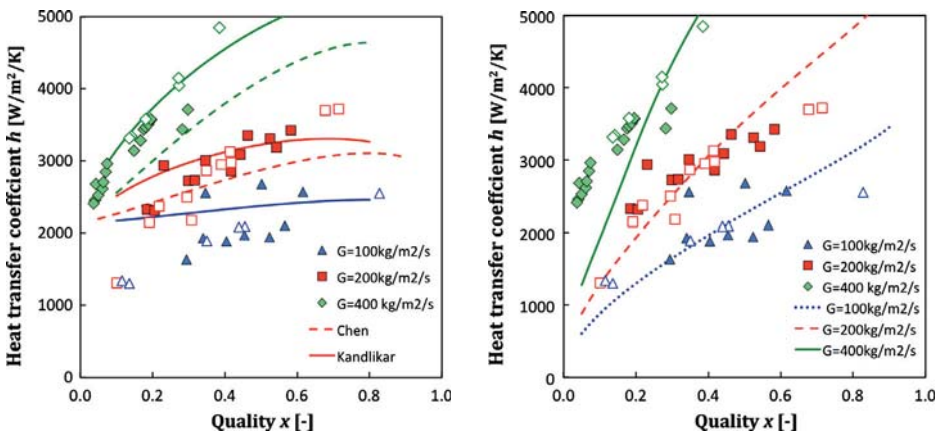

(a) *Comparison with Chen and Kandlikar correlations*

(b) *Comparison with Cioncolini and Thome's model.*

Fig. 19. Heat Transfer Coefficients versus quality for different mass fluxes in $1-g$ (closed symbols) and in $\mu-g$ (open symbols).

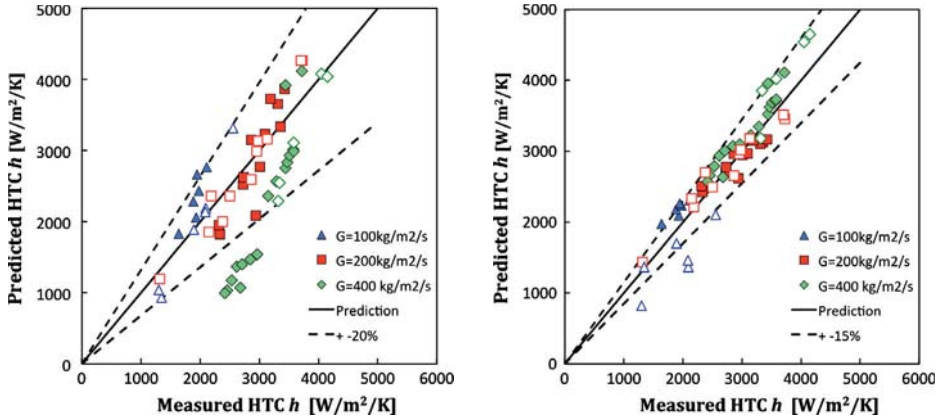

(a) *HTC calculated by eq.(32) using eq. (23) and (25)*

(b) *HTC calculated by eq.(32) and experimental values of δ and $u_\star$*

Fig. 20. Comparison of the Cioncolini and Thome' s model with measured values for different mass fluxes in $1-g$ (closed symbols) and in $\mu-g$ (open symbols).

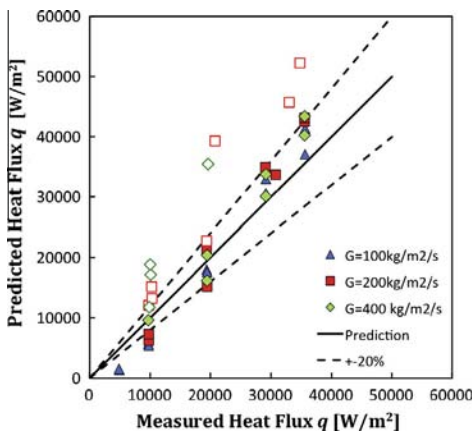

Fig. 21. Heat flux in subcooled boiling in $1-g$ (closed symbols) and in $\mu-g$ (open symbols).

near the wall on a range of dimensionless distance from the wall $0 < y^+ < 30$. Yet experimental dimensionless liquid film thicknesses in $1-g$ for $G > 100$ kg/s/m^2 correspond to $\delta^+ > 55$. Therefore, it can be assumed that a change in the film thickness due to various gravity levels will not consequently affect the velocity and temperature profiles near the wall, as long as the liquid film is thick enough ($\delta^+ > 30$). That can explained the low sensitivity $\delta^{0.1}$ in the heat transfer coefficient modelling and in the measurements for $G > 100$ kg/s/m^2.

For subcooled boiling, the flow regimes are mostly bubbly flows and also some slug flows. There are much fewer correlations that can predict HTC in subcooled boiling than in saturated boiling. Our data are compared to Chen' s correlation whose application can also be extended to flow boiling with a low level of subcooling (< 20 °C). The total heat flux is divided into one part due to convection of the subcooled liquid at temperature T_l and another part due to the bubble nucleation on the wall:

$$q = F(X)h_l(T_w - T_l) + h_{nb}S(T_w - T_{sat}) \tag{33}$$

The heat fluxes predicted by Eq. (33) are plotted versus the experimental values in Fig. 21.

For on-ground experiments, a reasonable agreement is obtained between Chen's correlation and the experimental data. In microgravity condition, the wall heat flux is significantly lower (20%) than in $1-g$ conditions, and much lower than expected from Chen's correlation. The reason for this discrepancy is not very clear. It seems that in microgravity, for moderate and low mass fluxes, larger bubbles are formed on the wall before they detach (see Fig. 7c and d). The frequency of detachment of the bubbles is a little bit lower in microgravity, which could explained the reduced contribution of the heat flux due to nucleate boiling.

5. Conclusion

This paper presents the results of flow boiling experiments performed under microgravity conditions during two parabolic flight campaigns and compared to parametric runs conducted on ground. The objective was to collect heat transfer, void fraction and wall friction data in flow boiling in a 6 mm inner diameter heated sapphire tube, using HFE-7000 as working fluid. Special attention was paid to the calculation of the vapour quality in order to characterise properly the subcooled boiling regimes, but it remains difficult to investigate flows with very low superficial vapour velocities. Annular flow, slug flow and bubbly flow have been observed in videos according to the vapour quality and the mass fluxes. The results show that the gravity level has little impact on the flow for mass fluxes superior to 400 kg/m^2/s whatever the flow pattern is. That is the reason why lower mass fluxes were investigated in this article. The transition between slug and annular flows seems to occur at lower qualities in microgravity.

Experimental frictional pressure drops data fit Lockhart and Martinelli's correlation (Eq. (10)) with a good agreement both in normal gravity and microgravity (the wall shear stress being similar for these two gravity levels), although Awad's correlation gives a better prediction in microgravity. The interfacial shear stress has also been measured. The interfacial friction factor is characteristic of transition regime between a smooth and a fully-rough turbulent flow since it depends both on the film thickness (roughness) and the Reynolds number of the vapour core. Wallis's correlation is not adapted to predict the interfacial shear stress in this situation. A correlation depending on both vapour Reynolds number and film thickness has been proposed (Eq. (17)).

In annular flow, the film thickness is much lower in microgravity than in normal gravity, which can be explained by the momentum balance equation of the liquid film.

The heat transfer coefficient in saturated boiling and annular flow regimes seems to be weakly affected by gravity for G values between 100 and 400 kg/m^2/s. For G equal to 200 and 400 kg/m^2/s, the correlation of Kandlikar gives a good prediction

of the heat transfer coefficient. The experimental data are also compared to the model of Cioncolini et Thome (Eq. (32)) that was developed for annular flow boiling. By using the experimental values for the wall shear stress and the film thickness, a very good agreement between the experimental data and the model was found. Despite the difference in the film thickness in $1-g$ and in $\mu-g$, the heat transfer coefficient is similar in $1-g$ and in $\mu-g$. This can be explained by the low dependency of the model to the film thickness. The heat transfer coefficient is mostly dependent of the wall shear stress, which is similar in $1-g$ and in $\mu-g$.

In subcooled boiling, the wall heat flux is compared to Chen's correlation (Eq. (33)). The influence of gravity is clearly visible on the results at low heat flux in microgravity, with heat transfer coefficient 20% lower in microgravity. The reason may be the lower bubble formation frequency under microgravity conditions.

In the future, new experiments at lower mass fluxes will be performed both on ground and in microgravity in order to highlight the gravity effect on larger ranges of parameters.

Acknowledgements

The authors would like to acknowledge the French and European Space Agencies CNES and ESA for having funded this study and the parabolic flight campaigns. The Fondation de Recherche pour l'Aéronautique et l'Espace is also thanked for its financial support.

References

Al-Arabi, M., 1982. Turbulent heat transfer in the entrance region of a tube. Heat Transfer Eng. 3, 76–83.
Awad, M.M., Muzychka, Y.S., 2010. Review and modeling of two-phase frictional pressure gradient at microgravity conditions. Fluid Engineering Division Summer Meeting ASME, Montreal.
Bousman, W.S., Dukler, A.E., 1993. Study of gas-liquid flow in microgravity: void fraction, pressure drop and flow pattern. Proceedings of the 1993 ASME Winter Meeting, New Orleans, LA, pp. 174–175.
Bousman, W.S., McQuillen, J.B., Witte, L.C., 1996. Gas-liquid flow patterns in microgravity: Effects of tube diameter, liquid viscosity and surface tension. Int. J. Multiphase Flow 22, 1035–1053.
Celata, G.P., Zummo, G., 2009. Flow boiling heat transfer in microgravity: recent progress. Multiphase Sci. Technol. 21, 187–212.
Chen, J.C., 1966. Correlation for boiling heat transfer to saturated fluids in convective flow. Ind. Eng. Chem. Proc. Des. Dev. 5, 322–339.
Chen, I.Y., Downing, R.S., Keshock, E., Al-Sharif, M., 1991. Measurements and correlation of two-phase pressure drop under microgravity conditions. J. Thermophys. 5, 514–523.
Cioncolini, A., Thome, J.R., Lombardi, C., 2009. Unified macro-to-microscale method to predict two-phase frictional pressure drops of annular flows. Int. J. Multiphase flows 35, 1138–1148.
Cioncolini, A., Thome, J.R., 2011. Algebraic turbulence modeling in adiabatic and evaporation annular two-phase flow. Int. J. Heat Fluid Flow 32, 805–817.
Cioncolini, A., Thome, J.R., 2012. Entrained liquid fraction prediction in adiabatic and evaporating annular two-phase flow. Nucl. Eng. Des. 243, 200–213.
Colin, C., Fabre, J., Dukler, A.E., 1991. Gas–liquid flow at microgravity conditions – I: Dispersed bubble and slug flow. Int. J. Multiphase Flow 17, 533–544.
Colin, C., Fabre, J., 1995. Gas–liquid pipe flow under microgravity conditions: influence of tube diameter on flow patterns and pressure drops. Adv. Space Res. 16, 137–142.
Colin, C., Fabre, J., McQuillen, J., 1996. Bubble and slug flow at microgravity conditions: state of knowledge and open questions. Chem. Eng. Com. 141–142, 155–173.
de Jong, P., Gabriel, K.S., 2003. A preliminary study of two-phase flow at microgravity: experimental data of film thickness. Int. J. Multiphase Flow 29, 1203–1220.
Dukler, A.E., Fabre, J.A., McQuillen, J.B., Vernon, R., 1988. Gas–liquid flow at microgravity conditions: flow pattern and their transitions. Int. J. Multiphase Flow 14, 389–400.
Elkow, K.J., Rezkallah, K.S., 1997. Void fraction measurements in gas–liquid flows under $1-g$ and $0-g$ conditions using capacitance sensors. Int. J. Multiphase Flow 23, 815–829.
Fang, X., Zhang, H., Xu, Y., Su, X., 2012. Evaluation of using two-phase frictional pressure drop correlations for normal gravity to microgravity and reduced gravity. Adv. Space Res. 49, 351–364.
Fore, L.B., Beus, S.G., Bauer, R.C., 2000. Interfacial friction in gas-liquid annular flow: analogies to full and transition roughness. Int. J. Multiphase Flow 26, 1755–1769.
Gnielinski, V., 1976. New equations for heat and mass transfer in turbulent pipe and channel flow. Int. Chem. Eng. 16, 359–368.
Harmathy, T., 1960. Velocity of large drops and bubbles in media of infinite and restrictive extent. AIChE J. 1, 289–295.
Jayawardena, S.S., Balakoaiah, V., Witte, L., 1997. Flow pattern transition maps in microgravity two-phase flows. AIChE J. 43, 1637–1640.
Kandlikar, S.G., 1990. A general correlation for saturated two-phase flow boiling heat transfer inside horizontal and vertical tubes. J. Heat Transfer 112, 219–228.
Kim, T.H., Kommer, E., Dessiatoun, S., Kim, J., 2012. Measurement of two-phase flow and heat transfer parameters using infrared thermometry. Int. J. Multiphase Flow 40, 56–67.
Lockhart, R.W., Martinelli, R.C., 1949. Proposed correlation of data for isothermal two-phase, two-component flow in pipes. Chem. Eng. Prog. Symp. Ser. 45, 39–48.
Lopez, J.C.B., Dukler, A.E., 1986. Droplet entrainment in vertical annular flow and its contribution to momentum transfer. AIChE J. 32, 1500–1515.
Lui, R.K., Kawaji, M., Ogushi, T., 1994. An experimental investigation of subcooled flow boiling heat transfer under microgravity conditions. In: 10th International Heat Transfer Conference Brighton, 7, pp. 497–502.
Niklin, D.J., Wilkes, J.O., Davidson, J.F., 1962. Two-phase flow in vertical tubes. Trans. Instn. Chem. Eng. 40, 61–68.
Ohta, H., 1997. Experiments on microgravity boiling heat transfer by using transparent heaters. Nucl. Eng. Des. 175, 167–180.
Ohta, H., 2003. Microgravity heat transfer in flow boiling. Adv. Heat Transfer 37, 1–76.
Reinarts, T.R., 1993. Adiabatic two phase flow regime data and modeling for zero and reduced (horizontal flow) acceleration fields. PhD dissertation, Univ. of Texas A&M.
Wallis, G.B., 1969. One Dimensional Two-Phase Flow. McGraw-Hill, New-York.
Zhao, L., Hu, W.R., 2000. Slug to annular flow transition of microgravity two-phase flow. Int. J. Multiphase Flow 26, 1295–1304.
Zhao, L., Rezkallah, K.S., 1993. Gas liquid flow patterns at microgravity conditions. Int. J. Multiphase Flow 19, 751–763.
Zhao, L., Rezkallah, K.S., 1995. Pressure drop in gas–liquid flow at microgravity conditions gas liquid flow patterns at microgravity conditions. Int. J. Multiphase Flow 21, 837–849.
Zuber, N., Findlay, J.A., 1965. Average volumetric concentration in two-phase systems. J. Heat Transfer, 453–468.

Proceedings of the 15th International Heat Transfer Conference, IHTC-15
August 10-15, 2014, Kyoto, Japan

IHTC15-9072

FLOW BOILING UNDER MICROGRAVITY CONDITIONS
Comparative study of two experimental data sets

M. Narcy[1*], A. Scammell[2], C. Colin[1], J. Kim[2]

[1]Fluid Mechanics Institute (IMFT), University of Toulouse, Toulouse, 31400, France
[2]University of Maryland, College Park, MD 20742, USA

ABSTRACT

A comparison is made of recent reduced gravity flow boiling data obtained using two independent test facilities which utilise different measurement techniques. The specifications and parameters of each test rig are described with both featuring 6 mm tubular channels through which either HFE-7000 or HFE-7100 is boiled. Parabolic flight campaigns provide the microgravity environment in which heat transfer and void fraction measurements are coupled with flow visualisation to provide insight into gravity's effect on two-phase flow.

KEY WORDS: Two-phase flow, boiling, microgravity, heat transfer, void fraction

1. INTRODUCTION

Two-phase thermal systems have been widely applied in many industries and engineering disciplines due to the improvement of heat transfer efficiency via the fluid latent heat. However, boiling is a highly complex process with many components such as heat and mass transfer, hydrodynamics, and interfacial phenomena, and these intricacies are further complicated for space applications when the effect of weightlessness is considered. It is therefore necessary to study and understand flow boiling and, specifically, the effect of gravity on flow regime, pressure drop, and heat transfer. Current microgravity (referred to as μ-g) flow boiling testing is limited by the opportunities for low gravity environments, resulting in a deficiency of data by which to test hypotheses and models. Nevertheless, several testing campaigns using parabolic flight have been completed in the last half-century that provide insight into gravity's effect on flow patterns, pressure drop, and heat transfer. Comprehensive state-of-the-art reviews have been completed by Colin et al. [1], Ohta [2], and Celata and Zummo [3].

One of the key requirements for predicting both pressure drop and heat transfer for flow boiling in a tubular geometry under microgravity conditions is the characterisation of flow regimes. Several studies have identified various flow patterns, and their transitions, at different superficial liquid and gas velocities (j_L and j_G, respectively) for both adiabatic gas-liquid flows and boiling flows. Using void fraction criteria, Colin et al. [4] and Dukler et al. [5] created maps to predict regime transitions in gas-liquid flows. Patterns such as bubbly, slug and annular flow were also seen by Ohta [2], Reinarts [6], and recently by Celata and Zummo [3] for saturated and subcooled flow boiling.

Cross-sectional void fraction measurements have been studied utilising several techniques including capacitance probes [7], conductance probes [4], and optical interference. Experimental data allow for the analysis of bubble dynamics such as the comparison of the mean gas velocity ($U_G = j_G / \alpha$) to the drift flux model for bubbly and slug flow, showing good agreement [6]. Average film thickness measurements using void fraction techniques have been reported for μ-g conditions [8, 9], but only for gas-liquid flows.

*Corresponding Author: mnarcyle@imft.fr

Recent work on flow boiling heat transfer in microgravity has yielded some advancement in the understanding of gravity variation on the heat transfer coefficient, but a thorough grasp of the topic is still lacking. Lui et al. [10] conducted heat transfer experiments for subcooled flow of R113 through 12 mm internal diameter test section. Heat transfer coefficients were found to be approximately 5 to 20% higher in microgravity, generally increasing with increasing quality. This trend was explained by the greater movement of vapour bubbles on the heated surface at higher qualities. Ohta [2,11] studied flow boiling of FC-72 and R113 in vertical transparent tubes (8 mm inner diameter), internally coated with a thin gold film to act as a heating element and resistive thermometer. Tests were performed at ground and microgravity conditions to investigate the effect of gravity on flow pattern and heat transfer. It was observed that at low mass fluxes, bubbles size in the nucleate boiling regime increased in microgravity, but no variation in heat transfer coefficient was seen. Ohta proposed that increased agitation of the fluid near the heated wall from nucleation was the main mechanism of heat transfer and is therefore unaffected by bubble size in the bulk fluid. At higher mass fluxes, annular flow was described as having a liquid-vapour interface that became smoother in microgravity. Under these conditions, a degradation in heat transfer was experienced in microgravity, and was explained by the interplay between liquid film thickness and the increased turbulence caused by the interfacial disturbances. Baltis [12], who performed subcooled flow boiling experiments with FC-72 in Pyrex tubes (2, 4, and 6 mm internal diameters) showed that the heat transfer coefficient can decrease by 30-40% or increase by 15-20% in microgravity compared to terrestrial gravity conditions. Bubbly flow observed at low mass fluxes showed an increase, no change, and a decrease in heat transfer for microgravity depending on the position along the heated tube. Their explanation considered the relative bubble size at each measurement position in microgravity compared to terrestrial gravity and attributed each condition to the convection enhancement provided by the passing bubbles. At higher qualities and low flow rates, intermittent/annular flow experienced little variation in flow structure or heat transfer coefficient as gravity level changed. It is evident from previous work that the variation in heat transfer with gravity level is dependent on several parameters such as mass flux, quality, and heat flux. However, it is also clear that the study of each parameter individually with respect to the heat transfer variation is not sufficient for a complete understanding of the heat transfer processes. The flow regime changes (partially determined by the aforementioned parameters) and the specific mechanisms of each regime present the most thorough explanation to the conditions under which heat transfer varies with gravity.

The objective of this work is to compare experimental techniques and collect microgravity flow boiling data from two independent experiments constructed by Institut de Mécanique des Fluides de Toulouse (IMFT), Toulouse, France and the University of Maryland (UMD), Maryland, USA. The test sections for both experiments were 6 mm tubular geometries heated by Joule effect and through which two 3M Novec fluids were circulated.

2. EXPERIMENTAL FACILITIES

Two hydraulic loops were designed in order to study boiling mechanisms both on ground and under microgravity conditions during parabolic flights.

2.1 Experimental facilities

UMD experimental set-up. The UMD experimental apparatus consisted of a hydraulic loop, transducers, and supporting electrical equipment required for the rig's functionality both in the lab and aboard parabolic flights. The working fluid used during testing was 3M Novec HFE-7100, a non-toxic dielectric fluid with a boiling temperature of 61°C at 1 bar. A schematic of the loop is shown in Figure 1. Liquid HFE-7100 was pumped using a Micropump gear pump and the flow rate was measured using an Omega turbine flowmeter. The liquid was then heated to a specified inlet subcooling temperature or quality using a stainless steel preheater before entering the test section in a vertical upward flow configuration. Preheater input power was supplied by a modified Silverstone computer power unit and controlled using pulse width modulation via a LabVIEW interface.

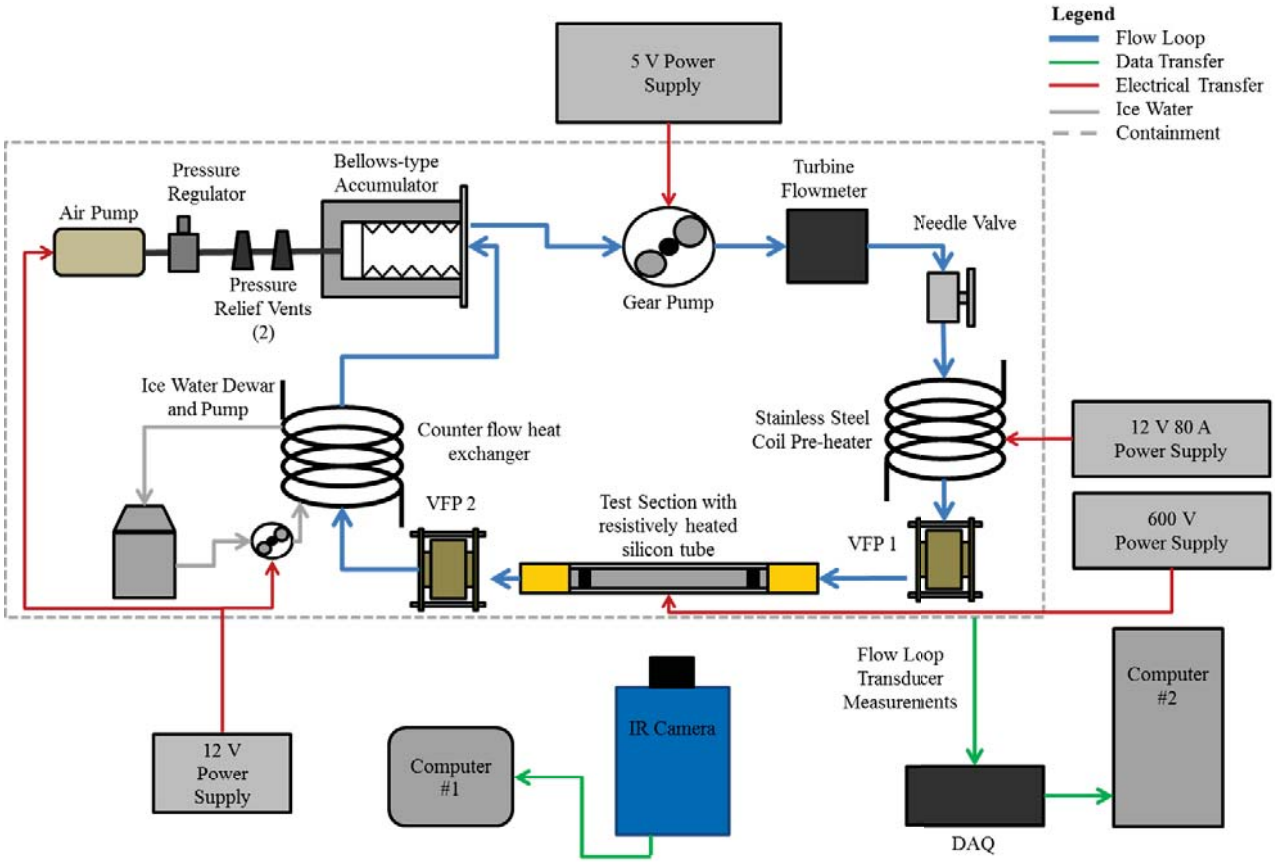

Fig. 1 Functional diagram for University of Maryland experimental test rig.

The test section consisted of a heated 6mm ID silicon tube, where the heat transfer measurements and flow visualization occur, and two void fraction sensors upstream and downstream of the silicon tube. The silicon is resistively heated using a high voltage power supply to either induce or continue boiling within the flow. Pressure taps were located at the inlet and outlet of the heat transfer measurement section for both differential and absolute pressure measurements.

Vapour exiting the test section was condensed and subcooled in a counterflow heat exchanger where the secondary fluid was ice water stored in a Dewar. A bellows-type accumulator was included after the condenser with the dry side open to the atmosphere, so that system pressure could be maintained at nominally 1 bar. This was accomplished on parabolic flights by pressurising the dry side of the bellows with an air pump regulated by an adjustable pressure relief valve. After leaving the accumulator, the working fluid was recirculated through the pump and cycled through the flow loop again.

Data was collected using an Omega 24-channel data acquisition system and recorded at a rate of 100 Hz using a LabVIEW interface. Infrared video for heat transfer measurements and flow visualisation was captured using an Electrophysics Silver 660M camera at a rate of 250 Hz and transmitted to a computer via Ethernet cable.

IMFT experimental set-up. The IMFT experimental apparatus consisted of a hydraulic loop similar to the UMD test loop, as shown in Figure 2. The working fluid was 3M Novec HFE-7000 with a boiling temperature of 36°C at 1 bar. A Micropump gear pump circulated the liquid through a Coriolis flowmeter and two serial preheaters. The test section consisted of a 6mm ID sapphire tube with an outer ITO coating between two void fraction probes. The transparent and conductive coating enables Joule heating and visualisation of the flow by means of a high-speed camera. Temperature was measured at various locations on the outer wall of the tube.

An adiabatic section at the outlet of the sapphire tube was used to obtain differential pressure measurements at constant temperature. The fluid was then condensed and subcooled in four cold plates using Peltier modules, fins and fans, in order to avoid cavitation in the pump. All measurements were acquired using a LabVIEW interface at a rate of 100 Hz.

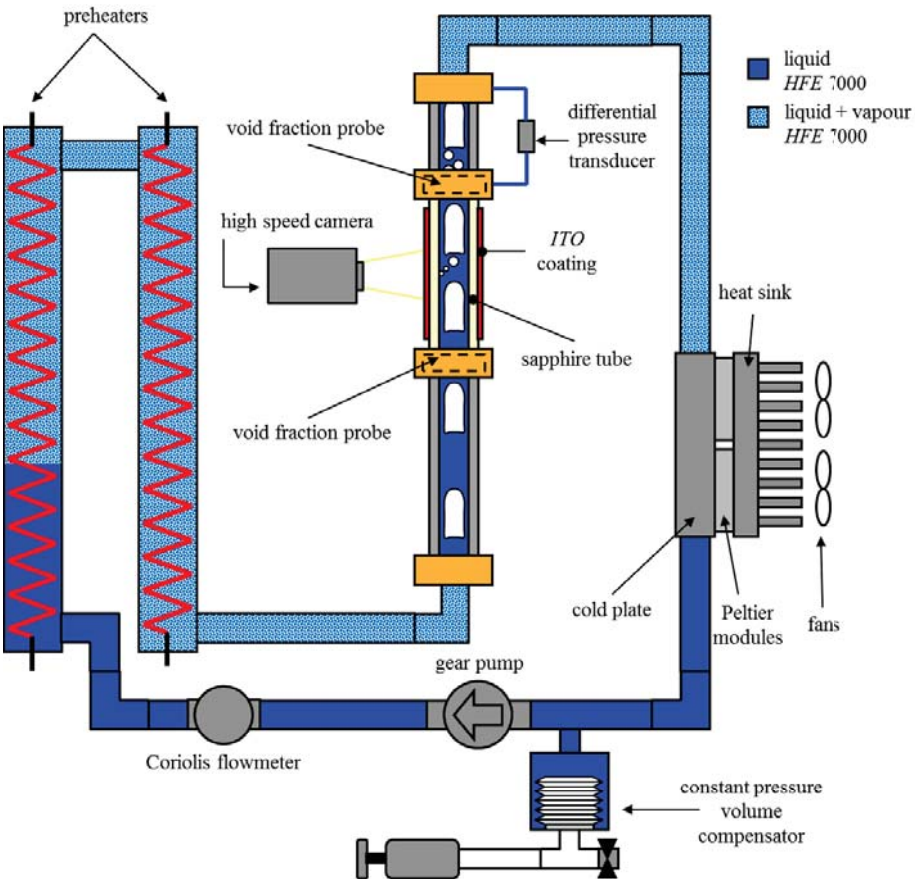

Fig. 2 Schematic of IMFT experimental test rig [13]

Working fluids. Because of the IR measurement technique used in the UMD experiment, it was preferred to use HFE-7100 as working fluid instead of HFE-7000 since its higher saturation temperature resulted in much larger infrared signatures that could be resolved more accurately. The main properties of these two fluids at 25°C are given in Table 1.

Table 1 Thermodynamic properties at 25°C for HFE-7000 and HFE-7100

Fluid	T_{sat} at 1 bar [°C]	ρ_V/ρ_L at T_{sat} [-]	ρ_L [kg.m^{-3}]	ν_L [m^2.s^{-1}]	h_{LV} [kJ.kg^{-1}]	Cp [J.kg^{-1}.K^{-1}]
HFE-7000	34	5.8 10^{-3}	1400.6	3.5 10^{-7}	142	1300
HFE-7100	61	6.2 10^{-3}	1500.2	3.8 10^{-7}	124	1183

2.2 Measurement techniques and uncertainties

Both experiments were instrumented to study pressure drop, void fraction and heat transfer. In particular, pressure transducers were used to measure the absolute pressure at various locations in order to determine the saturation temperature. Measurement techniques for temperature and void fraction measurements are presented in this section, along with the corresponding uncertainties in Table 2.

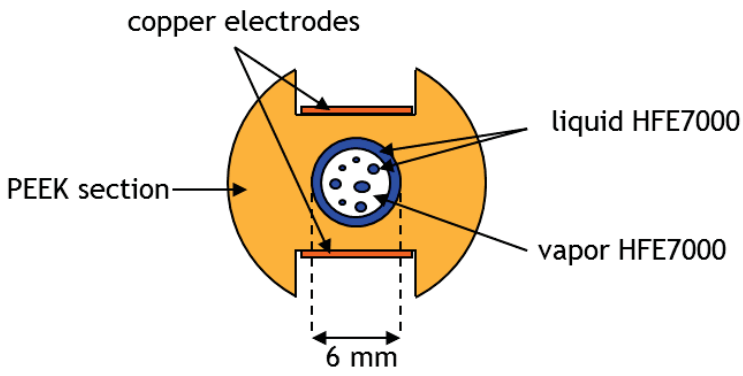

Fig. 3 Schematic of a void fraction probe

Temperature. Thermocouples for absolute temperature measurements were used at several locations in the flow loops for data analysis as well as calibration and safety purposes (UMD uses T-type thermocouples and IMFT uses K-type). The IMFT experiment also installed a T-type thermocouple for a precise differential temperature measurement along the sapphire tube of the test section. The tube itself was instrumented with Pt100 probes that measured the temperature of its outer wall. The UMD experiment used an IR camera to measure local heat transfer coefficient at many points along the centreline of the silicon tube.

Void fraction. IMFT designed and built specific void fraction probes to provide accurate data of the volumetric fraction of vapour at the inlet and outlet of the test sections in the two experiments. The sensors were capacitance probes using six copper electrodes (two measurement electrodes and four guard electrodes) placed on both sides of the two-phase flow for a non-intrusive measurement, as illustrated in Figure 3. Calibrations were performed with liquid HFE and Teflon rods whose permittivity was close to that of HFE vapour. The signal sensibility (i.e., the capacitance difference between the vapour state and the liquid state $\Delta C = C_L - C_V$) was around 0.3 pF while the accuracy on the capacitance measurement was 0.001 pF. The accuracy of the void fraction also depended on the calibration error, and was estimated at 7%.

Flow visualisations. The transparent ITO coating on the IMFT sapphire tube enabled visualisation of the flow using a high-speed camera. Only 30mm of the tube length was imaged with a spatial resolution of 33.3 pixels/mm. The UMD facility also provided flow visualisation, but the IR camera gives priority to the heat transfer coefficient measurements and flow videos were less clear due to radiative emission.

Table 2 Typical uncertainties for system parameters and measurements

	Parameter / measurement	Unit	UMD uncertainty	IMFT uncertainty
System parameters	Mass flux G	$kg.s^{-1}.m^{-2}$	5	5
	Working pressure P	mbar	1.3	2.5
Measurements	Temperature (thermocouple)	°C	0.12	0.2
	Temperature (Pt100 probes)	°C	-	0.1
	Temperature (IR camera)	°C	0.14	-
	Capacitance	meas. %	2	2

2.3 Parabolic flight campaign: microgravity conditions

Both experiments flew during parabolic flight campaigns on board the A300 ZERO-G of Novespace in Bordeaux, France. The results presented in this article were provided by one campaign for UMD (April 2013) and two campaigns for IMFT (May 2011 and April 2012).

These parabolic flight campaigns produce a near-weightless situation during three flights with 31 parabolas per flight. Each parabola provides up to 22 seconds of microgravity corresponding to a gravity level smaller than ±0.03g.

During any given parabola, the gravity level transitions between 1-g, 1.8-g, and µ-g may lead to pressure and mass flux variations within the test sections. The UMD experiment used a PID controller to stabilise the flow rate over a parabola but the IMFT facility had no regulation of the pump speed. The mass flux in the IMFT experiment was steady during the normal gravity phases, decreased slightly during 1.8 periods and then increased in microgravity. Only a few seconds were needed to stabilise the flow rate in µ-g. The UMD experimental points thus closely follow *G* isocurves on the flow pattern maps to be presented below while the IMFT data does not.

3. DATA PROCESSING AND SINGLE-PHASE FLOW VALIDATIONS

In this paper, heat transfer coefficients, void fraction and film thickness data are presented. These values were deduced from the measurements of wall and liquid temperature, heat flux, vapour quality and void fraction, and validated in single-phase flow by comparison with classical correlations. Transient experiments corresponding to transitions between the different gravity levels are not studied.

In the following sections, q is the wall heat flux delivered to the fluid, D is the inner diameter of the silicon/sapphire tube, and z is the distance from the inlet of the heated section.

3.1 Vapour quality

The mass vapour quality x is an important system parameter. It was calculated using an enthalpy balance equation in steady state for the mixture:

$$\frac{4\,q.z}{D} = G.\left(\left[x.h_{\mathrm{v,sat}}(z) + (1-x).h_{\mathrm{l}}(z)\right] - \left[x_0.h_{\mathrm{v,sat}}(0) + (1-x_0).h_{\mathrm{l}}(0)\right]\right) \quad (1)$$

where x_0 corresponds to the inlet vapour quality calculated from an energy balance on the preheater.

For saturated boiling regimes, the liquid temperature T_{l} was assumed to be the saturation temperature T_{sat}, and the vapour quality was equal to the thermodynamic quality. For subcooled boiling regimes, $x_0 = 0$, T_{l} is smaller than T_{sat} and the temperature of the vapour T_{v} is assumed to be equal to T_{sat}. The wall heat flux leads to an increase of the total enthalpy of the mixture, both by phase change and by increasing the liquid temperature, but the vapour quality is not equal to the thermodynamic quality. In this case, the temperature profile between the inlet and outlet of the test section is needed to calculate x.

The uncertainty in vapour quality is an issue for the calculations in subcooled boiling: by neglecting the error on geometrical and physical properties, the error of x was found to be around 2×10^{-3}, which is the order of magnitude of x itself.

3.2 Heat transfer coefficient

Different measurement techniques were used by the two experiments: an IR camera provided heat transfer coefficients for the UMD facility while the IMFT experiment processed temperature measurements in the liquid and on the outer surface of the sapphire tube.

The UMD experiment. Heat transfer measurements and flow visualisation were captured using an IR thermometry technique that utilised the transparency of silicon in the mid-IR optical range [14]. HFE-7100 passes through the 6mm ID/8mm OD single crystal silicon tube whose inner wall was coated with a thin thermally insulating layer of polyimide tape as can be seen in Figure 4. One half of the inner circumference was then covered with an IR opaque paint, containing carbon black, which allowed an effective inner wall

temperature to be measured through the silicon and polyimide layer. The same procedure was conducted for two strips aligned axially on the outer wall of the tube so that the effective outer wall temperature could be measured.

To determine the actual inner and outer wall temperatures, the optical properties of the various layers must be included. A coupled conduction and radiation problem was solved which accounted for absorption, emission, and reflection of thermal energy from the layers and the surroundings to determine the temperature profiles within the multilayer. The heat flux and heat transfer coefficient could then be calculated for every camera pixel along the axial length of the tube at much higher spatial resolution than traditional methods.

To complement the heat transfer measurements, the flow was also visualised using a set of six gold-plated mirrors (right image of Figure 4). In this way, the flow visualisation and heat transfer measurements could be captured simultaneously using a single camera.

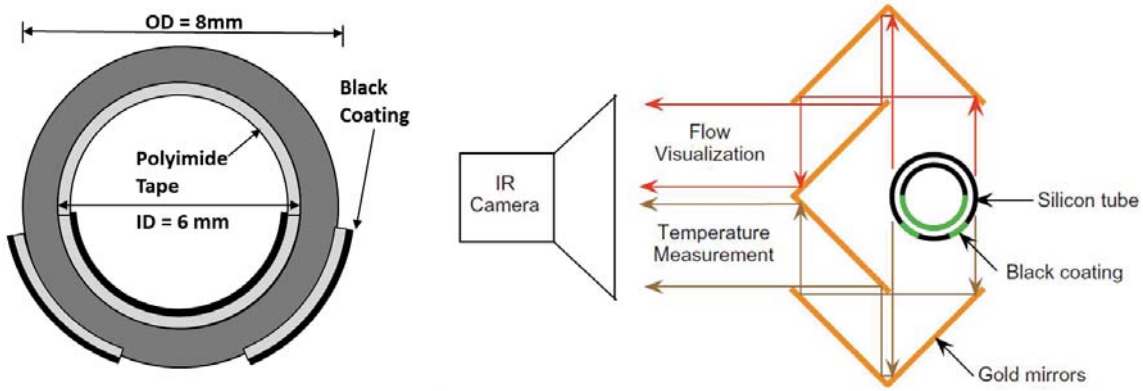

Fig. 4 Cross-sectional view of silicon tube with polyimide coating, black paint, and mirrors to provide simultaneous heat transfer measurements and flow visualisation (right image).

The infrared thermography technique was validated through single phase and two-phase vertical upward flow testing. In the case of single phase, liquid flowed through the heated silicon tube and the heat transfer coefficient along its length was measured. Comparison was then made between the experimental heat transfer coefficient and the Dittus-Boelter correlation with a correction factor for entrance effects proposed by Al-Arabi [15] as seen in Figure 5. Good agreement between the two is observed.

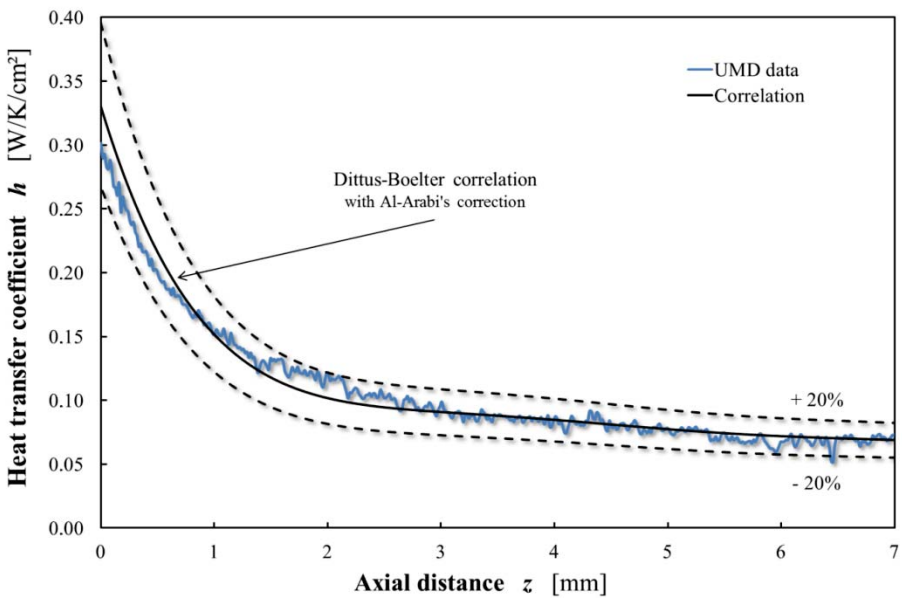

Fig. 5 Experimental heat transfer coefficient compared to Dittus-Boelter correlation with Al-Arabi correction for the parameters: HFE-7100, $Re = 5545$, $\Delta T_{sub} = 20°C$, $q = 1.1$ W/cm^2.

The IMFT experiment. In order to estimate the heat transfer coefficient (HTC) at the inner wall of the sapphire tube, the following assumptions were made: 1) temperature profiles were axisymmetric. 2) axial conduction and heat transfer by radiation were negligible. 3) heat losses were negligible.

The temperature at the inner wall of the tube T_{iw} was related to the temperature at the outer wall T_{ow} and heat flux q applied by Joule effect through the ITO coating according to the conduction equation:

$$T_{ow} - T_{iw} = q.ln\left(\frac{R_o}{R_i}\right).\frac{R_o}{k} \quad (2)$$

where R_o and R_i are the outer and inner diameter, respectively, and k the sapphire thermal conductivity. The heat transfer coefficient h could then be deduced from an energy balance through the tube:

$$h.(T_{iw} - T_{i\infty}) = q.\frac{R_o}{R_i} \quad (3)$$

By combining Equation (2) and Equation (3) and assuming a profile of liquid temperature between the inlet and outlet of the tube to obtain the liquid bulk temperature $T_{i\infty}$, the heat transfer could be calculated.

In order to validate the heat transfer data, experiments were performed in single-phase flow for a large range of mass fluxes. The results were corrected with Al-Arabi's correlation since the heat transfer regime was not fully established, and also compared with Gnielinski's correlation [16]. The experimental data showed good agreement with the correlations (with a maximum error of 17%).

4. RESULTS AND DISCUSSION

Experimental results concerning flow patterns, void fraction, and heat transfer are presented in this section.

4.1 Flow patterns

Three main flow patterns were observed under both microgravity and normal gravity conditions: bubbly flow, slug flow and annular flow. Intermediate regimes are classified as "transition flows".

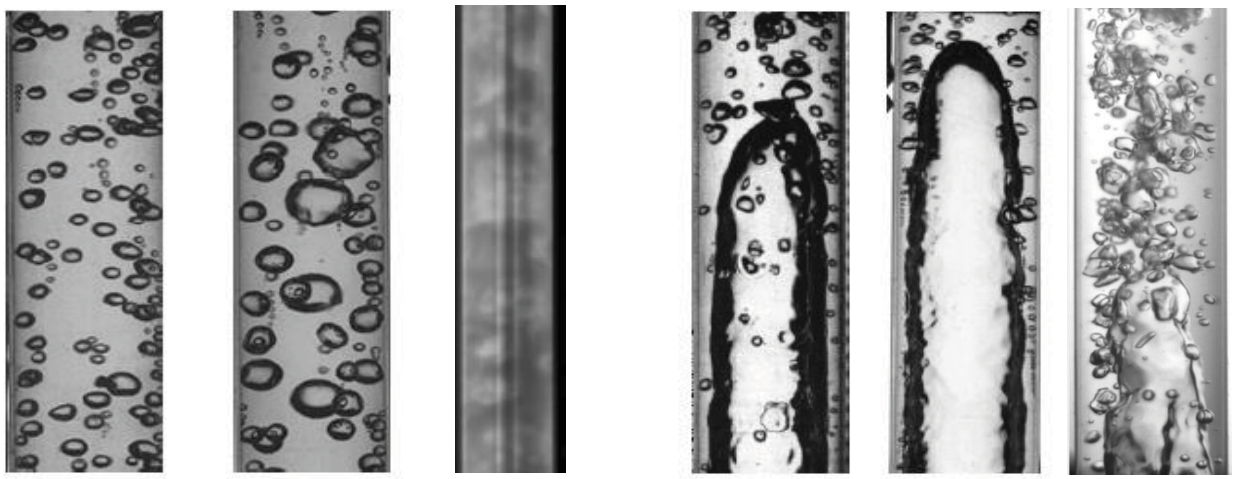

(*a*) (*b*) (*c*) (*d*) (*e*) (*f*)

Fig. 6 Flow visualisations for bubbly flow and slug flow
Bubbly flow (IMFT): G = 200 kg.s^{-1}.m^{-2}, ΔT_{sub} = 12°C, q = 2 W.cm^{-2} (*a*) in 1-g (*b*) in μ-g
Bubbly flow (UMD): G = 48 kg.s^{-1}.m^{-2}, ΔT_{sub} = 8°C, q = 1.62 W.cm^{-2} (*c*) in μ-g
Slug flow (IMFT): G = 200 kg.s^{-1}.m^{-2}, x = 0.05, q = 2 W.cm^{-2} (*d*) in 1-g (*e*) in μ-g
Slug flow (UMD): G = 88 kg.s^{-1}.m^{-2}, x = 0.05, q = 0.65 W.cm^{-2} (*f*) in 1-g

Bubbly flows occurred at low vapour qualities that corresponded with subcooled regimes. The difference between 1-g and μ-g was clearly visible in the videos for low mass fluxes (G < 250 kg.s^{-1}.m^{-2}), as seen in Figure 6: bubbles are larger in μ-g and are not deformed due to a smaller relative velocity compared to the velocity of the liquid phase, a higher rate of coalescence and a larger diameter at detachment. As quality increases, coalescence phenomenon leads to slug flows (Figure 6), churn flows and intermediate flows that are not clearly described. Taylor bubbles were observed, whose length increased with the vapour quality. For qualities above 0.1 corresponding to saturated flow boiling, annular flows mostly occurred, with liquid flowing at the wall around a vapour core as seen in Figure 7. For transition flows and annular flows, no visible difference could be seen in the videos.

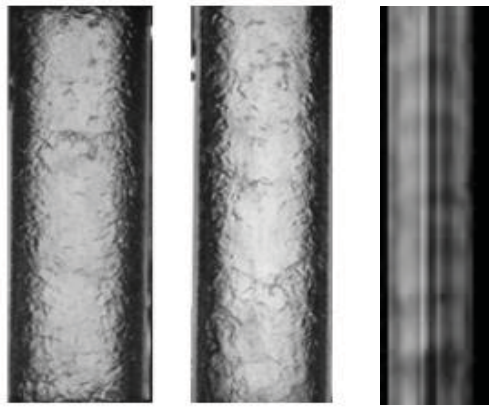

(*a*) (*b*) (*c*)

Fig. 7 Flow visualisations for churn flow and annular flow
Annular flow (IMFT): G = 200 kg.s^{-1}.m^{-2}, x = 0.20, q = 2 W.cm^{-2} (*a*) in 1-g (*b*) in μ-g
Annular flow (UMD): G = 49 kg.s^{-1}.m^{-2}, x = 0.28, q = 0.9 W.cm^{-2} (*c*) in μ-g

The evolution of these flow patterns according to the vapour quality is illustrated on the two flow pattern maps with the runs performed on-ground (Figure 8) and during parabolic flight campaigns (Figure 9). Regimes are plotted according to the superficial vapour velocity j_V and superficial liquid velocity j_L, along with isocurves of mass flux G and isocurves of vapour quality x. Only the UMD experiment investigated mass fluxes lower than G = 100 kg.s^{-1}.m^{-2}, under normal gravity and microgravity conditions.

At low qualities, for subcooled regimes, bubbly flows were mostly observed. The transition between bubbly and annular flow (including slug flows, churns flows and undescribed transition flows) corresponded to a large range of vapour quality around x = 0.1. At higher qualities in the saturated regimes, annular flows occurred. The same flow patterns were observed in 1-g and μ-g for about the same flow conditions.

Only the results for $G \leq$ 200 kg.s^{-1}.m^{-2} are presented in the next sections, since UMD data focuses on lower mass fluxes. A complete processing of IMFT data has already been discussed by Narcy *et al.* [13].

4.2 Void fraction and film thickness

For the specific case of annular flow (saturated regime), Cioncolini and Thome proposed an algebraic eddy viscosity model to describe the velocity profile in the turbulent liquid film [17]. The annular flow model they developed provides theoretical values for the void fraction, liquid film thickness, wall shear stress, and heat transfer coefficients.

The rate of liquid droplet entrainment in the gas core was evaluated with this model [18] in a previous work by Narcy *et al.* [13]. Over the range of parameters investigated in these experiments, the entrainment was found to be negligible.

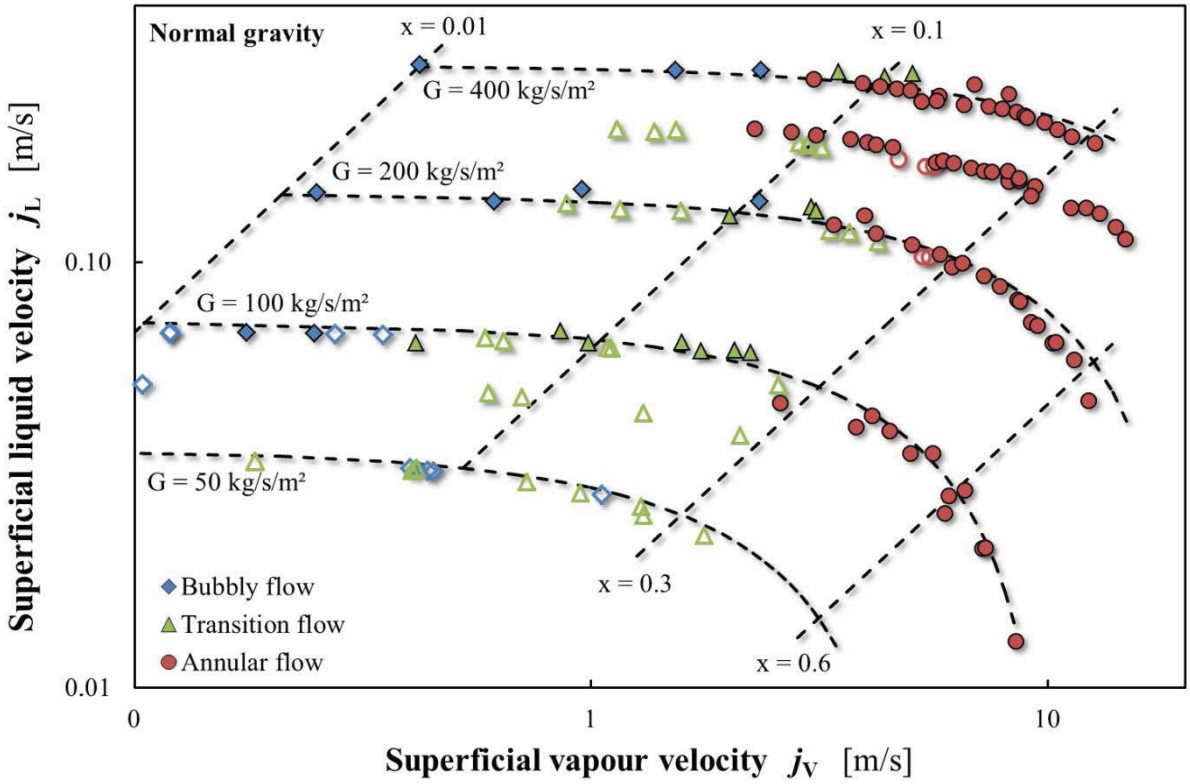

Fig. 8 Flow pattern map in 1-g for IMFT data (closed symbols) and UMD data (open symbols)

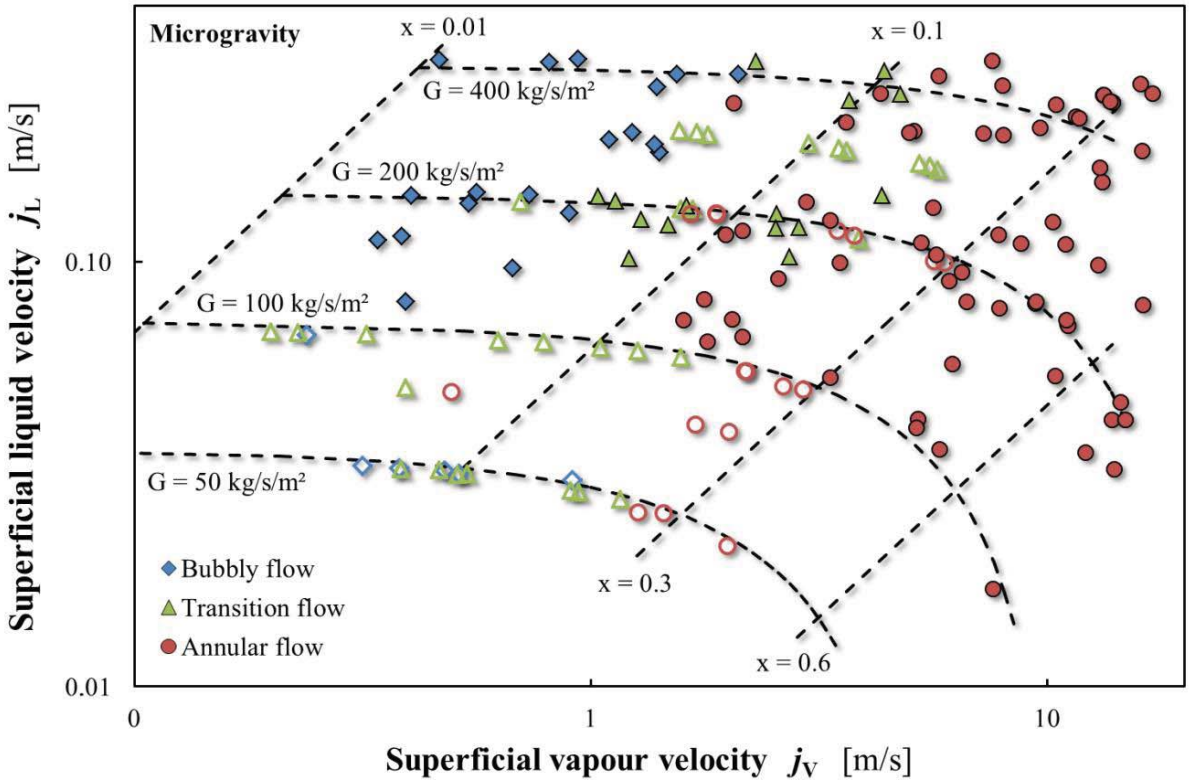

Fig. 9 Flow pattern map in μ-g for IMFT data (closed symbols) and UMD data (open symbols)

The liquid film thickness δ can therefore be determined according to α using geometrical considerations:

$$\delta = \frac{D}{2}\left(1 - \sqrt{\alpha}\right) \tag{4}$$

In Cioncolini's model, the void fraction is estimated according to:

$$\alpha = \frac{f.x^n}{1 + (f-1).x^n} \quad \text{with} \quad f = a + (1-a).\left(\frac{\rho_v}{\rho_l}\right)^{a_1} \quad \text{and} \quad n = b + (1-b).\left(\frac{\rho_v}{\rho_l}\right)^{b_1} \tag{5}$$

where a = -2.129, b = 0.3487, a_1 = -0.2186, b_1 = 0.515.

The liquid film thickness δ is given by:

$$\delta = y_*.\max\left[\sqrt{\frac{2\,\Gamma_{lf}^+}{R^+}}\,;\,0.0066\frac{\Gamma_{lf}^+}{R^+}\right] \tag{6}$$

where $y_* = \nu_l / u_*$ is the viscous length scale, $R^+ = D / 2y_*$ is the dimensionless tube radius, and Γ_{lf}^+ the dimensionless flow rate in the liquid film. Γ_{lf}^+ and u_*, the friction velocity, are given in Cioncolini *et al.* [19].

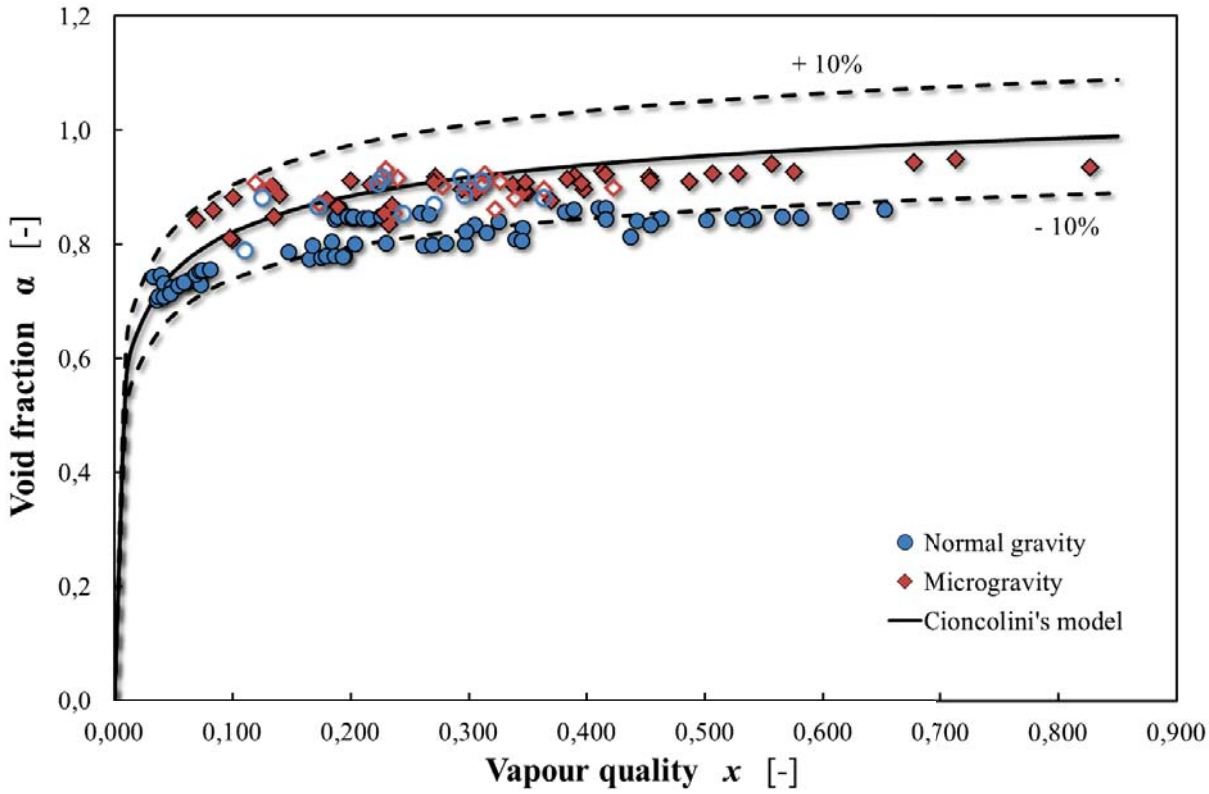

Fig. 10 Void fraction in 1-g and in μ-g compared with Cioncolini's model for IMFT data (closed symbols) and UMD data (open symbols)

The void fraction data in microgravity are well predicted by Equation (5) from Cioncolini's model for both experiments that provide consistent measurements, as can be seen in Figure 10. However, this equation overpredicts the measurements in normal gravity for the IMFT data set which highlights higher void fraction values in microgravity, whereas no clear difference between 1-g and μ-g is seen on the UMD measurements.

Equation (4) enables us to estimate the liquid film thickness for the runs performed in saturated boiling with annular flows. Only the UMD experiment provides measurements for low mass fluxes. In Figure 11, the film thickness is plotted according to the vapour quality for three mass fluxes under microgravity conditions. The accuracy on the measurements is about 20 μm.

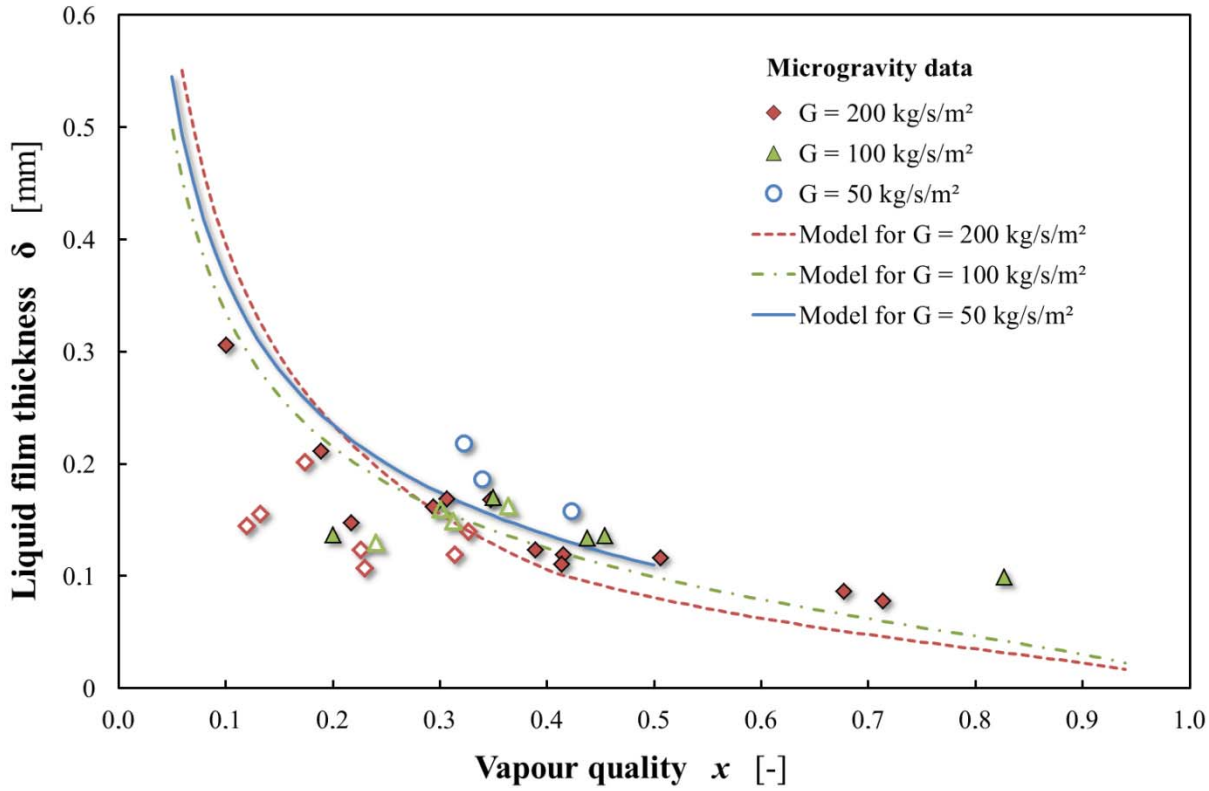

Fig. 11 Liquid film thickness in μ-g compared with Cioncolini's model for IMFT measurements (closed symbols) and UMD measurements (open symbols) – annular flow data

Despite the scattering around G = 100 kg.s^{-1}.m^{-2}, both the IMFT data and UMD data are consistent and in good agreement with the prediction of Equation (6), which was expected since Cioncolini's model well predicts the void fraction under microgravity conditions.

4.3 Heat transfer coefficient

Heat transfer data were calculated using the two techniques as describe above. Saturated boiling (mostly with annular flow) and subcooled boiling (corresponding to bubbly and slug flows) were investigated.

Saturated boiling. Experimental points in the annular flow regimes are presented in this sub-section. Cioncolini's model also provides an estimation of the heat transfer coefficient h [18]:

$$h = \frac{k_l}{\delta} 0.0776.\delta^{+0.9} Pr_l^{0.52} \qquad \text{with} \quad \delta^+ = \frac{\delta}{y_*} \tag{7}$$

where k_l is the thermal conductivity of the liquid phase and Pr_l the Prandtl number. This expression is valid for $10 < \delta^+ < 800$ and $0.86 < Pr_l < 6.1$.

In Figure 12, heat transfer coefficients in 1-g and μ-g are plotted according to the vapour quality for two mass fluxes. Comparisons are made with classical correlations (Kandlikar [20] and Chen [21]) and with Cioncolini's model. Experimental data correspond to various wall heat fluxes q. Indeed, this parameter has a rather small influence on the heat transfer coefficient and was therefore not distinctly identified, for clarity reasons. The two correlations are given for q = 2 W.cm^{-2}. No significant difference can be seen between normal gravity and microgravity conditions for vapour qualities $x > 0.2$, for any tested mass flux G. The IMFT data and UMD data are both consistent for the two gravity levels. Measurements at high mass fluxes and high qualities are in good agreement with Kandlikar's correlation while Chen's correlation well predicts measured data for lower mass fluxes or lower qualities.

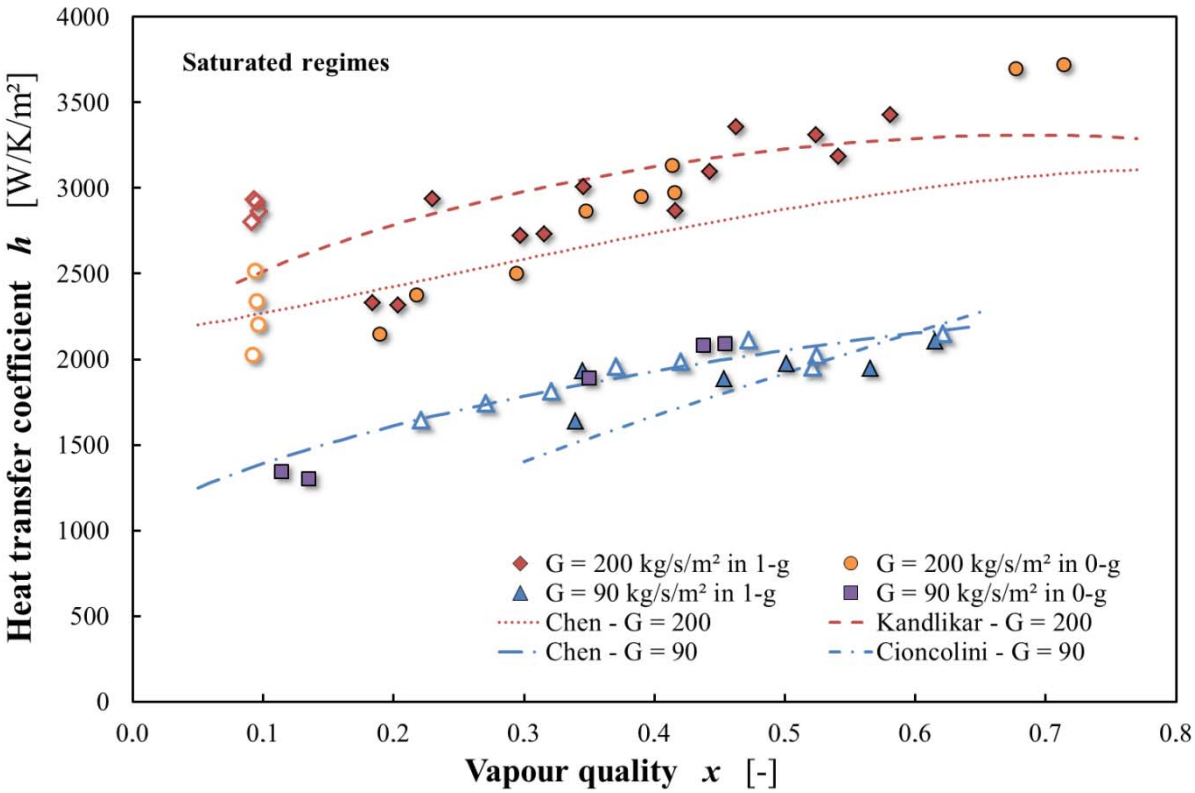

Fig. 12 Heat transfer coefficient for saturated data in 1-g and in μ-g compared with various correlations for IMFT measurements (closed symbols) and UMD measurements (open symbols)

For vapour qualities higher than 0.3 (corresponding to annular flows), the measurements agree well with Cioncolini's model (Equation (7)) both under normal gravity and microgravity conditions. The uncertainty of the heat transfer coefficient is estimated at ± 15% for both experiments.

Subcooled boiling. The runs that were used to investigate heat transfers in subcooled boiling mostly experienced bubbly flows.

An example is given in Figure 13, where a time trace of the heat transfer coefficient, gravity level, and test section outlet void fraction from the UMD data are plotted as a function of time. The heat transfer coefficient shown is a spatially averaged value over a 2 cm distance near the exit of the heated test section. Bubbly flow is experienced during all three gravity periods with bubble size increasing in microgravity compared with normal gravity. This transition can be verified by observing the increase in void fraction in microgravity.

In this example and in the other runs performed with the UMD experiment in bubbly flows, the heat transfer coefficients were approximately 20% lower in μ-g than in 1-g, due to the increase in void fraction.

The exact same trend is highlighted in the IMFT subcooled data set [13]: Chen's correlation, which can be extended to flow boiling with low levels of subcooling, predicts the heat transfer coefficient in normal gravity well but overpredicts *h* in microgravity by around 20%.

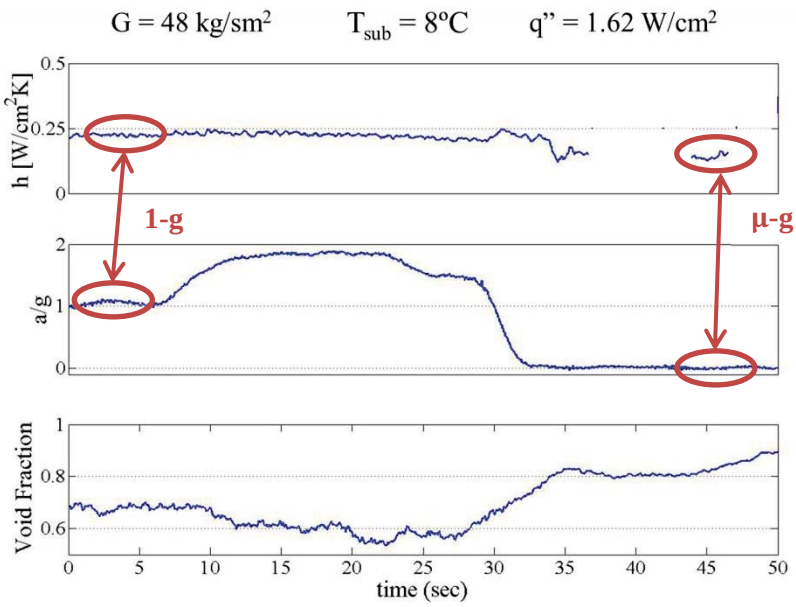

Fig. 13 Time trace plot of heat transfer coefficient, gravity level, and test section outlet void fraction for bubbly flow (UMD data)

5. CONCLUSIONS

This paper presents results of flow boiling experiments conducted in microgravity during parabolic flight campaigns using two experimental facilities with different measurement techniques. The objective was to collect and compare experimental data on flow patterns, void fraction, liquid film thickness and heat transfer. Both experiments circulated HFE fluids (HFE-7000 and HFE-7100) in 6mm inner diameter heated tubes.

Annular flow, slug flow and bubbly flow were observed under normal gravity and microgravity conditions, according to the vapour quality and mass flux. It remains difficult to provide an accurate description of all transition flows including slug flow and churn flow. The transitions between the well-described regimes seemed to occur at the same qualities in 1-g and μ-g.

Void fraction data for the two facilities were consistent in microgravity and in good agreement with the correlation proposed by Cioncolini *et al*. in their annular flow model. However, the IMFT data exhibited a thicker liquid film in 1-g whereas no clear influence of the gravity level was seen on the UMD data.

For saturated boiling, no significant difference between normal gravity and microgravity was observed on heat transfer coefficients. Kandlikar's correlation and Chen's correlation both yielded good predictions of the heat transfer coefficient depending on the vapour quality and the mass flux. Measurements of both experiments were consistent and in good agreement with the estimation of Cioncolini's model.
For subcooled boiling, the heat transfer coefficient was approximately 20% lower in microgravity than in normal gravity, which is believed to be caused by an increase in the void fraction at low mass qualities.

Further data processing and new experiments at lower mass fluxes will be performed to complete this comparative study.

ACKNOWLEDGMENT

The authors would like to acknowledge Novespace and the French Space Agency CNES for the flight opportunities. This research was also supported by NASA Grants NNX11AN49H and NNX09AK39A for the UMD experiment and by ESA, Project MANBO, and CNES for the IMFT experiment.

NOMENCLATURE / SUBSCRIPTS

h	heat transfer coefficient	(W/m^2/K)	e	environment
$h_{l,v}$	latent heat of vaporisation	(kJ/kg)	i	internal
j	superficial velocity	(m/s)	in	inlet conditions
Oh	Ohnesorge number	(-)	l	liquid phase
ΔT	subcooling	(°C)	o	outer
x	vapour quality	(-)	out	outlet conditions
α	void fraction	(-)	sat	saturated conditions
ε	electrical permittivity	(-)	sub	subcooled conditions
			v	vapour phase
			w	wall

REFERENCES

[1] Colin, C., Fabre, J., McQuillen, J., "Bubble and slug flow at microgravity conditions: state of the art knowledge and open questions", *Chem. Engng. Com.*, 141-142, pp. 155-173, (1996).

[2] Ohta, H., "Microgravity heat transfer in flow boiling", *Advances in heat transfer*, 37, pp. 1-76, (2003).

[3] Celata, G.P., Zummo, G., "Flow Boiling Heat Transfer in Microgravity: Recent Progress", *Multiphase Science and Technology*, 21 (3), pp. 187-212, (2009).

[4] Colin, C., Fabre, J., Dukler, A.E., "Gas-liquid flow at microgravity conditions – I: Dispersed bubble and slug flow", *Int. J. Multiphase Flow*, 17, pp. 533-544, (1991).

[5] Dukler, A.E., Fabre, J.A., McQuillen, J.B., Vernon, R., "Gas-liquid flow at microgravity conditions: flow pattern and their transitions", *Int. J. Multiphase Flow*, 14, pp. 389-400, (1988).

[6] Reinarts, T.R., *Adiabatic two phase flow regime data and modeling for zero and reduced (horizontal flow) acceleration fluids*, Ph.D. Thesis, Texas A&M University, (1993).

[7] Elkow, K.J., Rezkallah, K.S., "Void fraction measurements in gas-liquid flows under 1-g and 0-g conditions using capacitance sensors", *Int. J. Multiphase Flow*, 23 (5), pp. 815-829, (1997).

[8] Bousman, W.S., McQuillen, J.B., Witte, L.C., "Gas-liquid flow patterns in microgravity: Effects of tube diameter, liquid viscosity, and surface tension", *Int. J. Multiphase Flow*, 22 (6), pp. 1035-1053, (1996).

[9] de Jong, P., Gabriel, K.S., "A preliminary study of two-phase flow at microgravity: experimental data on film thickness", *Int. J. Multiphase Flow*, 29, pp. 1203-1220, (2003).

[10] Lui, R.K., Kawaji, M., Ogushi, T., "An Experimental Investigation of Subcooled Flow Boiling Heat Transfer Under Microgravity Conditions", 10th International Heat Transfer Conference, Brighton, vol. 7, pp. 497-502, (1994).

[11] Ohta, H., "Experiments on Microgravity Boiling Heat Transfer by Using Transparent Heaters", *Nuclear Engineering and Design*, 175, pp. 167-180, (1997).

[12] Baltis, C., Celata, G.P., Cumo, M., Saraceno, L., Zummo, G., "Gravity Influence on Heat Transfer Rate in Flow Boiling", *Microgravity Sci. Technol.*, 24, pp. 203-213, (2012).

[13] Narcy, M., De Malmazet, E., Colin, C., "Flow Boiling in tube under normal gravity and microgravity conditions", *Int. J. Multiphase Flow*, http://dx.doi.org/10.1016/j.ijmultiphaseflow.2013.11.011 , (2013).

[14] Kim, T. H., Kommer, E., Dessiatoun, S., Kim, J., "Measurement of Two-Phase Flow and Heat Transfer Parameters Using Infrared Thermometry", *Int. J. Multiphase Flow*, 40, pp. 56-67, (2012).

[15] Al-Arabi, M., "Turbulent Heat Transfer in the Entrance Region of a Tube", *Heat Transfer Eng.*, 3, pp. 76-83, (1982).

[16] Gnielinski, V., "Correlation for Boiling Heat Transfer to Saturared Fluids in Convective Flow", *Ind. And Eng. Proc. Design and Dev.*, 5 (3), pp. 322-329, (1966).

[17] Cioncolini, A., Thome, J.R., "Algebraic turbulence modeling in adiabatic and evaporating annular two-phase flow", *Int, J. of Heat and Fluid Flow*, 32, pp. 805-817, (2011).

[18] Cioncolini, A., Thome, J.R., "Entrained liquid fraction prediction in adiabatic and evaporating annular two-phase flow", *Nuclear Engineering and Design*, 243, 200-213, (2012).

[19] Cioncolini, A., Thome, J.R., Lombardi, C., "Unified macro-to-microscale method to predict two-phase frictional pressure drops of annular flows", *Int. J. Multiphase Flow*, 35, 1138-1148, (2009).

[20] Kandlikar, S.G., "A general correlation for saturated two-phase boiling heat transfer inside horizontal and vertical tubes", *J. Heat Transfer*, 112, 219-228, (1990).

[21] Chen, J.C., "Correlation for Boiling Heat Transfer to Saturated Fluids in Convective Flow," *Ind. and Eng. Proc. Design and Dev.*, 5 (3), pp. 322-329, (1966).

Bibliography

Al-Arabi, M. (1982). Turbulent heat transfer in the entrance region of a tube. *Journal of Heat Transfer Engineering*, 3:76–83.

Awad, M. and Muzychka, Y. (2008). Effective property models for homogeneous two-phase flows. *Experimental Thermal and Fluid Science*, 33(1):106–113.

Awad, M. and Muzychka, Y. (2010). Review and modelling of two-phase frictional pressure gradient at microgravity conditions. *Fluid Engineering Division Summer Meeting ASME*, (1).

Awad, M. and Muzychka, Y. (2014). Review and modelling of two-phase frictional pressure gradient at microgravity conditions. *Interfacial Phenomena and Heat Transfer*, 2(1):15–40.

Baldassari, C. and Marengo, M. (2013). Flow boiling in microchannels and microgravity. *Progress in Energy and Combustion Science*, 39:1–36.

Baltis, C., Celata, G., Cumo, M., Saraceno, L., and Zummo, G. (2012). Gravity influence of heat transfer rate in flow boiling. *Microgravity Science Technology*, 24:203–213.

Blasius, P. (1913). Das aehnlichkeitsgesetz bei reibungsvorgangen in flussigkeiten. *Forschungsheft*, 131:1–41.

Bousman, W. (1995). Studies of two-phase gas-liquid flow in microgravity. *NASA Contractor Report 195434*.

Bousman, W. and Dukler, A. (1993). Studies of gas-liquid flow in microgravity: void fraction, pressure drop and flow pattern. *Proceedings of the 1993 ASME Winter Meeting*, pages 174–175.

Bousman, W. and Dukler, A. (1994). Studies of gas-liquid flow in microgravity: void fraction, pressure drop and flow pattern. *8th Annual Microgravity Science and Space Processing Symposium*.

Bousman, W. and McQuillen, J. (1994). Characterisation of annular two-phase gas-liquid flows in microgravity. *NASA Conference Publication 3276*.

Bousman, W., McQuillen, J., and Witte, L. (1996). Gas-liquid flow patterns in microgravity: effects of tube diameter, liquid viscosity and surface tension. *International Journal of Multiphase Flow*, 22:1035–1053.

Brauckhoff, A. (2010). Capacitance measurement to evaluate the proportion of liquid and vapor in a biphasic flow. *Internship Report, University of Berlin.*

Buckingham, E. (1914). On physically similar systems; illustrations of the use of dimensional equations. *Physical Review*, 4(4):345–376.

Caniere, H. (2009). Flow pattern mapping of horizontal evaporating flow based on capacitive void fraction measurements. *PhD thesis, University of Gent.*

Celata, G. and Zummo, G. (2007). Flow pattern analysis of flow boiling in microgravity. *Multiphase Science and Technology*, 19(2):183–210.

Celata, G. and Zummo, G. (2009). Flow boiling heat transfer in microgravity: recent progress. *Multiphase Science and Technology*, 21(3):187–212.

Chen, I., Downing, R., Keshok, E., and Al-Sharif, M. (1991). Measurements and correlation of two-phase pressure drop under microgravity conditions. *Journal of Thermophysics*, 5:514–523.

Chen, J. (1966). Correlation for boiling heat transfer to saturated fluids in convective flow. *Industrial Engineering Chemistry Process Design and Development*, 5(3):322–339.

Chen, J. and Bennett, D. (2004). Forced convective boiling in vertical tubes for saturated pure components and binary mixtures. *AIChE Journal*, 26(3):454–461.

Chisholm, D. (1967). A theoretical basis for the lockhart-martinelli correlation for two-phase flow. *International Journal of Heat and Mass Transfer*, 10:1767–1778.

Chisholm, D. (1973). Pressure gradients due to friction during the flow of evaporating two-phase mixtures in smooth tubes and channels. *International Journal of Heat and Mass Transfer*, 16:347–348.

Cioncolini, A. and Thome, J. (2009). Unified macro-to-microscale method to predict two-phase frictional pressure drops of annular flows. *International Journal of Multiphase Flows*, 35:1138–1148.

Cioncolini, A. and Thome, J. (2011). Algebraic turbulence modeling in adiabatic and evaporation annular two-phase flow. *International Journal of Heat and Fluid Flow*, 32:805–817.

Cioncolini, A. and Thome, J. (2012a). Entrained liquid fraction prediction in adiabatic and evaporation annular two-phase flow. *Nuclear Engineering and Design*, 32:200–213.

Cioncolini, A. and Thome, J. (2012b). Void fraction prediction in annular two-phase flow. *International Journal of Multiphase Flows*.

Colebrook, C. and White, C. (1937). Experiments with fluid friction roughened pipes. *Proceedings of the Royal Society of London, Series A, Mathematical and Physical Sciences*, 161(906):367–381.

Colin, C., Fabre, J., and Dukler, A. (1991). Gas-liquid flow at microgravity conditions-i: dispersed bubble and slug flow. *International Journal of Multiphase Flow*, 17:533–544.

Colin, C., Fabre, J., and Kamp, A. (2012). Turbulent bubbly flow in a pipe under gravity and microgravity conditions. *Journal of Fluid Mechanics*, 711:469–515.

Colin, C., Fabre, J., and McQuillen, J. (1996). Bubble and slug flow at microgravity conditions: state of knwoledge and open questions. *Chemical Engineering Communications*, 141-142:155–173.

Collier, J. and Thome, J. (1994). Convective boiling and condensation. *Oxford Univeristy Press*.

Delhaye, J. (2008). Thermodynamique des réacteurs nucléaires. *EDP Science*.

DiMarco, P. (2012). Influence of force fields and flow patterns on boiling heat transfer performance: a review. *ASME Journal of Heat Transfer*, 134.

Dittus, E. and Boelter, L. (1930). Experiments with fluid friction roughened pipes. *Publication on Engineering*, 2:443.

Dukler, A., Fabre, J., McQuillen, J., and Vernon, R. (1988). Gas-liquid flow at microgravity conditions: flow pattern and their transitions. *International Journal of Multiphase Flow*, 14:389–400.

Eisenbraun, J. (2012). Liquid-vapor two-phase flows in microgravity. *Internship Report, University of Stuttgart*.

Elkow, K. and Rezkallah, K. (1997). Void fraction measurements in gas-liquid flows under 1-g and 0-g conditions using capacitance sensors. *International Journal of Multiphase Flow*, 23:815–829.

Fang, X., Zhang, H., Xu, Y., and Su, X. (2012). Evaluation of using two-phase frictional pressure drop correlations for normal gravity to microgravity and reduced gravity. *Advances in Space Research*, 49:351–364.

Feldmanis, C. (1966). Pressure and temperature changes in closed loop forced convection boiling and condesing processes under zero gravity conditions. *Annual Technical Meeting Proceedings, Institute of Environmental Sciences*.

Fore, L., Beus, S., and Bauer, R. (2000). Interfacial friction in gas-liquid annular flow: analogies to full and transition roughness. *International Journal of Multiphase Flow*, 26:1755–1769.

Forster, H. and Zuber, N. (1955). Dynamics of vapor bubbles and boiling heat transfer. *AIChE Journal*, 1:531–535.

Friedel, L. (1979). Improved friction pressure drop correlations for horizontal and vertical two-phase pipe flow. *European Two-Phase Flow Meeting*.

Gnielinski, V. (1976). New equations for heat and mass transfer in turbulent pipe and channel flow. *International Journal of Chemical Engineering*, 16:359–368.

Gungor, K. and Winterton, R. (1986). A general correlation for flow boiling in tubes and annuli. *International Journal of Heat and Mass Transfer*, 29:351–358.

Harmathy, T. (1960). Velocity of large drops and bubbles in media of infinite and restrictive extent. *AIChE Journal*, 1:289–295.

Huckerby, S. and Rezkallah, K. (1992). Flow pattern observations in two-phase gas liquid flow in a straight tybe under normal and microgravity conditions. *Processings of the National Heat Transfer Conference*, 2.

Jayawardena, S., Balakotaiah, V., and Witte, L. (1997). Flow pattern transition maps for microgravity two-phase flows. *AIChE Journal*, 43:1637–1640.

Kamp, A., Chester, A., Colin, C., and Fabre, J. (2001). Bubble coalescence in turbulent flows: a mechanistic model for turbulence induced coalescence applied to bubbly pipe flows under microgravity conditions. *International Journal of Multiphase Flow*, 27:1363–1396.

Kandlikar, S. (1990). A general correlation for saturated two-phase flow boiling heat transfer inside horizontal and vertical tubes. *International Journal of Heat Transfer*, 112:219–228.

Kew, P. and Cornwell, K. (1997). Correlations for the prediction of boiling heat transfer in small-diameter channels. *Applied Thermal Engineering*, 17:705–715.

Kim, S. and Mudawar, I. (2013). Universal approach to predicting saturated flow boiling heat transfer in mini/micro-channels - part. ii. two phase heat transfer coefficient. *International Journal of Heat and Mass Transfer*, 64:1239–1256.

Kim, T., Kommer, E., Dessiatoun, S., and Kim, J. (2012). Measurements of two-phase flow and heat transfer parameters using infrared thermometry. *International Journal of Multiphase Flow*, 40:56–67.

Lebaigue, O., Bouzou, N., and Colin, C. (1998). Results from the cyrene experiment: convective boiling and condensation of ammoniac in microgravity. *28th International Conference on Environmental Systems*.

Lockhart, R. and Martinelli, R. (1949). Proposed correlation of data for isothermal two-phase two-component flow in pipes. *Chemical Engineering Progress*, 45(1):39–48.

Lopez, J. and Dukler, A. (1986). Droplet entrainment in vertical annular flow and its contribution to momentum transfer. *AIChE Journal*, 32(1):1500–1515.

Lui, R., Kawaji, M., and Ogushi, T. (1994). An experimental investigation of subcooled flow boiling heat transfer under microgravity conditions. *10th International Heat Transfer Conference*, 7:497–502.

Müller-Steinhagen, H. and Heck, K. (1986). Flow boiling in tube under normal gravity and microgravity conditions. *Chemical Engineering and Processing: Process Intensification*, 20(6):297–308.

Narcy, M., de Malmazet, E., and Colin, C. (2014). Flow boiling in tube under normal gravity and microgravity conditions. *International Journal of Multiphase Flow*, 60:50–63.

Niklin, D. (1962). Two-phase flow in vertical tubes. *Chemical Engineering Progress*, 40:61–68.

Ohta, H. (1997). Experiments on microgravity boiling heat transfer by using transparent heaters. *Nuclear Engineering and Design*, 175:167–180.

Ohta, H. (2003). Microgravity heat transfer in flow boiling. *Advances in heat transfer*, 37:1–76.

Ohta, H. and Baba, S. (2013). Boiling experiments under microgravity conditions. *Experimental Heat Transfer: a Journal of Thermal Energy Generation, Transport, Storage, and Conversion*, 26(2-3):266–295.

Ohta, H., Fukiyama, H., Inoue, K., Yamada, Y., Ishikura, S., and Yoshida, S. (1994). Microgravity flow boiling in a transparent tube. *10th International Heat Transfer Conference*, (111).

Papell, S. (1962). An instability effect on two-phase heat transfer for subcooled water flowing under conditions of zero gravity. *American Rocket Society 17th Annual Meeting and Space Flight Exposition*.

Reinarts, T. (1993). Adiabatic two-phase flow regime data and modelling for zero and reduced (horizontal flow) acceleration fields. *University of Texas, PhD Dissertation.*

Reinarts, T., Best, F., and Hill, W. (1992). Definition of condensation two-phase flow behaviors for spacecraft design. *American Institute of Physics Conference, New York*, 1(246):1216–1225.

Riou, X., Colin, C., and Fabre, J. (2008). Bubble coalescence in gas-liquid pipe flow in microgravity. *ITT Bruxelles.*

Rouhani, S. and Axelsson, S. (1970). Calculation of void volume fraction in the subcooled and quality boiling regions. *International Journal of Heat Transfer*, 13:383–393.

Saito, M., Yamaoka, N., Miyazaki, K., Kinoshita, M., and Abe, Y. (1994). Boiling two-phase flow under microgravity. *Nuclear Engineering and Design*, 146:451–461.

Steiner, D. (1993). Chapter hbb. verein deutscher ingenieure. *VDI Wärmeatlas*, pages 451–461.

Sun, L. and Mishima, K. (2009). An evaluation of prediction methods for saturated flow boiling heat transfer in mini-channels. *International Journal of Heat and Mass Transfer*, 52(23-24):5323–5329.

Takamasa, T., Iguchi, T., Hazuku, T., Ibiki, T., and Ishii, M. (2003). Interfacial area transport of bubbly flow under microgravity environment. *International Journal of Multiphase Flow*, 29:291–303.

Vaschy, A. (1892). Sur les lois de similitude en physique. *Annales Télégraphiques*, 19:25–28.

Wallis, G. (1969). One dimensional two-phase flow. *McGraw-Hill.*

Wang, Z., Gabriel, K., and Manz, D. (2004). The influence of wave height on the interfacial friction in annular gas-liquid flow under normal and microgravity conditions. *International Journal of Multiphase Flow*, 30:1193–1211.

Whalley, P. (1987). Boiling, condensation and gas-liquid flow. *Oxford University Press.*

Zhao, J. (2005). Influence of bubble initial size on bubble-to-slug transition. *Journal of Engineering Thermophysics*, 26:793–795.

Zhao, J. (2010). Two-phase flow and pool boiling heat transfer in microgravity. *International Journal of Multiphase Flow*, 36:135–143.

Zhao, J. and Hu, W. (2000). Slug to annular flow transition of microgravity two-phase flow. *International Journal of Multiphase Flow*, 26:1295–1304.

Zhao, J., Xie, J., Lin, H., Hu, W., Ivanov, A., and Belyaev, A. (2001). Experimental studies on two-phase flow patterns aboard the mir space station. *International Journal of Multiphase Flow*, 27:1931–1944.

Zhao, L. and Rezkallah, K. (1993). Gas-liquid flow patterns at microgravity conditions. *International Journal of Multiphase Flow*, 19:751–763.

Zhao, L. and Rezkallah, K. (1995). Pressure drop in gas-liquid flow at microgravity conditions. *International Journal of Multiphase Flow*, 21:837–849.

Zuber, N. and Findlay, J. (1965). Average volumetric concentration in two-phase systems. *Journal of Heat Transfer*, pages 453–468.